

Thèse préparée à l'Université de Bretagne
Occidentale

pour obtenir le diplôme de DOCTEUR délivré de façon partagée
par L'Université de Bretagne Occidentale et l'Université de
Bretagne Loire

présentée par

Evangelia Batsi

Spécialité : Géosciences Marines

École Doctorale Sciences de la Mer et du Littoral

**Micro-seismicité et processus de fond de mer dans la
partie ouest de la Mer de Marmara: nouveaux résultats
fondés sur l'analyse des données de sismographes et
hydrophones sous-marins**

**Micro-seismicity and deep seafloor processes in the
Western Sea of Marmara: insights from the analysis of
Ocean Bottom Seismometer and Hydrophone data**



Thèse soutenue le 15 novembre 2017
devant le jury composé de :

Marco BOHNHOFF

Professeur Freie Universität Berlin and Helmholtz-Centre, et Chef de la section
Géomecanique et Rhéologie, GFZ, Rapporteur 1

Pascal BERNARD

Dr d'État, Physicien Titulaire, IPGP, Paris, Rapporteur 2

Louis GELI

Directeur de Recherche, Ifremer, Plouzané, Directeur de Thèse

Jacques DEVERCHERE

Professeur UBO-IUEM, Plouzané, Examinateur 1

Anne DESCHAMPS

Directrice de Recherche émérite du CNRS, Géoazur, Nice, Examinatrice 2

Ali PINAR

Professeur Université du Bosphore à Istanbul, Examinateur 3

Jean SCHMITTBUHL

Directeur de Recherche CNRS, IPGS, Strasbourg, Invité 1

Jean-Robert GRASSO

Chercheur, Physicien CNAP, ISTERre, Grenoble, Invité 2

*To my dear friend Olga who passed away
from cancer on the 10th of August 2017*

Table of Contents

Table of Contents.....	5
Acknowledgements.....	6
Abstract (in english).....	8
Résumé.....	10
Résumé étendu – Extended summary (in French).....	12
R.1 Contexte général et objectifs.....	12
R2. Structure du manuscrit.....	14
R3. Analyse de la micro-sismicité.....	15
R4. Analyse de signaux de courte durée.....	18
R5. Conclusions et perspectives.....	20
Conclusions.....	20
Perspectives.....	21
I. Introduction.....	23
I.1 General background.....	23
I.1.1 Geological context.....	23
I.1.2 Gas emissions from the Marmara seafloor.....	26
I.2 Objectives of the present work.....	28
I.2.1 Investigating the relations gas/micro-seismicity within the western SoM.....	28
I.2.2 Analysis of deep sea processes using OBS recordings.....	29
I.3 Structure of the manuscript.....	31
II. Discussing the 3 most recent micro-seismicity surveys based on OBS data from the Western SoM.....	32
II.1 Study by [Schmittbuhl et al, 2015].....	33
II.2 Study by [Yamamoto et al, 2017].....	34
II.3 Study by [Géli et al, 2018].....	37
III. An alternative view of the micro-seismicity along Main Marmara, Fault.....	103
III.1 High resolution study along the Main Marmara Fault (MMF).....	103
III.1.1 Foreword.....	103
III.1.2 Publication in review in BSSA.....	104
III.1.3 Implications not discussed in the BSSA Paper.....	229
III.1.3.1 On the use of b-values.....	229
III.1.3.2 On possible triggering effects.....	229
III.2 Deciphering the origin of the ultra-shallow (< 1 km) micro-seismicity.....	231
III.2.1 General considerations.....	231
III.2.2 Gas-related “ultra-shallow” seismicity.....	235
IV. Analysis of non-conventional signals.....	238
IV.1 Foreword.....	238
IV.2 New outcomes from the study of Short Duration Events (SDE) in the western SoM.....	239
V. Conclusion and perspectives.....	287
V.1 Conclusions.....	287
V.1.1 On the importance to improve earthquake location (particularly for shallow seismicity).....	287
V.1.2 On the existence of ultra-shallow seismicity within gas prone sediment layers.....	287
V.1.3 On the mechanical behaviour of the western segments of the SoM.....	287
V.1.4 On the strange, short duration events recorded by the OBSs.....	289
V.2 Perspectives for future research.....	289
V.2.1 Investigating the role of triggering effects on micro-seismicity.....	290
V.2.2 Investigating ultra-shallow seismicity by joint modelling of OBS/piezometer data.....	290
V.2.3 Further analysis and modelling of SDEs.....	290
References.....	292

Acknowledgements

I would like to acknowledge the following people who have contributed in different ways in the preparation of this PhD thesis.

First of all, a special mention goes to my PhD advisor Louis Géli for his continuous help, encouragement and patience throughout these three long years. Louis, thank you for your confidence in me, for always guiding me with enthusiasm and helping me to overcome the several difficulties that came along. Many thanks also goes to your family for their kindness and hospitality during my stay in Cambridge.

I am really thankful to Anthony Lomax and Jean Baptiste Tary for their great help and advices in processing seismic data, specifically their assistance with the earthquake location problem.

To Vincent Riboulot and Shane Murphy, for their help in processing seismic data and mostly for the constructive discussions, that significantly improved the study on ultra-shallow seismicity.

To Pascal Pelleau for his technical help with the OBS data. To Sylvain Bermell and Mathilde Pitel-Roudaut for their help with GIS tools. To Pauline Dupont, for always being there smiley, to support me with all the technical problems. To Mikael Evain for installing Linux software and for his help in technical questions.

To Bruno Marsset and Nabil Sultan for their help and support for improving my study.

To Gaye Bayrakci for providing us the algorithm of SDEs detection and to Joseph Ronzier for his assistance in the improvement of the algorithm. To Arthur Blouin for his assistance in interpreting the piezometric data.

Many thanks to INGV and KOERI colleagues for their hospitality and for providing us OBS data from their submarine networks.

To Frauke Klingelhofer that she was a real angel to me helping me to overcome all the major difficulties during the period of Louis's sabbatical leave and to Alison Chalm, the “mum of the laboratory” as they call her, that she stood there like a mum for me when I was phasing problems. Special thanks goes to all in general my colleagues at Ifremer, specifically the Department of Geosciences Marines that was actually my second home for three years, namely my “office-neighbours” and friends Pierre, Farah, Guillaume, David and many others for their warm hospitality and for all the beautiful and touching moments that we had together.

To Elisabeth Bondu of EDSM for her kindness and help.

To Brittany Region for offering me the PhD scholarship, to COST FLOW and the Scientific Direction of Ifremer for allowing me to carry out a mission at Cambridge University and to Ocean university of China in Qingdao, respectively.

To my dear family and friends around the world, f. George, f. Philippe, Sylvie, etc., who continue motivating me and supporting me for going through the several obstacles. Special thanks to my best friend and fiancé Gabriel, for his love, patience, support and encouragement during the last year of my PhD thesis, that surely without him this work could not have been accomplished.

I would like also to thank the people that I am might forgetting right now, that helped and supported me during this period.

Last but not least, I sincerely thank my dear friend Olga who passed away from cancer on the 10th of August 2017, to whom I dedicate this manuscript, for teaching me the way to fight against the difficulties, always with a big smile with never losing hope or faith.

Abstract (in english)

Since the devastating earthquakes of Izmit and Duzce, in 1999, east of Istanbul, the submerged section of the North Anatolian Fault (NAF), in the Sea of Marmara (SoM) has been the subject of an intense monitoring (mainly using land stations) and the target of numerous marine surveys. Still, the micro-seismicity remains poorly understood, mainly due to the difficulties of studying low-magnitude earthquakes in such submarine environments. In addition, although the connection of the SoM with the hydrocarbon gas system from the Thrace Basin is now well established, along with the presence of widespread gas within the sedimentary layers, the role of gas on seismicity is still not recognized. Here, we have used Ocean Bottom Seismometer (OBS) data from two submarine networks, from April 15th to July 31st, 2011 and from September 19th to November 15th, 2014.

Based on a high-resolution, 3D-velocity model, and on non-linear locations methods (NonLinLoc and NonDifLoc), our results show that:

1. We confirm the existence of strike-slip, micro-seismicity at great depths, particularly in the area where « repeaters » have been identified (at a depth of ~ 15 km), but we observe that not all micro-earthquakes are produced at crustal depths along the Main Marmara Fault.
2. In contrast, a large part of the micro-seismicity is produced in the basins, e.g. at shallow depths (< 6 à 8 km) : i) along secondary faults, oblique or parallel to the MMF and inherited from the complex, tectonic history of the North-Anatolian shear zone. Composite focal mechanisms, when available, indicate normal faulting in général but also reverse faulting at some places ; or ii) within the uppermost (< 1 km) sediment layers, containing gas pockets. Part of this ultra-shallow seismicity could well be triggered by the deep, strike-slip earthquakes of intermediate magnitude ($M_1 > 4.5$) that frequently occur along the western segments of the MMF.

In addition, at least two families of short duration events (SDEs) were detected. Namely:

1. the family (1) of “background SDEs” occurring on permanent, but irregular basis, at a rate of a few tens SDEs per day, resulting from many possible, local causes (i. e. near any individual OBS), e. g.: natural degassing from the seafloor, biological activity near the seabed, bioturbation (known to be very active at the Mamrara seafloor).
2. the family (2) of “swarmed SDEs”, occurring by sequences of a few hours, recorded more or less at the same time (e. g. within one hour) at distant OBSs. Each sequence is characterized by “swarms” of SDEs, lasting during ~ 20 to 30 minutes, separated by phases of relative quietness of ~ 10 minutes. This family includes two sub-families: (i) the first includes events recorded only by the geophone and (ii) the second includes SDEs recorded by both the geophone and the hydrophone, and characterized by a periodicity of ~ 1.6 to 2 seconds. Several causes could generate these kind of periodic signals like: anthropogenic causes (e. g. submarines), marine mammals, gas emissions, etc, but also tremors from the fault. The hypothesis that these signals could be causatively related to earthquakes (local or remote) cannot be precluded.

These results strongly advocate for the implementation of dense arrays of seafloor observatories in the SoM and raise the need for further research in terms of numerical modeling.

Keywords: micro-seismicity, earthquake location, ocean bottom seismometers, gas-related seismicity

Résumé

Depuis les séismes dévastateurs de 1999 d'Izmit et de Duzce, à l'est d'Istanbul, la partie immergée de la Faille Nord Anatolienne (FNA) en Mer de Marmara a fait l'objet d'une surveillance intense et de nombreuses campagnes océanographiques. Malgré cela, la micro-sismicité demeure mal connue. Par ailleurs, alors que la connexion avec le système pétrolier du Bassin de Thrace est désormais établie, le rôle du gaz sur la sismicité n'a toujours pas été véritablement identifié. Dans ce travail, nous avons analysé des données d'OBS acquises lors de 2 déploiements dans la partie ouest de la Mer de Marmara (d'avril à juillet 2011 et de septembre à novembre 2014). Nos résultats de localisation établis à partir d'un modèle 3D de vitesses et les méthodes non-linéaires (NonLinLoc, NonDiffLoc) de Lomax montrent que :

1. Si nous confirmons l'existence de microséismes en décrochement, se produisant à grande profondeur, notamment dans la zone (à ~ 15 km) où des « répéteurs » ont été identifiés, nous observons que les séismes ne se produisent pas tous à des profondeurs crustales, le long de la faille de Marmara (ou Main Marmara Fault - MMF).
2. *A contrario*, une grande partie de la micro-sismicité se produit dans les bassins à faible profondeur (< 6 à 8 km) : i) le long de failles secondaires, obliques ou parallèles à la MMF, héritées de l'histoire tectonique complexe de la FNA. Les mécanismes au foyer « composites », quand ils ont pu être calculés, sont généralement en faille normale, parfois en chevauchement ; ou ii) dans des couches de sédiments superficiels (à des profondeurs inférieures à quelques centaines de mètres), caractérisées par la présence de poches de gaz libre. Une partie de cette sismicité pourrait être déclenchée par les séismes profonds, de magnitude intermédiaire ($M_1 > 4.5$) qui se produisent régulièrement le long de la MMF.

Par ailleurs, nous distinguons 2 familles de signaux transitoires de courte durée (< 1 s):

- i. La famille (1) des SDE se produisant de manière permanente mais discontinue (« background SDE activity »), à raison de quelques dizaines de SDE par jour. Les causes de

ces SDE sont vraisemblablement locales (i.e. proches de l'OBS). Entre autres : la bioturbation (abondante en Mer de Marmara) ; l'activité biologique (i. e. poissons heurtant les capteurs) ; le micro-bullage de fond de mer ; le transfert de fluides à l'interface eau/sédiment ; les micro-mouvements de sédiments ; etc.

- ii. La famille (2) des SDE se produisant par séquences s'étalant sur quelques heures ; chaque séquence étant constituée de « paquets » ou « d'essaims » (« swarmed SDEs ») d'environ 20 à 30 minutes, suivis d'une période de calme relatif d'environ une dizaine de minutes. On distingue deux sous-familles : la famille 2a des SDE enregistrés uniquement sur les 3 composantes du sismomètre ; et la famille 2b des SDE enregistrés sur les 4 composantes, dont l'hydrophone. A l'échelle individuelle, les SDE de cette dernière famille (2b) apparaissent de manière périodique (toutes les 1.6 s à 2 s environ). Les « paquets » étant plus ou moins corrélés d'un OBS à l'autre, les causes ne sont pas locales, au niveau d'un OBS particulier. On citera, entre autres : la présence de mammifères marins ; l'activité anthropogénique (sous-marins) ; l'effondrement de cavités riches en gaz ; mais aussi l'existence de « tremors » le long de la faille ; etc. Enfin, l'hypothèse d'une relation de causalité avec la sismicité (locale ou lointaine) ne peut pas être exclue.

Ces travaux en appellent à l'implantation d'observatoires de fond mer et ouvrent la voie à des perspectives prometteuses de modélisation numérique.

Mots-clés: *micro-sismicité, localisation, sismomètres de fond de mer, sismicité induite par le gaz.*

Résumé étendu – Extended summary (in French)

R.1 Contexte général et objectifs

La Mer de Marmara est située à l'extrémité Ouest de la Faille Nord Anatolienne (FNA), le long de laquelle la plaque Anatolienne coulisse relativement à la plaque Eurasienne à raison de 22mm/an environ, sur une longueur de 1200 km. La FNA est régulièrement affectée par des séismes destructeurs. Peuplée de 12 millions d'habitants, la région d'Istanbul est située le long du secteur submergé de la FNA, en Mer de Marmara, qui n'a pas été affecté par un séisme important depuis au moins 1766. De ce fait, la ville d'Istanbul est considérée comme étant exposée à un fort aléa sismique.

Depuis les séismes dévastateurs de 1999, qui ont fait 20000 victimes dans la région d'Izmit et de Duzce, à l'est d'Istanbul, la Mer de Marmara a fait l'objet de nombreuses campagnes océanographiques. Une littérature abondante existe désormais sur l'évolution tectonique de la FNA et sur les principales caractéristiques géologiques de la Mer de Marmara. Le lecteur est invité à s'y reporter, en consultant par exemple les synthèses de [Sengör et al, 2005] et [Sengör et al, 2011], ainsi que les références citées. Ici, nous rappellerons brièvement les principales caractéristiques à garder en tête pour comprendre le présent travail de thèse:

- Avant d'entrer en Mer de Marmara, la FNA se sépare en trois branches. Située sur la branche nord, la Mer de Marmara est composée de 3 bassins profonds, le bassin de Tekirdag, le bassin Central et le bassin de Çınarcik, séparés par 2 hauts bathymétriques, les hauts

Ouest et Central. Les bassins, avec des profondeurs d'eau entre 1100 et 1300 m, sont des fosses allongées plus ou moins dans la direction Est-Ouest remplis d'une épaisseur de 4 à 6 km de sédiments d'âge Plio-Quaternaire. On doit donc s'attendre à de fortes variations de vitesses sismiques dans les bassins.

- En Mer de Marmara, la FNA traverse des séries Eocène, situées dans le prolongement du Bassin de Thrace, contenant des hydrocarbures, notamment des gaz, qui remontent jusqu'à la surface le long des failles. D'après [Dupré et al, 2015], les sites d'émissions de gaz sont réparties le long de la faille de Marmara, mais également sur le bord des bassins ou au sommet des anticlinaux. D'après les données de sismique réflexion « Haute Résolution » 3D acquises au sommet du « Haut Ouest », les couches sédimentaires superficielles sont parfois riches en gaz en libre.

Malgré toute l'importance des réseaux terrestres permanents de surveillance sismique et malgré les nombreuses campagnes réalisées à partir de sismomètres temporaires de fond de mer, la micro-sismicité le long des segments immergés de la FNA, en Mer de Marmara, demeure encore mal connue. Par ailleurs, le rôle du gaz sur la micro-sismicité reste à étudier.

Le **premier objectif** de la présente thèse est donc de préciser la micro-sismicité dans le domaine marin, suivant une approche « haute résolution », basée sur le modèle de vitesse 3D, établi par Ifremer à partir de toutes les connaissances géologiques et géophysiques acquises en Mer de Marmara au cours des 15 dernières années.

Le **deuxième objectif** est d'étudier les relations entre la présence de gaz et la sismicité.

Au cours de notre analyse, nous avons pu mettre à jour de nombreux signaux transitoires, de courte durée (< 1 s), associés à des processus physiques vraisemblablement variés, pouvant siéger soit dans la colonne d'eau, en fond de mer ou en profondeur. Le **troisième objectif** est d'étudier ces signaux, afin d'en déterminer l'origine.

R2. Structure du manuscrit

Cette thèse est construite à partir d'articles soumis dans des revues internationales. Par ailleurs, avons fait le choix de la langue anglaise. Le manuscrit est composé de 5 parties :

- La première partie est une introduction, présentant le contexte général et les objectifs.
- La deuxième partie est une synthèse des deux études de micro-sismicité les plus récentes utilisant des données OBS, que ce soit en combinaison avec des données terrestres [Schmittbuhl et al, 2015] ou avec des données de fond de mer uniquement [Yamamoto et al, 2017] et [Géli et al, 2018] (en cours d'expertise à *Nature Scientific Reports*). Compte tenu du temps que j'ai passé à ce dernier papier, la version en cours d'expertise est intégralement incluse dans le présent manuscrit.
- La troisième partie constitue le cœur de ma thèse. Il s'agit d'une étude « haute résolution » de la sismicité de la partie Ouest de la Mer de Marmara, fondée sur l'analyse de deux jeux de données OBS couvrant les périodes respectives du 15 avril au 31 juillet 2011 et du 19 septembre au 14 novembre 2014. Cette partie fait l'objet d'une publication. L'une, en cours d'expertise au *Bulletin of Seismological Society of America*, décrit les résultats des localisations.
- La quatrième partie est une étude des signaux de courte durée (< 1 s) que l'on enregistre de manière systématique sur les OBS déployés en Mer de Marmara. Les travaux font l'objet

d'une publication soumise à *Deep Sea Research II*.

- La cinquième partie, enfin, fait état des conclusions et perspectives.

R3. Analyse de la micro-sismicité

L'étude de [Géli et al, 2018]. Le 25 juillet 2011, un séisme de magnitude 5.1, suivi d'une quantité inhabituelle de répliques, s'est produit en Mer de Marmara, sous le « Haut Ouest » (« Western High »), pratiquement à l'aplomb d'un système hydro-géologique connu pour contenir des indices d'hydrocarbures : émissions de gaz en fond de mer ([Géli et al, 2008], [Dupré et al, 2015]) ; présence d'hydrates de gaz [Bourry et al, 2009], de volcans de boue et de gaz libre dans les sédiments superficiels [Thomas et al, 2012] ; etc.

Par chance, ce séisme a pu être enregistré, non seulement par le réseau permanent d'OBS câblés du KOERI, mais aussi par le réseau temporaire d'OBS qui avait été déployé par l'Ifremer du 15 avril au 31 juillet 2011. Ce séisme et sa séquence de répliques ont donc pu être étudiés en détail [Géli et al, 2018]. Pour ce faire, un modèle de vitesses 3D a été spécifiquement développé, pour tenir compte des particularités géologiques de la Mer de Marmara et les logiciels *NonLinLoc* et *NonDiffLoc* de localisation d'Anthony Lomax ont été mis en oeuvre (voir [Lomax et al, 2009] et les références *ad hoc* sur le site <http://alomax.free.fr/alss/>).

Les résultats montrent que les répliques se produisent pour l'essentiel dans les sédiments, à des profondeurs inférieures à 6 km :

- entre 2 et 5 km, ce qui, d'après les données de géochimie et de flux de chaleur, correspond à la fenêtre à gaz ;
- à des profondeurs inférieures à 2 km, à l'intérieur des couches sédimentaires réputées riches en gaz.

Ces résultats, très différents de ceux des travaux les plus récents ([Karabulut et Aktar, 2013] ;

[Schmittbuhl et al, 2015]), méritaient d'être vérifiés, d'autant plus que la station centrale du réseau temporaire, qui se trouvait pratiquement à l'aplomb de l'épicentre, avait cessé de fonctionner (les stations les plus proches étaient situées à une dizaine de kilomètres de l'épicentre). Pour lever les ambiguïtés, un deuxième déploiement d'OBS a donc été réalisé par Ifremer, du 19 septembre au 14 novembre 2014, lors de la campagne MARSITE-Cruise. L'analyse de ces données de 2014 et la ré-analyse des données OBS de 2011, exposées ci-après, constitue le cœur de mon travail de thèse.

Étude de la micro-sismicité à partir des données de 2011 et 2014. J'ai suivi la même démarche que celle proposée par [Géli et al, 2018], à partir du même modèle-3D de vitesses et en utilisant les mêmes méthodes d'Anthony Lomax, tant pour la détection et association des phases, que pour la localisation d'évènements. Seuls les évènements répondant aux critères de qualité fixés par la méthode de localisation ont été conservés pour l'analyse, ce qui représente seulement 20% du nombre total d'évènements détectés.

Les résultats, soumis au *Bulletin of Seismological Society of America* montrent que :

- Tous les séismes ne se produisent pas nécessairement à des profondeurs crustales, suivant des mécanismes focaux de décrochement, le long de la « faille principale de Marmara » (ou Main Marmara Fault - MMF).
- Des microséismes, caractérisés par des mécanismes en décrochement, se produisent de manière répétée vers environ 15 km de profondeur, sous forme de « répéteurs », à l'instar de ce qui a déjà été observé par [Schmittbuhl et al, 2016] et [Bonhoff et al, 2017]. Nous proposons, sans pouvoir la démontrer, l'hypothèse qu'il pourrait y avoir une corrélation entre ces répéteurs et l'occurrence de séismes le long de la faille de Ganos. Cette hypothèse reste à vérifier au moyen de méthodes statistiques adaptées.
- A contrario, une grande partie de la micro-sismicité se produit à faible profondeur (< 6 à 8 km) :

- le long de failles secondaires, obliques ou parallèles à la MMF, héritées de l'histoire tectonique complexe de la zone de faille Nord-Anatolienne. Les mécanismes au foyer « composites », quand ils ont pu être calculés, sont généralement en faille normale. Des mécanismes en chevauchement, associés à des structures « inverses » en fleur, ont également été calculés.
- dans les sédiments superficiels, à des profondeurs < 1 à 2 km, en général dans des zones caractérisées par de fortes émissions de gaz détectées en fond de mer. Ces séismes pourraient bien être, pour partie, déclenchés par la zone de faille.

La question des séismes « ultra-superficiels ». Il est généralement admis que les sédiments meubles proches de la surface sont trop mous pour accumuler l'énergie élastique nécessaire pour fabriquer des ruptures cassantes, susceptibles d'engendrer des séismes : « leur rhéologie ne le permet pas ». C'est pourquoi nous avons consacré une partie (trop courte, hélas) de notre travail à étudier en détail la sismicité « ultra-superficielle ». Pour ce faire, nous avons positionné en profondeur les répliques du séisme de magnitude 5.1 du 25 juillet 2011 se trouvant à l'intérieur de la boîte de sismique 3D « haute-résolution » acquise en 2009 sur le haut ouest [Thomas et al, 2012]. Aux erreurs de localisation près, ces séismes apparaissent systématiquement être associés à des failles normales décalant des couches de sédiments riches en gaz. Sachant que ces séismes « ultra-superficiels » se sont produits suite au choc principal de magnitude 5.1, nous proposons qu'ils résultent de la combinaison de deux effets : i) le transfert de contrainte liée à la secousse principale, qui crée de la micro-fracturation le long des chemins de migration de gaz, favorisant ainsi sa remontée ; ii) le gaz remontant des profondeurs jusqu'aux couches de surface, représente une source de surpression qui contribue à déclencher les séismes, non seulement le long des conduits de

migration du gaz, mais également dans les couches « ultra-superficielles », elles-mêmes riches en gaz.

R4. Analyse de signaux de courte durée

Les OBS sont des instruments extrêmement sensibles, constitués de 4 composantes (2 horizontales, 1 verticale et 1 hydrophone), initialement conçus pour enregistrer les séismes. Du fait de leur sensibilité, les OBS enregistrent tous types de signaux. La moindre perturbation du sédiment en fond de mer peut engendrer un signal susceptible d'être enregistré par l'OBS. L'existence de signaux de courte durée (< 1 s) a été rapportée pour la première fois en 1981 par [Burkisk et al, 1981]. A partir d'enregistrements OBS déployés à différentes profondeurs, dans différents environnements dans le Pacifique, ces auteurs avaient proposé que ces signaux pouvaient avoir une origine biologique (poissons ou autres).

Pris individuellement, ces signaux (ici appelés SDE pour Short Duration Event) ne sont pas enregistrés d'un OBS à l'autre. Les SDE ne présentant *a priori* aucun intérêt pour la détection des séismes, ils n'ont jamais l'objet d'attention particulière de la part des sismologues. Il a fallu attendre le début des années 2000 pour qu'on s'y intéresse de nouveau, lorsqu'on s'est rendu compte que ces signaux apparaissaient de manière systématique. En effet, la bioturbation, l'activité biologique dans la colonne d'eau (y compris celle des mammifères marins), la circulation de fluides à l'interface eau/sédiment, les émissions de gaz, tout cela peut créer des perturbations à l'interface eau/sédiment qui pourraient à l'origine des signaux observés de courte durée. Près des suintements froids, notamment, dans des environnements sédimentaires riches en gaz (hydrocarbures, méthane biogénique, hydrates de gaz, etc), les SDE apparaissent systématiquement et en grand nombre, ce qui laisse penser qu'ils pourraient être la signature de phénomènes de dégazage de fond de mer.

En Mer de Marmara, ces signaux ont été étudiés pour la première fois par Jean-Baptiste Tary, au cours de sa thèse [Tary, 2012 ; Tary et al, 2012] puis par [Embriaco et al, 2013] ; [Bayrakci et al, 2013] ; [Casellato, 2014]. Du fait de la présence systématique de gaz dans les sédiments superficiels, il a été proposé que les SDE pouvaient résulter de l'effondrement des parois de micro-cavités remplies de gaz, proches de l'interface eau/sédiment.

L'analyse présentée ici des données enregistrées par les OBS et hydrophones de fond de mer déployés en 2011 et 2014 permet de distinguer 2 familles de SDE:

- 1) Les SDE se produisant de manière permanente mais discontinue, à raison de quelques centaines de SDE par jour. Ces SDE sont généralement de faible magnitude et enregistrés uniquement sur les 3 composantes du sismomètre (et généralement pas sur l'hydrophone, sauf si celui-ci est placé très près du sol). Ils sont censés représenter une activité dite « de fond » (« background SDE activity »), qui peut avoir plusieurs causes possibles: la bioturbation, l'activité benthique, les perturbations liées aux courants de fond ou aux entrées de fluide, l'effondrement de micro-cavités engendré par l'expulsion de gaz, etc.
- 2) Les SDE se produisant par « paquets » ou « essaims » (swarmed SDEs), que l'on peut subdiviser en 2 sous_familles :
 - Sous-famille 2a: Les SDE enregistrés uniquement sur les 3 composantes du sismomètre (et généralement pas sur l'hydrophone, sauf si celui-ci est placé très près du sol) se produisant par « paquets ». D'après notre analyse, fondée sur des critères de corrélation visuelle, il semble que ces SDEs apparaissent en réponse à des sollicitations sismiques (séismes locaux ou éloignés), mais cela reste à prouver.

- Sous-famille 2b: Enfin, les SDE enregistrés sur les 4 composantes, dont l'hydrophone, se produisant de manière périodique, toutes les 2 secondes environ. Les signaux apparaissent par séquences s'étalant sur quelques heures ; chaque séquence étant constituée de « paquets » d'environ 20 à 30 minutes, suivis d'une période de calme relatif d'environ une dizaine de minutes. Les SDE de cette famille ont une fréquence plus élevée (i.e. entre 30 et 50 Hz) que les SDE des familles 1 et 2a. Plusieurs causes sont invoquées pour les expliquer : anthropogéniques (par exemple, des sous-marins) ; biologiques (par exemple mammifères marins) ; ou sismologiques. La coïncidence (d'après notre analyse visuelle) entre l'apparition de ces SDE et l'occurrence de séismes n'exclut pas l'hypothèse d'une relation de causalité avec la sismicité (locale ou lointaine).

Cette nouvelle analyse de SDEs s'avère être extrêmement prometteuse, tant pour la connaissance des processus de fond de mer, que pour l'étude de la réponse sismique des sédiments superficiels. Mais cette analyse, qui a permis de faire des observations inédites, mais inexpliquées est essentiellement fondée sur des critères de corrélation visuelle. Pour progresser, il est désormais nécessaire d'automatiser les procédures et de passer à la modélisation.

R5. Conclusions et perspectives

Conclusions

1. La complexité des problèmes de localisation en Mer de Marmara exige le déploiement d'un grand nombre de stations de fond de mer, réparties de manière équilibrée de part et d'autre de la faille principale (MMF).
2. Nos travaux ont permis de révéler l'existence d'une importante micro-sismicité dans la partie ouest de la Mer de Marmara, localisée dans les bassins, à des profondeurs focales

inférieures à 6 km, le long de failles secondaires.

3. En outre, il existe une sismicité ultra-superficielle (à des profondeurs $z <$ quelques centaines de mètres), qui apparaît être déclenchée par les séismes de magnitude intermédiaire ($M_1 > 4.5$) dans les couches de sédiments riches en gaz.
4. Les OBS enregistrent des signaux transitoires de courte durée (< 1 s), appelés SDE (pour short duration events) dont l'origine demeure toujours inconnue à ce jour. Nos travaux ont permis de distinguer plusieurs familles de signaux. Les processus à l'origine de ces signaux n'ont pas pu être identifiés de façon certaine, mais plusieurs candidats sont possibles. A l'échelle locale (i. e. au voisinage immédiat de l'OBS), on citera –entre autres : la bioturbation (qu'on sait être abondante en Mer de Marmara) ; les perturbations générés par l'activité biologique (par exemple : poissons heurtant les capteurs) les phénomènes de micro-bullage de fond de mer ; le transfert de fluides à l'interface eau/sédiment ; les micro-mouvements des sédiments engendrés par les courants de fond ; etc. A l'échelle de la Mer de Marmara, diverses causes, naturelles ou anthropogéniques, peuvent être invoquées : la sismicité -lointaine ou locale- ; l'existence de tremors non documentés à ce jour ; la présence de mammifères marins ou de sous-marins ; etc.

Perspectives

Notre travail a permis de faire un grand nombre d'observations inédites. Notre approche, essentiellement qualitative, ouvre la voie à la modélisation numérique :

1. Modéliser les phénomènes de déclenchement. Notre étude fait apparaître l'hypothèse d'une corrélation possible entre la sismicité en Mer de Marmara et la sismicité lointaine (le long de la faille de Ganos, en particulier). La corrélation doit être vérifiée et l'hypothèse de causalité, testée par un travail de modélisation approfondi.
2. Modéliser numériquement le rôle du gaz sur la sismicité.
3. Modéliser la sismicité "ultra-superficielle", en utilisant, notamment, les données du

piézomètre et des OBS. En particulier, tester les hypothèses suivant lesquelles i) les SDEs pourraient être associés à des tremors sismiques; ii) il y aurait une relation de causalité entre les SDE et la sismicité (locale ou lointaine).

4. Modéliser les évènements de courte durée (SDE).

I. Introduction

I.1 General background

I.1.1 Geological context

The North Anatolian Fault (NAF) is a right-lateral strike-slip fault that accommodates a relative motion of 20-27 mm/yr between the Eurasian and the Anatolian plates, generating numerous destructive earthquakes along its 1200 km length, from its junction to the East Anatolian Fault to the Gulf of Ganos (Figures I.1.1.1 and I.1.1.2) (e.g. see the review of [Sengör *et al*, 2005] and references herein).

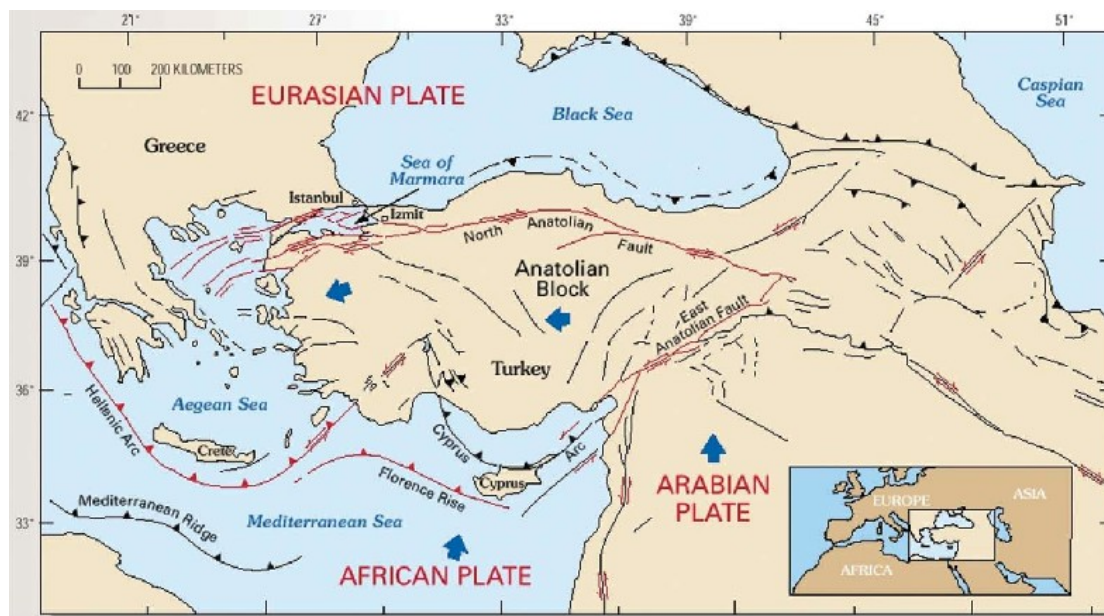


Figure I.1.1.1: General tectonic map of Turkey showing the: North Anatolian Fault (NAF), East Anatolian Fault, Hellenic and Florence trenches. The Sea of Marmara (SoM) is indicated with a black arrow, between the Black Sea and the Aegean Sea. The main structural features of the area are shown with red and black lines. Blue arrows show relative motion between the plates. (Source USGS).

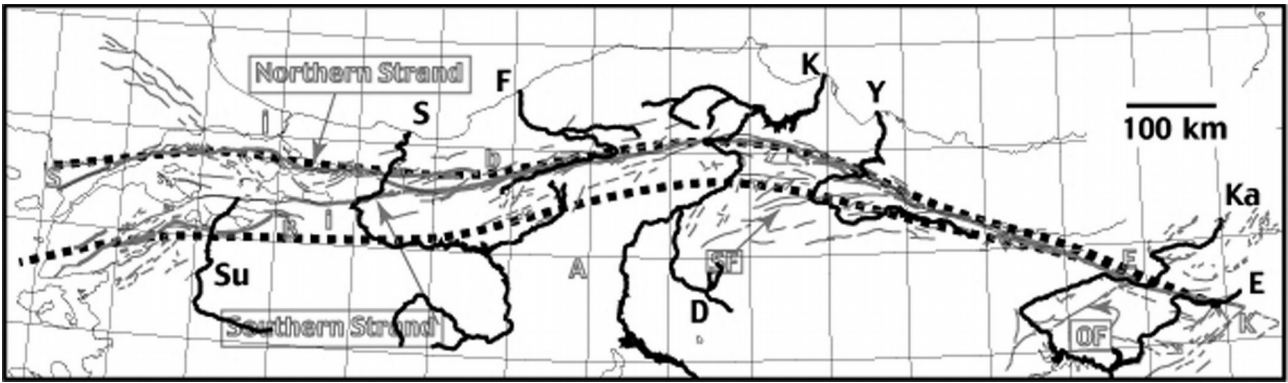


Figure I.1.1.2: From [Sengör et al, 2014]. The North Anatolian Shear Zone (NASZ: delimited by discontinuous lines) and the courses of the major rivers traversing it. Key to abbreviations, from east to west (black letters): E, Elmalı/Peri (tributary of the Murat before the construction of the Keban Dam); Ka, Karasu (Elmalı/Peri + Karasu = Fırat (Euphrates) without Murat (outside this map)); Y, Yesilirmak; K, Kızılırmak; D, Delice; F, Filyos (/Yenice/Ara./Sog'anlı (formerly Ulu.ay)/Gerede Suyu); S, Sakarya; Su, Susurluk. Grey letters in outline show locations of some cities and tectonic features: A, Ankara; B, Bursa; b, Bolu; E, Erzincan; I, Istanbul; I, Iznik (lake); K, Karlöva; OF, Ovacık Fault; SF, Sungurlu Fault. Notice that significant abrupt deflections of river courses are confined to the area of the NASZ. Following [Sengör et al. 2005], the faults shown to be parts of the NASZ in the southern part of the Tokat Lobe are here left out of the NASZ because of their as yet uncertain relationship to the NASZ and to the geometry of the major river courses (slightly modified from [Sengör et al. 2005], fig. 6.

During the 20th century, a series of destructive earthquakes occurred along the NAF with an apparent propagation more or less from east to west, until 1999, year of the last catastrophic events in Izmit and Düzce. The SoM is situated between the 1912 (e.g. Ganos, M7.4 event) and the 1999 ruptures along the only part of the fault that has not ruptured since 1766 (see Figure I.1.1.3). The Marmara region is thus considered to be within a seismic gap where the probability of occurrence of an earthquake of magnitude greater than 7, is high (e.g. [Aochi & Ulrich, 2015]).

Since the devastating earthquakes of 1999, a large amount of geological, geophysical and geochemical data were collected, which allowed the scientific community to have a detailed view of the submarine domain. It is not the scope of this study to review all the abundant literature that

exists on the evolution of the NAF, particularly in the Marmara Region. We will just invite the reader to refer to the reviews of [Sengör *et al*, 2005] and [Sengör *et al*, 2015] and restrict ourselves to briefly recall the points, which we think, are of direct relevance to our work. These points concern the evolution of the Marmara shear zone, the relation with the gas-bearing Thrace Basin and the formation of the deep, submerged basins.

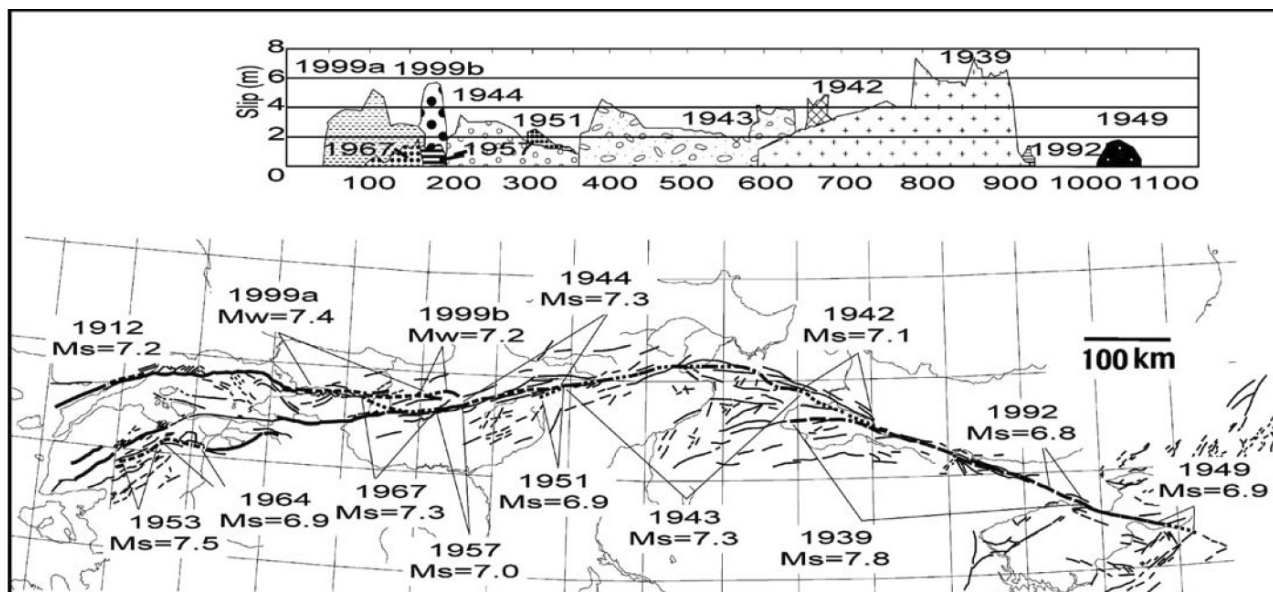


Figure I.1.1.3: From [Sengör *et al*, 2005]. Earthquakes and related fault displacement along the North Anatolian Fault (NAF) since December 26/27, 1339 Erzincan earthquake. Note the remarkable east-to-west migration of the major shocks, first emphasized by [Egeran and Lahn 1944]. The figure has been compiled from [Şaroğlu *et al*, 1987, 1992], [Eyidoğan *et al*, 1991], [Barka, 1996], [Barka *et al*, 2000a] and [Akyüz *et al* 2000].

The present-day NAF more or less follows the late Cretaceous Intra-Pontide suture zone, which formed after the closure and subduction of the Tethyan Ocean (*e.g.* [Sengör and Yilmaz, 1981; Okay *et al*, 1996; Okay and Tuysuz, 1999]). In this context, the Thrace Basin developed during the Late Cretaceous – Early Eocene as a fore-arc basin by closure of the Neotethys Ocean. The North Anatolian Shear Zone (NASZ) developed during the Middle-Late Miocene (~ 11-13 Ma) formed a

keirogen (e.g. a broad shear zone concentrating a large variety of tectonic structures linked to the shear deformation), delimited today by the Northern Strand and the Southern Strand respectively (e.g. [Sengör et al, 2005], [Sengör et al, 2015]). As the NASZ keirogen propagated and widened westwards, the West-Northwest-striking Thrace system connected to the Marmara area. Since the middle-late Miocene, the North Anatolian shear zone evolved from a pull-apart system, to a transpressional regime, and finally to a recent (< than ~ 450 ka, after [Grall et al, 2012]) strain localization along a single through-going strike-slip fault, named the Main Marmara Fault or MMF (e. g. [Aksu et al, 2000]; [Le Pichon et al, 2001]; [Le Pichon et al, 2003]; [Imren et al, 2001]; [Meade et al, 2002] ; [Rangin et al, 2004]).

The present-day SoM thus results from the interplay between a ~N120 E fault zone, likely related to the gas-bearing Thrace Basin, and the East-West NASZ ([e.g. Yaltirak, 2002]). The specific, geologic inheritance described above explains that under the SoM, the NAF splits into a complex fault network with numerous fault strands of varying dip and strike, forming three prominent ~1250 m-deep basins, separated by NE trending transpressional highs, respectively from east to west : the Çınarcık Basin ; the Central High ; the Kumburgaz Basin ; the Central Basin ; the Western High; the Tekirdag basins. Due to the high sedimentation rate and to the High deformation rate (e.g. [Çagatay et al, 2000]; [Çagatay et al, 2009]), these deep basins developed as troughs, filled by Plio-quaternary sediments characterized by slow seismic velocities: about 4 km of sediment thickness in the Tekirdag basin; and ~ 6 km in the Çınarcık and Central basins (e.g. [Bécel, 2006; Carton et al, 2007; Bécel et al, 2010]).

I.1.2 Gas emissions from the Marmara seafloor

A number of studies since 1999 have revealed the existence of widely-spread gas emissions from the Marmara seafloor (e.g. [Alpar, 1999]; [Halbach et al, 2004]; [Kuşçu et al, 2005] ; [Géli et al,

2008]; [Zitter et al, 2008]). Based on the detailed analysis of multibeam echo sounder data, with water column records, [Dupré et al, 2015], (Figure I.1.2.1), showed that “acoustically detected gas emissions are spatially controlled by a combination of factors, including fault and fracture networks in connection to the MMF system and inherited faults, the nature and thickness of sediments (e.g., occurrence of impermeable or gas-bearing sediments and landslides), and the connectivity between the seafloor and gas sources, particularly in relation to the Eocene Thrace Basin”.

Although the relationship between seepage and fault activity is not one to one (e.g. active faults do not necessarily conduct gas, and scarps corresponding to deactivated fault strands may continue to channel fluids), Dupré et al [2015] pointed out that occurrence of gas emissions appears to be correlated with the distribution of microseismicity. These authors particularly underlined that “the relative absence of earthquake-induced ground shaking along parts of the Istanbul-Silivri and Princes Islands segments is likely the primary factor responsible for the comparative lack of gas emissions along these fault segments”.

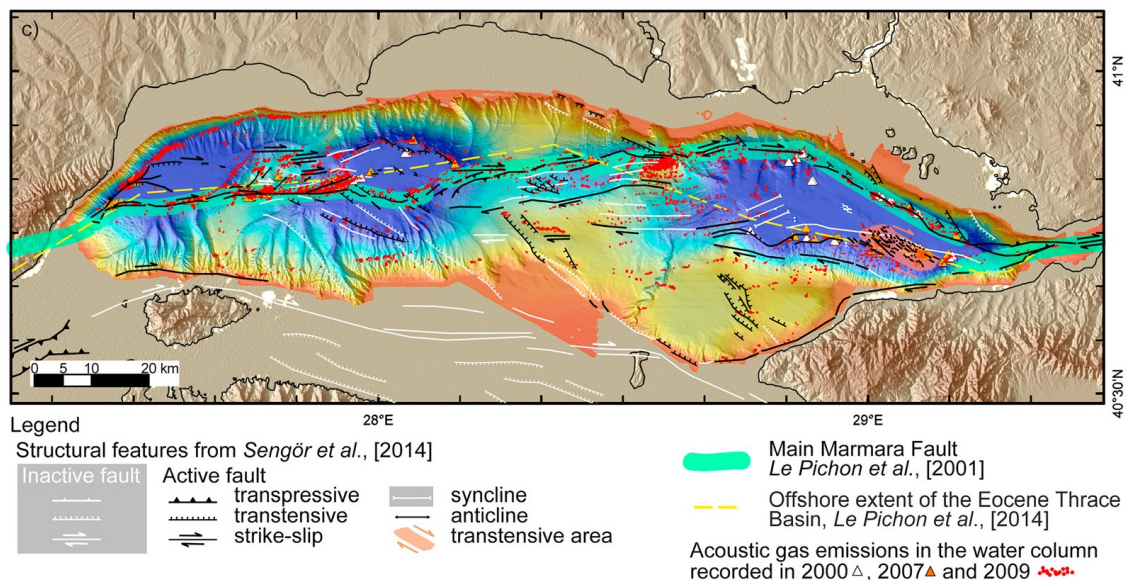


Figure I.1.2.1: From [Dupré et al 2015]. Bathymetric map of the SoM. Fault networks from [Sengör et al. 2014] with the offshore extent of the Eocene Thrace Basin from [Le Pichon et al, 2014]. Red dots indicate acoustically detected gas emissions sites after [Dupré et al 2015].

I.2 Objectives of the present work

I.2.1 Investigating the relations gas/micro-seismicity within the western SoM

The primary objective of this work is to study the relations between seismicity and gas occurrence within the sediment layers below the Sea of Marmara.

The connexion with hydrocarbon gas systems (such as the Thrace basin) and the wide-spread occurrence of gas within the sediment layers are unique characteristics of the SoM, compared to other large, active, continental transform faults, such as the San Andreas Fault system in California, the NAF system in northern Turkey, the Alpine Fault in New Zealand, and the Altyn Tagh Fault in the northern Tibetan Plateau. Still, these characteristics and the influence of gas occurrence on the seismicity pattern have received little attention so far.

A preliminary 25-day test conducted with four Ifremer OBS in 2007 revealed the existence of a cluster of 13 small-magnitude earthquakes that occurred in less than 30 hr at shallow crustal depth below the western slope of the Tekirdag basin, where intensive gas emissions escaping from the seafloor have also been found [Tary *et al*, 2011]. Based on this study, [Tary *et al*, 2011] suggested that tectonic strain below the western slope of the Tekirdag basin likely « contributes to maintain a high permeability in fault zones and that the fault network provides conduits for deep-seated fluids to rise up to the seafloor ».

A new deployment was performed by Ifremer in the western SoM from April, 15th to July, 31st, 2011, to complement the permanent, cabled OBS network operated by KOERI. The results were

first published as early as 2013 in an internal report by [*Cros and Géli, 2013*]. These results confirmed the relation between gas and seismicity through the detailed analysis of the aftershock sequence that followed the M 5.1 earthquake of July, 25th, 2011, below the Western High, where numerous gas emissions along with gas hydrates were documented. As early as in 2013, *Cros and Géli [2013]* found (and published in an internal report) that most aftershocks occurred at shallow depth (<6 km), within gas prone sediment layers.

Because the results were at odds with previous views that considered that the micro-seismicity was essentially crustal, a new OBS deployment was performed by Ifremer in 2014, from September, 19^h to November 14th, 2014.

During my PhD thesis, I contributed to the paper of [*Géli et al, 2018*] which is eventually in press in *Nature Scientific Reports*. The core of my work, however, was the analysis of the OBS data that was remaining unpublished in [*Géli et al, 2018*]. Namely: the full OBS dataset of 2014 and the OBS dataset of 2011 for the period preceding the M 5.1 earthquake of July, 25, 2011.

I.2.2 Analysis of deep sea processes using OBS recordings

The secondary objective of this work is to perform a systematic analysis of the strange, short duration (< 1 s) signals that are commonly recorded with the OBSs deployed in the SoM

Another aspect of the OBS recordings from the SoM that has been not so often discussed so far, is the systematic existence of puzzling, short duration events, hereafter called **Short Duration Events**

(SDE), which were also found to occur in different geological environments around the world such as the Mediterranean Sea, the Gulf of Guinean, off coast Taiwan, the Sea of China, etc. In the SoM, SDEs were described by the following characteristics (e.g. [Tary et al, 2012]; [Embriaco et al, 2013]; [Bayrakci et al, 2013], see also Figure I.2.2.1): (i) Signal duration less than 0.8 sec, (ii) frequencies ranging between 4 to 30 Hz, (iii) one single-wave train, with no identified P or S-wave arrivals, (iv) recorded locally by only one OBS station and (v) not recorded by the hydrophone. The presence of gas in superficial sediments, along with analogies with laboratory experiments, conducted [Tary et al, 2012] to suggest that these events could be produced by gas migration followed by the collapse of fluid-filled cavities or conduits (Figure I.2.2.2). In this manuscript, we present a systematic study that provides a revised interpretation of SDEs, based on the analysis of different data sets, including OBS data from the deployment in 2011.

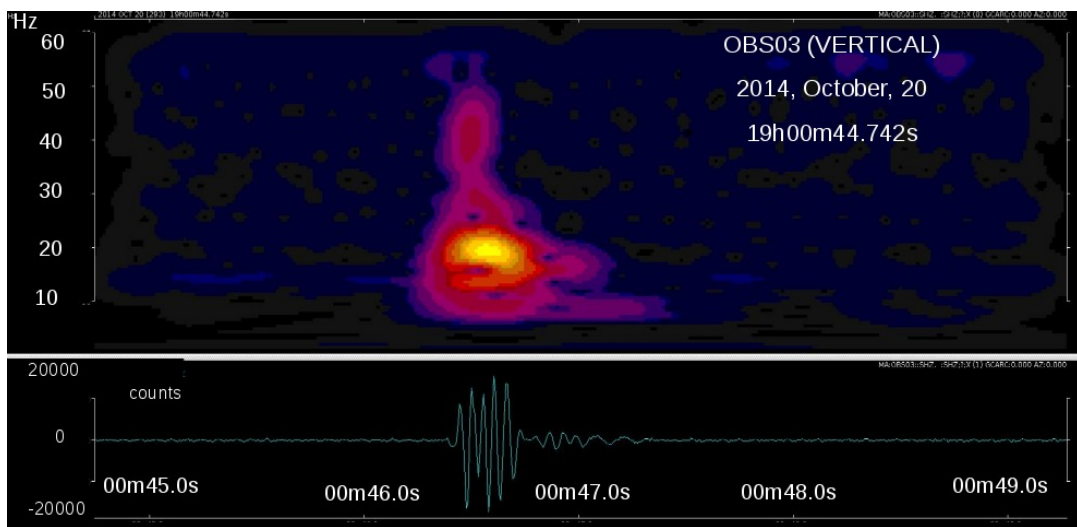


Figure 1.2.2.1: Example of spectrogram (upper panel) and seismogram (bottom panel) of a SDE recorded on the 20th of October 2014 on the vertical component of OBS03.

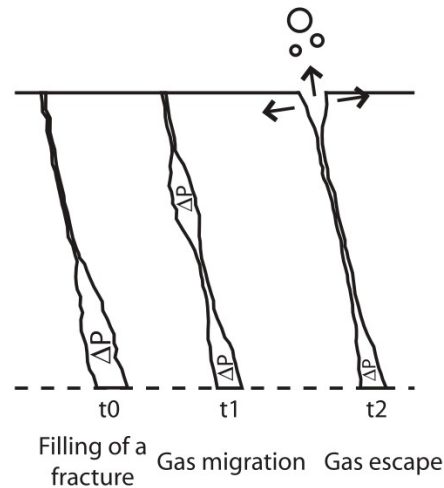


Figure 1.2.2.2: From [Tary et al 2012]. Mechanism proposed for generating SDE in three steps: gas migration; escape through a sub-vertical conduit; and collapse of the cavity.

I.3 Structure of the manuscript

The present PhD thesis is focused on the characterization of the micro-seismicity and on the analysis of the short-duration events recorded with the OBSs deployed in the western part of the SoM. The present manuscript is therefore divided into five parts.

- Part I is this short introduction, including the geological background and scope of this work.
- Part II summarizes the most recent, systematic studies carried out by other authors on the micro-seismicity below the SoM, e.g. [Schmittbuhl et al, 2015] and [Yamamoto et al, 2017]. Part II also includes the full paper of [Géli et al, 2018], on which I spent a considerable amount of time analysing the OBS data (characterization and correlation of seismograms, quality control of picking, writing appendixes, etc.).
- Parts III and IV are associated with the main results of the *PhD* thesis.
- Part III presents the results of the high-resolution study that we have conducted on micro-seismicity below the western SoM, based on two OBS deployments, from April 15th to July 31st, 2011 and from September 19th to November 14th, 2014, respectively. This part includes

the manuscript by *Batsi et al, 2017* (in review in the *Bulletin of the Seismological Society of America, BSSA*) describes the results of the micro-seismicity study. This paper is the core of the *PhD* work.

- Part IV represents a systematic study of the short duration events that are systematically recorded by OBSs within the Sea of Marmara. This part includes the revised version of *Batsi et al, 2017, Deep Sea Research II, DSR II*, (in review).
- Part V discusses the conclusions of the work along with the perspectives for future research.

II. Discussing the 3 most recent micro-seismicity surveys based on OBS data from the Western SoM

Several, systematic OBS studies have been carried out to improve hypocenter locations below the SoM, by using data from submarine stations only (e.g. [*Sato et al, 2004*], [*Tary et al, 2011*], [*Yamamoto et al, 2017*], [*Géli et al, 2018*]) or from a combination of OBSs and land stations (e.g. [*Bulut et al, 2009*] and [*Schmittbuhl et al, 2015*]). The results obtained by the three most recent, systematic studies are summarized hereafter, e.g.: [*Schmittbuhl et al, 2015*]; [*Yamamoto et al, 2017*]; [*Géli et al, 2018*]. It is important to note that complementary, specific studies were also carried out, in search of seismic repeaters below the Western Sea of Marmara. The reader is warmly invited to refer to these studies, published by [*Schmittbuhl et al, 2016*] and by [*Bohnhoff et al, 2017*].

II.1 Study by [Schmittbuhl et al, 2015]

[Schmittbuhl et al, 2015], analyzed the seismicity along the Main Marmara Fault (MMF) below the SoM during the period of 2007-2012, by using all the available land stations around the SoM (e.g. 132 seismic stations, in total) and by including also the data from two permanent (e.g. KOERI and MAM) and two ocean temporary seismic networks (e.g. CINNET on land and Ifremer OBSs at sea). For their analysis they assumed a 1D velocity structure. They used the 1D model of [Karabulut et al, 2011] as initial velocity model for the inversion to obtain a new velocity model and station residuals using a catalog of more than 500 events and 80 stations in the western Marmara region. The catalog includes data from the temporary deployment of Ifremer's OBSs in 2011 and permanent OBS of KOERI. Absolute and relative locations were derived by SEISAN HYPOCENTER (e.g. [Lienert and Havskov, 1995]; [Havskov and Ottemoller, 1999]) and HYPODD (e.g. [Waldhauser and Ellsworth, 2000]) softwares respectively.

The location results indicate (among many other things) that the earthquakes of magnitude $M > 4.5$ are followed by swarms of aftershocks which appear to be vertically distributed from the base of the crust up to the sediment surface. Particularly, by considering the geographical and depth distribution of the seismicity during this period, they have concluded that the seismicity along the four basins from west to east (e.g. Tekirdag, Central, Kumburgaz and Cinarcik, see Figure II.1.1, for more details) is characterized as followed:

- i. To the west, in the Tekirdag and Central basin, significant seismicity is found to be occurring and to be distributed over a wide depth range (from 17 km depth to the surface);
- ii. In the central SoM, the Kumburgaz basin is characterized by sparse seismicity;
- iii. To the east, the Princes islands segment in the Cinarcik basin is characterized by a segment of intensive seismicity located at a depth of ~ 10 km, bounded by 2 vertical patches of seismicity, distributed from ~ 10 km up to the surface.

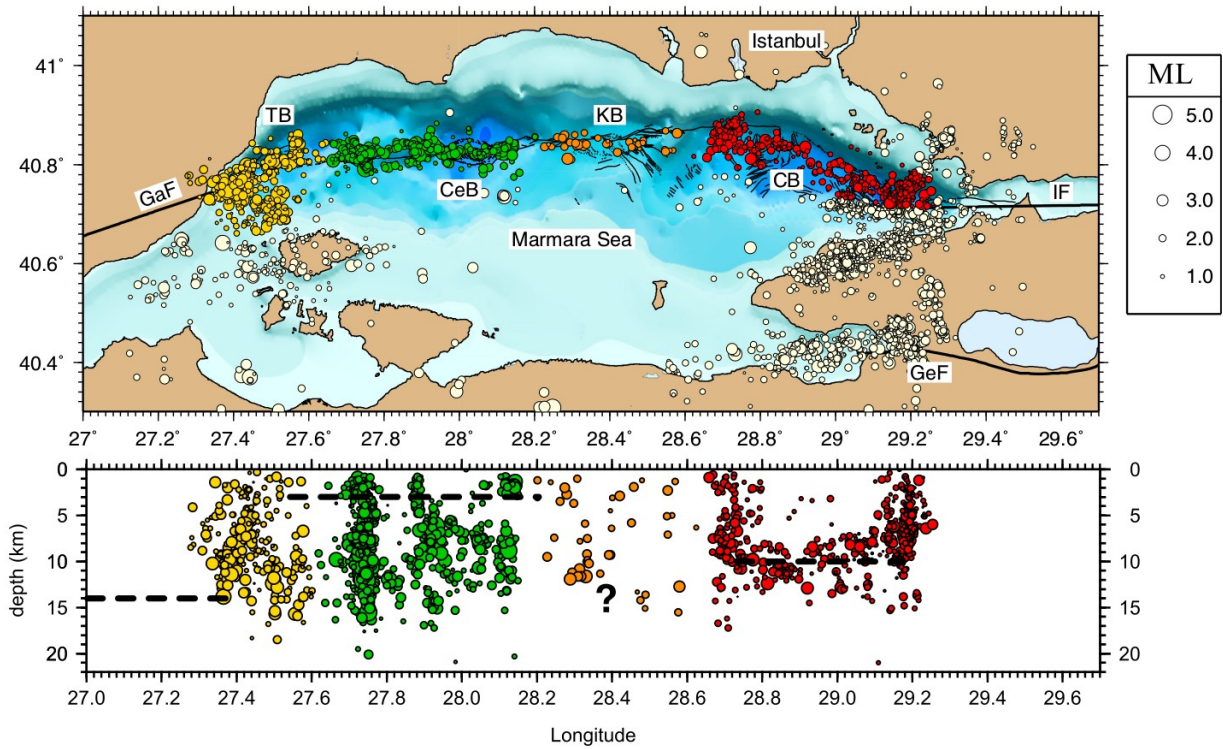


Figure II.1.1: From [Schmittbuhl et al, 2015]. Map (upper panel) and cross-section (bottom panel) of the seismicity recorded along the Main Marmara Fault (MMF) from 2007 to 2012. The different domains are represented with different colors namely: Tekirdag basin (TB) in yellow, the Central Basin (CeB) in green, the Kumburgaz basin (KB) in orange and the Cinarcik basin (CB) in red. White color corresponds to regional seismicity away from MMF. Bathymetry is from [Le Pichon et al, 2001]. Dotted lines in cross-section show the geodetically estimated locking depth of each domain. Abbreviations for: GaF: Ganos fault, IF: Izmit fault, GeF: Gemlik fault.

II.2 Study by [Yamamoto et al, 2017]

As stated by [Yamamoto et al, 2017], seismic catalogues along the SoM, which were derived by mostly using land stations and some OBS data for a small period of time and within a sparse interval [e.g. Schmittbuhl et al, 2015], most probably contain hypocenters that were inaccurately determined in the absence of OBS stations since ambiguities in the onshore structure could increase

the location error. Consequently, a different approach was suggested by [Yamamoto et al, 2017], who strictly used only OBS data for studying the seismicity over a recording period of 10 months, from September 2014 up to June 2015.

In their study, a 1D velocity model by [Yamamoto et al, 2015] was used for deriving the initial locations and then double-difference (DD) relocation and 3D seismic tomography inversion were applied on the data for accounting in this way the local-scale heterogeneity of the velocity structure. Their hypocenter results have an accuracy of around 0.2 km and indicate that (see Figure II.2.1):

- iii. beneath the Western High there is no micro-earthquake activity from the seafloor to 8 km depth.
- iv. under the eastern Central Basin the upper limit of the seismicity is only at about 5 km depth, several seismically inactive regions were identified within the upper crust along the MMF that are probably accumulating strain towards the next large earthquake.

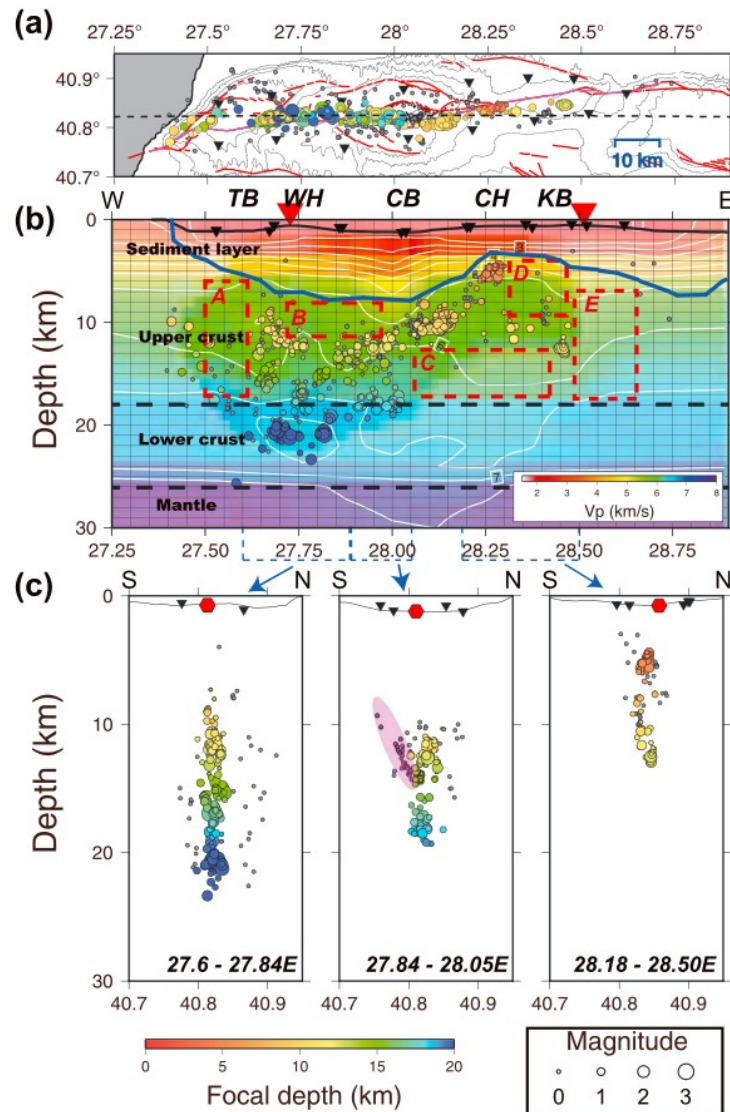


Figure II.2.1: From [Yamamoto et al, 2017]. (a) Relocation map of the on-fault hypocenters. Gray circles are for the off-fault earthquakes. Circles are proportional to magnitude, calculated within [Yamamoto et al, 2017] study. (b) E-W vertical profile of the hypocenter distributions along latitude 40.8218°N (dashed line in Figure 8a). The background colors show the P wave velocity profile extracted along latitude 40.8218°N (e.g. Figure 13 of [Bayrakci et al 2013]) from the tomographic model of [Yamamoto et al, 2017] study. Blue line indicates the depth to sedimentary basement [Bayrakci et al, 2013]; the upper and lower black dashed lines indicate intra-crustal and Moho discontinuities [Bécel et al, 2009], respectively. Red dashed rectangles A to E indicate the on-fault areas of low seismicity. Red inverted triangles indicate the seafloor extensometer observation points (eastern point [Sacik et al, 2016] and western point [Yamamoto et al, 2016]). (c) N-S vertical profiles of hypocenters for intervals 27.6 to 27.84°E, 27.84 to 28.05°E, and 28.18 to 28.50°E. Shaded purple indicates another fault-like structure from the hypocenter distribution under the western Central Basin.

II.3 Study by [Géli et al, 2018]

[Géli et al, 2018] studied the aftershock sequence that followed the M5.1 deep (~ 12 km) strike-slip earthquake on the 25th of July 2011, in the Western part of the SoM. The sequence was successfully recorded by the temporary seismic network of 9 OBS stations, deployed by Ifremer in 2011, with the exception of the central station that stopped working just one month before the occurrence of the mainshock. Then a high resolution study was achieved, by: (i) using strictly only OBS stations, (ii) using a 3D velocity model, specifically tailored for the western part of the SoM, that accounted for the velocity contrast at the seafloor interface and the sharp geometry of the basins (e.g. for more information, the reader could refer to Appendix 1 of [Géli et al, 2018]) and (iii) considering only well constrained relocated events, based on common seismological criteria (e.g. 110 events out of 550 were obtained in total, by using the non-linear software NLDiffLoc, e.g. [Lomax et al, 2014]; [De Landro et al, 2015]).

Based on the above and on a combination of geophysical (heat flow) and geochemical arguments, [Géli et al, 2018], demonstrated that a great number of the aftershocks occurred at depths within the gas window (~ 2 to 4 km below sea floor (bsf), in addition to ultra-shallow aftershocks (at depth < 1 km).

My contribution as co-author to the article by [Géli et al, 2018], was the re-analysis of the OBS datasets, by re-examining all location results and by providing computation errors. A considerable re-interpretation of the data allowed and confirmed the reliability of the shallow seismicity results.

ARTICLE WITH SUPPLEMENTARY MATERIAL

Gas related seismicity within the Istanbul seismic gap, by [Géli et al, 2017]

Scientific Reports

Detailed Status Information

Manuscript #	SREP-16-51867E
Current Revision #	6
Other Versions	SREP-16-51867-T SREP-16-51867A-Z SREP-16-51867B-Z SREP-16-51867C SREP-16-51867D SREP-16-51867E
Submission Date	24th February 18
Current Stage	Quality Check Started
Title	Gas and seismicity within the Istanbul seismic gap
Manuscript Type	Original Research
Corresponding Author	Dr. Louis Geli (louis.geli@ifremer.fr) (IFREMER)
Contributing Authors	Dr. Pierre Henry , Dr. Celine Grall , Dr. Jean-Baptiste Tary , Antony Lomax , Miss Evangelia Batsi , Dr. Estelle Cros , Prof. Cemil Gürbüz , Miss Sezim Işık , Dr. Celal Sengor , Xavier Le Pichon , Dr. Livio Ruffine , Dr. Stéphanie Dupré , Dr. Vincent Riboulot , Dr. Yannick Thomas , Dr. Dogan Kalafat , Dr. Gaye Bayrakci , Mr. Quentin Coutellier , Mr. Thibault Regnier , Prof. Graham Westbrook , Mr. Hakan Saritas , Prof. Günay Cifci , Prof. Namik Cagatay , Sinan Ozeren , Naci Görür , Mike Tryon , Prof. Marco Bohnhoff , Dr. Luca Gasperini , Dr. Frauke Klingelhoefer , Dr. Carla Scalabrin , Mr. Jean-Marie Augustin , Dr. Davide Embriaco , Mrs. Giuditta Marinaro , Dr. Francesco Frugoni , Dr. Stephen Monna , Dr. Giuseppe Etiope , Prof. Paolo Favali , Dr. Anne Becel
Authorship	Yes
Abstract	Understanding micro-seismicity is a critical question for earthquake hazard assessment. Since the devastating earthquakes of Izmit and Duzce in 1999, the seismicity along the submerged section of North Anatolian Fault within the Sea of Marmara (comprising the "Istanbul seismic gap") has been extensively studied in order to infer its mechanical behaviour (creeping vs locked). So far, the seismicity has been interpreted only in terms of being tectonic-driven, although the Main Marmara Fault (MMF) is known to strike across multiple hydrocarbon gas sources. Here, we show that a large number of the aftershocks that followed the M 5.1 earthquake of July, 25th 2011 in the western Sea of Marmara, occurred within a zone of gas overpressuring in the 1.5-5 km depth range, from where pressurized gas is expected to migrate along the MMF, up to the surface sediment layers. Hence, gas-related processes should also be considered for a complete interpretation of the micro-seismicity ($M < 3$) within the Istanbul offshore domain.
Techniques	Physical sciences techniques [Imaging techniques]; Physical sciences techniques [Materials characterization];
Subject Terms	Earth and environmental sciences/Solid Earth sciences Earth and environmental sciences/Natural hazards

RESEARCH ARTICLE

Gas and seismicity within the Istanbul seismic gap

L. Géli¹, P. Henry², C. Grall^{2,3}, J.-B. Tary^{1,4}, A. Lomax⁵, E. Batsi¹, V. Riboulot¹, E. Cros¹, C. Gürbüz⁶, S. E. Işık⁶, A. M. C. Sengör⁷, X. Le Pichon², L. Ruffine¹, S. Dupré¹, Y. Thomas¹, D. Kalafat⁶, G. Bayrakci^{1,8}, Q. Coutellier¹, T. Regnier¹, G. Westbrook^{1,9}, H. Saritas^{10,11}, G. Çifçi¹¹, M. N. Çağatay⁷, M. S. Özeren⁷, N. Görür⁷, M. Tryon⁸, M. Bohnhoff¹², L. Gasperini¹³, F. Klingelhoefer¹, C. Scalabrin¹, J.-M. Augustin¹, D. Embriaco¹⁴, G. Marinaro¹⁴, F. Frugoni¹⁴, S. Monna¹⁴, G. Etiope¹⁴, P. Favali¹⁴, A. Bécel³

¹Ifremer, Centre de Bretagne, Plouzané, France

²CEREGE, Aix-Marseille University, CNRS, Marseille, France

³Lamont-Doherty Earth Observatory, Palisades, NY, USA

⁴Universidad de los Andes, Bogotá, Colombia

⁵ALomax Scientific, 06370 Mouans-Sartoux, France

⁶Kandilli Observatory and Earthquake Research Institute, Boğaziçi University, Istanbul, Turkey

⁷Istanbul Technical University, Istanbul, Turkey

⁸Ocean and Earth Science, National Oceanography Centre, Southampton, UK

⁹School of Geography, Earth and Environmental Sciences, University of Birmingham, UK

¹⁰Mineral Research & Exploration General Directorate, MTA, Ankara, Turkey

¹¹Institute for Marine Science and Technology, Dokuz Eylül Üniversitesi, İzmir, Turkey

¹²Deutsches Geo-Forschungs Zentrum, GFZ, Potsdam, Germany

¹³Institute of Marine Science, ISMAR-CNR, Bologna, Italia

¹⁴Istituto Nazionale di Geofisica e Vulcanologia, INGV, Roma, Italia

¹⁵Faculty of Environmental Science and Engineering, Babes-Bolyai University, Cluj-Napoca, Romania

Correspondence to louis.geli@ifremer.fr

Abstract

Understanding micro-seismicity is a critical question for earthquake hazard assessment. Since the devastating earthquakes of Izmit and Duzce in 1999, the seismicity along the submerged section of North Anatolian Fault within the Sea of Marmara (comprising the "Istanbul seismic gap") has been extensively studied in order to infer its mechanical behaviour (creeping vs locked). So far, the seismicity has been interpreted only in terms of being tectonic-driven, although the Main Marmara Fault (MMF) is known to strike across multiple hydrocarbon gas sources. Here, we show that a large number of the aftershocks that followed the M 5.1 earthquake of July, 25th 2011 in the western Sea of Marmara, occurred within a zone of gas overpressuring in the 1.5-5 km depth range, from where pressurized gas is expected to migrate along the MMF, up to the surface sediment layers. Hence, gas-related processes should also be considered for a complete interpretation of the micro-seismicity (~ M<3) within the Istanbul offshore domain.

Since 1939, the North Anatolian Fault (NAF) -one of the most active strike-slip faults on Earth, like for instance the San Andreas Fault or the Altyn Tagh Fault- has produced an unique sequence of M>7 earthquakes, starting from eastern Anatolia

and propagating to the west towards Istanbul^{1,2,3}. Prior to this sequence, which ended in 1999 with the devastating earthquakes of Izmit and Duzce, causing more than 20000 casualties at the eastern end of the Sea of Marmara, the fault ruptured in 1912. This earlier rupture developed in the west at the transition into the North Aegean, leaving the Marmara section of the NAF as the only part of the fault not being activated since 1766. The Istanbul-Marmara region between the 1912 and 1999 ruptures is thus generally considered to represent a seismic gap with an earthquake potential^{4,5} of M up to 7.4. Intensive surveys have been conducted since 1999 to investigate the main branch of the NAF below the Sea of Marmara to better understand its seismotectonic setting and the resulting seismic hazard for the densely populated (>15 million) greater Istanbul region.

Geological and geophysical, marine surveys since 2000 have revealed the geometry of the submarine Main Marmara Fault (MMF) system^{6,7}. Seismological studies have shown that the seismicity along the MMF exhibits a strong lateral variability⁸⁻¹⁴. Seismicity in the Sea of Marmara is unevenly distributed and concentrates in spatial and temporal clusters^{8,11}. In the western part of the MMF (e.g. the Tekirdag Basin, the Western High and the Central Basin) (Fig.1), seismicity appears to be localized in several restricted active zones, while the central part, which encompasses the Kumburgaz Basin and the Central High, is comparatively seismically silent. In the Cinarcik Basin, offshore Istanbul, at the western termination of the 1999 Izmit rupture, the installation of seismometer arrays on the Prince Islands at 2-3 km from the main fault led to the identification of a 30 by 8 km aseismic patch that was interpreted as a locked zone on the MMF¹¹. A major aspect of seismic hazard assessment is to determine the mechanical behaviour of these potentially dangerous locked segments, which may rupture during the next expected Marmara earthquake. The presence of the water cover above the fault trace and the absence of islands to the south of the fault limits the use of GPS data in estimating the strain accumulation and slip deficit along each of the segments¹⁵. Efforts are presently on the way to collect acoustic-based geodetic data and encouraging results have recently been obtained¹⁶. Still, the detailed analysis of micro-seismicity maps remains critical.

To date, the micro-seismicity along the MMF has always been interpreted strictly for its tectonic origin (as a result of fault deformation mode and behaviour), while the potential role of gas-related processes to induce shallow micro-seismicity has been disregarded, although gas (generally methane) is known to be widespread on the Marmara seafloor¹⁷⁻²³. In the Western Sea of Marmara, events of magnitude greater than ~ 4.2 regularly occur, generating large sequences of aftershocks, that appear to be vertically distributed below sites where a high density of gas seeps have been identified along the MMF²¹⁻²². "Vertical swarms dramatically appear in the recently published map of relocated earthquakes⁸ from 2007 to 2012, particularly for the aftershocks that followed the M_L 4.2, 4.7 and 5.1 events of 24/01/2009, 25/07/2011 and 07/06/2012, which all occurred where the density of gas emissions is maximum^{16,17} (in figure 1, note that along the Central High and Kumburgaz fault segments, gas emissions are not found within the fault valley, but on adjacent structures, for instance on top of the Central High). However, the seismicity map shown in Figure 1 is based on a 1D velocity model¹⁰, that fits to the velocity structure onshore but not to the one from the deep offshore. This probably has severe implication for the precise earthquake depth determination, particularly for shallow seismicity.

Hence, before any further analysis can be conducted, improved depth determinations of shallow earthquakes are needed. Here, we present new, high-resolution location results for the sequence of aftershocks that followed the M_L 5.1 earthquake that struck on July 25th, 2011 at a depth of ~ 11 -14 km²⁴ below the "Western High", a sedimentary anticline structure -up to ~ 7 to 8 km thick- where gas emissions, associated with traces of oil and gas hydrates, have been sampled²³. The sequence of aftershocks (550 events detected in total) was monitored by a local network of two permanent cabled Ocean Bottom Seismometers (OBS) operated by KOERI and nine temporary autonomous stations deployed by IFREMER²⁵. Unfortunately, the OBS located right above the hypocentral region failed a few days before the mainshock, limiting the depth-resolution. To improve the depth resolution, P- and S-wave arrivals were all manually checked to control the pick quality and to avoid misleading picks due to micro-events produced by gas expulsion at the seabed^{26,27}. Then, special care was given to the velocity model. Since the basins of the Sea of Marmara are filled with more than 5 km of Plio-Quaternary soft ("slow") sediments, the seismic velocity structure offshore is drastically different from the one onshore. For instance, based on deep-penetration, multi-channel seismic data²⁸, the P-wave velocities were reported to be very low for the sea-bottom deposits, especially in the deep bathymetric trough (1.6 to 1.8 km/s) and gradually increasing from the sea-bottom to the pre-kinematic basement, where they reach values of 4 to 4.2 km/s. Additional data provided by OBS wide-angle reflection and refraction seismics¹³ indeed indicate that P-wave velocities in troughs do not exceed 2 km/s within the first kilometer below seafloor (bsf) nor 2.5 km/s between 2 and 3 km bsf. We thus tested a number of velocity models, 1D and 3D encompassing either the whole Marmara region^{29,30} or the deep, sub-marine domain *stricto-sensu*^{25,31}.

The results presented here (Figure 2) were obtained using a 3D-model that was specifically tailored for the 20 km x 60 km area covered by the offshore network, with a grid node spacing of 750 m x 750 m x 200 m, using all available geological and geophysical information for the Sea of Marmara (see Reference 25 and details in Appendix 1). Different location methods were tested³²⁻³³. Here we present results obtained using the NLLoc inversion algorithm³²⁻³³ for absolute location, and NLDiffLoc³³⁻³⁴ for relative locations, which are less sensitive to the event location and origin time. This turned out to be possible only over a limited number of events (112 in total), due to computation instabilities, which resulted in "water" relocations for the most shallow events³⁵. The resulting location errors (Figure 3) are less than about 200 m on the horizontal components (E-W and N-S). In contrast, on the vertical component, depth location errors are distributed between 0 and 500 m for most events (only 7 events out of 112 have an error > 500 m); as expected, errors (expressed as the ratio between error and depth) dramatically increase for the most shallow earthquakes.

Only a few events are located within the crystalline basement, at crustal depths greater than 8 km. Most aftershocks are located within the 6 to 8 km thick sedimentary pile that forms the Western High³¹, with a great number of them located within the uppermost layers, at depths shallower than ~ 1.5 km. The zoomed view (Figure 4) reveals that the epicentres of the mainshock and of all aftershocks are located to the north of the fault trace. Within the Plio-Pleistocene sedimentary pile, aftershocks are not all located along the main fault plane. In addition, the mainshock

is not exactly located at the apex of the surface trace of the Main Marmara Fault, but ~ 800 m to the north, which suggests that the main fault plane may not be strictly vertical, but slightly inclined (by about 4°) relatively to the vertical.

The aftershocks were superimposed on the multichannel seismic section collected in 2001, during the Seismarmara cruise^{28,36} (see also in Reference 37, page 160). Different groups of aftershocks can be described, depending on depth (Figure 5):

- i) between 5 and 7 km below seafloor (bsf), aftershocks appear to occur at the base of the pre-kinematic basement, along the main fault but also along secondary faults that are known to intersect the Main Marmara Fault, based on deep, seismic imaging;
- ii) between ~ 5 and 1.5 km bsf, aftershocks appear to be aligned along a secondary fault, related to the on-going opening of a small pull-apart basin on the western side of the Western High. The composite focal mechanism computed with HASH^{38,39} for a number of well defined earthquakes (see list in Appendix 3) indicate predominant normal faulting;
- iii) at depths above 1.5 km, where a great number of aftershocks occurs, the epicentres are spread out away from the fault trace, within gas-prone sedimentary environments.

To examine the potential role of gas, let us now provide details on the gas that were sampled in the Western High area. Geochemical analysis²³ have shown that the gases are of thermogenic origin, with a composition similar to Eocene Thrace Basin gas fields⁴⁰. However, the isotopic composition of gases emitted at the seafloor indicate oil biodegradation and secondary generation of microbial methane at less than 80°C^{41,42}, that may have occurred within a reservoir or during migration. The pore fluids sampled from sediment strata at the same site where liquid hydrocarbons and gas are expelled are enriched in chloride, lithium, strontium and barium⁴³. The application of different geo-thermometers indicates fluid/sediment interaction within the temperature window of ~ 75 to 150°C, a narrower 75-130°C range being obtained with Li geo-thermometers, commonly applied to oil-bearing sedimentary basins⁴². The expulsion of brines together with oil and gas suggests that these seepage sites are fed by leakage from an over-pressured zone, which is also supported by the diapiric nature of the fluid conduit (see Supp. Mat., Appendix 5). The heat flow measured at the surface is lowered by the effect of sediment blanketing, with a mean value of 35±7 mW/m², however basin models⁴⁴ constrain the probable range of crustal heat flow below the western high between 50 and 70 mW/m². Temperature vs. depth profiles were calculated using different models to describe the evolution of conductivity with depth⁴⁵ and assuming that the heat transfer at the basin scale is conductive (advection is neglected) (see details in Supp. Mat. Appendix 4). Within all uncertainties, the possible depth range of the source of over-pressured fluids is thus estimated as 2-to-5-km depth. It remains possible that gas and pressure generation also occurs at greater depths where Thrace Basin source rocks are present as thermogenic gas generation can occur up to more than 200°C.

Many sources could be on the way from the source rock to the seafloor, with different geochemical or biogeochemical processes occurring at different levels. At shallow levels, the gas migration pathways were mapped down to a few hundred meters beneath the Western High seabed, using 3D, high-resolution seismic data collected

in 2009⁴⁶ (Figure 6). All over the 3D survey area, reflections of very strong amplitude and opposite seismic polarity compared to that of the surrounding seabed suggest the presence of free gas immediately below the reflecting horizons. This view is coherent with both acoustic, offshore surveys and visual observations showing that, where horizons are faulted and/or crop out at the seafloor, gas emissions are observed in the water column. In contrast, at unfaulted locations, several horizons appear to collect the gas migrating from depth. This is probably because they are of higher porosity and permeability than the dominant, clay-rich lithology. The data also reveal that gas follows buoyancy-driven, upward migration paths in permeable layers and along faults, controlled by the regional strain field as it is expressed in the seafloor topography, with the primary E-W orientation parallel to the NAF and secondary tectonic orientations oblique to the NAF⁴⁷. Locally, mud volcano-like structures may also offer preferential pathways for the gas to migrate up to the seafloor.

The general picture that finally comes out is that gas is conveyed from gas-rich, deep sources (located between ~ 1.5 and ~ 5 km) up to the seafloor along the Main Marmara fault zone system. Beneath the main fault valley, gas tends to follow buoyancy-driven migration paths through permeable layers, up to the crest of the anticline folds that border the main fault valley (Supp. Info., Appendix 5). This suggests that most of the aftershocks that occurred within and above the gas window are likely linked to gas-related processes, e.g. the mainshock triggered not only "purely tectonic", but also "gas-related" aftershocks. The main shock could have triggered the pressurization and activation of the faults located within or above the deepest gas sources. Alternatively, gas ex-solution from sediment pore fluids could have occurred in response to the main shock; the resulting increase of compressibility of the fault material could have then triggered some of the aftershocks, as predicted by the Piau-Maury-Fitzenz model⁴⁸, which was successfully used to describe the effect of fluid compressibility on the rupture process at oceanic fracture zones⁴⁹. It is important to note that soft, marine sediments (with velocities < 2 to 3 km/s^{13,35}) are generally not expected to be able to host earthquakes. However, recent results from laboratory experiments on clays at high slip-rates (i.e. > 2 m/s)^{50,51} have shown that clays can react seismically to rupture that propagates into it, one such example being the 2011 Tohoku earthquake where 30 m of slip is estimated to have occurred in clay like material⁵². A similar scenario could apply to explain the ultra-shallow events that occurred at depths of less than a few hundred meters. Also, it is likely that the gas-prone sediment layers that were present in 2009, based on high-resolution 3D seismics, were still there in 2011 and that the aftershocks were triggered by gas over-pressurization. In contrast, because the 2009 cruise predates the aftershock sequence of 2011, there is no direct evidence that the ultra-shallow aftershocks of 2011 directly induced new gas emissions in the water column.

In conclusion, the present work reveals the existence of shallow micro-seismicity in the Sea of Marmara. Most events of the aftershock sequence appear to be located within or above the gas window below the Western High, at shallow (2-5 km) and ultra-shallow (< 2 km) levels. It is hence suggested that part of part of these aftershocks are likely gas-induced. The characterization of micro-seismicity as evidence -or not- of creep along the North Anatolian fault segments^{8,53}, as well as the

search for seismic tremors, similar to those that occurred prior to the 1999, Izmit earthquake⁵⁴, are challenges of critical importance for seismic hazard assessment and mitigation within the "Istanbul seismic gap". However, the precise hypocenter location and the classification of micro-seismicity into either tectonic earthquakes, either gas-related events, are prerequisites. These can be achieved only by the implementation of permanent, networks of deep seafloor observatories in the immediate vicinity of the fault.

Methods.

Building a high-resolution, 3D-velocity model²⁵ (see Figures in Supp. Mat., Appendix A1). A model with a 750 m x 750 m x 200 m grid spacing was built, for the Western Sea of Marmara (40°43'N - 40°54'N – 27°30'E – 28°15'E), in order to account for the velocity contrast at the water/sediment interface and for the slow seismic velocities within the sediment infill in the main Marmara Trough. All available, multibeam bathymetry and wide-angle seismic data from the area were used. The model was developed following the six steps described below:

1. The tomographic model of *Bayrakci et al.³¹* was used to describe the velocity structure of the pre-kinematic basement and the velocity structure down to 12 km below the Marmara sea-level. This model (see Figure 13a in Ref. 31) is based on a low-resolution grid of 6 km x 6 km x 2 km. The iso-velocity contours of the pre-kinematic basement were superposed to the bathymetric map and used as guide lines to define 9 "basement domains" (Figure A1-1).
2. For each domain, a "typical" velocity profile down to 12 km depth was calculated by averaging all velocity profiles within the given domain (Figures A1-2a, A1-2b, A1-2c).
3. A dense, high-resolution sub-grid was then defined (Figure A1-3), with grid spacing 750 m x 750 m x 200 m, by sub-dividing the tomographic grid of *Bayrakci et al.³¹*.
4. Each node M of the dense sub-grid was ascribed: i) to the water depth inferred from the high resolution bathymetric grid of *Le Pichon et al.⁶*; ii) to a given domain N (with N=1 to 9, as defined in Figure A1-3). The velocity structure at grid node M for the upper 12 km is provided by the characteristic velocity profile of domain N.
5. Below 12 km and down to 36 km, the velocity structure is assumed to depend on longitude and inferred from wide-angle reflexion results (see Figure 3 of *Bécel et al.⁶⁶*. Velocities of 6.7 km/s and 8 km/s were ascribed to the lower crust and upper mantle respectively (see example in Figure A1-4).
6. Each point of the fine sub-grid is thus characterized by: the exact depth at grid node, the "domain" number, the "typical" velocity profile above 12 km, the depth of lower crust and the depth of Moho.

The high-resolution grid was used for computing absolute and relative locations using Lomax's software³³. For computing relative locations using HypoDD-3D³², a degraded, 3D grid was used due to grid size limitations and to avoid border effects.

Geotherm estimation below the Western High (see Figures in Supp. Mat., Appendix A4). To estimate the depth range at which temperatures ranging between 75°C and 80°C might be expected, eight thermal profiles (e.g. sediment temperature versus depth below seafloor) were obtained (see plots in Figure A4-2) along with thermal conductivity measurements performed on co-located cores. The observed spatial variability of thermal gradients (Figure A4-2) suggests that the heat transfer to

the surface is likely influenced by a variety of processes (including sediment thermal blanketing, fluid circulation, gas hydrate related perturbation, topography, etc) that appear difficult to model, mainly due to the scarcity of thermal measurements. We therefore rather use the initial heat flow value of $68.10^{-3} \text{ W.m}^{-2}$ that was derived by *Grall et al*⁴⁷ from the detailed study of the thermal and subsidence history of the Central Basin. Indeed, the sedimentary column is thick at the Western High but sedimentation rate since at least the last hundred thousand years is no greater than 1.5 mm/a ⁴⁷. Thus the sediment thermal blanketing should not change drastically the present-day heat flow at the seafloor.

Let us consider that: i) that this value (hereafter referred to as Q_b), represents a reasonable proxy for the basal heat flow below the Western High area; and ii) that at the scale of the area, heat flow is conductive, e.g. conservative.

Then:

$$k(z) \frac{dT}{dz} = Q_b \quad (1)$$

which yields :

$$T(z) = T_0 + \int_0^z \frac{Q_b}{k(z)} dz \quad (2)$$

where $T(z)$ and $k(z)$ are temperature and thermal conductivity, respectively. Following [*Pribnow et al, 2000*]⁴⁵, we have tested two different approaches to describe the variation for porosity with depth:

- The linear approach:

$$k(z) = k_0 + Az \quad (3)$$

$$T(z) = T_0 + \frac{Q_b}{A} \text{Log}\left(1 + \frac{Az}{k_0}\right) \quad (4)$$

where k_0 and A are the thermal conductivity at the surface ($0.83 \text{ W K}^{-1} \text{ m}^{-1}$) and the thermal conductivity gradient, respectively. Using the compilation of [*Pribnow et al, 2000*], based on the data collected during Legs 101 to 180 of the Ocean Drilling Programme, we tested different values for A (from 0.4 to $1.4 \times 10^{-3} \text{ W K}^{-1} \text{ m}^{-2}$).

- The "porosity approach", which assumes that $k(z)$ depends on porosity and that porosity exponentially increases with depth due to compaction:

$$\varphi(z) = \varphi_0 e^{-az} \quad (5)$$

and

$$k(z) = \varphi(z)k_w + (1 - \varphi(z))k_g \quad (6)$$

$$k_g = k_0 + \frac{\varphi_0}{1 - \varphi_0} (k_0 - k_w) \quad (7)$$

where $\varphi(z)$ and φ_0 are porosity at depth z and at sediment surface, respectively, while a stands for Athy's compaction factor, k_w and k_g for thermal conductivity of seawater and sediment grains. The thermal conductivity of grains (k_g) is derived from surface sediment porosity and conductivity as stated in (7).

Using the above formulae, an analytical expression of temperature is found for integral in (1):

$$T(z) = T_0 + \frac{Q_b}{k_s a} \text{Log} \left| \frac{k(z) \varphi_0}{k_0 \varphi(z)} \right| \quad (8)$$

Using bottom water temperature of 14°C, temperatures at depth z are found, based on expressions (4) or (8).

Acknowledgements: *This work is based on the results of 15 years of continuous, marine investigations in the Sea of Marmara, conducted within both bi-lateral collaborations (France-Turkey; Italy-Turkey) and EU-funded Research Programmes, e.g. the ESONET Network of Excellence (contract N° 036851) and the MARSITE Integrated Project (contract N° 308417). Jean-François Rolin and Roland Person, coordinators of ESONET, as well as Nurcan Özel and Meral Agualdis, respectively coordinator and project manager of MARSITE are warmly acknowledged. Acknowledgements are also addressed to the Turkish Navy and to the Turkish Hydrographic Service (SHOD) for supporting the operations at sea, particularly our correspondent, Captain Erhan Gezgin; to the personnel of the French Embassy in Ankara, particularly Mrs Bonnafous-Boucher; to CNRS and to Ifremer for funding operations at sea of R/V Le Suroit, R/V Pourquoi pas? and R/V Urania, respectively; to the Institute of Marine Science and Technology of the University of Izmir for support with R/V Piri Reis; to Pascal Pelleau, Mikaël Roudaut and Ronan Apprioual for their technical support; to professor Oguz Özel, for his support for using R/V Yunuz of Istanbul University; to the personnel of Ineris -Armand Lizeur, Emmanuel Klein and Pascal Bigarré- for their support in using the SYTMIS software; to Jean Schmittbuhl, Hayrullah Karabulut and Michel Bouchon for fruitful discussions and for providing unpublished manuscript; to Miraille Laigle and Alfred Hirn for providing the deep-seismic data from the Seismarmara Cruise; to COST action FLOWS for support to collaboration between EU and Turkey on transform-type plate boundary studies. Anthony Lomax worked as a MARSITE sub-contractor, under CNRS-Contract N° MA201301A; Estelle Cros worked under a grant from Institut Carnot Ifremer-Edrome, Contract reference number 06/11/2013. Intense use was made of Global Mapping Tools (GMT)⁵⁷. Data available on <http://doi.org/10.17882/49764>.*

REFERENCES

1. Barka, A. A. Slip distribution along the North Anatolian Fault associated with large earthquakes of the period 1939–1967, *Bull. Seismol. Soc. Am.*, **86**, 1238–1254 (1996).
2. Stein, R. S., Barka, A. A., Dieterich, J. H. Progressive failure on the North Anatolian fault since 1939 by earthquake stress triggering, *Geophys. J. Int.*, **128**, 594–604 (1997).
3. Şengör, A. M. C., Tüysüz O., İmren C., Sakiç M., Eyidoğan H., Görür, N., Le Pichon, X., Rangin C. The North Anatolian Fault: A new look, *Annu. Rev. Earth Planet. Sci.*, **33**, 37–112, doi:10.1146/annurev.earth.32.101802.120415 (2005).
4. Parson T., Recalculated probability of M>7 earthquakes beneath the Sea of Marmara. *J. Geophys. Res.*, **109**, doi:10.1029/2003JB002667 (2004)
5. Ambraseys, N.N. The Seismic Activity of the Marmara Sea Region over the last 2000 years. *Bull Seismo Soc Am*, **92**: 1-18 (2002).
6. Le Pichon, X., Şengör, A.M.C., Demirbag, E., Rangin, C., İmren, C., Armijo, R., Görür, N.; Çagatay, N.; Mercier de Lepinay, B.; Meyer, B.; Saatçılar, R.; Tok, B. The active Main Marmara Fault, *Earth Planet. Sci. Lett.*, **192**, 595–616 (2001)
7. Şengör, A. M. C., Grall, C., İmren, C., Le Pichon, X., Görür, N., Henry, P., Karabulut, H., Siyako, M., (2014), The geometry of the North Anatolian transform fault in the Sea of Marmara and its temporal evolution: Implications for the development of intracontinental transform faults, *Can. J. Earth Sci.*, **51**(3), 222–242, doi:10.1139/cjes-2013-0160 (2014)
8. Schmittbuhl, J., Karabulut, H., Lenligné, O., Bouchon, M. Seismicity distribution and locking depth along the Main Marmara Fault, Turkey, *Geochemistry, Geophysics, Geosystems*, DOI 10.1002/2015GC006120 (2016)
9. Bulut F., et al., Ellsworth W. L., Bohnhoff M., Aktar M., and Dresen G. Spatiotemporal Earthquake Clusters along the North Anatolian Fault Zone Offshore İstanbul, *Bull. Seism. Soc. Am.*, **101**, No. 4, 1759–1768, doi: 10.1785/0120100215, (2011)
10. Karabulut, H., Schmittbuhl, J., Özalaybey, S., Lenligné, O., Kömeç-Mutlu, A., Durand, V., Bouchon, M., Daniel, G., Bouin, M.-P. (2011), Evolution of the seismicity in the eastern Marmara Sea a decade before and after the 17 August 1999 Izmit earthquake, *Tectonophysics*, **510**, 17–27 (2011).
11. Bohnhoff, M., Bulut F., Dresen G., Malin P.E., Eken T., Aktar M. An earthquake gap south of İstanbul. *Nature Communications*, **4**, doi: 10.1038/ncomms2999 (2013)
12. Sato, T., Kasahara, J., Taymaz, T., Ito, M., Kamimura, A., Hayakawa, T., Tan, O. A study of microearthquake seismicity and focal mechanisms within the Sea of Marmara (NW Turkey) using ocean bottom seismometers (OBSs), *Tectonophysics*, **391:303**, 314. doi:10.1016/j.tecto.2004.07.018 (2004)
13. Tary, J.-B., Géli, L., Henry, P., Natalin, B., Gasperini, L., Çomoglu, M., Çagatay, N., and Bardainne T., Sea-Bottom Observations from the Western Escarpment of the Sea of Marmara, *Bull. Seism. Soc. Am.*, **101** (2), 101, 775–791, doi: 10.1785/0120100014 (2011)
14. Yamamoto, Y., N. Takahashi, A. Pinar, D. Kalafat, S. Citak, M. Comoglu, R. Polat, and Y. Kaneda, Geometry and segmentation of the North Anatolian Fault beneath the Marmara Sea, Turkey, deduced from long-term ocean bottom seismographic observations, *J. Geophys. Res. Solid Earth*, **122**, 2069–2084, doi:10.1002/2016JB013608 (2017).
15. Ergintav S., Reilinger R. E., Çakmak, R., Floyd, M., Cakir, Z., Doğan, U., King, R. W., McClusky, S., Özener, H. İstanbul's earthquake hot spots: Geodetic constraints on strain accumulation along faults in the Marmara seismic gap, *Geophys. Res. Lett.*, **41**, 5783–5788, doi:10.1002/2014GL060985 (2014)
16. Sakic, P., Piété, H., Ballu, V., Royer, J.-Y., Kopp, H., Lange, D., Petersen, F., Özener, M. S., Ergintav, S., Géli, L., Henry, P., Deschamps, A., No significant steady state surface creep along the North Anatolian Fault offshore İstanbul: Results of 6 months of seafloor acoustic ranging, *Geophys. Res. Lett.*, **43**, 6817–6825, doi:10.1002/2016GL069600 (2016)
17. Kuscu, I., Okamura, M., Matsuoka, H., Gökaşan, E., Awata, Y., Tur, H., Şimşek, M., Keçer, M., Seafloor gas seeps and sediment failures triggered by the August 17, 1999 earthquake in the Gulf of İzmit, Sea of Marmara, NW Turkey, *Tectonophysics*, **215**, 3-4, 193-214 (2005)
18. Gasperini, L., Polonia, A., Del Bianco, F., Etiope, G., Marinaro, G., Favali, P., Italiano, F., Çagatay, N. Gas seepage and seismogenic structures along the North Anatolian Fault in the eastern Sea of Marmara, *Geochem. Geophys. Geosyst.*, **13**, Q10018, doi:10.1029/2012GC004190 (2012).
19. Ruffine, L., Germain Y., Polonia A., De Prunele A., Croguennec C., Donval J.-P., Pitel-Roudaut M., Ponzevera E., Caprais J.-C., Brandily C., Grall C., Bollinger C., Geli L., Gasperini L. (2015), Pore

- water geochemistry at two seismogenic areas in the Sea of Marmara, *Geochem. Geophys. Geosyst.*, **16**, 2038–2057, doi:10.1002/2015GC005798.
20. Halbach, P. E., Holzbecher, E., Reichel, Th., Moche R., Migration of the sulphate–methane reaction zone in marine sediments of the Sea of Marmara—can this mechanism be tectonically induced?, *Chem. Geol.*, **205**(1-2), 73-82 (2004)
 21. Géli, L., Henry, P., Zitter, T., Dupré, S., Tryon, M., Çagatay, N., Mercier de Lépinay, B., Le Pichon, X., Sengör, A. M. C., Görür, N., Natalin, B., Uçarkus, G., Volker, D., Gasperini, L., Burnard, P., Bourlange, S. & the MarNaut Scientific Party (2008). Gas emissions and active tectonics within the submerged section of the North Anatolian Fault zone in the Sea of Marmara. *Earth Planet. Sci. Lett.*, **274**(1-2): 34-39 (2008).
 22. Dupré S., Scalabrin C., Grall C., Augustin J.-M., Henry P., Görür N., Sengör A. M. C., Çagatay N., Guérin C., Clouet H., Géli L. Tectonic and sedimentary controls for widespread gas emissions in the Sea of Marmara, Results from systematic, ship-borne multibeam echosounder water column imageries, *J. Geophys. Res., Solid Earth*, **120**, doi: 10.1002/2014JB011617 (2015)
 23. Bourry, C., Chazalon, B., Charlou, J.-L., Donval, J.-P., Rufine, L., Henry, P., Géli, L., Çagatay, N., Inan, S., Moreau, M., Free gas and gas hydrates from the Sea of Marmara, Turkey: Chemical and structural characterization. *Chem. Geol.*, doi:10.1016/j.chemgeo.2009.03.007 (2009)
 24. Karabulut, H., & Aktar, M. Strategies and tools for Real Time Earthquake Risk Reduction (REAKT), Eu-Funded Project, FP7/2007-2013, Theme: ENV.2011.1.3.1-1, *Deliverable D2.2*, 22/03/2013 (2013)
 25. Cros, E., & Géli, L. Caracterisation of microseismicity in the Western Sea of Marmara: implications in terms of seismic monitoring, *Project Report, Institut Carnot Ifremer-Edrome, Abondement 2011, N°06/11/2013, 29 pages*, available on-line: <http://dx.doi.org/10.13155/38916> (2013)
 26. Tary, J.-B., Géli, L., Henry, P., Guennou, C., Sultan, N., Çagatay, N., Vidal, I., Micro-events produced by gas migration and expulsion at the seabed: a study based on sea bottom recordings from the Sea of Marmara, *Geophys. J. Int.*, doi: 10.1111/j.1365-246X.2012.05533.x (2012)
 27. Embricco, D., Marinaro, G. Frugoni, F., Giovanetti, G., Monna, S., Etiopo, G., Gasperini, L., Çagatay, N., Favali, P., Monitoring of gas and seismic energy release by multiparametric benthic observatory along the North Anatolian Fault in the Sea of Marmara (NW Turkey), *Geophys. J. Int.*, doi: 10.1093/gji/ggt436 (2013).
 28. Laigle, M., Bécel, A., de Voogd, B., Hirn, A., Taymaz, T., Ozalaybey, S., & the Members of the SEISMARMARA Leg1. A first deep seismic survey in the Sea of Marmara: whole crust and deep basins. *Earth Planet. Sci. Lett.* **270**, 168–179 (2008).
 29. Gürbüz C., Işık, S. E., Cros, E., Géli, L., High Resolution Micro Earthquake Characterization, *Deliverable D8_2, EU MARSITE PROJECT (New Directions in Seismic Hazard Assessment through Focused Earth Observation in the Marmara Supersite)*. <http://archimer.ifremer.fr/doc/00278/38915/> (2013).
 30. Işık, S. E. Three-D, P-wave velocity structure of the Marmara Region using local earthquake tomography, *Masters Thesis, Bogazdici Universitesi*, (2014).
 31. Bayrakci G., Laigle, M., Becel, A., Hirn, A., Taymaz, T., Yolsal-Cevikbilen, S., Team, Seismarmara, 3-D sediment-basement tomography of the Northern Marmara trough by a dense OBS network at the nodes of a grid of controlled source profiles along the North Anatolian fault, *Geophys. J. Int.*, doi: 10.1093/gji/ggt211 (2013)
 32. Waldhauser, F., HypoDD: A computer program to compute double-difference earthquake locations, *USGS Open File Rep.*, **01-113** (2001)
 33. Lomax, A., et al. (2009). Earthquake Location, Direct, Global-Search Methods, in *Complexity In Encyclopedia of Complexity and System Science*, Part 5, Springer, New York, pp. 2449-2473, doi:10.1007/978-0-387-30440-3.
 34. Lomax, A., Satriano, C., Vassalo M. (2012), Automatic picker developments and optimization: FilterPicker - a robust, broadband picker for real-time seismic monitoring and earthquake early warning, *Seism. Res. Lett.*, **83**, 531-540, doi:10.1785/gssrl.83.3.531 (2012)
 35. Lomax, A. Mise en oeuvre et support pour logiciels de traitement automatisé de données sismologiques acquises dans le cadre du projet Européen FP7 Marsite, *Contract report, Reference CNRS MA201301A*, available on line: http://alomax.net/projects/marsite/MA201301A_report_v0.2.pdf (2014)
 36. Bécel, A., Laigle, M., de Voogd, B., Hirn, A., Taymaz, T., Yolsal-Cevikbilen, S., Shimamura, H., North Marmara Trough architecture of basin infill, basement and faults, from PSDM reflection and OBS refraction seismics, *Tectonophysics* **490** (2010) 1–14
 37. Grall, C., La Faille Nord Anatolienne dans sa portion immergée en mer de Marmara : Evolution du

- réseau de failles et migration de fluides, Thèse de Doctorat de l'Université Aix-Marseille (*PhD Thesis* (2013))
38. Hardebeck, J.L. and Shearer, P.M. Using S/P Amplitude Ratios to Constrain the Focal Mechanisms of Small Earthquakes, *Bull. Seism. Soc. Am.*, **93**, 2434-2444 (2003).
 39. Hardebeck, J.L. and Shearer, P.M., (2008). HASH : A Fortran program for computing Earthquake First-Motion Focal Mechanisms -v1.2 – January 31, (2008)
 40. Hosgörmez, H., & Yalçın, M. N., (2005), Gas-source rock correlation in Thrace basin, Turkey, *Mar. Pet. Geol.*, **22**, 901–916
 41. Ruffine, Fandino-Torres O., Etoubleau J., Cheron S., Donval J.-P., Germain Y., Ponzevera E., Guyader V., Dennielou B., Etiopo G., Gasperini L., Bortoluzzi G., Henry P., Grall C., Çagatay M. N., Charlou J.-L., Géli L. Geochemical dynamics of the natural-gas hydrate system in the Sea of Marmara, offshore Turkey, *Advances in Natural Gas Technology*, ISBN 978-953-51-0507-7, pp. 29-56 (2012).
 42. Head, I., Martin Jones, D., Larter, S. R., Biological activity in the deep subsurface and the origin of heavy oil, *Nature*, **426**, 344-352 (2003)
 43. Tryon, M.D., Henry, P., Çagatay, M. N., Zitter, T., Géli, L., Gasperini, L., Burnard, P., Bourlange, S., Grall, C. Pore fluid chemistry of the North Anatolian Fault Zone in the Sea of Marmara: A diversity of sources and processes. *Geochemistry Geophysics Geosystems*, **11**, Q0ad03 , doi: 10.1029/2010gc003177 (2010)
 44. Grall C., Henry, P., Y. Thomas, G.K. Westbrook, M.N. Çagatay, B. Marsset, H. Saritas, G. Çifçi, Géli L., Heat flow in the Sea of Marmara Central Basin, possible implications for the tectonic evolution of the North Anatolian Fault, *Geology*, **40**:3-6, doi:10.1130/G32192.32191 (2012).
 45. Pribnow, D. F. C., Kinoshita, M., and Stein, C.A. Thermal Data Collection and Heat Flow Recalculations for Ocean Drilling Program Legs 101-180, ODP Archive N° 0120432 (2000)
 46. Thomas, Y., Marsset, B., Westbrook, G. K., Grall, C., Géli, L., Henry, P. Cifçi, C., Rochat, A., and Saritas, H., (2012), Contribution of high-resolution 3D seismic near-seafloor imaging to reservoir scale studies: application to the active north Anatolian Fault, Sea of Marmara, *Near Surface Geophysics*, **10**, 291-301, doi:10.3997/1873-0604.2012019
 47. Grall, C., Henry, P., Thomas, Y., Westbrook, G. K., Çagatay, M. N., Marsset, B., Saritas, H., Çifçi, G., Géli L. Slip rate estimation along the western segment of the Main Marmara Fault over the last 330 ka by correlating Mass Transport Deposits, *Tectonics*, 10.1002/2012TC003255 (2013).
 48. Maury, V., Piau, J.-M., Fitzenz, D., Mechanical effect of the presence of gas on faults modeled as a sandwiched Cam-Clay material in *Harmonising Rock Engineering and the Environment (12th ISRM Internat. Congress on Rock Mechanics Beijing Oct. 2011) (eds Qian, Q. & Zhou, Y.)* (CRC Press, 2011); <http://dx.doi.org/10.13140/2.1.1077.1849> (2011)
 49. Géli, L., Piau, J.-M., Dziak, R., Maury, V., Fitzenz, D., Coutellier, Q., Henry, P., Broseta, D., Steele-MacLennan, M., Driesner, T., Seismic Precursors linked to Highly Compressible Fluids at Oceanic Transform Faults, *Nature Geoscience*, doi:10.1038/NGEO2244 (2014)
 50. Faulkner, D. R., T. M. Mitchell, J. Behnken, T. Hirose, and T. Shimamoto (2011), Stuck in the mud? Earthquake nucleation and propagation through accretionary forearcs, *Geophys. Res. Lett.*, **38**(18), doi:10.1029/2011GL048552
 51. Aretusini S., S. Mitterpergher, O. Pimper, E. Spagnuolo, A. F. Gualtieri, and G. Di Toro (2017), Production of nanoparticles during experimental deformation of smectite and implications for seismic slip, *Earth and Planetary Science Letters*, **463**, 221–231, doi:10.1016/j.epsl.2017.01.048.
 52. Romano, F., E. Trasatti, S. Lorito, C. Piromallo, A. Piatanesi, Y. Ito, D. Zhao, K. Hirata, P. Lanucara, and M. Cocco (2014), Structural control on the Tohoku earthquake rupture process investigated by 3D FEM, tsunami and geodetic data, *Sci. Rep.*, **4**, doi:10.1038/srep05631.
 53. Schmittbuhl, J., Karabulut, H., Lengliné, O. and Bouchon, M., Long-lasting seismic repeaters in the Central Basin of the Main Marmara Fault, *Geophys. Res. Lett.*, **43**, 9527–9534, doi:10.1002/2016GL070505 (2016).
 54. Bouchon, M., Karabulut, H., Aktar, M., Özalaybey, S., Schmittbuhl, J., Bouin, M.-P. Extended Nucleation of the 1999 Mw 7.6 Izmit Earthquake, *Science*, **331**, 877, doi:10.1126/science.1197341 (2011)
 55. Bécel, A., Laigle M., de Voogd, B., Hirn, A., Taymaz, T., Galvé, A., Shimamura H., Murai Y., Lépine J.-C., Sapin M., Özalaybey, S., Moho, crustal architecture and deep deformation under the North Marmara Trough, from the SEISMARMARA Leg 1 offshore–onshore reflection–refraction survey, *Tectonophysics* **467**, 1-21 (2009)
 56. Wessel, P., Smith, W.H.F. New version of the generic mapping tools released. *EOS, Transactions American Geophysical Union* **76**, 329 (1995)

Author's contribution:

LG headed the ESONET/Marmara Demonstration Mission and Work Package 8 within Marsite; collected and analyzed the data; wrote the paper.

PH was co-P.I. of the ESONET/Marmara Demonstration Mission; chief of the MarNaut Cruise of R/V L'Atalante in 2007 which led to the discovery of gas emissions from the Marmara seafloor; collected and analyzed the data; co-chief of the Marmesonet cruise of R/V Le Suroit and Marsite cruise of R/V Pourquoi pas?; wrote the paper.

NC was co-P.I. of the ESONET/Marmara Demonstration Mission; co-chief of the Marmesonet cruise of R/V Le Suroit and Marsite cruise of R/V Pourquoi pas?

CG has acquired and processed the heat flow data, and contributed to the modelling of those data. She also did the structural interpretation of the 2D and 3D-seismic data from the Western High and contributed to the paper writing.

JBT did the earthquake locations using HypoDD-3D, improved the interpretation of the OBS data and contributed to the paper writing.

AL developed the other codes (NonLinLoc and NonLinDifLoc) used for earthquake locations and guided the seismological work.

EB re-analyzed the OBS datasets, checked all locations results provided computation errors and re-interpretation of the data

EC analysed the data using the SYTMIS software and did the first set of earthquake locations using different methods (HypoDD-1D and NonLinLoc 3D) and different velocity models.

CG and DK established KOERI's cabled seafloor observatory network and collected part of the seismological data used in the paper.

CG and SI produced a catalog of relocated earthquakes based on a 3D model at the scale of the Marmara region.

AMCS and XLP initiated the French-Turkish cooperation in 1999 and were at the origin of many of the ideas developed since then on the evolution of the North-Anatolian Fault, ideas on which this paper is based. Contributed to paper writing.

LR, MT and GE contributed to geochemical data analysis and to paper writing.

SD, CS and JMA collected, processed and analyzed the acoustic data for water column imaging collected during the Marmesonet cruise of R/V Le Suroit and during the Marsite cruise of R/V Pourquoi pas? .

YT acquired and processed the 3D seismic data from the Western High.

GB contributed to the OBS data analysis and to the design of the High-Resolution 3D-Velocity model.

QC was the main contributor for the High-Resolution 3D-Velocity model used in the paper. Contributed to writing Appendix 2.

TR contributed to the data analysis and drafted figures 3 and 4.

VR, GW, HS contributed to the seismo-stratigraphic analysis of the 3D seismic data.

GC was co-P.I. of the ESONET/Marmara Demonstration Mission; headed the PIRMARA Cruise of R/V Piri Reis in 2009 that collected seismic data outside the 3D box.

SO contributed to data analysis and paper writing.

NG was at the start of the French-Turkish collaboration; contributed to the geological interpretation; was PI of Marsite Work Package 7.

MB and FK contributed to paper writing.

LGa (Gasparini) was co-P.I. of the ESONET/Marmara Demonstration Mission; chiefed 3 cruises of R/V Urania in the Sea of Marmara (for sediment and pore fluid sampling and instrument deployment and recovery).

DE, GM, FF, SM contributed to data acquisition and analysis.

PF was co-P.I. of the ESONET/Marmara Demonstration Mission.

AB provided the migrated section shown in Figure 5 which greatly contributed to improve the interpretation of the OBS data.

Additional Information

Competing financial interests: The author(s) declare no competing financial interests.

FIGURE CAPTIONS

Figure 1: Seismicity (after ref. 8) and gas emissions within the Sea of Marmara. a) Full seismicity map from 2007 to 2012 based on the recordings from 132 land stations, as well as from temporary seabottom networks, including 5 cabled observatories from 2009 to 2011 and 10 autonomous stations deployed by Ifremer from april 2011 to july 2011 (see location of stations in Ref. 8). The Western Sea of Marmara is regularly affected by earthquakes of magnitude > 4.5. The two earthquakes of magnitude > 4.0 which occurred in 2013 and 2015 were therefore added to complete the general pattern of seismicity in this area (locations from KOERI catalog). For all maps, thin black lines indicate major structural features, from Reference3. b) Selected micro-earthquakes with epicentres located within the boxes shown in panel A, respectively centered along the MMF and within the southern part of the Cinarçik Basin. Coloured dots indicate those aftershocks that occurred within the Western Sea of Marmara, 7 days after the earthquakes of magnitude > 4 (years 2007 to 2012 only). Blue: 27/04/2009; pink: 03/10/2010; red: 25/07/2011; green: 07/06/2012. c) Sites of acoustically detected gas emissions (red dots), from Reference 22. TB: Tekirdag Basin. WH: Western High; KB: Kumburgas Basin; CH: Central High; CiB: Cinarçik Basin. Note that in the Central High and the in the Kumburgas basins, gas is not found within the Main Marmara Fault Valley, nor along the Fault trace, but on top of adjacent structures or at the edge of basins (see references 21 and 22). d) Depth of selected earthquakes plotted versus longitude, with events from aftershock sequences represented using the same colour code as in panel B. Orange dots indicate events from the area delineated by the orange box (Panel B) in the South Cinarçik Basin; Violet dots are for events from the area delineated by the 2 violet boxes shown in Panel B. Color bar for bathymetry is displayed in Figure 2. All panels were created with GMT software, Version 4.5.11.

Figure 2: Panel a displays hypocenter relative locations (red dots) for the aftershocks that followed the M 5.1 earthquake of July 25, 2011. Locations were obtained using manual picks and the high-resolution P-wave velocity model described in Appendix 1. Triangles indicate OBS locations. Thick black line indicates the seismic profile collected in 2001 during the Seismarmara Cruise^{28,36} shown in Figures 5. Thin black lines are for active faults⁷. Panels b and c display the cross-sections of depth below sea-level along an East-West line crossing at 40.80°N and along a North-South line crossing at 27.78°E, respectively, with the aftershocks and the velocity structure extracted from the P-wave velocity grid (Appendix 1). The two iso-velocity lines at 4.2 and 5.2 km/s correspond to the syn-kinematic and post-kinematic basement, respectively^{28,31}. Red star indicates the absolute location of the M_w 5.1 earthquake (the position obtained with land and sea-bottom stations is consistent within 0.5 km with the position obtained using OBSs only). First, absolute locations of all the events of the aftershock sequence were obtained using the NonLinLoc³³ software package. Then relative locations were computed using NonLDiffLoc³³ on a selection of "well-constrained" events, e.g.: number of stations ≥ 7; RMS < 250 msec; gap ≤ 150°; error in depth smaller than z. Image created with GMT software, Version 4.5.11.

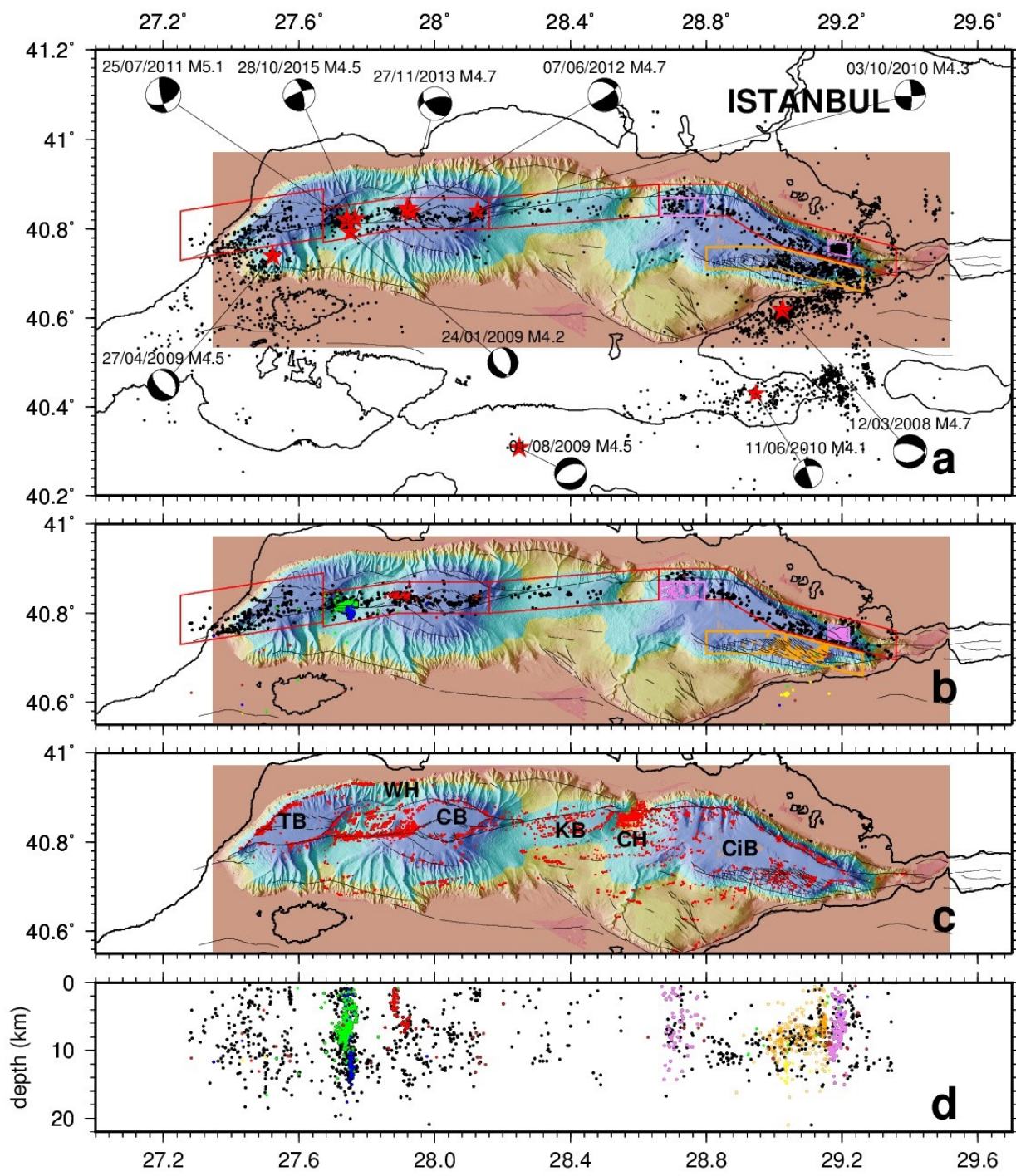
Figure 3: Location errors of the aftershocks shown in Figure 2. a) latitude-longitude plane; b) longitude-depth plane; c) latitude-depth plane. Panel d) displays the distribution of location errors in the 3 directions: depth (delta z); South-North (delta (y)); Est-West (delta(x)). Image created with GMT software, Version 4.5.11.

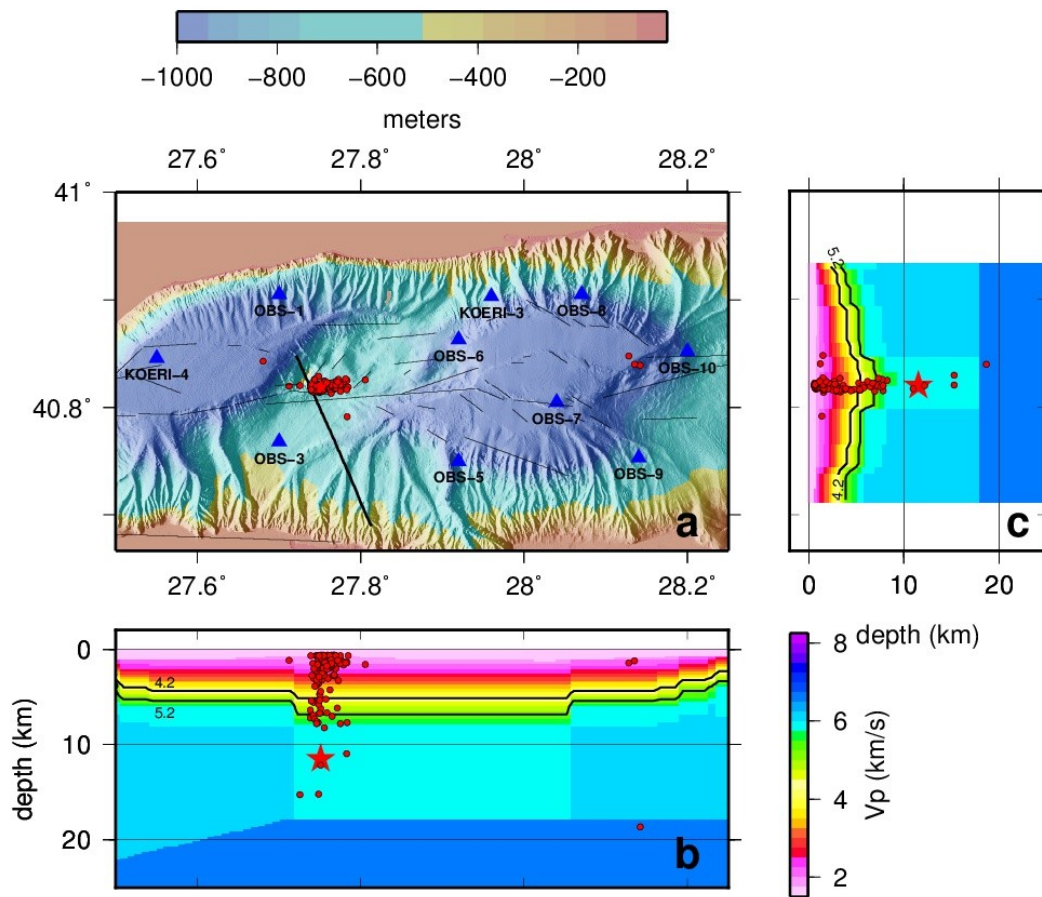
Figure 4: Epicenter locations for the aftershocks that followed the M 5.1 earthquake of July 25, 2011, superposed on a high-resolution bathymetric grid derived from a combination of near-seafloor AUV data³⁷ and on an unpublished, bathymetric grid having a resolution of 10 m, based on data collected in 2014 during the Marsite cruise of R/V Pourquoi pas?. White and blue dots are respectively epicenters within and below the sedimentary basin. Green dots indicate the location of the gas emission that were acoustically detected²² in 2009, using the multibeam echasounder EM302 of R/V Le Suroit. Note that there is no clear overlap between the seismicity (from 2011) and seafloor gas emissions (detected in 2009), e.g. there is no direct evidence that the ultra-shallow aftershocks of 2011 directly induced gas emissions in the water column. Thin black line indicates the track of the seismic section displayed in Figure 5. The thickened segment represents the location of the 3D, High-Resolution seismic image shown in Figure 6. The continuous red line indicates the trace of the right-lateral, strike-slip, Main Marmara Fault. Red dotted lines show secondary faults indicating the complexity of the fault network

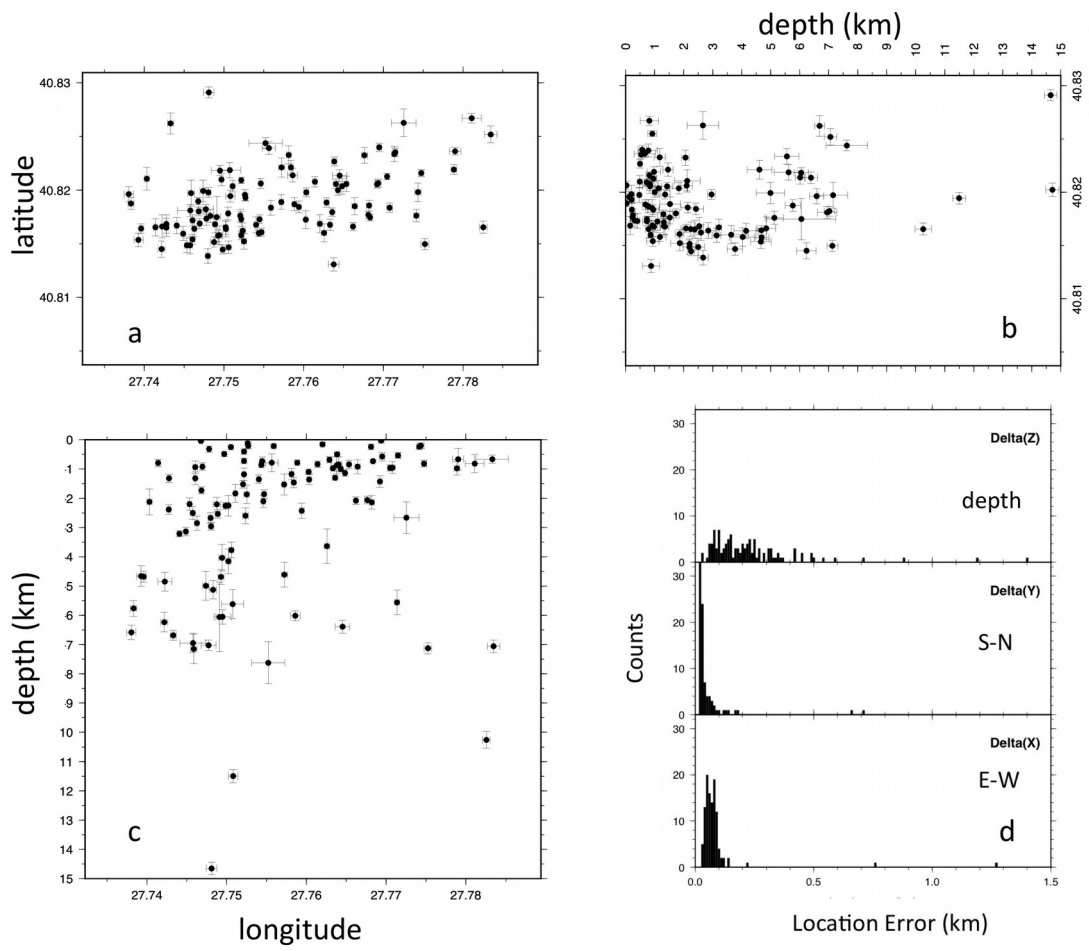
linked to the MMF. The thicker, east-west oriented, dotted line is also shown in the seismic section displayed in Figure 5. Image created with Arc-GIS, version v3.0.

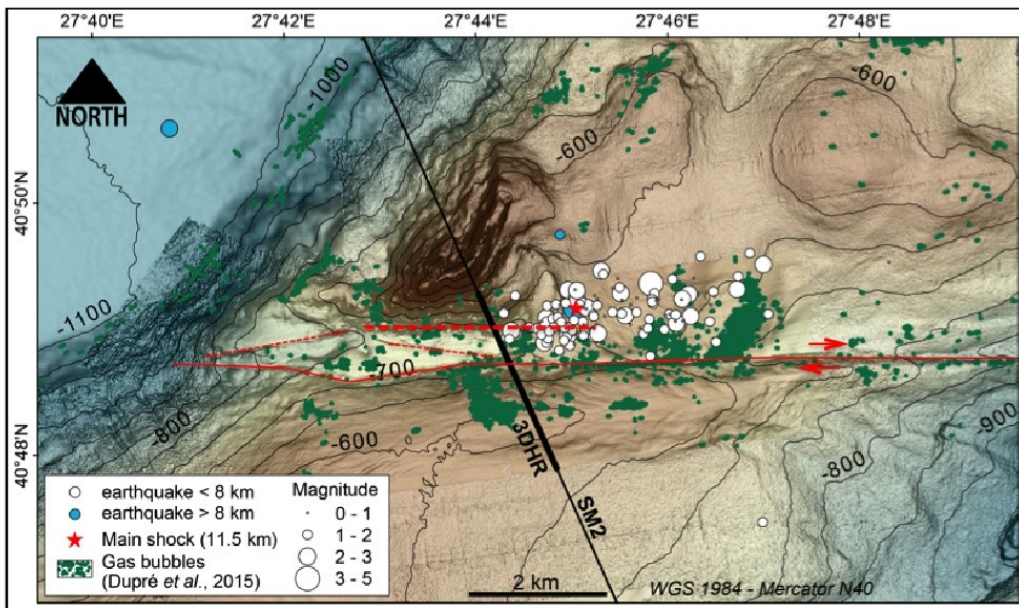
Figure 5: Left panel displays the hypocenters of the aftershock sequence, superimposed on the seismic section (see track line in Figure 2) that was shot during the Seismamara cruise^{28,36} in 2001 in the Western High area. The migration was obtained after stack and time-migrated, by using 5 main velocity intervals based on velocity analysis for the sedimentary layers and constraints from refraction modelling for the crust: the water-column, the shallow sediment interval, the deep sediment interval, the interval between the basement and the detachment, and the crustal layer below the detachment. Velocity in the water is settled constant at 1500 m/s and velocity increases linearly in other intervals. The average velocity in the shallow sediment is 1700 m/s, 2400 m/s for the deep sediment interval, 3300 m/s between the acoustic basement and the detachment, and is 5500 m/s in the crust below the detachment. Line-drawing (partly based on Reference 37, page 160) is displayed in right panel along with the locations of the aftershocks that followed the M 5.1 earthquake of July, 25, 2011. Continuous red line indicates the MMF. The dotted line within the sedimentary basin indicates the east-west oriented, secondary fault displayed in Figure 4. The earthquakes (at depths between 2 and 4 km) that were used to compute the composite focal mechanism using HASH^{38,39} are listed in Appendix 3. Image created with GMT software, Version 4.5.11.

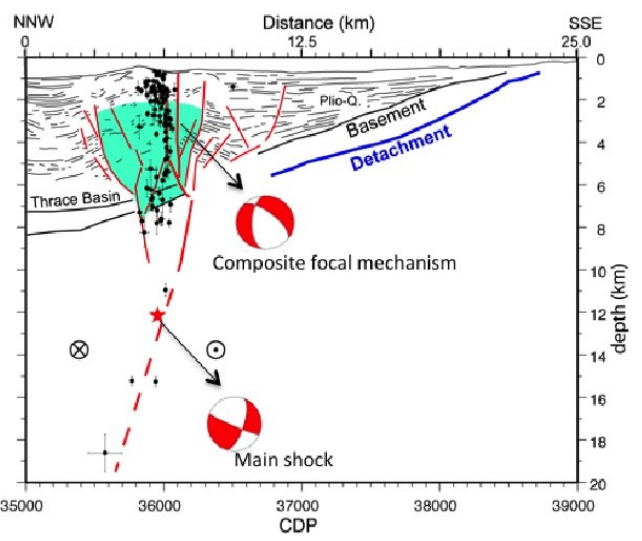
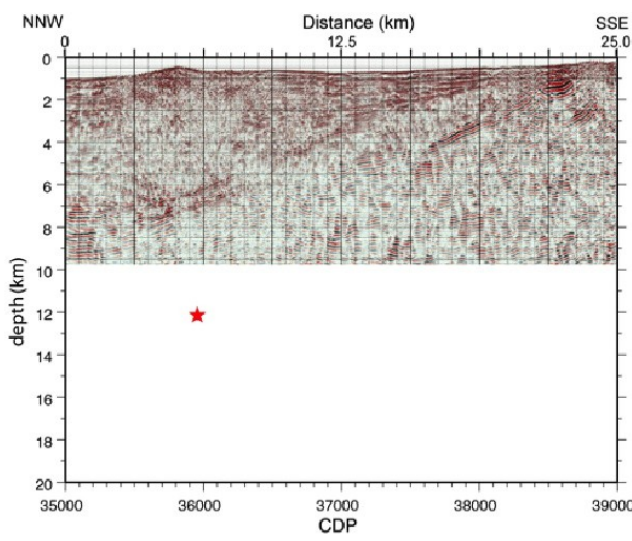
Figure 6: Seismic section extracted from the high-resolution 3D seismic box shot in 2009⁴⁶ along the thick black line displayed in Figure 5, with a simplified, tentative interpretation. Image created with Arc-GIS, version v3.0.

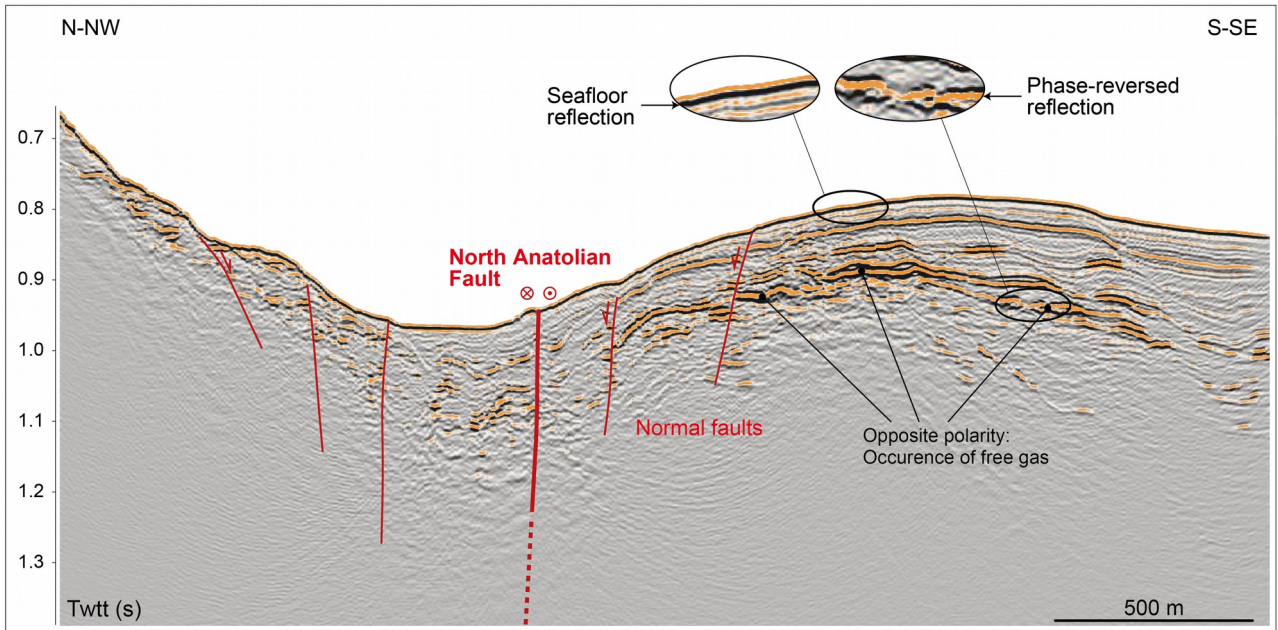












SUPPLEMENTARY INFORMATION

Manuscript title: Gas and seismicity within the Istanbul seismic gap

Authors list: L. Géli¹, P. Henry², C. Grall^{2,3}, J.-B. Tary^{1,4}, A. Lomax⁵, E. Batsi¹, V. Riboulot¹, E. Cros¹, C. Gürbüz⁶, S. Isik⁶, A. M. C. Sengör⁷, X. Le Pichon², L. Ruffine¹, S. Dupré¹, Y. Thomas¹, D. Kalafat⁶, G. Bayrakci^{1,8}, Q. Coutellier¹, T. Regnier¹, G. Westbrook^{1,9}, H. Saritas^{10,11}, G. Cifçi¹¹, M. N. Çağatay⁷, M. S. Özeren⁷, N. Görür⁷, M. Tryon⁸, M. Bohnoff¹², L. Gasperini¹³, F. Klingelhoefer¹, C. Scalabrin¹, J.-M. Augustin¹, D. Embriaco¹⁴, G. Marinaro¹⁴, F. Frugoni¹⁴, S. Monna¹⁴, G. Etiope¹⁴, P. Favali¹⁴, A. Bécel³

¹Ifremer, Centre de Bretagne, Plouzané, France

²CEREGE, Aix-Marseille University, CNRS, Marseille, France

³Lamont-Doherty Earth Observatory, Palisades, NY, USA

⁴Universidad de los Andes, Bogotá, Colombia

⁵ALomax Scientific, 06370 Mouans-Sartoux, France

⁶Kandilli Observatory and Earthquake Research Institute, Boğaziçi University, Istanbul, Turkey

⁷Istanbul Technical University, Istanbul, Turkey

⁸Ocean and Earth Science, National Oceanography Centre, Southampton, UK

⁹School of Geography, Earth and Environmental Sciences, University of Birmingham, UK

¹⁰Mineral Research & Exploration General Directorate, MTA, Ankara, Turkey

¹¹Institute for Marine Science and Technology, Dokuz Eylül Üniversitesi, Izmir, Turkey

¹²Deutsches Geo-Forschungs Zentrum, GFZ, Potsdam, Germany

¹³Institute of Marine Science, ISMAR-CNR, Bologna, Italia

¹⁴INGV, Roma, Italia

APPENDIX 1: Building a specifically designed, high-resolution, 3D, seismic velocity model for the Western Sea of Marmara

Written by Louis Géli, Quentin Coutellier, Jean-Baptiste Tary, Gaye Bayrakci & Cemil Gürbüz

In parallel to the study reported here, a complementary study was conducted within the EU-Funded MARSITE Project (www.marsite.eu), with among other targets, the objective to improve the characterization of the near-fault micro-seismicity, particularly along the central part of the SoM. To meet this objective, velocity models were developed by KOERI and by Ifremer to improve earthquake location in the Sea of Marmara, following two different approaches:

- KOERI has developed a 3D velocity model for the whole Marmara Region (within latitudes 39.5°N - 42.5°N and longitudes 26.0°E - 30.5°E), including land and seabottom stations, with grid spacing of 9 km x 9 km x 3 km (Gürbüz *et al.*, [2013], Isik [2014]).
- Ifremer has developed a different, but complementary approach, for the Western Sea of Marmara (40°43'N - 40°54'N - 27°30'E - 28°15'E). A high resolution velocity model with a 750 m x 750 m x 200 m grid spacing was built, using multibeam bathymetry and wide-angle seismic data, in order to account for the velocity contrast at the water/sediment interface and for the slow seismic velocities within the sediment infill in the main Marmara Trough (Cros and Géli, [2013]).

The fine-scale 3D-velocity model was developed following the six steps described below:

1. The tomographic model of Bayrakci *et al.* [2013] was used to describe the velocity structure of the pre-kinematic basement and the velocity structure down to 12 km below the Marmara sea-level. This model (see Figure 13a of Bayrakci *et al.*, [2013]) is based on a low-resolution grid of 6 km x 6 km x 2 km. The iso-velocity contours of the pre-kinematic basement were superposed to the bathymetric map and used as guide lines to define 9 domains (Figure A1-1).
2. For each domain, a "typical" velocity profile down to 12 km depth was calculated by averaging all velocity profiles within the given domain (Figures A1-2a, A1-2b, A1-2c).
3. A dense, high-resolution sub-grid was then defined (Figure A1-3), with grid spacing 750 m x 750 m x 200 m, by sub-dividing the tomographic grid of Bayrakci *et al.* [2013].
4. Each node M of the dense sub-grid was ascribed: i) to the water depth inferred from the high resolution bathymetric grid of Le Pichon *et al.* [2001]; ii) to a given domain N (with N=1 to 9, as defined in Figure A1-3). The velocity structure at grid node M for the upper 12 km is provided by the characteristic velocity profile of domain N.
5. Below 12 km and down to 36 km, the velocity structure is assumed to depend on longitude and inferred from wide-angle reflexion results (see Figure 10 of Bécel *et al.* [2009]. Velocities of 6.7 km/s and 8 km/s were ascribed to the lower crust and upper mantle respectively (see example in Figure A1-4).
6. Each point of the fine sub-grid is thus characterized by: the exact depth at grid node, the "domain" number, the "typical" velocity profile above 12 km, the depth of lower crust and the depth of Moho.

The high-resolution grid was used for computing absolute and relative locations using Lomax's software (e.g. [Lomax *et al.*, 2000], [Lomax *et al.*, 2009]). For computing relative locations using HypoDD-3D [Waldhauser, 2001], a degraded, 3D grid was used due to grid size limitations and to avoid border effects.

References:

- Bayrakci G., Laigle, M., Bécel, A., Hirn, A., Taymaz, T., (2013), 3-D sediment-basement tomography of the Northern Marmara trough by a dense OBS network at the nodes of a grid of controlled source profiles along the North Anatolian fault, *Geophys. J. Int.*, doi: 10.1093/gji/ggt211
- Bécel, A.; Laigle, M.; de Voogd, B.; Hirn, A.; Taymaz, T.; Galvé, A.; Shimamura, H.; Murai, Y.; Lépine, J.-C.; Sapin, M. & Özalaybey, S. (2009). Moho, crustal architecture and deep deformation under the North Marmara Trough, from the SEISMARMARA Leg 1 offshore-onshore reflection-refraction survey, *Tectonophysics* **467**: 1-21
- Cros, E., & Géli, L. (2013), Caractérisation of microseismicity in the Western Sea of Marmara: implications in terms of seismic monitoring, *Project Report, Institut Carnot Ifremer-Edrome, Abonnement 2011, N°06/11/2013, 29 pages*, available on-line: <http://dx.doi.org/10.13155/38916>
- Gürbüz C., Isik S. E., Geli L., Cros E. (2013). High Resolution Micro Earthquake Characterization, *Deliverable D8_2, EU MARSITE PROJECT (New Directions in Seismic Hazard Assessment through Focused Earth Observation in the Marmara Supersite)*. <http://archimer.ifremer.fr/doc/00278/38915/>
- Işık, S. E. (2014) 3D, P-wave velocity structure of the Marmara Region using local earthquake tomography, *Masters Thesis*, Bogazdici Universitesi.
- Le Pichon, X., A. M. C. Sengor, E. Demirbag, C. Rangin, C. Imren, R. Armijo, N. Gorur, and N. Cagatay (2001), The active Main Marmara Fault, *Earth Planet. Sci. Lett.*, **192**, 595–616.
- Lomax, A., A. Michelini, A. Curtis (2009), Earthquake Location, Direct, Global-Search Methods, in Complexity In *Encyclopedia of Complexity and System Science, Part 5, Springer, New York*, pp. 2449-2473, doi:10.1007/978-0-387-30440-3.
- Lomax, A., J. Virieux, P. Volant and C. Berge, (2000), Probabilistic earthquake location in 3D and layered models: Introduction of a Metropolis-Gibbs method and comparison with linear locations, in *Advances in Seismic Event Location*, Thurber, C.H., and N. Rabinowitz (eds.), Kluwer, Amsterdam, 101-134.
- Waldhauser, F., HypoDD: A computer program to compute double-difference earthquake locations, *USGS Open File Rep.*, **01-113**, 2001. [pdf](#)

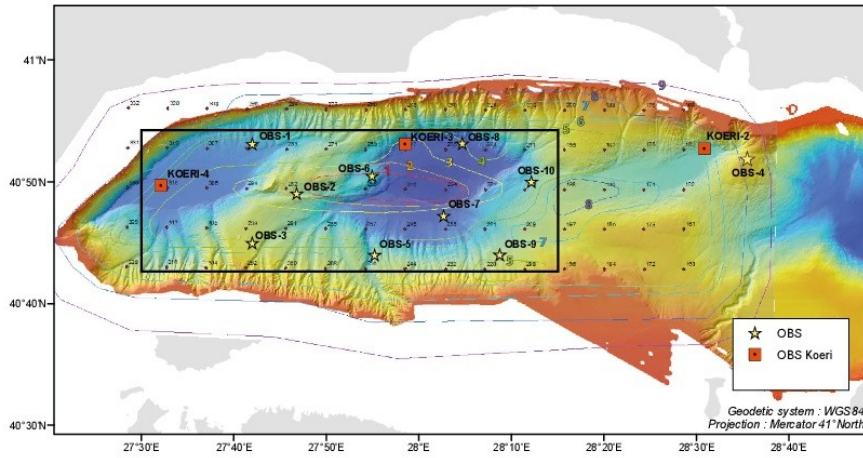


Figure A1-1: Bathymetric of the Western Sea of Marmara, based on the high-resolution, 38-m grid from Le Pichon et al, [2001], with iso-contours of pre-kinematic basement depth, from Figure 13a of Bayrakci et al [2013]. Iso-contours define 9 domains (labelled from 1 to 9), characterized by a specific velocity profile. Numbered black dots are nodes of the low-resolution grid (6 km x 6 km x 2 km) of Bayrakci [2013]. Black, rectangle frame indicates the area selected for the definition of the high-resolution grid shown in Figure A1-3. Yellow stars are Ifremer's autonomous, short period OBSs. Red squares are KOERI's permanent, cabled OBSs. Image created with GMT software, Version 4.5.11.

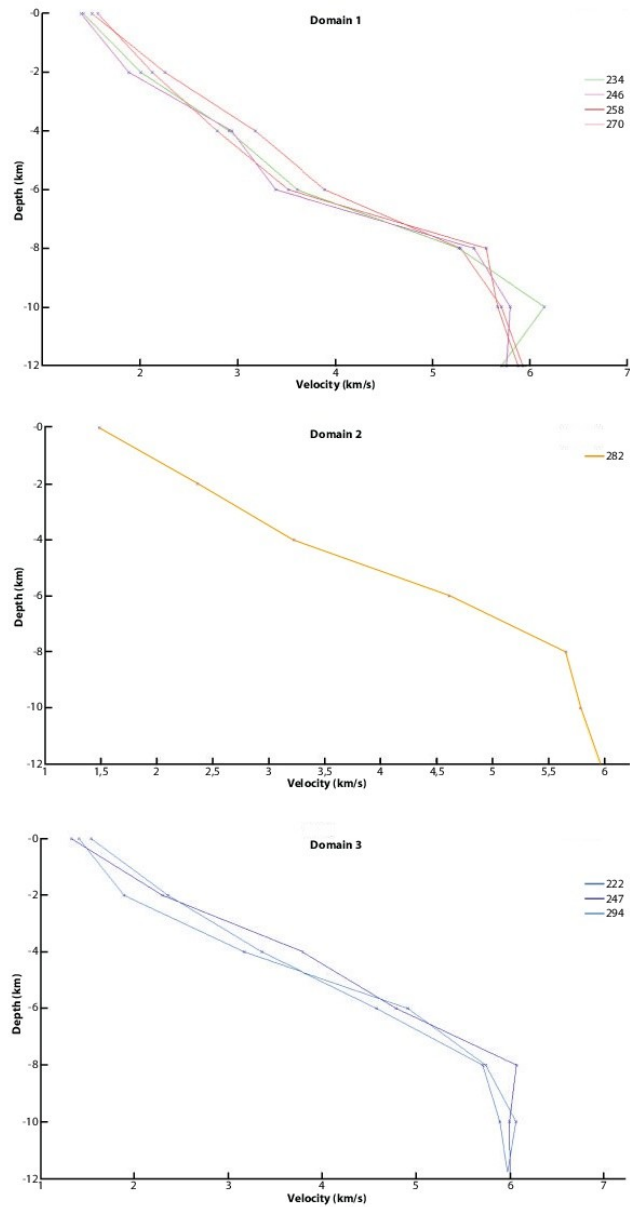


Figure A1-2a: Vertical velocity profiles (from 0 to 12 km depth below seafloor) below each node of the low-resolution, tomographic grid of Bayrakci et al [2013], within, respectively domains 1, 2 and 3 (see domain delineation in Figure A1-1). Image created with GMT software, Version 4.5.11.

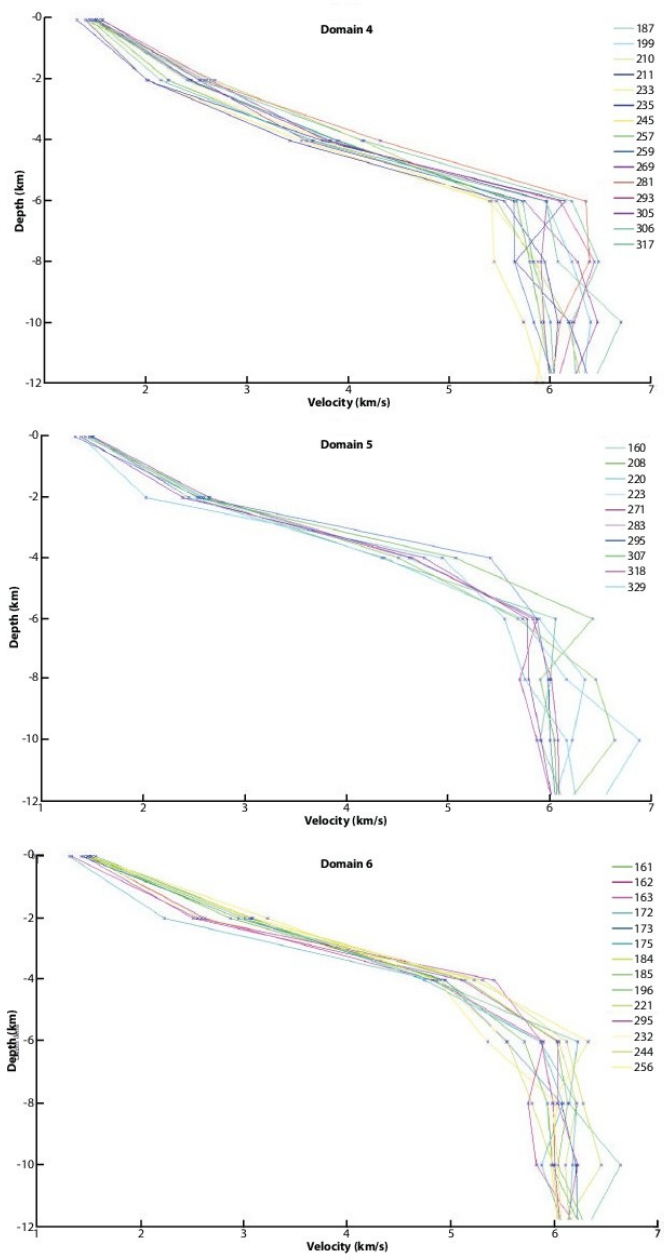


Figure A1-2b: Vertical velocity profiles (from 0 to 12 km depth below seafloor) below each node of the low-resolution, tomographic grid of Bayrakci et al [2013], within, respectively domains 4, 5 and 6 (see domain delineation in Figure A1-1). Image created with GMT software, Version 4.5.11.

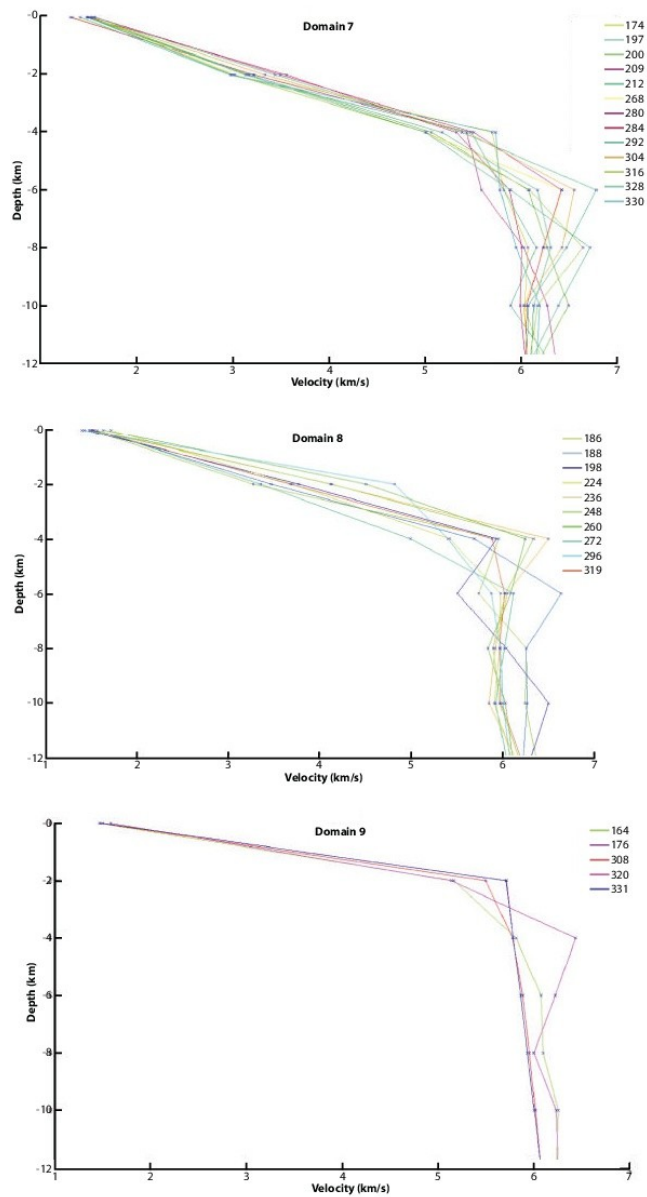


Figure A1-2c: Vertical velocity profiles (from 0 to 12 km depth below seafloor) below each node of the low-resolution, tomographic grid of Bayrakci et al [2013], within, respectively domains 7, 8 and 9 (see domain delineation in Figure A1-1). Image created with GMT software, Version 4.5.11.

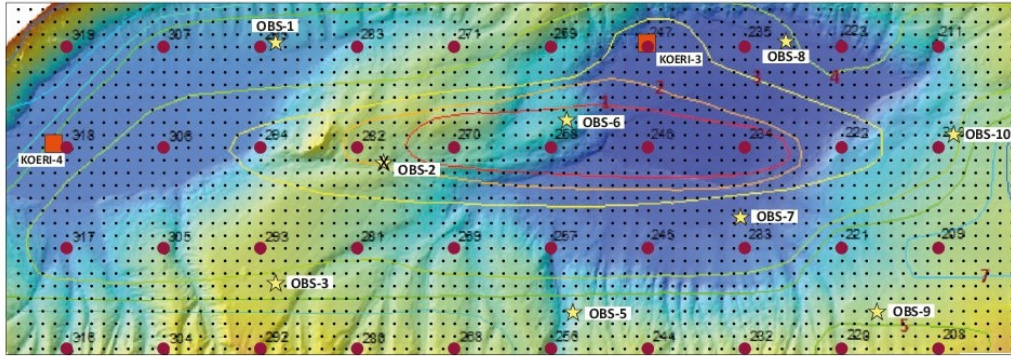


Figure A1-3: Bathymetric map of study area within the Western Sea of Marmara. Black dots indicate node locations for the high-resolution grid, with spacing of 750 m x 750 m x 200 m. Red dots indicate node locations for the low-resolution (6 km x 6 km) tomographic grid of *Bayrakci et al. [2013]*. Labels from 1 to 9 on basement iso-contours indicate domain number (see caption Fig. A1-1). KOERI's cabled OBSs and Ifremer autonomous OBSs are marked as red squares and yellow stars, respectively. The yellow star corresponding to Ifremer OBS-2 is crossed because OBS-2 stopped recording before the M_w 5.1 earthquake of July 25th, 2011. *Image created with ArcGIS, v3.*

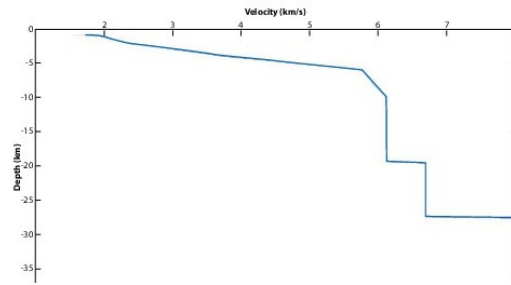


Figure A1-4: Example of velocity profile finally obtained for node located within domain 4, at longitude 27°37.56'E, latitude 40°46.50'N. The typical velocity profile of domain 4 is used for $z < 12$ km. For $z > 12$ km, velocities and interface depth for lower Crust and Moho depth are inferred as a function of longitude, based on wide-angle and refraction seismics results (e.g. see Figure 10 of Bécel et al [2009]). Image created with GMT software, Version 4.5.11.

APPENDIX 2

Testing velocity models on aftershocks relocation

Written by Estelle Cros

With contributions of Louis Géli, Anthony Lomax and Jean-Baptiste Tary

The aftershock sequence following the M_w 5.1 earthquake of July, 25th, 2011

To monitor the fault segment of the NAF in the SoM, a non-permanent network of ten OBSs with four components was deployed (Figure A2-1) and recorded data during 107 days, from April 15th to July 31st (unfortunately OBS 2 failed and stopped recording after June 30th, 2011). The network was designed to complement the permanent submarine monitoring system of the Kandilli Observatory and Earthquake Research Institute (KOERI) and to carry out a high resolution characterization of earthquakes within the Western part of the SoM, including the Tekirdag basin, the Western High and the Central basin [Cros and Géli, 2013].

KOERI's cabled OBSs were permanent stations, equipped with GURALP CMG-3, broad-band seismometers, synchronized with GPS clocks. In contrast, Ifremer OBSs were autonomous (non-permanent) equipped with 3-component, short-period (4.5 Hz) seismometers and one hydrophone. *In-situ* photographs have shown that seismometer capsules are entirely covered by sediments, providing reasonable coupling with the seafloor [e.g. Tary et al, 2011]. Based on laboratory results obtained in comparable pressure and temperature, the drifts of the OBSs' internal clocks (~ 0.3 s per month) were linearly corrected for each instrument.

Event detection was first performed using a STA/LTA algorithm through the Sytmsis® software. The problem found was that electronic signals and non-seismic, short-duration events (e.g. [Tary et al, 2012], [Embriaco et al, 2013]) were also detected by the algorithm. Hence, the picking of the first arrivals was done manually and all these type of events were removed during this process. Almost 700 events were detected and picked manually (Figure A2-2). Most of the seismicity occurred during July 2011, with an amount of ~ 550 events. This high rate of seismicity is associated to a sequence of aftershocks that followed a M_w 5.2 earthquake, which occurred on July 25th at 17h57 (Figure A2-3).

Manual picking on the OBS network proved to be very efficient to improve the detection threshold. For comparison: the catalog available on the website of the European-Mediterranean Seismological Center (EMSC) reports 145 events during the recording period, with only 70 in July 2011 (Figure A2-2). An automatic method for picking, earthquake association and location was also developed by Lomax [2014]. This automated method proved to be also efficient, as ~ 380 aftershocks were eventually located. Hereafter, we only report the results obtained from manual picking.

Velocity models

Earthquake location was performed step by step, using 1D- and 3D- velocity models. Four, 1D-models were compared (Figure 4):

- the model of Tary et al. [2011]
- a model based on Bécel [2006] and Bécel et al [2009]
- the model of Gurbuz et al. [2000],
- an average velocity model based on all these previous models.

The model derived by Gurbuz et al. [2000] is well adapted for on shore network, but does not account for the effect of the slow-velocity, surficial sediment layers. The model of Bécel et al [2006] is derived from wide-angle seismic data from an East-West profile across the Sea of Marmara and provides a good estimate of the pre-kinematic, average crustal structure. The 1D velocity model calculated by

Tary *et al.* [2011] is a composite model based on: i) high-resolution wide angle OBS data from the Tekirdag basin for the first 4km reported in Tary *et al.* [2011]; and ii) the seismic structure derived by Bécel *et al.* [2009] for depth > 4 km. Finally, a smooth model composed of the three others models was calculated to combine the informations from the different 1D velocity models (Figure A2-4).

Locations calculated using these four different models allow us to select one model that was well adapted for this network and for the earthquakes detected within the recording period. The best results were obtained using the 1D velocity model of Tary *et al.* [2011]. This model was thus used hereafter, whenever a 1D model was necessary.

One-dimensional models however do not account for the lateral variability of bathymetry and velocity structure. To encompass these complexities in the calculation of earthquake locations, different 3D-velocity models were used.

First, the 3D tomographic model of Bayrakci *et al.* [2013] having a grid spacing of 6km/6km/2km was used (Figure A2-5). The pre-kinematic basement (associated to a velocity of 4.2km/s) can be extracted from the model and is observed at a depth of 6.5 km for its deepest part in the Western high region. However, the relatively large grid spacing considerably smooths the effect of bathymetry. In order to correct for bathymetry and properly account for the effect of basin geometry, high-resolution, 3D-velocity models were built for the 20 km x 60 km area covered by the submarine network, using all available geological and geophysical information from the Sea of Marmara (see details in Appendix 2). This information includes, most particularly: i) high-resolution multibeam bathymetric grids [Le Pichon *et al.*, 2001]; ii) seismic velocity grids based on 3D, crustal tomography [Bayrakci *et al.*, 2013] and on 2D, wide-angle seismics [Bécel *et al.*, 2009]; iii) fault mapping and basin geometry line-drawing, based on the interpretation of all existing seismic profiles (e.g. [Şengör *et al.*, 2014]).

Two high-resolution models -hereafter named BCC (from Bayrakci, Coutellier, Cros)- were built:

- BCC-1 with grid mesh size of 1500 m x 1500 m x 400 m
- BCC-2 with grid mesh size of 750 m x 750 m x 200 m.

Earthquake location of the M 5.1 earthquake, aftershock sequence: results

This section strictly focuses on the fine characterization of the 3-days long aftershock sequence that followed the Mw 5.1 earthquake which occurred on July, 25th, 2011, at 17h57 (Fig. 9). The fine scale characterization was obtained following a two-steps procedure: 1) absolute locations were first obtained using a 3D-velocity model and NLLoc, a non linear routine developed by Lomax (see references); then, relative locations were obtained using HYPODD [Waldhauser *et al.*, 2000] and the 1-D velocity model of Tary *et al.* [2011].

Unfortunately, the OBS located above the mainshock hypocenter did not function. As a result, relative relocation, using HypoDD (1D and 3D) [Waldhauser, 2001] or NonLinLoc-3D [Lomax *et al.*, 2012], was performed with relative distant stations (~15 km). This turned out to be possible only over a limited (~ 20%) number of events, likely due to computation instabilities, which resulted in "air" or "water column" relocations for the most shallow events (see also Appendix 4). This result does not prove, but is consistent with the existence of an important proportion of shallow events.

Also note that, for the events associated to this aftershock sequence, the number of P-arrivals picks is not evenly distributed from one OBS to the other (Figure A2-6). Thus, we hereafter consider the results from two sub-networks: i) the complete network, except OBS 4 (located far from the network center); ii) a specific sub-network defined by 4 stations symmetrically distributed on a circle more or less centered on the mainshock: 3 IFREMER OBSs (OBS1, OBS6 and OBS3), and one KOERI station (KOERI4). In order to check for the existence of possible artifacts related to the uneven distribution of OBSs, we considered only those events having arrivals picks on these 4 OBSs.

Locations using the 6 km x 6 km x 2 km 3D-velocity model of Bayrakci et al [2013] (Figs. A2-7 and A2-8).

Absolute locations are evenly distributed between the sea-floor and 15 km at depth, with most of the seismicity concentrated on the Western High (Figure A2-7 top). Still, many aftershocks are located away from the mainshock and delineate an E-W trend below the Tekirdag Basin. Relative localization using HypoDD strongly reduces the RMS and focuses the seismicity along the fault on top of the Western High. Still, many events are found in the Tekirdag Basin along the same E-W trend (Figure A2-7 middle). In the vertical section (Figure A2-7 bottom), relative locations appear distributed into 2 groups of events, between the sea-floor and 6 km depth, and between 6 and 12 km depth, respectively.

If one considers only those events having arrival picks on the 4 stations symmetrically distributed around the mainshock (e.g. OBS1, OBS6, OBS3 and KOERI4), most absolute locations appear to be mostly focused on the Western High and located at a depth above 15 km (Figure A2-8 top). Relative localization using HypoDD results in enhanced focusing above the Western High with shallower events (depth < 10 km). Interestingly, two groups of earthquakes appear: one with depths between 0 and 5 km; and one with depths between 8 and 14 km.

Locations using the Bayrakci-Coutellier-Cros 3D-velocity model with grid mesh size of 1500 m x 1500 m x 400 m (BCC-1 model) (Figs. A2-9 and A2-10).

Absolute locations are dispersed within the Tekirdag Basin, with E-W trends (Fig. A2-9 top). Relative locations obtained with HypoDD are more focused near the epicenter of the mainshock (Fig. A2-9 middle) and shallower (Fig. A2-9 bottom) than with the Bayrakci's model.

If one considers only those events having arrival picks on the 4 stations symmetrically distributed around the mainshock (e.g. OBS1, OBS6, OBS3 and KOERI4), absolute and relative locations appear to be much more focused and closer from the fault (Figure A2-10 top and middle) than those obtained with the Bayrakci et al. [2013] model (Figure A2-8 top and middle). Two different groups of events clearly appear: one with relative location depths between 0 and 5 km; and one with relative location depths between 8 and 14 km (Fig. A2-10).

Location using the Bayrakci-Coutellier-Cros 3D-velocity model with grid mesh size of 750 m x 750 m x 200 m (BCC-2 model) (Fig. A2-11 and A2-12).

The general trends described above (with BCC-1 model) are enhanced when using the BCC-2 model. Absolute locations are dispersed within the Tekirdag Basin, with E-W trends (Fig. A2-11 top). Relative locations obtained with HypoDD are more focused near the epicenter of the mainshock (Fig. A2-11 middle) and shallower (Fig. A2-11 bottom) than with the Bayrakci's or the BCC-1 model.

If one considers only those events having arrival picks on the 4 stations symmetrically distributed around the mainshock (e.g. OBS1, OBS6, OBS3 and KOERI4), both absolute and relative locations appear to be more focused and closer from the fault (Figure A2-12 top and middle) than those obtained with the Bayrakci et al. [2013] and BCC-1 models (respectively Fig. A2-8 and A2-9, top and middle). Again, two different groups of events clearly appear: one with relative location depths between 0 and 5 km; and one with relative location depths between 8 and 14 km (Fig. A2-12 bottom to be compared with Fig. A2-10 bottom and Fig. A2-8 bottom).

REFERENCES

- Bécel, A. (2006). Structure sismique de la Faille Nord Anatolienne en Mer de Marmara, *PhD Thesis, Université Denis Diderot*.
- Bécel, A.; Laigle, M.; de Voogd, B.; Hirn, A.; Taymaz, T.; Galvé, A.; Shimamura, H.; Murai, Y.; Lépine, J.-C.; Sapin, M. & Özalaybey, S. (2009). Moho, crustal architecture and deep deformation under the North Marmara Trough, from the SEISMARMARA Leg 1 offshore-onshore reflection-refraction survey, *Tectonophysics* **467**: 1-21.
- Bayrakci, G.; Laigle, M.; Bécel, A.; Hirn, A.; Taymaz, T.; Yolsal-Cevikbilen, S. & team, S. (2013). *3-D sediment-basement tomography of the Northern Marmara trough by a dense OBS network at the nodes of a grid of controlled source profiles along the North Anatolian fault*, *Geophys. J. Int.* **194** : 1335-1357
- Bohnhoff, M.; Bulut, F.; Dresen, G.; Malin, P. E.; Eken, T. & Aktar, M. (2013). An earthquake gap south of Istanbul, *Nat Commun.* **4**:1999, doi:10.1038/ncomms2999
- Cros, E., & Géli, L. (2013), Caractérisation de microseismicité in the Western Sea of Marmara: implications in terms of seismic monitoring (Caractérisation de la micro-sismicité dans la partie occidentale de la faille Nord-Anatolienne en Mer de Marmara : implications en termes de stratégie de surveillance de l'activité sismique), *Project Report, Institut Carnot Ifremer-Edrome, Abondement 2011, N°06/11/2013, 29 pages*, available on-line: <http://dx.doi.org/10.13155/38916>
- Gürbüz, C.; Aktar, M.; Eyidogan, H.; Cisternas, A.; Haessler, H.; Barka, A.; Ergin, M.; Türkelli, N.; Polat, O.; Üçer, S.; Kuleli, S.; Baris, S.; Kaypak, B.; Bekler, T.; Zor, E.; Bicmen, F. & Yoruk, A. (2000). The seismotectonics of the Marmara region (Turkey): results from a microseismic experiment, *Tectonophysics* **316** : 1-17.
- Géli, L.; Henry, P.; Zitter, T.; Dupré, S.; Tryon, M.; Cagatay, M.; de Lépinay, B. M.; Le Pichon, X.; Sengor, A.; Gorur, N.; Natalin, B.; Uçarkus, G.; Ozeren, S.; Volker, D.; Gasperini, L.; Burnard, P.; Bourlange, S. & the Marnaut Scientific Party (2008). Gas emissions and active tectonics within the submerged section of the North Anatolian Fault zone in the Sea of Marmara, *Earth Plan. Sci. Lett.* **274** : 34-39.
- Hergert, T.; Heidbach, O.; Bécel, A. & Laigle, M. (2011). *Geomechanical model of the Marmara Sea region. 3-D contemporary kinematics*, *Geophysical Journal International* **185** : 1073-1089.
- Hubert-Ferrari, A.; Barka, A.; Jacques, E.; Nalbant, S. S.; Meyer, B.; Armijo, R.; Tapponnier, P. & King, G. C. P. (2000). Seismic hazard in the Marmara Sea region following the 17 August 1999 Izmit earthquake, *Nature* **404** : 269-273.
- Karabulut, H.; Schmittbuhl, J.; Özalaybey, S.; Lengliné, O.; Kömeç-Mutlu, A.; Durand, V.; Bouchon, M.; Daniel, G. & Bouin, M. (2011). *Evolution of the seismicity in the eastern Marmara Sea a decade before and after the 17 August 1999 Izmit earthquake*, *Tectonophysics* **510** : 17-27.
- Laigle, M.; Bécel, A.; de Voogd, B.; Hirn, A.; Taymaz, T. & Özalaybey, S. (2008). *A first deep seismic survey in the Sea of Marmara: Deep basins and whole crust architecture and evolution*, *Earth and Planetary Science Letters* **270** : 168-179.
- Le Pichon, X.; Sengor, A.; Demirbag, E.; Rangin, C.; Imren, C.; Armijo, R.; Gorur, N.; Cagatay, N.; Mercier de Lépinay, B.; Meyer, B.; Saatçilar, R. & Tok, B. (2001). *The active Main Marmara Fault*, *Earth Plan. Sci. Lett.* **192** : 595-616.
- Lomax, A., C. Satriano and M. Vassallo (2012), Automatic picker developments and optimization: FilterPicker - a robust, broadband picker for real-time seismic monitoring and earthquake early-warning, *Seism. Res. Lett.* , **83**, 531-540, doi: 10.1785/gssrl.83.3.531.
- Lomax, A. and A. Michelini (2012), Tsunami early warning within 5 minutes, *Pure and Applied Geophysics*, **169**, doi: 10.1007/s00024-012-0512-6.
- Lomax, A., A. Michelini, A. Curtis (2009), Earthquake Location, Direct, Global-Search Methods, in *Complexity In Encyclopedia of Complexity and System Science, Part 5, Springer, New York*, pp. 2449-2473, doi:10.1007/978-0-387-30440-3.
- Lomax, A., J. Virieux, P. Volant and C. Berge, (2000), Probabilistic earthquake location in 3D and layered models: Introduction of a Metropolis-Gibbs method and comparison with linear locations, in *Advances in Seismic Event Location, Thurber, C.H., and N. Rabinowitz (eds.), Kluwer, Amsterdam*, 101-134
- Lomax, A., (2014), Mise en oeuvre et support pour logiciels de traitement automatisé de données sismologiques acquises dans le cadre du projet Européen FP7 Marsite, *Contract report, Reference CNRS MA201301A*, available on line: http://alomax.net/projects/marsite/MA201301A_report_v0.2.pdf

- Meade, B. J.; Hager, B. H.; McClusky, S. C.; Reilinger, R. E.; Ergintav, S.; Lenk, O.; Barka, A. & Özener, H. (2002). *Estimates of Seismic Potential in the Marmara Sea Region from Block Models of Secular Deformation Constrained by Global Positioning System Measurements*, *Bull. Seism. Soc. Am.*, **92** : 208-215.
- Meghraoui, M.; Aksoy, M. E.; Akyuz, H. S.; Ferry, M.; Dikbas, A. & Altunel, E. (2012). Paleoseismology of the North Anatolian Fault at Güzelköy (Ganos segment, Turkey): Size and recurrence time of earthquake ruptures west of the Sea of Marmara, *Geochemistry, Geophysics, Geosystems* **13**.
- Orgülü, G. (2011). *Seismicity and source parameters for small-scale earthquakes along the splays of the North Anatolian Fault (NAF) in the Marmara Sea*, *Geophysical Journal International* **184** : 385-404.
- Lee, W. . K., & Stewart, S. W., 1981. *Principles and applications of microearthquake networks*. Academic Press, .
- Tary, J. B.; Géli, L.; Henry, P.; Natalin, B.; Gasperini, L.; Comoglu, M.; Cagatay, N. & Bardainne, T. (2011). Sea-Bottom Observations from the Western Escarpment of the Sea of Marmara, *Bull. Seism. Soc. Am.*, **101** : 775-791.
- Tryon, M. D.; Henry, P. & Hilton, D. R. (2012). Quantifying submarine fluid seep activity along the North Anatolian Fault Zone in the Sea of Marmara, *Marine Geology* **315-318** : 15-28.
- Waldhauser, F. & Ellsworth, W. L. (2000). A Double-Difference Earthquake Location Algorithm: Method and Application to the Northern Hayward Fault, California, *Bull. Seism. Soc. Am.*, **90** : 1353-1368.

FIGURE CAPTIONS

Fig. A2-1: Bathymetric map of the Western and Central part of the Sea of Marmara. The study area is delineated by coordinates $40^{\circ}43'N - 40^{\circ}54'N - 27^{\circ}30'E - 28^{\circ}15'E$ (OBS 4 and KOERI 2 are not within this study area). Image created with GMT software, Version 4.5.11.

Fig. A2-2: Number of events by day recorded on the catalog of the European-Mediterranean Seismological Center (EMSC) (top) and detected by the network of OBS (bottom). Image created with GMT software, Version 4.5.11.

Fig. A2-3: Details of the histogram, showing the number of events (over 6 hours periods) detected by the different OBSs, following the Mw 5.1 earthquake that occurred on July 25th, 2011, at 17:57. Almost half of the aftershocks occurred within the first 12 hours after the mainshock. Image created with GMT software, Version 4.5.11.

Fig. A2-4: 1-D velocity models used in the present study. In black the model of Gurbuz et al. [2000], in green the model of Bécel [2006], in red the model from Tary et al. [2011] and in blue a model calculated from the three others. Image created with GMT software, Version 4.5.11.

Fig. A2-5: After Bayrakci et al [2013]. Map view at 2, 4, 6 and 8 km depths of the inversion results. Grid node (black dots) spacing is 6 km x 6 km x 2 km. Grey hexagons are receivers (OBSs and land stations) of the survey. The white points are the considered shots. The white contour (RDE = 0.05) surrounds the well-resolved nodes identified by the checkerboard test. The black contour (DWS = 50) surrounds the nodes, which have been inverted during the inversion. The black crosses are the inverted nodes whereas the red ones are the fixed ones [Bayrakci et al. 2013]. Image created with GMT software, Version 4.5.11.

Fig. A2-6: Number of P-arrival picks detected at each OBS (IFREMER and KOERI). Image created with GMT software, Version 4.5.11.

Fig. A2-7: Top : Absolute locations of aftershocks using the 3D velocity model of Bayrakci et al. [2013] and NLOC (e.g. Lomax et al, [2000] ; Lomax et al [2009]). Middle : relative locations using the 1D velocity model of Tary et al. [2011] and hypoDD [Waldhauser et al, 2000]. Bottom : Vertical cross-section showing depth distribution of epicenters (relative locations). Image created with GMT software, Version 4.5.11.

Fig. A2-8 In order to check for possible artifacts related to the uneven distribution of OBSs, we

considered a specific sub-network defined by 4 stations symmetrically distributed on a circle more or less centered on the mainshock : 3 IFREMER OBSs (OBS1, OBS6 and OBS3), and one KOERI station (KOERI4). Only those events having arrivals picks on the 4 OBSs are here considered in the present figure. Top : Absolute locations of aftershocks using the 3D velocity model of Bayrakci et al. [2013] and NLLC (e.g. Lomax et al, [2000] ; Lomax et al [2009]). Middle : relative locations using the 1D velocity model of Tary et al. [2011] and hypoDD [Waldhauser et al, 2000]. Bottom : Vertical cross-section showing depth distribution of epicenters (relative locations). Image created with GMT software, Version 4.5.11.

Fig. A2-9 Top : Absolute locations of aftershocks using the BCC-1, 3D velocity model (1.5 km x 1.5 km x 0.4 km) and NLLC (e.g. Lomax et al, [2000] ; Lomax et al [2009]). Middle : relative locations using the 1D velocity model of Tary et al. [2011] and hypoDD [Waldhauser et al, 2000]. Bottom : Vertical cross-section showing depth distribution of epicenters (relative locations). Image created with GMT software, Version 4.5.11.

Fig. A3.10: In order to check for possible artifacts related to the uneven distribution of OBSs, we considered a specific sub-network defined by 4 stations symmetrically distributed on a circle more or less centered on the mainshock : 3 IFREMER OBSs (OBS1, OBS6 and OBS3), and one KOERI station (KOERI4). Only those events having arrivals picks on the 4 OBSs are here considered in the present figure. Top : Absolute locations of aftershocks using the BCC-1, 3D velocity model (1.5 km x 1.5 km x 0.4 km) and NLLC (e.g. Lomax et al, [2000] ; Lomax et al [2009]). Middle : relative locations using the 1D velocity model of Tary et al. [2011] and hypoDD [Waldhauser et al, 2000]. Bottom : Vertical cross-section showing depth distribution of epicenters (relative locations). Image created with GMT software, Version 4.5.11.

Fig. A2-11: Top : Absolute locations of aftershocks using the BCC-2, 3D velocity model (750 m x 750 m x 200 m) and NLLC (e.g. Lomax et al, [2000] ; Lomax et al [2009]). Middle : relative locations using the 1D velocity model of Tary et al. [2011] and hypoDD [Waldhauser et al, 2000]. Bottom : Vertical cross-section showing depth distribution of epicenters (relative locations). Image created with GMT software, Version 4.5.11.

Fig. A2-12: In order to check for possible artifacts related to the uneven distribution of OBSs, we considered a specific sub-network defined by 4 stations symmetrically distributed on a circle more or less centered on the mainshock : 3 IFREMER OBSs (OBS1, OBS6 and OBS3), and one KOERI station (KOERI4). Only those events having arrivals picks on the 4 OBSs are here considered in the present figure. Top : Absolute locations of aftershocks using the BCC-2, 3D velocity model (750 m x 750 m x 200 m) and NLLC (e.g. Lomax et al, [2000] ; Lomax et al [2009]). Middle : relative locations using the 1D velocity model of Tary et al. [2011] and hypoDD [Waldhauser et al, 2000]. Bottom : Vertical cross-section showing depth distribution of epicenters (relative locations). Image created with GMT software, Version 4.5.11.

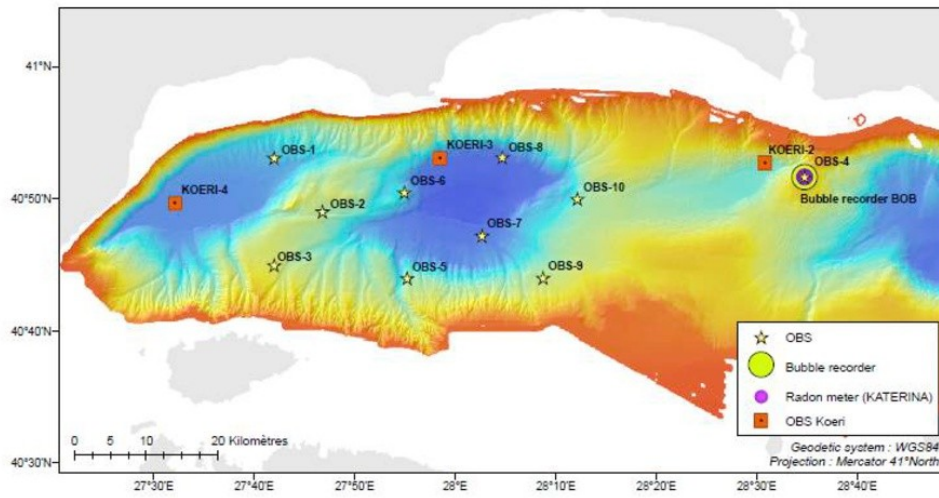


Figure A2-1: Bathymetric map of the Western and Central part of the Sea of Marmara. The study area is delineated by coordinates $40^{\circ}43'N - 40^{\circ}54'N - 27^{\circ}30'E - 28^{\circ}15'E$ (OBS 4 and KOERI 2 are not within this study area). Image created with GMT software, Version 4.5.11.

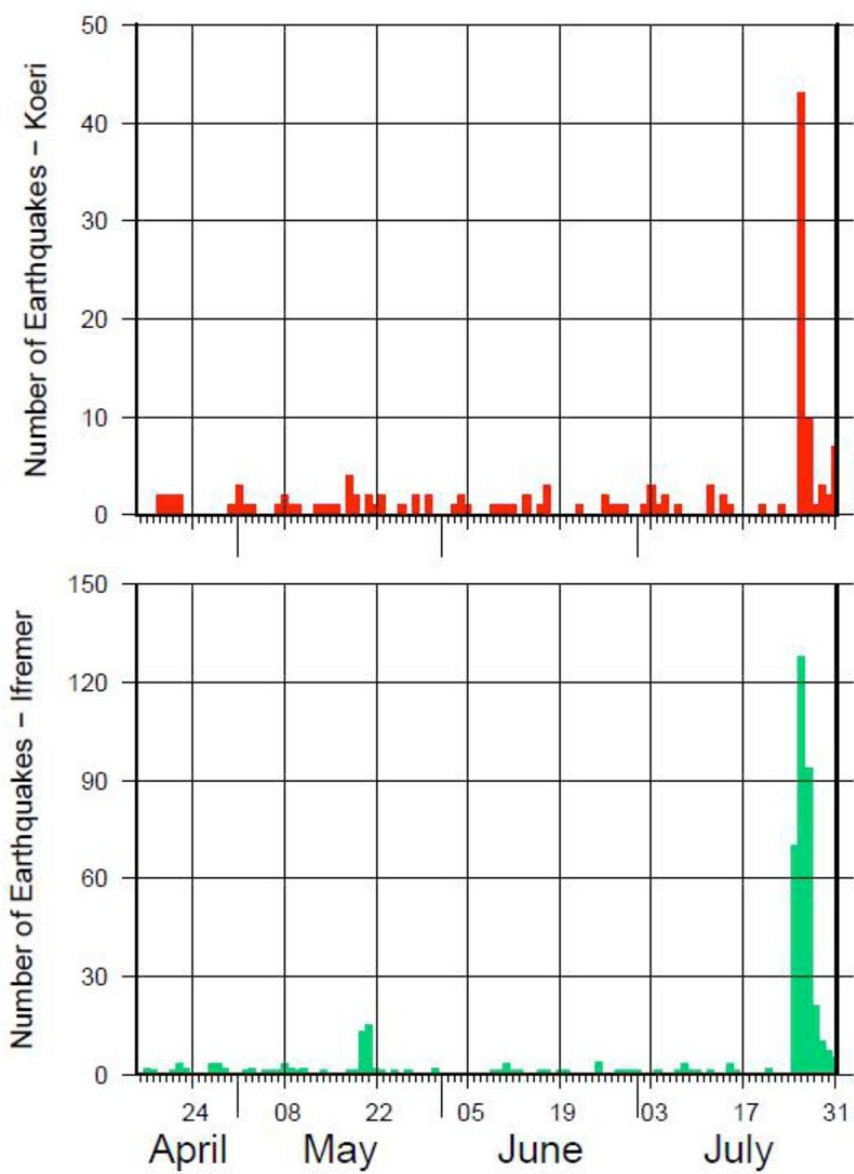


Figure A2-2: Number of events by day recorded on the catalog of the European-Mediterranean Seismological Center (EMSC) (top) and detected by the network of OBS (bottom). *Image created with GMT software, Version 4.5.11.*

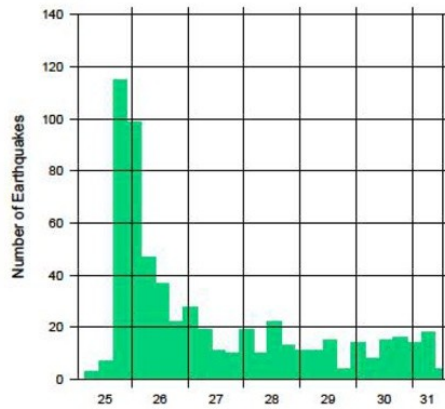


Figure A2-3: Details of the histogram, showing the number of events (over 6 hours periods) detected by the different OBSs, following the Mw 5.1 earthquake that occurred on July 25th, 2011, at 17:57. Almost half of the aftershocks occurred within the first 12 hours after the mainshock. Image created with GMT software, Version 4.5.11.

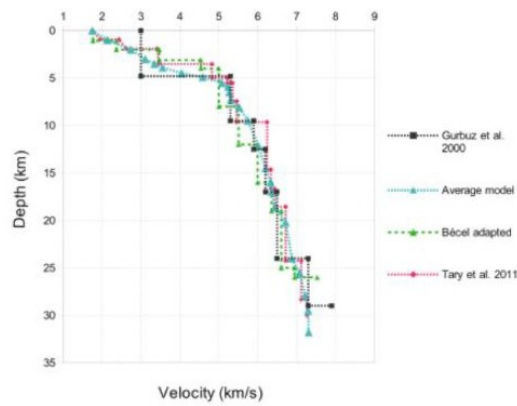


Fig. A2-4: 1-D velocity models used in the present study. In black the model of Gurbuz et al. [2000], in green the model of Bécel [2006], in red the model from Tary et al. [2011] and in blue a model calculated from the three others. Image created with GMT software, Version 4.5.11.

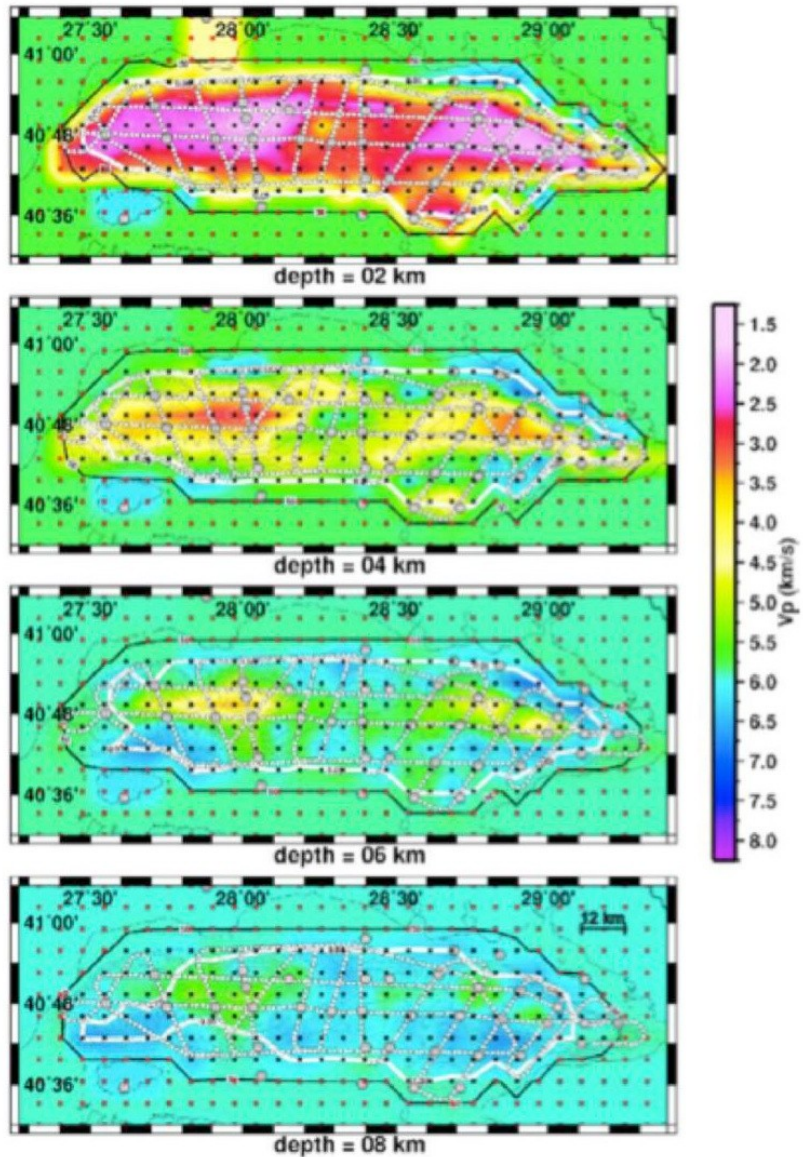


Fig. A2-5: After Bayrakci et al [2013]. Map view at 2, 4, 6 and 8 km depths of the inversion results. Grid node (black dots) spacing is 6 km x 6 km x 2 km. Grey hexagons are receivers (OBSs and land stations) of the survey. The white points are the considered shots. The white contour (RDE = 0.05) surrounds the well-resolved nodes identified by the checkerboard test. The black contour (DWS = 50) surrounds the nodes, which have been inverted during the inversion. The black crosses are the inverted nodes whereas the red ones are the fixed ones [Bayrakci et al. 2013]. Image created with GMT software, Version 4.5.11.

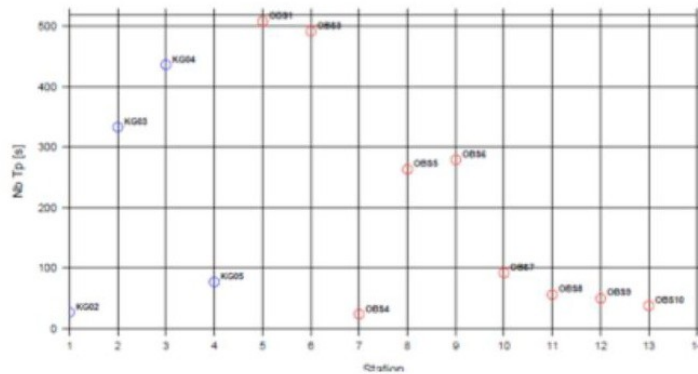


Fig. A2-6 Number of P-arrival picks detected at each OBS (IFREMER and KOERI). Image created with GMT software, Version 4.5.11.

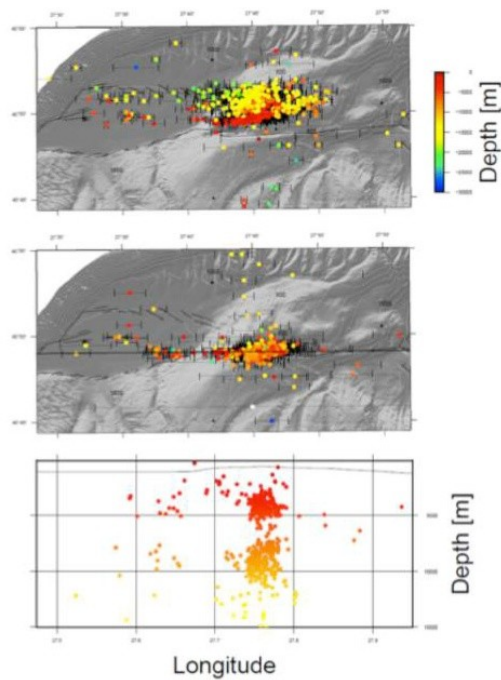


Fig. A2-7: Top : Absolute locations of aftershocks using the 3D velocity model of Bayrakci et al. [2013] and NLLOC (e.g. Lomax et al, [2000] ; Lomax et al [2009]). Middle : relative locations using the 1D velocity model of Tary et al. [2011] and hypoDD [Waldhauser et al, 2000]. Bottom : Vertical cross-section showing depth distribution of epicenters (relative locations). Image created with GMT software, Version 4.5.11.

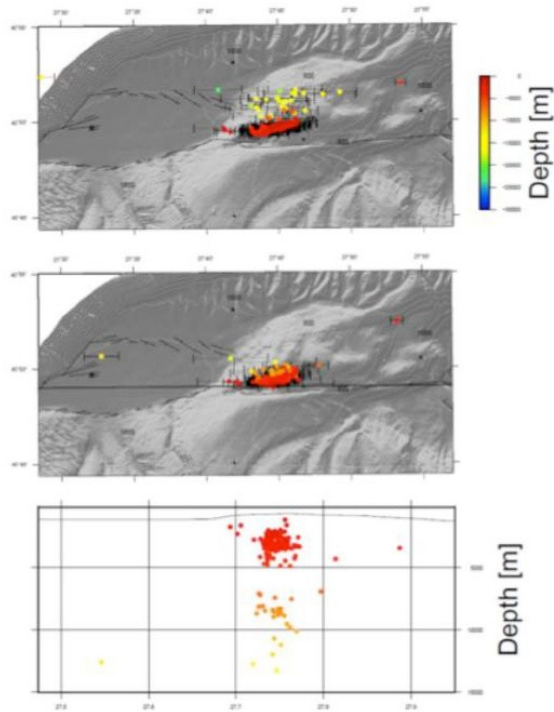


Fig. A2-8 In order to check for possible artifacts related to the uneven distribution of OBSs, we considered a specific sub-network defined by 4 stations symmetrically distributed on a circle more or less centered on the mainshock : 3 IFREMER OBSs (OBS1, OBS6 and OBS3), and one KOERI station (KOERI4). Only those events having arrivals picks on the 4 OBSs are here considered in the present figure. Top : Absolute locations of aftershocks using the 3D velocity model of Bayrakci et al. [2013] and NLLoc (e.g. Lomax et al, [2000] ; Lomax et al [2009]). Middle : relative locations using the 1D velocity model of Tary et al. [2011] and hypoDD [Waldhauser et al, 2000]. Bottom : Vertical cross-section showing depth distribution of epicenters (relative locations). Image created with GMT software, Version 4.5.11.

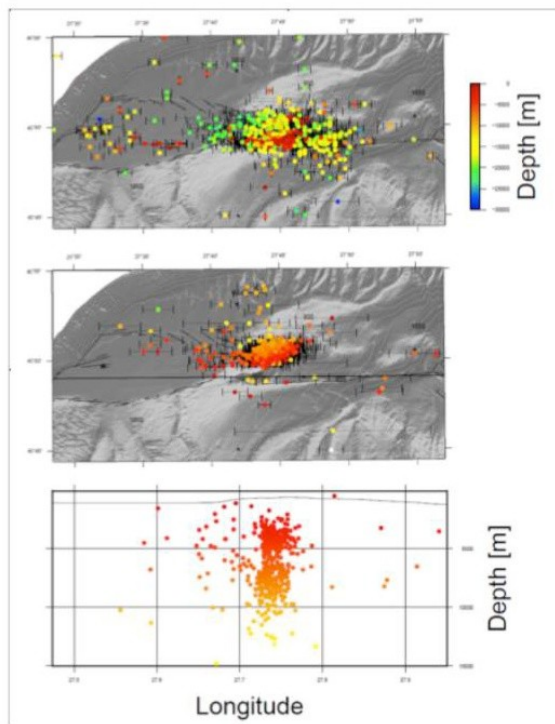


Fig. A2-9 Top : Absolute locations of aftershocks using the BCC-1, 3D velocity model (1.5 km x 1.5 km x 0.4 km) and NLLOC (e.g. Lomax et al, [2000] ; Lomax et al [2009]). Middle : relative locations using the 1D velocity model of Tary et al. [2011] and hypoDD [Waldhauser et al, 2000]. Bottom : Vertical cross-section showing depth distribution of epicenters (relative locations). Image created with GMT software, Version 4.5.11.

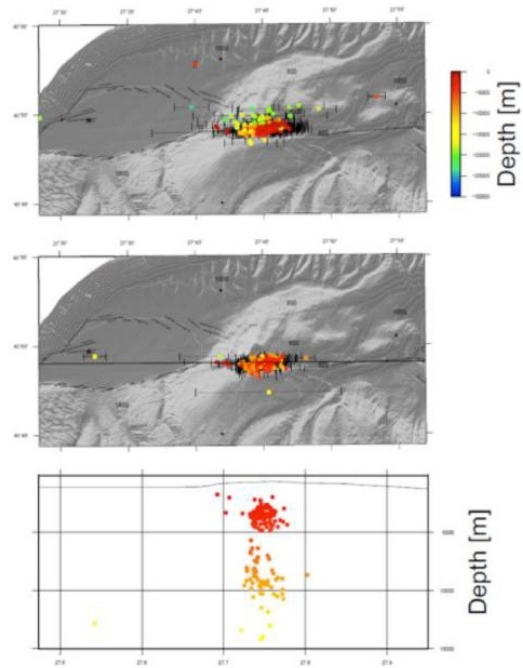


Fig. A2.10: In order to check for possible artifacts related to the uneven distribution of OBSs, we considered a specific sub-network defined by 4 stations symmetrically distributed on a circle more or less centered on the mainshock : 3 IFREMER OBSs (OBS1, OBS6 and OBS3), and one KOERI station (KOERI4). Only those events having arrivals picks on the 4 OBSs are here considered in the present figure. Top : Absolute locations of aftershocks using the BCC-1, 3D velocity model (1.5 km x 1.5 km x 0.4 km) and NLLOC (e.g. Lomax et al, [2000] ; Lomax et al [2009]). Middle : relative locations using the 1D velocity model of Tary et al. [2011] and hypoDD [Waldhauser et al, 2000]. Bottom : Vertical cross-section showing depth distribution of epicenters (relative locations). Image created with GMT software, Version 4.5.11.

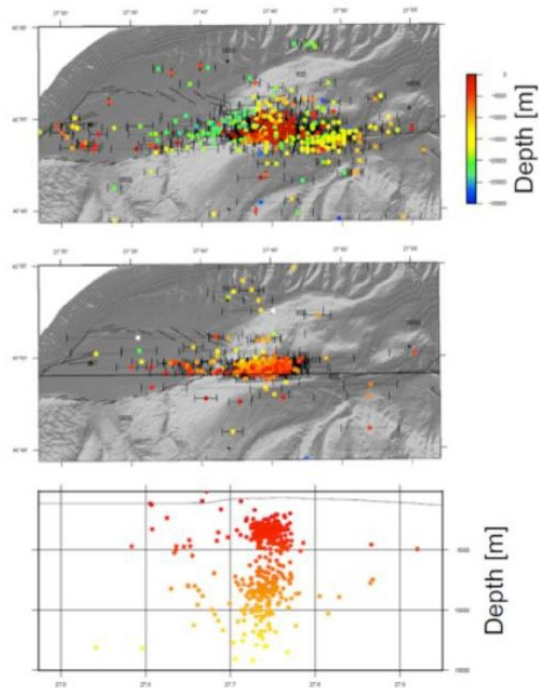


Fig. A2-11: Top : Absolute locations of aftershocks using the BCC-2, 3D velocity model (750 m x 750 m x 200 m) and NLLOC (e.g. Lomax et al, [2000] ; Lomax et al [2009]). Middle : relative locations using the 1D velocity model of Tary et al. [2011] and hypoDD [Waldhauser et al, 2000]. Bottom : Vertical cross-section showing depth distribution of epicenters (relative locations). Image created with GMT software, Version 4.5.11.

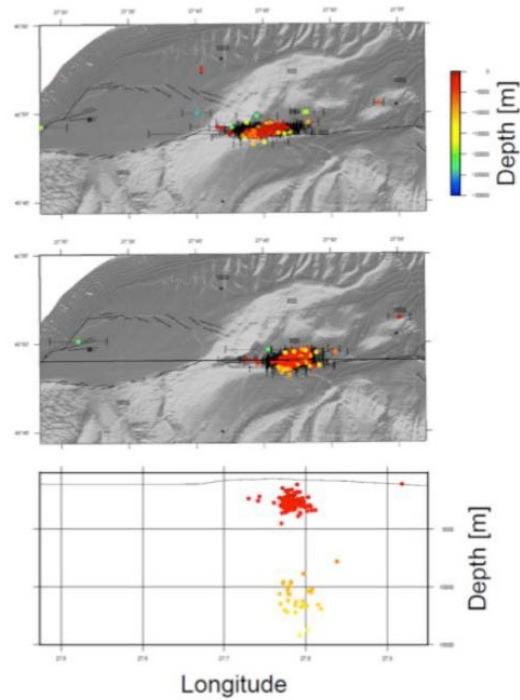


Fig. A2-12: In order to check for possible artifacts related to the uneven distribution of OBSs, we considered a specific sub-network defined by 4 stations symmetrically distributed on a circle more or less centered on the mainshock : 3 IFREMER OBSs (OBS1, OBS6 and OBS3), and one KOERI station (KOERI4). Only those events having arrivals picks on the 4 OBSs are here considered in the present figure. Top : Absolute locations of aftershocks using the BCC-2, 3D velocity model (750 m x 750 m x 200 m) and NLOC (e.g. Lomax et al, [2000] ; Lomax et al [2009]). Middle : relative locations using the 1D velocity model of Tary et al. [2011] and hypoDD [Waldhauser et al, 2000]. Bottom : Vertical cross-section showing depth distribution of epicenters (relative locations). Image created with GMT software, Version 4.5.11.

APPENDIX 3
GELI_SREP-16-51867_APPENDIX3_FINAL

List of relocated aftershocks triggered by the M 5.1 earthquake of July 25th, 2011 below the Sea of Marmara

Lines finishing with "HASH" indicate those earthquakes that have been used to compute a composite focal mechanism with HASH method (e.g. [Hardebeck and Shearer, 2003]; [Hardebeck and Shearer, 2008]).

References

Hardebeck, J.L. and Shearer, P.M., (2003). Using S/P Amplitude Ratios to Constrain the Focal Mechanisms of Small Earthquakes, *Bulletin of the Seismological Society of America*, 93, 2434-2444.
 Hardebeck, J.L. and Shearer, P.M., (2008). HASH: A Fortran program for computing Earthquake First-Motion Focal Mechanisms -v1.2 - January 31

YY	Mo	DD	HH	min	sec	lat	lon	depth	M _l	ex	ey	ez
2011	7	25	17	57	33.759	40.819431	27.750807	-11.499000	5.1	0.060000	0.050000	0.227000
2011	7	25	18	2	42.352	40.821918	27.778866	-0.977988	1.7	0.053000	0.028000	0.233000
2011	7	25	18	4	34.131	40.818432	27.759413	-2.425820	1.5	0.060000	0.022000	0.260000
2011	7	25	18	7	41.272	40.821350	27.764523	-6.392250	1.1	0.062000	0.075000	0.227000
2011	7	25	18	11	3.946	40.816814	27.748871	-2.536190	1.0	0.089000	0.023000	0.143000
2011	7	25	18	14	44.935	40.816612	27.766193	-2.083400	0.9	0.041000	0.020000	0.133000
2011	7	25	18	15	27.044	40.816216	27.752365	-2.598190	1.1	0.082000	0.029000	0.271000
2011	7	25	18	18	24.008	40.820786	27.761404	-0.837845	0.8	0.054000	0.023000	0.110000
2011	7	25	18	24	21.578	40.817490	27.749113	-6.056920	0.8	0.215000	0.037000	1.189000
2011	7	25	18	31	25.096	40.818356	27.755905	-0.213655	0.7	0.076000	0.019000	0.068000
2011	7	25	18	37	49.705	40.818558	27.768202	-2.138260	0.9	0.055000	0.024000	0.226000
2011	7	25	19	21	46.109	40.824375	27.755228	-7.622220	2.4	0.057000	0.175000	0.713000
2011	7	25	20	27	55.856	40.816772	27.763325	-0.979471	1.0	0.058000	0.019000	0.050000
2011	7	25	20	46	19.381	40.821373	27.758614	-6.016800	1.7	0.069000	0.051000	0.169000
2011	7	25	20	54	42.009	40.817627	27.774149	-0.242670	0.9	0.062000	0.027000	0.068000
2011	7	25	20	55	11.677	40.815983	27.754362	-0.862758	2.2	0.033000	0.017000	0.080000
2011	7	25	20	57	7.607	40.815800	27.749414	-4.034590	1.6	0.095000	0.033000	0.452000 HASH
2011	7	25	20	58	59.732	40.816532	27.750210	-2.251200	1.0	0.075000	0.024000	0.351000
2011	7	25	21	13	26.951	40.791153	27.783297	-0.661734	0.9	0.092000	0.173000	0.137000
2011	7	25	21	20	52.292	40.820580	27.765345	-0.845829	0.8	0.079000	0.023000	0.149000
2011	7	25	21	28	35.160	40.816368	27.750235	-4.150620	1.2	0.080000	0.024000	0.421000 HASH
2011	7	25	21	36	2.710	40.818691	27.758835	-0.782731	0.9	0.068000	0.019000	0.087000
2011	7	25	21	38	27.921	40.815788	27.752163	-1.179000	1.0	0.044000	0.021000	0.219000
2011	7	25	21	46	51.210	40.818008	27.746834	-1.734070	1.1	0.046000	0.019000	0.116000
2011	7	25	21	55	51.740	40.815361	27.739273	-4.665650	1.2	0.070000	0.048000	0.355000 HASH
2011	7	25	21	57	44.987	40.820908	27.752178	-0.724823	0.8	0.033000	0.019000	0.082000
2011	7	25	22	0	37.534	40.814465	27.749849	-2.257610	1.1	0.047000	0.020000	0.117000
2011	7	25	22	35	1.716	40.814854	27.745348	-2.197140	1.9	0.075000	0.022000	0.214000
2011	7	25	22	47	9.692	40.821266	27.770475	-0.960408	1.7	0.034000	0.020000	0.100000
2011	7	25	22	48	34.486	40.816544	27.782555	-10.257900	0.8	0.062000	0.041000	0.29000
2011	7	25	23	5	39.640	40.817280	27.754457	-0.731253	0.7	0.045000	0.020000	0.145000
2011	7	25	23	19	26.254	40.819622	27.738045	-6.585730	0.8	0.078000	0.049000	0.245000
2011	7	25	23	20	20.935	40.816086	27.754702	-1.861580	1.4	0.042000	0.021000	0.151000
2011	7	25	23	35	42.583	40.819546	27.752638	-0.122316	1.6	0.057000	0.017000	0.069000
2011	7	25	23	59	9.000	40.820988	27.749704	-0.486965	0.5	0.065000	0.016000	0.079000
2011	7	26	0	42	39.445	40.818359	27.770784	-0.951129	1.4	0.049000	0.028000	0.197000
2011	7	26	1	0	12.520	40.816616	27.742247	-4.846300	0.7	0.120000	0.073000	0.321000 HASH
2011	7	26	1	6	43.238	40.817947	27.763597	-1.299030	1.0	0.044000	0.016000	0.081000
2011	7	26	1	52	50.681	40.817177	27.746067	-1.317560	1.4	0.059000	0.019000	0.221000
2011	7	26	2	27	12.293	40.825191	27.783472	-7.062270	1.4	0.085000	0.066000	0.219000
2011	7	26	2	29	43.519	40.821865	27.750734	-5.615620	0.5	0.079000	0.116000	0.492000 HASH
2011	7	26	2	35	49.205	40.823612	27.779015	-0.664657	0.9	0.038000	0.059000	0.369000
2011	7	26	3	23	0.318	40.817333	27.747803	-0.318697	1.1	0.068000	0.015000	0.101000

2011	7	26	3	23	7.579	40.818893	27.757208	-1.528590	1.2	0.076000	0.021000	0.353000
2011	7	26	4	37	34.894	40.817451	27.768347	-0.732141	1.4	0.034000	0.017000	0.063000
2011	7	26	5	4	21.888	40.818844	27.762892	-0.682499	0.6	0.048000	0.023000	0.099000
2011	7	26	5	19	0.774	40.826267	27.772551	-2.665670	1.2	0.144000	0.131000	0.540000
2011	7	26	5	28	19.289	40.839230	28.142277	-17.534100	0.8	1.266000	0.656000	0.881000
2011	7	26	5	36	47.072	40.818748	27.738325	-5.766200	0.9	0.062000	0.032000	0.268000 HASH
2011	7	26	6	2	39.577	40.820538	27.769218	-1.427060	0.8	0.041000	0.022000	0.196000
2011	7	26	6	35	33.297	40.816017	27.762562	-3.637100	1.0	0.094000	0.027000	0.590000
2011	7	26	6	37	57.030	40.817612	27.752043	-1.523800	1.1	0.065000	0.018000	0.130000
2011	7	26	7	12	44.812	40.819790	27.748047	-2.961600	0.6	0.052000	0.025000	0.135000
2011	7	26	7	20	4.667	40.813862	27.747988	-2.674630	0.9	0.078000	0.023000	0.177000
2011	7	26	7	35	3.878	40.813087	27.763771	-0.879162	1.2	0.069000	0.058000	0.286000
2011	7	26	8	25	58.176	40.823372	27.771366	-5.555770	0.7	0.081000	0.024000	0.418000 HASH
2011	7	26	8	46	29.190	40.816521	27.742756	-2.384820	0.7	0.094000	0.020000	0.159000
2011	7	26	9	59	41.846	40.820618	27.754610	-2.103570	0.6	0.053000	0.018000	0.201000
2011	7	26	10	22	46.159	40.825493	27.805195	-0.920796	0.7	0.029000	0.031000	0.153000
2011	7	26	10	26	19.471	40.819733	27.711847	-0.473366	0.5	0.080000	0.015000	0.063000
2011	7	26	10	30	21.331	40.816860	27.762030	-0.156155	0.7	0.094000	0.022000	0.055000
2011	7	26	10	48	9.180	40.817307	27.752171	-0.403453	0.8	0.077000	0.019000	0.088000
2011	7	26	10	50	5.981	40.818214	27.747742	-7.028020	1.0	0.050000	0.079000	0.178000
2011	7	26	11	3	52.670	40.821823	27.749489	-6.053760	2.2	0.053000	0.090000	0.249000
2011	7	26	12	14	23.484	40.814499	27.742170	-6.232930	0.7	0.084000	0.037000	0.336000
2011	7	26	14	44	42.379	40.843136	27.680277	-25.509300	1.5	0.761000	0.713000	1.399000
2011	7	26	16	18	17.493	40.815395	27.746065	-0.935856	1.1	0.053000	0.024000	0.214000
2011	7	26	17	19	36.145	40.820370	27.751101	-1.833300	1.4	0.060000	0.019000	0.310000
2011	7	26	19	15	17.377	40.815212	27.752506	-1.870670	0.9	0.081000	0.027000	0.313000
2011	7	26	19	45	28.232	40.829102	27.748108	-14.650300	1.0	0.056000	0.056000	0.212000
2011	7	26	21	44	28.948	40.816528	27.741415	-0.796585	0.7	0.088000	0.018000	0.121000
2011	7	26	22	28	34.738	40.823235	27.767639	-2.058960	1.2	0.081000	0.030000	0.133000
2011	7	26	23	5	49.268	40.822105	27.757240	-4.613740	0.7	0.098000	0.033000	0.424000 HASH
2011	7	26	23	18	57.630	40.821583	27.774755	-0.817410	1.2	0.036000	0.026000	0.114000
2011	7	27	1	6	53.909	40.820374	27.764826	-1.137760	0.9	0.082000	0.018000	0.104000
2011	7	27	1	30	49.476	40.814671	27.750582	-3.769950	0.6	0.065000	0.025000	0.266000
2011	7	27	2	4	8.257	40.819794	27.760338	-1.356690	0.7	0.048000	0.023000	0.174000
2011	7	27	7	38	16.265	40.818504	27.766407	-0.923795	0.5	0.089000	0.028000	0.243000
2011	7	27	7	39	30.759	40.817699	27.768108	-0.242922	0.6	0.041000	0.019000	0.081000
2011	7	27	8	21	35.681	40.819805	27.774345	-0.202807	0.5	0.096000	0.032000	0.095000
2011	7	27	8	40	22.215	40.816769	27.754026	-1.348200	0.5	0.082000	0.019000	0.150000
2011	7	27	8	53	19.209	40.826210	27.743307	-6.685130	0.5	0.109000	0.031000	0.171000
2011	7	27	9	48	39.364	40.818966	27.746773	-0.037935	0.7	0.038000	0.016000	0.030000
2011	7	27	9	54	55.778	40.820225	27.725117	-14.713900	0.6	0.069000	0.059000	0.231000
2011	7	27	10	21	54.645	40.819927	27.747383	-4.994490	0.9	0.113000	0.033000	0.489000 HASH
2011	7	27	15	34	32.105	40.823910	27.755653	-0.784939	1.1	0.066000	0.067000	0.306000
2011	7	27	20	55	47.824	40.815945	27.744890	-3.135910	0.9	0.073000	0.019000	0.148000
2011	7	27	21	40	38.168	40.819309	27.752707	-0.210890	0.8	0.037000	0.020000	0.089000
2011	7	27	22	44	15.426	40.821056	27.740309	-2.123820	1.3	0.119000	0.026000	0.446000
2011	7	28	0	55	14.212	40.816841	27.742762	-1.321120	0.9	0.095000	0.016000	0.139000
2011	7	28	1	10	40.236	40.823986	27.769501	-0.574948	0.9	0.044000	0.025000	0.150000
2011	7	28	1	39	14.252	40.816879	27.746952	-0.918418	0.9	0.052000	0.016000	0.132000
2011	7	28	1	44	50.652	40.816395	27.746264	-2.849680	0.9	0.082000	0.021000	0.246000
2011	7	28	3	28	23.153	40.817825	27.750534	-0.254746	1.1	0.067000	0.016000	0.070000
2011	7	28	6	14	54.680	40.814960	27.775223	-7.129040	0.9	0.057000	0.041000	0.191000
2011	7	28	9	34	6.758	40.822674	27.763832	-0.493470	3.3	0.046000	0.023000	0.060000
2011	7	28	11	35	18.085	40.819996	27.764313	-1.001330	1.1	0.054000	0.020000	0.076000
2011	7	28	16	54	30.753	40.816696	27.744074	-3.210350	1.1	0.085000	0.019000	0.101000
2011	7	29	1	10	10.672	40.814861	27.745739	-2.506140	1.1	0.087000	0.024000	0.221000
2011	7	29	1	51	46.690	40.818104	27.745768	-6.947060	1.5	0.061000	0.135000	0.330000
2011	7	29	9	1	59.355	40.816410	27.739592	-4.679300	1.4	0.050000	0.021000	0.186000 HASH
2011	7	29	13	30	48.176	40.817596	27.748293	-5.126970	1.0	0.069000	0.038000	0.318000 HASH

2011	7	29	14	27	43.220	40.819725	27.745876	-7.148010	1.1	0.136000	0.035000	0.503000	
2011	7	29	21	4	22.831	40.820583	27.764042	-0.839774	1.1	0.051000	0.026000	0.250000	
2011	7	30	3	41	55.533	40.822121	27.758406	-1.462720	1.1	0.070000	0.023000	0.175000	
2011	7	30	3	48	36.609	40.823280	27.758135	-1.171310	0.7	0.094000	0.024000	0.196000	
2011	7	30	6	27	5.510	40.826706	27.781101	-0.819320	0.9	0.048000	0.100000	0.315000	
2011	7	30	10	31	48.249	40.815159	27.748770	-2.207350	1.0	0.052000	0.041000	0.238000	
2011	7	30	16	30	53.164	40.815746	27.749296	-4.690450	1.1	0.063000	0.032000	0.253000	HASH
2011	7	30	21	8	35.998	40.820644	27.769365	-0.030947	1.5	0.042000	0.028000	0.029000	
2011	7	31	7	18	16.526	40.823521	27.771490	-0.535226	1.0	0.044000	0.026000	0.101000	

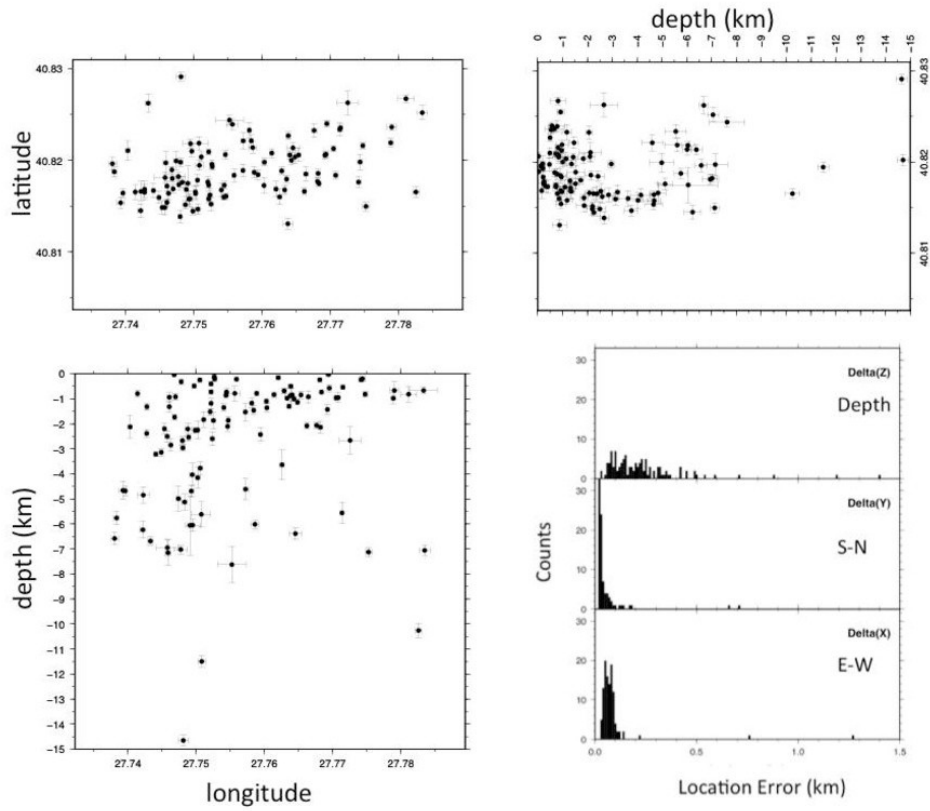


Figure A3-1. Location errors of the above listed aftershocks that followed the July, 25th, 2011 mainshock. a) latitude-longitude plane; b) longitude-depth plane; c) latitude-depth plane. Panel d) displays the distribution of location errors in the 3 directions: depth (Δz); South-North (Δy); Est-West (Δx). Image created with GMT software, Version 4.5.11.

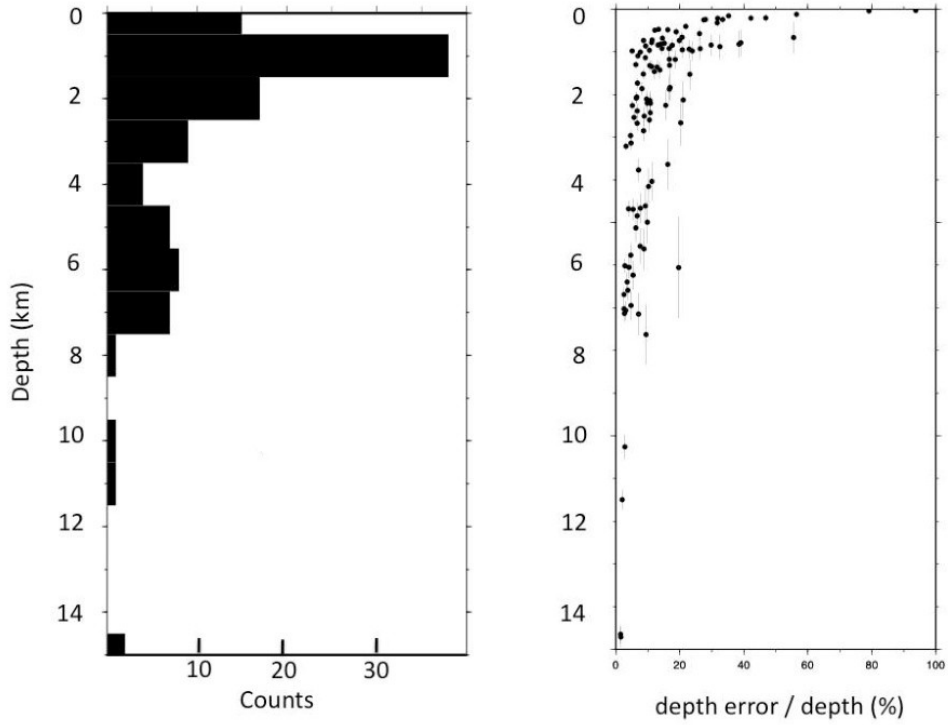


Figure A3-2. Depth distribution of the aftershocks that followed the July, 25th, 2011 mainshock. Right panel indicates the relative depth error, expressed as the ratio between the depth location error and depth, displayed vs depth. Image created with GMT software, Version 4.5.11

APPENDIX 4: Estimation of geotherm below the Western High area within the Sea of Marmara

Written by Louis Géli, Céline Grall, Pierre Henry

To estimate the depth range at which temperatures ranging between 75°C and 80°C might be expected, eight thermal measurements (Figure A4-1) were obtained from the Western High, where the 3D high-resolution seismic survey was shot: 3 during the Marmesonet Cruise of *R/V Le Suroit* in 2009 and 5 during the *Marm-2010* cruise of *R/V Urania* in 2010. The measurements were made using autonomous digital temperature probes fitted at different levels on the barrel of a gravity corer. Because of frictional heating produced by the penetration of each probe, the temperature within the sediments was recorded during 7 to 10 min after the penetration and extrapolated to infinite time to yield the ambient, equilibrium temperature in the unperturbed sediment [e.g., *Langseth, 1965*]. Plots of sediment temperature versus depth below seafloor provide thermal profiles (Figure A4-2):

- i) within the fault valley, 2 linear profiles, with gradients of respectively, 50.9 K.km⁻¹ and 57.8 K.km⁻¹, were obtained ;
- ii) south of the fault, 2 measurements were made, both at gas emission sites exhibiting linearity and gradient values of 30.7 K.km⁻¹ and 35.3 K.km⁻¹, respectively
- iii) north of the fault, 3 measurements were made: the 2 that were collected a few hundreds of meters away from the mud volcano-like structure exhibit linearity and gradients values ranging between 41.5 K.km⁻¹ and 43.1 K.km⁻¹; the one profile located from the mound itself departs from linearity (with a meaningless average gradient value of 8.9 K.km⁻¹), likely due to the presence of gas and gas hydrates at this site.

Thermal conductivity measurements were performed on cores using the needle probe method [*Von Herzen and Maxwell, 1959*]. Measurements displayed little variability, near 0.84 ± 0.07 W m⁻¹ K⁻¹, so the surface heat flow is simply obtained by multiplying the measured thermal gradient by the measured thermal conductivity [*Grall et al, 2012*]. The important, observed spatial variability of thermal gradients (Figure A4-2) suggests that the heat transfer to the surface is likely influenced by a variety of processes (including sediment thermal blanketing, fluid circulation, gas hydrate related perturbation, topography etc) that appear difficult to model, mainly due to the scarcity of thermal measurements. To estimate the temperature profile that may be expected, we test different values of basal heat flow (48, 58 and 68.10⁻³ W.m⁻²), based on the detailed study of the thermal and subsidence history of the Central Basin of [*Grall et al [2012]*]. Indeed, the sedimentary column is thick at the Western High but sedimentation rates since at least the last hundred thousand years doesn't reach value higher than 1.5 mm/a [*Grall et al., 2013*]. Thus the sediment thermal blanketing should not change drastically the present-day heat flow at the seafloor. Let us consider here: i) that this value (hereafter referred to as Q_b), represents a reasonable proxy for the basal heat flow below the Western High area; and ii) that at the scale of the area, heat flow is conductive, e.g. conservative. Then:

$$k(z)\frac{dT}{dz} = Q_b \quad (1)$$

which yields :

$$T(z) = T_0 + \int_0^z \frac{Q_b}{k(z)} dz \quad (2)$$

where T(z) and k(z) are temperature and thermal conductivity, respectively. Following [*Pribnow et al, 2000*], we have tested two different approaches to describe the variation for porosity with depth:

- The linear approach:

$$k(z) = k_0 + Az \quad (3)$$

$$T(z) = T_0 + \frac{Q_b}{A} \text{Log}\left(1 + \frac{Az}{k_0}\right) \quad (4)$$

where k_0 and A are the thermal conductivity at the surface ($0.83 \text{ W K}^{-1} \text{ m}^{-1}$) and the thermal conductivity gradient, respectively. Using the compilation of [Pribnow et al, 2000], based on the data collected during Legs 101 to 180 of the Ocean Drilling Programme, we tested different values for A (from 0.4 to $1.4 \times 10^{-3} \text{ W K}^{-1} \text{ m}^{-2}$).

- The "porosity approach", which assumes that $k(z)$ depends on porosity and that porosity exponentially increases with depth due to compaction:

$$\varphi(z) = \varphi_0 e^{-az} \quad (5)$$

and

$$k(z) = \varphi(z)k_w + (1 - \varphi(z))k_g \quad (6)$$

where $\varphi(z)$ and φ_0 are porosity at depth z and at sediment surface, respectively, while a stands for Athy's compaction factor, k_w and k_g for thermal conductivity of seawater and sediment grains. The thermal conductivity of grains (k_g) is derived from surface sediment porosity and conductivity as stated below:

$$k_g = k_0 + \frac{\varphi_0}{1 - \varphi_0} (k_0 - k_w) \quad (7)$$

Using the above formulae, an analytical expression of temperature is found for integral in (1):

$$T(z) = T_0 + \frac{Q_b}{k_s a} \text{Log} \left| \frac{k(z) \varphi_0}{k_0 \varphi(z)} \right| \quad (8)$$

Using bottom water temperature of 14°C , temperatures at depth z are found, based on expressions (4) or (8).

References:

- Grall, C., Henry, P., Tezcan, D., Mercier de Lépinay, B., Bécel, Géli, L., Rudkiewicz, J.-L., Zitter, T., Harmegnies, F., (2012), Heat flow in the Sea of Marmara Central Basin, possible implications for the tectonic evolution of the North Anatolian Fault, *Geology*, 40: 3-6, doi:10.1130/G32192.32191.
- Grall C., Henry, P., Y. Thomas, G.K. Westbrook, M.N. Çagatay, B. Marsset, H. Saritas, G. Çifçi, L. Géli, Slip rate estimation along the western segment of the Main Marmara Fault over the last 330-430 ka by correlating Mass Transport Deposits, (2013), *Tectonics*, 10.1002/2012TC003255.
- Langseth, M., (1965), Langseth, M. G. (1965), Techniques of measuring heat flow through the ocean floor, in *Terrestrial Heat Flow, Geophys. Monogr. Ser.*, vol. 8, edited by W. H. K. Lee, pp. 58–77, AGU, Washington, D. C.
- Pribnow, D. F. C., M. Kinoshita, and C. A. Stein (2000), Thermal data collection and heat flow recalculations for ODP legs 101 – 180, *Rep. 0120432, Inst. for Jt. Geosci. Res., Leibniz Inst. for Appl. Geosci.*, Hannover, Germany. Available at <http://www.odp.tamu.edu/publications/heatflow/>
- Von Herzen, R. P., and A. E. Maxwell (1959), The measurement of thermal conductivity of deep sea sediments by a needle probe method, *J. Geophys. Res.*, 64, 1557–1563.

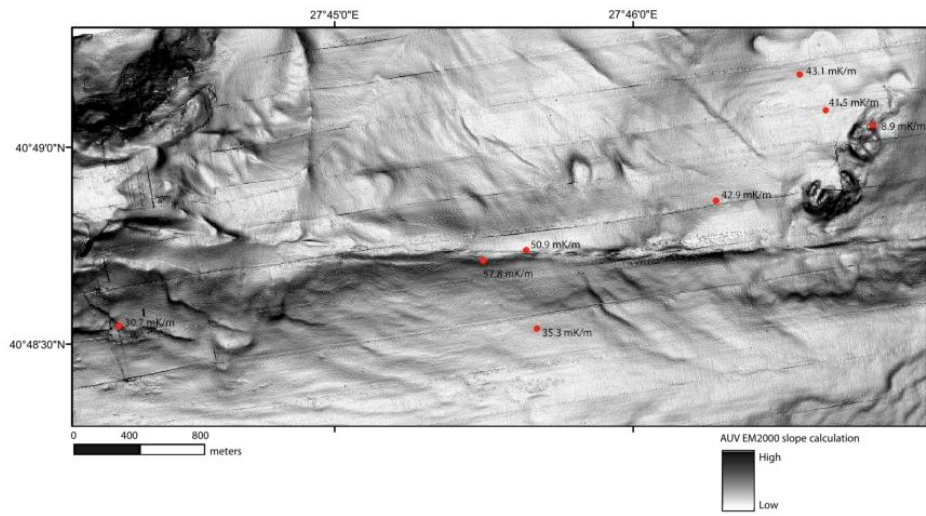


Figure A4-1 : Location (red dots) of thermal measurements performed in 2009 and 2010 in the Western High area. Thermal gradients values are indicated. *Image created with GMT software, Version 4.5.11.*

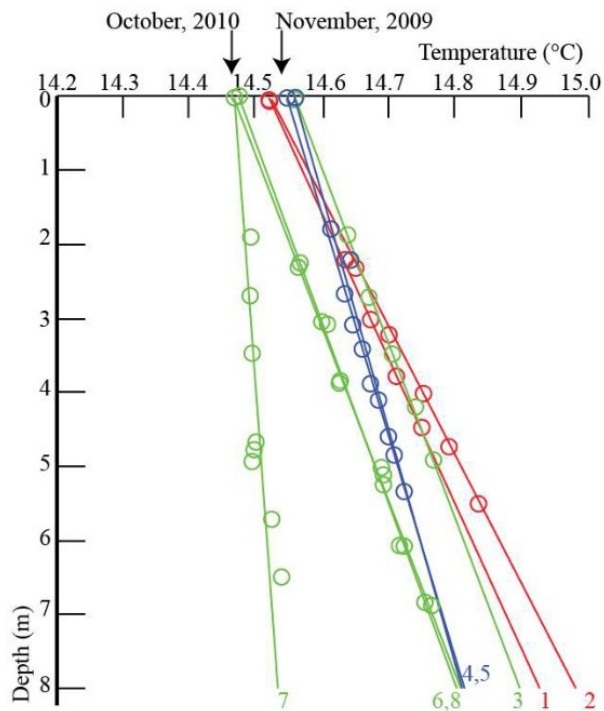


Figure A4-2: Synthesis of the 8 Thermal gradient profiles collected at the Western High. Red profiles refer to measures collected within the fault valley; blue profiles are measures conducted south of the fault and green profiles are the ones acquired north of the Main Fault. Slight differences of seafloor temperature correspond to seasonal variations. Refer to table 1 for linear thermal gradient values deduced and measurement locations. *Image created with GMT software, Version 4.5.11.*

FID	Latitude	Longitude	Thermal Gradient (°C/km)
1	40.811883	27.758283	50.9
2.	40.812316	27.760683	57.8
3.	40.814416	27.771267	42.9
4.	40.809116	27.737950	30.7
5.	40.809000	27.761283	35.3
6.	40.818250	27.777400	41.5
7.	40.817600	27.780016	8.9
8.	40,819750	27,775950	43.1

Table 1: 8 station location and thermal gradient values.

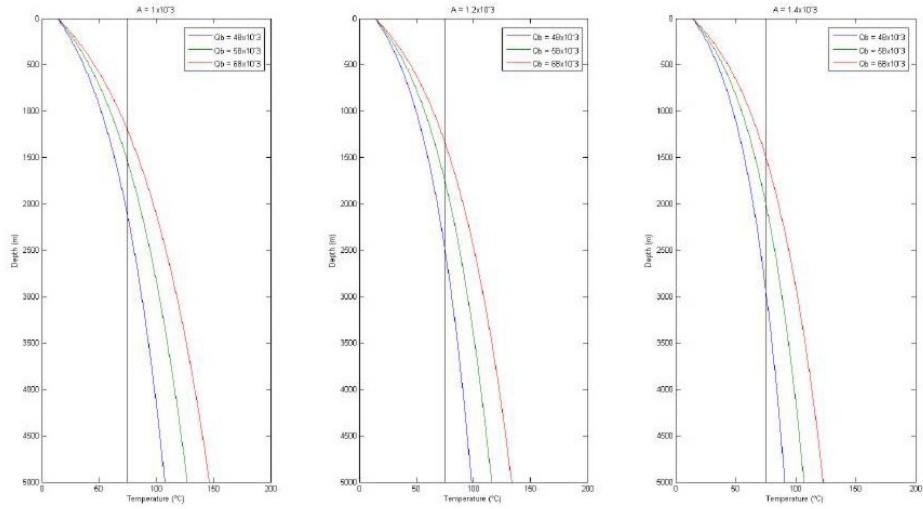


Figure A4-3a : Geotherms computed for different values of input parameters for the model assuming linear variations in thermal conductivity with depth. Thermal conductivity of surface sediments (k_0) is equal to $0.8 \text{ W.K}^{-1}.\text{m}^{-1}$. From left to right, A varies from 0.8×10^{-3} to $1.2 \times 10^{-3} \text{ W.K}^{-1}.\text{m}^{-2}$. For each case, different values of basal heat flow are tested (from 48 to 68 $\text{mW}.\text{m}^{-2}$). Image created with GMT software, Version 4.5.11.

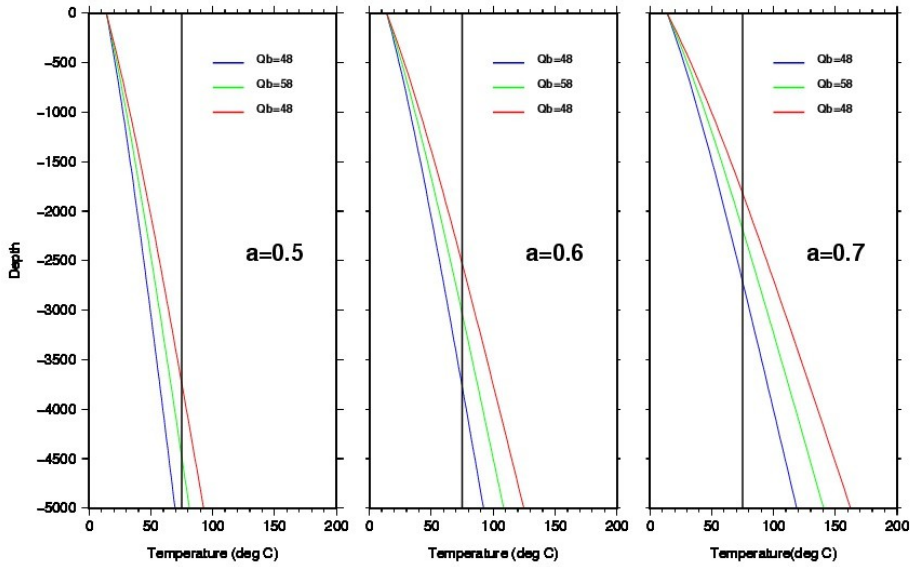


Figure A4-3b: Geotherms computed for different values of input parameters, for the model assuming that thermal conductivity with depth depends on sediment porosity and that porosity exponentially increases with depth. Thermal conductivity (k_0) and porosity (φ_0) of surface sediments are equal to $0.8 \text{ W.K}^{-1}.\text{m}^{-1}$ and 0.7 , respectively. From left to right, the compaction factor is respectively equal to 0.5 , 0.6 , 0.7 km^{-1} . For each case, different values of basal heat flow are tested (from 48 to 68 mW.m^{-2}). Image created with GMT software, Version 4.5.11.

APPENDIX 5

High-resolution, 3D- seismic structure of the upper sediments layers below the Western High area

In order to prepare for the implementation of permanent, multiparameter seafloor observatories in the Sea of Marmara, site surveys were conducted within the EU-funded Marmara Demonstration Mission from April 2008 to September 2010. In particular, 3D high-resolution seismic data were collected from the Western High (Figure A5-1), where oil and gas seeps were found, with the objective to image the connections between the fluid migration conduits and the main fault system, a few hundred meters beneath the seabed.

The seismic experiment is described in detail in [Thomas et al, 2012]. Of particular interest is the existence on the northern side of the NAF of a mound related to a mud-diapir-like structure, having a broadly circular cross-section (Fig. A5-2). This structure is capped by carbonate crusts that pierce the crest of a NE-SW oriented anticline, beneath the location where gas hydrates and hydrocarbons were sampled [Bourry et al, 2009], less than 600 m from the NAF main fault trace. It is associated with two other diapirs, aligned NE-SW below the axis of the anticline and deepening away from the fault zone.

Reflections from the seabed above the mound are locally of very strong amplitude and opposite seismic polarity compared to that of the surrounding seabed. This is almost certainly caused by authigenic carbonate outcrops at the seafloor and by the presence of very shallow gas immediately below. This view is coherent by both acoustic surveys and visual observations of gas escaping into the water column and of carbonates at the seabed. All three structures pierce through seismic horizons that are well mapped all over the study area and are characteristically of high amplitude and negative-polarity [Thomas et al, 2012]. Where horizons are faulted and/or crop out at the seafloor, gas emissions are observed in the water column. In contrast, at unfaulted locations, several horizons appear to collect the gas migrating from depth.

The data also reveal that gas follows buoyancy-driven, upward migration paths in permeable layers and along faults (Fig. A5-3). These paths are controlled by the regional strain field as it is expressed in the seafloor topography, with the primary E-W orientation parallel to NAF and by the secondary tectonic orientations revealed by compressive and extensional features respectively oriented NE-SW and NW-SE [Grall et al, 2013]. The NAF forms a valley, towards which the adjacent sediment layers are dipping, allowing gas to rise updip, from the valley to the shoulders of the fault. Locally, the conduits of the mud volcano-like structures also offer preferential pathways for the gas to migrate up to the seafloor.

References:

- Bourry, C., *et al*, (2009). Free gas and gas hydrates from the Sea of Marmara, Turkey: Chemical and structural characterization. *Chem. Geol.*, doi:10.1016/j.chemgeo.2009.03.007
- Dupré S., Scalabrin C., Grall C., Augustin J.-M., Henry P., Görür N., Sengör A. M. C., Cagatay N., Guérin C., Clouet H., Géli L. Tectonic and sedimentary controls for widespread gas emissions in the Sea of Marmara, Results from systematic, ship-borne multibeam echosounder water column imageries, *J. Geophys. Res., Solid Earth*, **120**, doi: 10.1002/2014JB011617 (2015)
- Grall, C., *et al*, (2013) Slip rate estimation along the western segment of the Main Marmara Fault over the last 330 ka by correlating Mass Transport Deposits, *Tectonics*, 10.1002/2012TC003255.
- Thomas, Y., *et al*, (2012), Contribution of high-resolution 3D seismic near-seafloor imaging to reservoir scale studies: application to the active north Anatolian Fault, Sea of Marmara, *Near Surface Geophysics*, **10**, 291-301, doi:10.3997/1873-0604.2012019

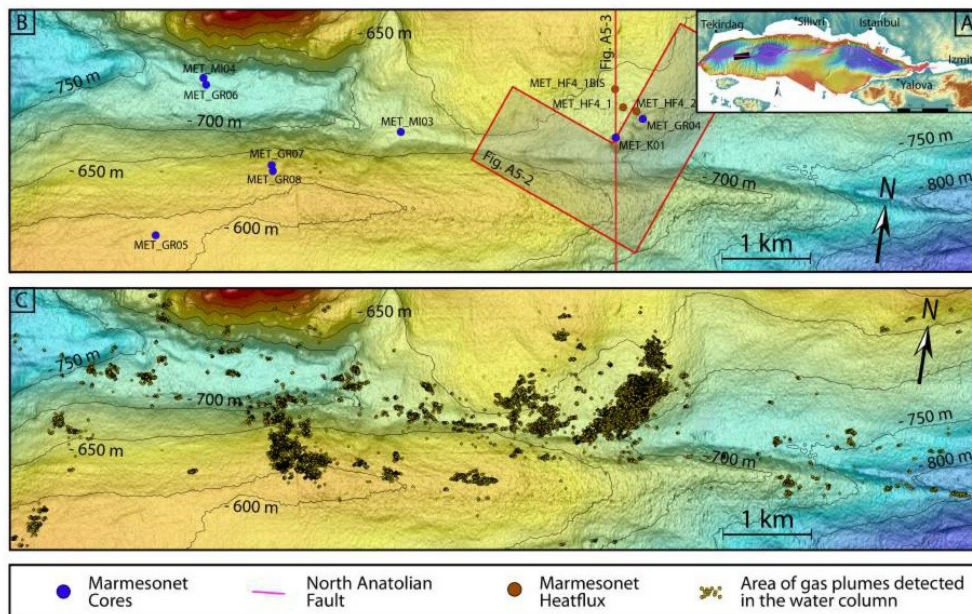


Figure A5-1: A) Inset indicates the location of the area surveyed with High-Resolution 3D seismics [Thomas *et al*, 2012]. B) Detailed bathymetry of the survey area, inferred from HR-seismics, with a lateral resolution of 5m. The shaded area indicates the area represented in Figure A5-2. The North-South red line shows the location of the cross-section shown in Figure A5-3. C) Same as Panel B, with location of gas emissions sites (black dots) detected during the Marmesonet cruise of *R/V Le Suroit* in 2009 [Dupré *et al*, 2015].

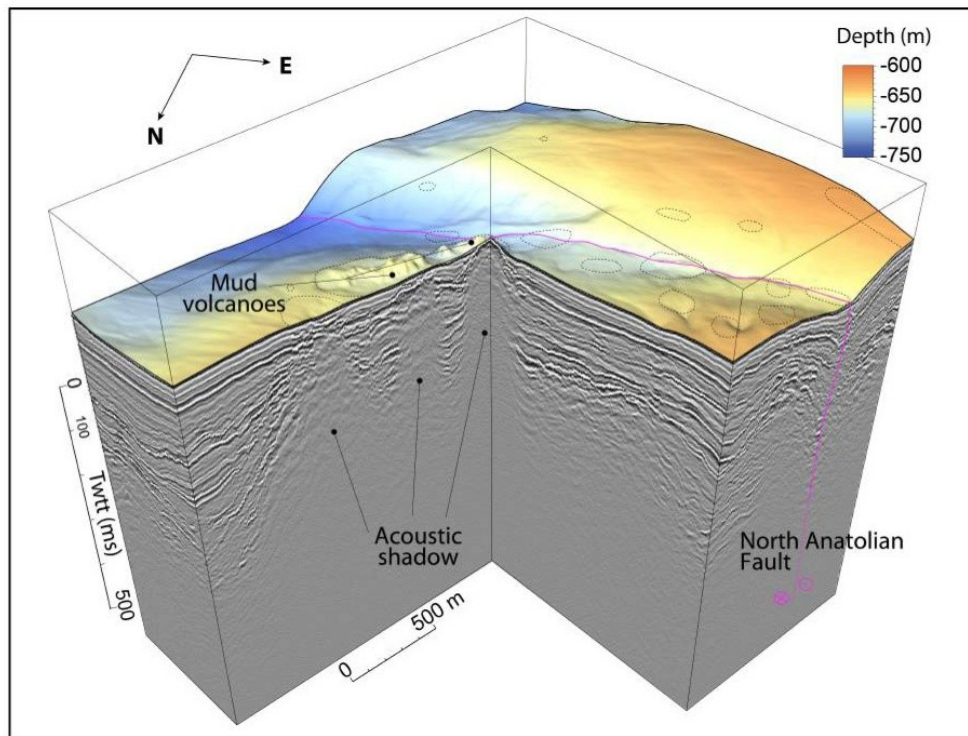


Figure A5-2: Detailed 3D view showing the geometry of the mud-volcano complex relatively to the North-Anatolian Fault Zone (purple line). See details of 3D, HR seismics in [Thomas et al, 2012].

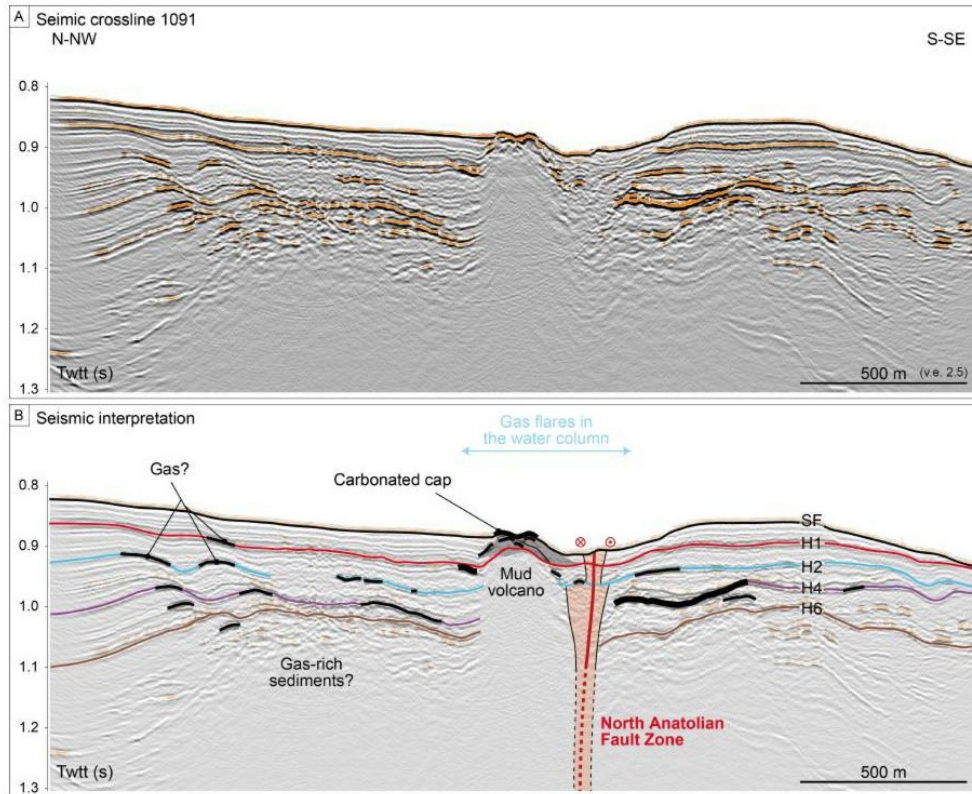


Figure A5-3: Interpreted, North-South section extracted from the HR-3D seismics box (see location in figure A5-1). Reflectors (H1 to H5) are described in [Grall et al, 2013].

III. An alternative view of the micro-seismicity along Main Marmara, Fault

III.1 High resolution study along the Main Marmara Fault (MMF)

III.1.1 Foreword

The study of low-magnitude micro-seismicity is quite challenging, especially in submarine environments. In the SoM, the specific, 3D-velocity structure and the presence of gas within the upper sediment layers are essential parameters to be taken into account when studying the micro-seismicity associated to the MMF.

The work described in this section is a continuation of the study by [*Géli et al, 2018*], which was focused on the analysis of the aftershock sequence that followed the Ml 5.1 earthquake of July, 25th, 2011 (see §II.3). During the 2011 deployment, however, the central station stopped one month before the occurrence of the mainshock. A new deployment was therefore carried out for 2 months (September 19th to November 14th) in 2014 with a denser network of OBSs, located closer to the fault, for complementing and improving in this way the analysis of the micro-seismicity in the western part of the SoM.

The first version of the manuscript (entitled “*An alternative view of the micro-seismicity along the Western Main Marmara Fault*”), was submitted in February 2017 to the *Bulletin of the Seismological Society of America (BSSA)*. The last, revised version presented below was eventually sent for review on December 14th, 2017. Our approach differs from the one of previous authors, as indicated below:

- (a) we consider a focused network geometry, specifically designed for studying the micro-seismicity below the western High, using OBS data only,
- (b) we use the 3D, high-resolution velocity model, of [Géli et al, 2018], which was built up by using all the available geological and geophysical information from the SoM,
- (c) we restrict our analysis to a limited number of earthquakes, e.g. only to those events that comply with the seismological criteria that were set up (e.g. outliers and not well-constrained events were removed from the catalogue, hence ~ 80% of the earthquakes were eliminated),
- (d) we use non-linear methods, as developed by Anthony Lomax (<http://alomax.free.fr/alss/>) we use all the available information (multichannel seismics, heat flow, fluid geochemistry, sedimentology) to interpret our location results.

III.1.2 Publication in review in BSSA

ARTICLE

An alternative view of the micro-seismicity along the Western Marmara Fault,

by [Batsi et al, 2017]

BSSA (in review)

Bulletin of the Seismological Society of America
An alternative view of the micro-seismicity along the Western Main Marmara Fault
 --Manuscript Draft--

Manuscript Number:	BSSA-D-17-00258R1
Article Type:	Article
Section/Category:	Regular Issue
Full Title:	An alternative view of the micro-seismicity along the Western Main Marmara Fault
Corresponding Author:	Evangelia Batsi Ifremer Plouzané, FRANCE
Corresponding Author's Institution:	Ifremer
Corresponding Author E-Mail:	Evangelia.Batsi@ifremer.fr
Order of Authors:	Evangelia Batsi Anthony Lomax Jean-Baptiste Tary Frauke Klingelhoefer Vincent Riboulot Shane Murphy Pierre Henry Stephen Monna Nurcan Meral Özel Dogan Kalafat Hakan Saritas Günay Cifçi Namik çagatay Luca Gasperini Louis Géli
Abstract:	A detailed study, based on Ocean Bottom Seismometers (OBS) recordings from two recording periods (3.5 months in 2011 and 2 months in 2014) and on a high-resolution, 3D-velocity model, is presented here, that provides an alternative view of the micro-seismicity along the submerged section of the North-Anatolian Fault, within the western Sea of Marmara (SoM). The non-linear probabilistic software packages of NonLinLoc and NLDiffLoc were used. Only those earthquakes that comply with the following location criteria (e.g. representing 20% of the total amount of events) were considered for analysis: i) number of stations ≥ 5 ; ii) number of phases ≥ 6 including both P and S; (iii) RMS location error ≤ 0.5 sec, (iv) azimuthal gap $\leq 180^\circ$. The location results indicate that not all earthquakes occurred as strike-slip events at crustal depths (> 8 km) along the axis of the Main Marmara Fault (MMF). In contrast, the following features were observed: 1) A significant number of earthquakes occurred off-axis, with a predominantly normal focal mechanism, at depths between 2 and 6 km, along tectonically active, structural trends oriented E-W or SW-NE.; 2) A great number of earthquakes were also found to occur within the upper sediment layers (at depths < 2 km), particularly in the areas where free gas is suspected to exist, based on high-resolution 3D, seismics. Part of this "ultra-shallow" seismicity appears to occur in response to deep earthquakes of intermediate (ML $\sim 4 - 5$)

Powered by Editorial Manager® and ProduXion Manager® from Aries Systems Corporation

	magnitude. Because our results are significantly different from those of previous workers (e.g. Schimttbul 2015 and Yamamoto et al 2017), it is important to acknowledge the uncertainty for the shallowest earthquakes. Resolving the depth of the shallow seismicity is left for future studies using adequate experimental design ensuring source-receiver distances of the same order as hypocentral depths.
Author Comments:	I greatly acknowledge you if you could proceed with a fast track review
Suggested Reviewers:	
Opposed Reviewers:	
Response to Reviewers:	I will include this information in files that will be uploaded

1 **An alternative view of the micro-seismicity along**
2 **the Western Main Marmara Fault**

3

4 Evangelia Batsi¹, Anthony Lomax², Jean-Baptiste Tary³, Frauke Klingelhoefer¹, Vincent Riboulot¹, Shane
5 Murphy¹, Pierre Henry⁴, Stephen Monna⁵, Nurcan Meral Özel⁶, Dogan Kalafat⁶, Hakan Saritas⁷, Günay Cifçi⁷,
6 Namik Çagatay⁸, Luca Gasperini⁸, Louis Géli¹

7

8 1. Institut français de recherche pour l'exploitation de la mer (Ifremer), Marine Geosciences Research Unit, CS
9 70, 20280 Plouzané, France

10 2. ALomax Scientific, 320 Chemin des Indes, 06370, Mouans Sartoux, France

11 3. Universidad de los Andes, Departamento de Geociencias, Bogota DC, Columbia

12 4. Centre Européen de Recherche et d'Enseignement de Géosciences de l'Environnement (CEREGE), 13331
13 Marseille Cedex 3

14 5. Istituto Nazionale di Geofisica e Vulcanologia (INGV), Via di Vigna Murata, 605, 00143 Roma, Italy

15 6. Kandili Observatory and earthquake research institute (KOERI), 34684 Cengelkoy – Istanbul / TURKEY

16 7. Dokuz Eylül University (DEU), Cumhuriyet Bulvarı No: 144 35210 Alsancak / İZMİR, Turkey

17 8. Istanbul Technical University (ITU), Department of Geology, Faculty of Mines, 34469 Maslak, Istanbul,
18 Turkey

19

20

21

22

23

24

1

25 **Abstract**

26

27 A detailed study, based on Ocean Bottom Seismometers (OBS) recordings from two
28 recording periods (3.5 months in 2011 and 2 months in 2014) and on a high-resolution, 3D-
29 velocity model, is presented here, that provides an alternative view of the micro-seismicity
30 along the submerged section of the North-Anatolian Fault, within the western Sea of Marmara
31 (SoM). The non-linear probabilistic software packages of NonLinLoc and NLDiffLoc were
32 used. Only those earthquakes that comply with the following location criteria (e.g. representing
33 20% of the total amount of events) were considered for analysis: i) number of stations ≥ 5 ; ii)
34 number of phases ≥ 6 including both P and S; (iii) RMS location error ≤ 0.5 sec, (iv)
35 azimuthal gap $\leq 180^\circ$. The location results indicate that not all earthquakes occurred as
36 strike-slip events at crustal depths (> 8 km) along the axis of the Main Marmara Fault
37 (MMF). In contrast, the following features were observed: 1) A significant number of
38 earthquakes occurred off-axis, with a predominantly normal focal mechanism, at depths
39 between 2 and 6 km, along tectonically active, structural trends oriented E-W or SW-NE.;
40 2) A great number of earthquakes were also found to occur within the upper sediment
41 layers (at depths < 2 km), particularly in the areas where free gas is suspected to exist,
42 based on high-resolution 3D, seismics. Part of this “ultra-shallow” seismicity appears to occur
43 in response to deep earthquakes of intermediate ($M_L \sim 4 - 5$) magnitude. Because our results are
44 significantly different from those of previous workers (e.g. Schimttbul 2015 and Yamamoto et al
45 2017), it is important to acknowledge the uncertainty for the shallowest earthquakes. Resolving the
46 depth of the shallow seismicity is left for future studies using adequate experimental design
47 ensuring source-receiver distances of the same order as hypocentral depths.

48

49 **Introduction**

50

51 The study and understanding of seismicity for large and devastating earthquakes as well as
52 for background micro-seismicity is of fundamental importance for earthquake hazard
53 assessment. Hence, considerable effort is spent world-wide for characterizing active faults
54 through enhanced seismic monitoring. In submarine environments, however, the presence of the
55 water column makes monitoring particularly complicated and difficult. Because deep-sea
56 environments are remote, hostile and corrosive, there are to date only a few permanent
57 deep sea-floor observatory networks funded at the national or international level, e.g.
58 offshore Japan (DONET for Dense Oceanfloor Network system for Earthquakes and
59 Tsunamis), Canada (NEPTUNE), USA (MARS) and at some sites of Europe (EMSO, for
60 European Multidisciplinary Seafloor and water-column Observatory). Due to their elevated
61 maintenance costs, offshore facilities require more detailed and more specific justification
62 than onshore facilities. The case of the submerged section of the North Anatolian Fault
63 (NAF), within the SoM, is a strong motivator in that respect.

64

65 The highly active, right lateral strike-slip North Anatolian Fault (NAF), has produced
66 devastating historical earthquakes along its 1600 km long trace (e.g., *Ambraseys and Finkel*,
67 *[1995]*). In 1912, the fault was ruptured by the Ganos earthquake, which ended at the
68 Western extremity of Marmara Sea (e.g., *Ambraseys and Finkel, [1987]*). To the east of
69 SoM, the spatial progression of earthquake events along this fault system has a more or
70 less westward progression since 1940, with a sixty years sequence of rupturing towards
71 Istanbul (e.g. *Stein et al, [1997]*). The last destructive earthquake occurred at the eastern
72 end of the SoM (1999 Izmit and Duzce earthquakes) and therefore the next large ($M_w >$
73 7) earthquake is now expected to nucleate within the SoM, putting at risk the 15 Millions

3

74 inhabitants of the Istanbul megacity (*Pondard et al., [2007]; Parsons et al., [2004]*).

75 As a result, the SoM (see Figure 1a) was extensively surveyed since 1999, allowing a
76 wealth of geological, geophysical and geochemical data to be collected. The Main Marmara
77 Fault (MMF) system was identified as a major target for the implementation of seafloor
78 observatories and important preparatory work was done to address this long term challenge.
79 In 2009 and 2010, five cabled sea-bottom seismometers were deployed on the Marmara
80 seafloor by KOERI, which collected broadband data until 2013. Site surveys and autonomous
81 instrument deployments were conducted within EU-funded projects, respectively the
82 ESONET/MARMARA-DM Project (2008-2011, e.g. *Géli, et al, [2011]*) and the MARSITE
83 Project (2012-2016). Here, we present a high-resolution seismological study of the Western
84 SoM, based on all the geological knowledge acquired since 1999 and on the Ocean Bottom
85 Seismometers (OBS) data collected within the latter two projects, in 2011 and 2014
86 respectively (see Figure 1b).

87

88 This work complements a previous study by *Géli et al [2017]*, based on a part of the 2011
89 dataset, that showed the existence of shallow, gas-related seismicity, based on the
90 combination of seismological and geochemical arguments. Because there was no station at
91 the center of the OBS network during the last month of the 2011 experiment, a new
92 deployment was carried out in 2014, with a denser network, closer to the fault (see Figure
93 1b). The results obtained with a high resolution 3D velocity model provide new insights
94 on the nature of the micro-seismicity and on the behaviour of the western segments of the
95 MMF.

96

97

98 **Geological background: specificities to take into account for**
99 **precise earthquake location**

100

101 According to *Sengör et al [2005]*, the NAF formed by a progressive strain localization,
102 mostly along an interface juxtaposing subduction-accretion material to its south and older
103 and stiffer continental basements to its north. The shear-related, post-Miocene deformation
104 produced four separate basins within the Marmara shear zone, filled with Plio-Quaternary
105 sediment sequences, respectively from west to east: the Tekirdag Basin, the Central basin,
106 the Kumburgaz Basin and the Cinarçik Basin. After the numerous bathymetric and seismic
107 surveys that were conducted since 1999 (e.g. *Le Pichon et al, [2001]*; *Imren et al., [2001]*;
108 *Armijo et al., [2002]*; *Rangin et al, [2004]*; *Carton et al, [2007]*; *Shillington et al, [2012]*), the
109 currently active fault traces are now well known. So are the main trends of the basins and
110 crust structure, based on deep seismic soundings (e.g. *Laigle et al 2008*, *Bécel et al,*
111 *2006*, *Bayrakci et al, 2013*). From these surveys, it becomes clear that: i) the geological
112 structure along the MMF is essentially 3D from the surface to the deep crust, both along
113 and across the strike of the fault and ii) the central part of the Marmara Trough is filled
114 with “soft” Plio-Quaternary sediment sequences, more than 5 km thick. These features are
115 key elements to take into account when deriving appropriate velocity models for high-
116 resolution earthquake location near the fault zone.

117

118 Another aspect that should be considered is the existence of widespread gas emissions from
119 the Marmara seafloor (e. g. [*Kuscu et al, 2005*], [*Géli et al, 2008*], [*Dupré et al, 2015*])
120 and the realization that the NAF within the SoM cuts across hydrocarbon gas prone
121 sediment layers (e. g. [*Bourry et al, 2009*]). As stated in [*Dupré et al, 2015*], the distribution

5

122 of gas emissions in the SoM appears to be correlated by a number of controlling factors,
123 e.g.: the fault and fracture networks; the nature and thickness of sediments; the connectivity
124 between the seafloor and the gas sources; and the microseismicity. Hence, the role of gas
125 must be identified and discriminated from the tectonics. To reach this goal, it is necessary to
126 improve the depth determination of shallow seismicity using near-by monitoring stations and
127 detailed velocity models, that take into account the upper sedimentary layers.

128 **3D velocity-structure of the Western Sea of Marmara**

129 Given the considerations above, specific 3D velocity-models are required to account for: i)
130 the sharp seafloor topography; ii) the slow P-wave velocity of Plio-Quaternary sediments;
131 iii) the differences in the deep crustal structure between the northern and southern parts of
132 the NAF. Published 3D-models do exist with grid spacing of 9×9 km and 10×10 km
133 for the Marmara Region (e. g. [Gürbüz et al, 2013] and [Yamamoto et al, 2017],
134 respectively] and grid spacing of 6×6 km for the Marmara offshore domain (e. g.
135 [Bayrakci et al, 2013]). The horizontal grid-spacing (9, 10 and 6 km, respectively) of these
136 models is too large however, to account for both the velocity contrast at the seafloor
137 interface and the sharp geometry of the basins, as well as the expected heterogeneities of
138 the velocity structure across the strike of the MMF. Hence, here we rather use the high-
139 resolution, 3D-velocity model (with a grid node spacing of $750 \text{ m} \times 750 \text{ m} \times 200 \text{ m}$) that
140 was specifically tailored by Ifremer for the $20 \text{ km} \times 60 \text{ km}$ area covered by the submarine
141 networks deployed in 2011 and 2014, in the Western SoM (see Figure 2a and details
142 reported in [Cros and Géli, 2013] and in [Gürbüz et al, 2013]). This model is based on all
143 available geological and geophysical data from the SoM, including: i) the high-resolution
144 (38 m) bathymetric grid from [Le Pichon et al, 2001]; ii) the 3D, P-wave velocity grid

145 derived from seismic tomography by [Bayrakci et al, 2013]; iii) the deep crustal velocities
146 inferred from 2D, wide-angle, 2D seismics by [Bécel, A, et al, 2009]; iv) the fault
147 mapping and basin geometry line-drawing, based on the interpretation of all existing seismic
148 profiles (e.g. [Sengör et al, 2005]; [Sengör et al, 2014]).

149

150 **Data**

151 The two following seismological datasets were analysed (see details Tables 1 and 2 and Figure
152 1b):

153 - Dataset-1 was recorded from April 15th to July 31st, 2011, by 10 autonomous, 3
154 components (1 vertical and 2 non-oriented horizontal) short-period (4.5 Hz) OBSs from
155 Ifremer and by 2 permanent, cabled broad-band, 3 components OBSs operated by
156 KOERI. Unfortunately, the central station of the network, OBS02, stopped recording on
157 July 1st, 2011.

158 - Dataset-2 was recorded from September 19th to November 14th, 2014, by 9 autonomous, 3
159 components (1 vertical, 2 non-oriented horizontal) short-period (4.5 Hz) from Ifremer
160 and by 1 autonomous, broad-band OBS operated by INGV (e.g. OBS13). Note that
161 two autonomous, short-period OBS were also deployed by Ifremer, from the 1st until
162 the 15th of November near gas emissions sites (e.g. close to the central station
163 OBS04).

164 It is important to note that to guide our analysis, we also used:

165 - high-resolution 3D- and 2D-seismic data collected in 2009 with R/V Le Suroit and
166 with R/V Piri Reis, respectively. The full description of the 3D-acquisition system and
167 dataset is detailed in [Thomas et al, 2012]).

- 168 - multi-channel, deep seismic lines collected in 2001 during the Seismara Cruise of R/V Le
169 Nadir (e.g. *Laigle et al [2008]*; *Bécel et al [2009]*; *Bécel et al [2010]*).
- 170 - an unpublished bathymetric grid of the Central Basin and Western High, having a
171 node spacing of 10 meters, based on multibeam echosounder system data collected
172 in 2014 with *R/V Pourquoi Pas?* (see Data and Resource section). This 10-m grid
173 (courtesy of Charline Guérin of Ifremer) is available on request to the authors.

174

175 **Tools and Methodology**

176 **Location procedure**

177

178 For both OBS datasets of 2011 and 2014 recording periods, the same methodological approach
179 was used, based on the non-linear methods developed by Anthony Lomax. The 3D-location
180 process (fully described in *Lomax [2014]*) includes the 5 following steps:

181

182 1) Picking: The picking was performed using respectively the FilterPicker routine (e.g. *Lomax*
183 *et al, [2012]*) for the OBS dataset of 2014, and the Sytmis software package for the OBS
184 dataset of 2011 (see Data and Resources Section). The 3 components of the geophone were
185 used for this analysis. Specifically the vertical component was used for the detection of P-
186 wave arrivals while the two non-oriented horizontal components were used for the S-wave
187 onsets (e.g. strong velocity contrasts in areas with shallow sediments could generate
188 converted phases, hence their identification on vertical channels could be misleading). The
189 picks were all visually checked. Uncertain picks were systematically removed. Manual

8

190 corrections -when needed- were applied to the remaining picks
191
192 2) Phase association: the Early-est routine of the Lomax Package was run to perform phase
193 association and to determine the initial earthquake locations for step 3, using the 1D (VP and
194 VS) model described in *Cros and Géli [2013]* (see also [*Lomax, 2014*]). In this initial phase, a
195 non-constant VP/VS ratio was used in the 1D velocity model.
196
197 3) Station corrections and initial 3D locations: NonLinLoc software was applied without
198 station corrections using our high resolution, 3D P-velocity model (with a constant VP/VS
199 ratio equal to 1.78), to compute a preliminary set of absolute locations and station corrections.
200
201 4) Absolute locations: The accuracy of travel-time was successfully improved by applying
202 station corrections for both P and S travel time grids. The objective was to account (i) for the
203 near-surface deviations of seismic velocities from the applied model [*e.g Hausmann et al,*
204 *2010*], since all models (including 3D) do not take into account the real velocity variations (e.
205 g. shallow, near-station, smaller scale and potentially low velocity structure cannot or are not
206 modelled). NonLinLoc was applied using the 3D, P-velocity model (with VP/VS=1.78),
207 along with the station corrections and the absolute locations resulting from step 3, to compute
208 the final absolute locations after 3 iterations.
209
210 5) Relative locations: NLDiffLoc was eventually run to compute the relative locations based
211 on the final absolute locations. NLDiffLoc performs a differential earthquake location
212 based on the double difference equation from *Waldhauser and Ellsworth [2000]*. The
213 double difference code is using as input files the: (i) initial absolute locations (e.g. derived

214 from NLLoc; see step 4) and (ii) differential traveltimes (e.g. derived from Loc2ddct tool)
215 which are calculated for a specified maximum distance between event couples. The relative
216 coordinates (e.g. x, y, z and t) are optimized for a set of hypocenters given a set of differential
217 phase arrival time measures at each station for multiple hypocenters. This is achieved by
218 using a non-linearized global search (e.g. a Metropolis random walk, [Lomax *et al*, 2009],
219 which maximizes the probabilistic solution likelihood as the hypocenter coordinates are
220 perturbed. A double-difference equation from [Waldhauser and Ellsworth, 2000] is then
221 evaluated for determining the misfit and the solution likelihood by using an L1 norm which is
222 more robust with outlier data (e.g. in contrast to L2 norm which is equivalent to what
223 HypoDD is using).

224

225 The following criteria were used for “well constrained events” : (i) Number of stations ≥ 5 , (ii)
226 $\text{RMS} \leq 0.5$ sec, (iii) azimuthal gap $\leq 180^\circ$, and (iv) number of phases ≥ 6 including both
227 P and S phases. Consequently, only a small percentage (around 20 %) of the recorded
228 seismicity was considered (e.g. 191 and 78 relocated earthquakes for the 2011 and 2014
229 recording periods, respectively).

230

231 **Multiplet analysis**

232

233 The GISMO collection of Matlab tool boxes for seismic waveform analysis, (see Data and
234 Resources section) was used for multiplet analysis. The determination of cross-correlations and
235 lag times was performed for all pairs of events (e.g. no “master” events) and the cross
236 correlation was calculated for different time windows. More specifically, different tests were

237 performed for the cross-correlations on all three components of the geophone. For each
238 component (i) only P-waves were considered, (ii) only S -wave and (iii) a larger window
239 was taken into account to consider the whole wave train of the earthquake (e.g. 1 sec before
240 P-wave arrival and 2 sec after S-wave arrival). The best results were obtained in case (iii) were
241 cross correlations were applied on the vertical component, which were eventually considered for
242 this study. These events were located using the 1D and 3D velocity model, respectively and
243 the same location procedure was followed (see Methodology paragraph). Location errors are
244 of the same order of magnitude, e.g.: within ± 0.05 km horizontally and within ± 0.13 km
245 vertically.

246

247 **Computation of Focal mechanisms**

248

249 HASH software (e.g. *Hardebeck and Shearer [2008]*) was used for computing focal mechanisms
250 of single events of $M > 3$. Due to the fact that the majority of the events were micro-earthquakes (e.g.
251 $M < 2$), composite focal mechanisms were also computed with HASH for the highly correlated
252 events obtained from the multiplet analysis. For both cases (e.g. single and composite), at least 8
253 P-wave first motion polarities (measured on the vertical component) were considered (see
254 Supplementary information).

255

256

257

258

259 **Comparing 1D-models, based on synthetics**

260

261 Different tests were made to evaluate the effect of the different 1D-models on earthquake
262 locations, with the following procedure: i) One arbitrary event was positioned below the
263 Western High, at 40.80°N, 28°E and at 2 different depths, 2 km (Trial 1) and 12 km (Trial
264 2) respectively; ii) Synthetic travel times were computed using the 3D velocity model, for
265 the stations of the 2011 network (data-set 1); iii) these synthetic travel times were used for
266 relocating the corresponding synthetic epicenters, using the “1D-this study” and the 1D-
267 model of [Karabulut *et al*, 2011], respectively (see Figure 2b). As expected, over-simplified
268 1D models (e.g. models that represent the velocity structure of the on-shore domain),
269 produce very important effects on earthquake depth determination, particularly for shallow
270 events below the deep, submerged basins (see Table 3).

271

272 In the common practice, 1D-location results are significantly improved by using station corrections,
273 and 1D-models are refined at each iteration. To be efficient, however, station corrections require
274 that rays propagate vertically below the station, a valid assumption only for deep-seated earthquakes
275 and smoothly varying media. For shallow earthquakes generating oblique rays in slow, P-wave
276 velocity sediments, 1D-locations with station corrections are less efficient than 3D-locations with
277 station corrections. Therefore, when only OBS are included, it is strongly recommended to
278 use *ad hoc* 1D-models that take into account the velocity structure of the upper sediment
279 layers in order to properly detect the shallow, micro-seismicity.

280

281 **Discussion on location results, based on case studies**

282 To illustrate the importance of 3D effects, three representative case studies are
283 discussed here below, with the purpose of comparing the relative locations results obtained
284 by NLDiffLoc using “appropriate 1D” models vs the 3D velocity-model. The “appropriate
285 1D model” used in this study is based on [Géli and Cros, 2013] and shown in Figure 2b.
286 For each case study the 10 meters bathymetric grid (see for instance Figure 3) and a selection of a
287 highly correlated events (with a cross correlation coefficient ≥ 0.8 , see for example Figure
288 4) that occurred as clusters or as triplets were considered for the analysis.

289

290 - Case study 1: seismicity from the base of the basin (~ 5 km):

291 The first case study includes a triplet of earthquakes of local average magnitude M_1 1.65, that
292 occurred on the 25th of October, 2014, in the Western High area (see Figures 5, 6a, 6b, 7
293 and Table 4). When using the 1D velocity model, hypocenters are located within less than 1
294 km to the south of the fault zone and at a depth of $10.3 \text{ km} \pm 0.3 \text{ km}$ below seafloor. In
295 contrast, with the 3D, high-resolution velocity model, the triplet is found to be located 3 km
296 to the north of the fault zone, at a depth of 6.2 km below seafloor, e.g. at the base of the
297 sedimentary basin. The computed composite focal mechanism (see supplementary information)
298 obtained with the 3D locations indicates a predominantly, normal fault motion, with a small
299 strike-slip component. In contrast the composite focal mechanism obtained of the 1D locations
300 indicates strike-slip motion) and composite focal mechanism for this triplet is not available in
301 *Yamamoto et al, [2017]*. Our location results differ from those obtained by *Yamamoto et al,*
302 *[2017]*, who found that the cluster was located underneath OBS4, at an hypocentral depth of 15 km
303 (below sealevel), using as well: (i) a 3D velocity model, with a larger mesh grid (10×10
304 km^2) and (ii) only OBS data, with a sparse coverage of 4 OBSs in our study area (see

13

305 Figures 6a and 6b). The seismograms plotted for earthquake 2 (Figure 7) indicate that the P-wave
306 arrived first at OBS04. Consequently we infer that, if as proposed by *Yamamoto et al [2017]*, the
307 events were located at 15 km below sea-level underneath OBS04, then the travel time difference t_s-
308 t_p would be minimum at OBS04, which is not the case. In addition, t_s-t_p values are respectively
309 greater at OBS07 and OBS03 (located on the northern side of the MMF) compared to those at
310 OBS08 and OBS01 (located on the northern side). These observations underline the 3-dimensional
311 structure of the medium: i) the central part of the Western High (e.g. in the vicinity of OBS4) is
312 characterized by mud volcanoes and by gas-prone, low velocity sediment layers; ii) seismic
313 velocities are lower along than across the strike of the MMF. Our 3D model does not fully account
314 for this very small-scale heterogeneity (due to computational difficulties), but does a better job than
315 1D models. Based on high-resolution, 2D-reflection seismics and on high-resolution bathymetry
316 (Figure 8), we know that: i) the geological structure of the upper sediment layers is very
317 asymmetric from south to north of the fault zone, e. g. essentially 3D; ii) very large
318 perturbations in seismic velocity related to the presence of mud volcanoes are expected in the area
319 near OBS4; iii) the hypocenters obtained using the 3D-velocity model of this study are located
320 close to normal faults and gas emission sites from the seafloor. Still, based on the above there
321 is no quantitative criteria to favour our locations compared to Yamamoto's.

322

323 - Case study 2: shallow seismicity within the upper sediment layers (< 2 km):

324 The second case study regards a triplet of events (with correlation > 0.8) that occurred on
325 19th of May 2011 and 23rd of June 2011 (see Figures 9a and 9b and Table 5) of local average
326 magnitude M_1 0.9. With the 1D velocity model, the computed epicenters are spread out over
327 an area of more than ~ 20 km² within the eastern part of the Central Basin and the depth
328 distribution of the individual hypocenters is dispersed, at 3 km, 15 km, and 20 km,

329 respectively. In contrast, with the 3D velocity model, the computed epicenters are clustered
330 over an area of $\sim 2 \text{ km}^2$ at the base of the escarpment bordering the south-eastern part of
331 the Central Basin, while the hypocenters are located within the first two kilometers of
332 sediments, in an area where numerous gas emission sites have been found and where
333 reverse faulting is present (e.g. [Armijo et al, 2002]; [Bécel et al, 2010]). In both cases, the
334 computed composite focal mechanism indicates reverse faulting . It is interesting to note that the
335 1D locations are unstable, with 3 very different depths (3, 15 and 20 km) found for 3 highly
336 correlated events, while the 3D-locations yield comparable depths for the 3 events and smaller
337 confidence ellipsoids. The cluster being more or less near the center of the OBS network, small
338 variations in the velocity model are expected to generate large variations in depth determination,
339 resulting in important location instabilities. The seismograms for earthquake 3 (Figure 10) indicate
340 equivalent P-wave arrival times at OBS8 and at OBS10, but differences in t_s-t_p greater than 0.4 s.
341 Also, the P-wave arrives 0.2 s earlier, but t_s-t_p is slightly greater (4.0 s) at OBS7 compared to OBS9.
342 These observations suggest large 3D-heterogeneities in the seismic velocity structure, notably with
343 faster velocities across than along strike. In addition, the computed reverse composite focal
344 mechanism is consistent with the presence of a positive (e.g. compressive) flower structure, based
345 on the multichannel seismic profile SM 47 collected during the Seismarmara cruise in 2001 across
346 the NE corner of the Central Basin (Figure 11, after Bécel et al, [2010]). Gas emissions have been
347 detected near the epicentral area, confirming that the faults rooted in the upper sediment layers are
348 tectonically active, allowing gas to migrate up to the seafloor.

349

350 - Case study 3: deep, crustal seismicity:

351 Finally the third case study concerns a cluster of 10 earthquakes of local average magnitude
352 M_l 1.6, that occurred in 2014, below the western part of the Central Basin (see Figure 12

353 and Table 6). Regardless the model used (1D vs 3D), the computed epicenters are relatively
354 well clustered over areas of less than 10 km², and hypocenters are at crustal depths, within
355 the 12-15 km depth range. The composite focal mechanism indicates strike-slip faulting. The
356 composite focal mechanism is consistent with strike-slip at crustal depth; comparable to the
357 repeaters from the same area reported in *Schmittbuhl et al [2016]*. The only difference between 1D
358 vs 3D hypocenters is that the events located with a 1D model are to the south of the fault
359 trace, while those located with the 3D-model are within the shear zone to the north of the
360 MMF. Based on the deep, multi-channel seismic soundings collected during the Seismarmara
361 cruise in 2001, the 3D locations (within the inner basin) appear to be consistent with geology (e.g.
362 *[Laigle et al, 2008]*).

363

364 As expected, for all case studies, differences in relative location results appear to be significant
365 for shallow (< 6 km) seismicity (case studies 1 & 2), but relatively minor for deep seismicity
366 (e.g. > 10 km, case study 3). In all cases, both our 1D and 3D relative location results are
367 seismologically “well-constrained” based on the criteria that we had set up (see paragraph:
368 Tools and Methodology) . Nevertheless, the computed probability density functions (pdf) indicate
369 that the 3D locations have smaller confidence ellipsoids for each event (see Figures 6b, 8b, 10).
370 Smaller RMS errors in travel time differences (|measured - calculated|) are generally smaller for 3D
371 locations, except for events 1 and 2 of case study 1 (Figure 13).

372 For each case study, our 3D location results are consistent with the geological knowledge that was
373 acquired throughout the numerous cruises that were conducted in the Sea of Marmara since 1999.
374 Although our focal mechanisms have been constrained by a limited number of polarities, the
375 systematic geological consistency of our results cannot be due only to pure coincidence: the deep
376 events (d>10 km) from the case studies have a dominantly strike-slip focal mechanism, while

377 the majority of shallow events ($d < 5-6$ km), have a dominantly normal focal mechanism,
378 except for the noticeable example depicted in case study 2 where events located near a compressive,
379 flower structure exhibit a reverse focal mechanism.

380

381 **Discussion**

382 **An alternative view of micro-seismicity within the Sea of Marmara**

383 Our 3D location results provide an alternative view of the micro-seismicity within the Western Sea
384 of Marmara (Figures 14 and 15 and Table 7) compared to the most recent studies by Yamamoto et al
385 2017 and Schmittbul et al 2015. In the present study, earthquakes are found to occur not only along
386 the axis of the Main Marmara Fault, but also off-axis, along secondary faults from the
387 NAF System (see Figure 16). The deep events ($d > 8-10$ km) occurring along the MMF, have a
388 dominantly strike-slip focal mechanism. In contrast, the majority of shallow events ($d < 5-6$ km),
389 occur off-axis and have a dominantly normal focal mechanism, except at some specific places
390 characterized by compressive deformation. The diversity of the focal mechanisms is consistent
391 with the results found by previous results (e.g. Pinar *et al*, 2003; Sato et al, 2004; Örogülü *et al*,
392 2017).

393

394 Our results also reveal that there are two categories of shallow (< 6 km) seismicity.

- 395 ● The first category consists in events located within or at the base of the “post-kinematic”,
396 Plio-Quaternary basins (e.g. Bayrakci et al, 2013), at depths of $\sim [2 ; 6]$ km and
397 along tectonically active, structural trends oriented E-W or SW-NE.
- 398 ● The second category includes “ultra-shallow” events, occurring at depths shallower than
399 $\sim 1-2$ km. Focal mechanisms may indicate either normal faulting, either reverse (e.g.

17

400 earthquakes occurring along the Western High and the Central Basin, respectively),
401 depending on the local context (see for instance Figure 17), hypocentres are located
402 within gas prone sediment layers, based on 3D high-resolution seismics [Thomas et
403 al, 2012]. Such seismicity must be discriminated from the tectonic-related seismicity that
404 occurs at crustal levels.

405

406 **Comparison with the view of Yamamoto's et al, 2017**

407 In this paper we focus on the comparison with the view proposed by Yamamoto et al, 2017, which
408 is also based on the use of only OBS data and the use of a 3D velocity model. Figure 18 displays the
409 location of the events that were detected in common in this work and in Yamamoto's, during the
410 overlapping period from September 19th to November 14th, 2014 (Table 8). The location results
411 provide very different views. West of 27°50'E, Yamamoto et al, 2017 find systematically deep,
412 strike-slip events occurring along the MMF and along EW striking associated structures. These
413 locations are consistent with pure strike-slip motion along the MMF. In contrast our locations
414 suggest normal faulting along SW-NE striking features north of the MMF.

415

416 The differences in the tw sets of locations result in differences in:

- 417 i) The location method: linear versus non linear (see discussion in Husen and Hardebeck,
418 2010).
- 419 ii) The network geometry: we used a network of more than 9 OBS evenly distributed within a
420 circle of less than 10 km centred on the Western High; Yamamoto et al, 2017, used an
421 elongated network of 10 OBS stations distributed all along the MMF.
- 422 iii) The 3D velocity model (see § on the Construction of the 3D Western Marmara Fault).

423 Besides the limitations of our work (see *ad hoc* paragraph below), we consider that the network
424 geometry and the 3D-velocity model that we use are more appropriate to take into account the
425 heterogeneity of the Marmara Trough. The implications of our location results are discussed
426 hereafter.

427

428 **Implication in terms of triggered “ultra-shallow” (< 2 km) seismicity**

429 Of particular interest is the swarm of aftershocks triggered by the M_1 5.1 strike-slip earthquake
430 (see Table 8) that occurred below the Western High on the 25th of July, 2011. *Géli et al*
431 [2017] proposed that part of these aftershocks occurred within gas-prone sediment layers located
432 shallower than ~ 6 km depth below seafloor, with a predominantly normal focal mechanism
433 (see Table 9). In addition, most of the ultra-shallow (< 2 km) aftershocks occurred along normal
434 (or reverse) faults within sediment layers.

435

436 Interestingly, almost all ultra-shallow earthquakes that occurred during the two recording periods of
437 2011 and 2014 belong to this aftershock sequence, that followed the M_1 5.1 earthquake of July, 25,
438 2011. In “normal periods” (e.g. in between two successive earthquakes of moderate magnitude)
439 there is hardly any “ultra-shallow” seismicity. This would suggest that the ‘ultra-shallow’, soft
440 sediments -generally considered to behave aseismically- can also respond seismically to stress
441 changes caused by nearby deeper earthquakes, which are at least intermediate in size (i.e. $M_1 > 4.5$).
442 This may be explained by observations in rock physics experiments on wet clay-rich sediment
443 where there is a change from velocity strengthening (i.e. an aseismic regime) at slow slip-rates to
444 velocity weakening (i.e. seismic) at high slip-rate (*Faulkner et al.*, [2011], *Aretusini et al.*, [2017]).
445 *Faulkner et al.*, [2011] have postulated that this switch is due to due thermal pressurization of pore
446 fluid in the clay. Therefore a possible explanation for the ultra-shallow events are that abrupt stress

447 changes caused by the deeper main shocks may have been large enough to switch the normally
448 aseismic response of the sediment to a seismic one.

449 This could also explain why *Yamamoto et al [2017]* did not detect any “ultra-shallow” seismicity,
450 as no earthquake of magnitude $M_1 > 4$ occurred during the 10 months of recording, from September
451 2014 to July 2015 (e.g. read in *Yamamoto et, 2017*, page 2080: “*Because we recorded no*
452 *earthquakes of $M_L > 4$, and no events within the sediment layer of the Western High, we consider*
453 *that microearthquakes identified in the sedimentary layer by other researchers may be aftershocks*
454 *triggered by moderate earthquakes in upper crust beneath the Western High, as suggested by Cros*
455 *and Géli [2013]”).*

456

457 ***Implications in terms of seismic hazards (creeping versus locked)***

458 Our work underlines the difficulties that prevent the accurate depth determination of low magnitude
459 earthquakes, in absence of numerous, near-fault, sea-bottom stations. Consequently, caution is
460 required for interpreting micro-seismicity maps based on low-magnitude threshold. As an example,
461 the micro-seismicity within the Sea of Marmara reported by [*Schmittbuhl et al, 2015*] for the period
462 from 2007 to 2012 is plotted in Figure 19 for different threshold levels. For low magnitude
463 thresholds, the maps of micro-seismicity exhibit swarms of vertically distributed events, related to
464 the large uncertainties in depth determinations. These ill-resolved, vertical swarms entirely
465 disappear for threshold magnitudes above $M_1 \sim 3$ (Figure 18), suggesting that depth determinations
466 for earthquakes of magnitude above $M_1 \sim 3$ may well be used. Between 2007 and 2012, almost all
467 earthquakes of $M_1 > 3$ have occurred at a depth greater than ~ 8 km, along the western segments of
468 the MMF, where most of the gas emissions from the seafloor are found. In contrast no earthquake of
469 magnitude > 3 has occurred along the eastern segments of the MMF, from the Gulf of Izmit to the

20

470 west of Istanbul.

471 Previous studies (e.g. [Schmittbuhl *et al*, 2015], [Schmittbuhl *et al*, 2016], [Yamamoto *et al*, 2016]
472 and [Bohnhoff *et al*, 2017]) have proposed that the western part of the MMF could be subject to
473 deep crustal creeping, while the segment crossing the Central High, from the Kumburgas basin to
474 the entrance of the Bosphorus, could be locked (based on results from 6 months of acoustic ranging,
475 which did not reveal any significant steady-state surface creep along the MMF offshore Istanbul
476 [Sakic *et al*, 2016]).

477 Our results do not contradict this view. Creeping at crustal levels likely induces deformation within
478 the upper, sediment layers, which in turn contribute to maintain high permeability within the
479 damage zone, which in turn may enhance gas migration up to the surface. In addition the repeated
480 earthquakes of intermediate magnitude may trigger aftershocks in relation with the presence of gas
481 within the gas source (at depth ranging from ~ 1.5 to 5 km) and within the uppermost, gas-prone
482 sediment layers, which may result in gas emission from the seafloor.

483

484 **Limitations of our work and perspectives for future research**

485 The conflicting depth estimates, certainly pose several questions on the accuracy of the locations,
486 regarding the different methods and velocity models, used here versus the ones of previous studies.
487 Finding the correct earthquake locations in submarine environments is quite a challenge, that mostly
488 depends on (i) the methodology used (e.g. linear versus non-linear techniques), (ii) the velocity
489 model and iii) the network geometry.

490 By any means, our approach like any other approach has its limitations and advantages. The
491 assumption of a constant V_p/V_s ratio during the location procedure, due to the absence of an S
492 wave velocity model, might have led to a location bias (e.g. Maurer and Kradolfer, 1996). Also,
493 the 3D velocity model of this study, does not account for the across-fault variability within the

21

494 upper sediment structure, which is clearly visible in the seismic sections crossing the Western High
495 (e.g. Figure 8). Specifically, due to technical difficulties, the short scale variability due to the
496 presence of gas below the Western High and the variability between the northern flank and of the
497 southern flank were not considered when building the 3D model of this study.

498 Yet, besides the limitations of the current approach, here we do think that two different types of
499 seismicity (e.g. deep versus shallow seismicity < 6km) occur in the western part of the SoM, and
500 the plausible reasons why the previous studies did not succeed to obtain shallow events in their
501 catalogues, are the following: (i) a different geometry of the seafloor seismic network and a
502 consideration of only OBS data were considered for this analysis, (ii) the use of a 3D high
503 resolution velocity model, which was build up with all the available geological and geophysical
504 information from the SoM (see 3D velocity-structure of the Western Sea of Marmara), (iii) only a
505 limited number of earthquakes was used for the analysis, complying the criteria discussed in Data
506 and Methodology paragraph (e.g. outliers and not well-constrained events were removed from the
507 catalogue, ~ 80% of the earthquakes was eliminated), (iv) the use of non-linear methods, improved
508 the accuracy of the location solution and (v) extraneous information based on independent
509 observations (e.g. multichannel seismics, high-res 3D seismics, high-res bathymetry) is used for the
510 interpretation of event locations and focal mechanisms.

511 The perspectives for future work are:

512 (i) Merge OBS datasets of Yamamoto's 2017 and of this study's for the overlapping observing
513 periods.

514 (ii) Use a variable V_p/V_s at every single step of the location procedure.

515 (iii) Implement an OBS network with an appropriate layout allowing the depth determination
516 of shallow earthquakes.

517 (iv) Use land stations for improving the quality of focal mechanisms determinatons.

518 **Data and Resources**

519

520 • The two following seismological datasets were analyzed (see details Tables 1 and 2
521 and in Figure 1b) and are available on request to the authors:

522 ➤ Dataset-1 was recorded from 15th of April to 31st of July , 2011, by 10
523 autonomous, short-period (4.5 Hz) OBSs from Ifremer and by 2 permanent,
524 cabled broad-band OBSs operated by KOERI. Unfortunately, the station in the
525 center of the network stopped recording on 1st of July , 2011. Available on:
526 <http://www.seanoe.org/data/00386/49764/>

527 ➤ Dataset-2 was recorded from September 19th to 14th of November , 2014, by
528 9 autonomous, short-period (4.5 Hz) from Ifremer and by 1 autonomous,
529 broad-band OBS operated by INGV. Note that two autonomous, short-period
530 OBS were also deployed by Ifremer, from the 1st until the 15th of November
531 near the gas emissions site. Available on:
532 <http://www.seanoe.org/data/00385/49656/>

533 • An unpublished bathymetric grid of the Central Basin and Western High, having a
534 node spacing of 10 meters, based on multibeam echosounder system data collected
535 in 2014 with *R/V Pourquoi Pas?* This 10-m grid (courtesy of Charline Guérin of
536 Ifremer) is available on request to the authors.

537 • High-resolution 3D- and 2D-seismic data collected in 2009 with *R/V Le Suroit* and
538 with *R/V Piri Reis*, respectively. The full description of the 3D-acquisition system
539 and dataset is detailed in [Thomas *et al*, 2012]). Finally, multi-channel, deep seismic

540 lines collected in 2001 during the Seismara Cruise of R/V Le Nadir (e.g. *Laigle et al*
541 *[2008]*; *Bécel et al [2009]*; *Bécel et al [2010]*).

542 • The Gismo collection of Matlab tool boxes was used for seismic waveform analysis,
543 that could be found in <https://geoscience-community-codes.github.io/GISMO/> (last
544 acceded February 2017).

545 • The Sytmis software package for used for the 2011 OBS dataset

546 (<http://www.ineris.fr/centredoc/3202-fp-sytmisauto-0804-an.pdf>)

547 • The non-linear methods developed by Anthony Lomax were used
548 (<http://alomax.free.fr/alss/>)

549 • The following scientific reports available on-line were used:

550 Cros, E., and Géli, L. (2013). Characterization of microseismicity in the Western Sea of
551 Marmara: implications in terms of seismic monitoring, Project Report, Institut
552 Carnot Ifremer-Edrome, Abondement 2011, N°06/11/2013, 29 pages,
553 <http://dx.doi.org/10.13155/38916>

554

555 Géli L., Çağatay, N., Gasperini, L., Favali, P., Henry P., and Çifçi, G., (2011). ESONET
556 WP4 – Demonstration Missions. Marmara-DM final report,
557 <http://archimer.ifremer.fr/doc/00032/14324/>

558

559 Gürbüz C., Isik S. E., Géli, L., Cross, E., (2013). High Resolution Micro Earthquake
560 Characterization, Deliverable D8_2, EU MARSITE PROJECT (New Directions in
561 Seismic Hazard Assessment through Focused Earth Observation in the Marmara
562 Supersite), [http://archimer.ifremer.fr/doc/00278/38915/.](http://archimer.ifremer.fr/doc/00278/38915/)

563

564 Lomax, A., and Michelini, A., (2013). Users Guide for Early-est, Earthquake Rapid Location Sytem
565 with Estimation of Tsunamigenesis, http://early-est.rm.ingv.it/early-est_users_guide.pdf

566

567 Lomax, A., (2014). Mise en oeuvre et support pour logiciels de traitement automatisé de
568 données sismologiques acquises dans le cadre du projet Européen FP7 Marsite,
569 Contract report, Reference CNRS, MA201301A,
570 http://alomax.net/projects/marsite/MA201301A_report_v0.2.pdf.

571

572

573 Husen, S., & Hardebeck J.L. (2010) Earthquake location accuracy, Community Online Resource for
574 Statistical Seismicity Analysis, *doi:10.5078/corssa-55815573*. Available at [http://www.-](http://www.-corssa.org)
575 [corssa.org](http://www.-corssa.org).

576

577

578

579

580

581

582

583

584

585

586

587 **Acknowledgments**

588

589 This paper is part of the PhD of Evangelia Batsi, supported by Ifremer and by Région
590 Bretagne (“bourse ARED”). The OBS data were collected with the ESONET Network of
591 Excellence (contract N° 036851) and the MARSITE Integrated Project (contract N° 308417).
592 Jean-François Rolin and Roland Person, coordinators of ESONET as well as Meral Agualdis
593 project manager of MARSITE are warmly acknowledged. Acknowledgements are also
594 addressed to the Turkish Navy and to the Turkish Hydrographic Service (SHOD) for
595 supporting the operations at sea, particularly our correspondent, Captain Erhan Gezgin; to
596 the personnel of the French Embassy in Ankara, specially Mrs Bonnafous-Boucher; to CNR
597 and to Ifremer for funding operations at sea of R/V Le Suroit, R/V Pourquoi pas? and R/V
598 Urania, respectively; to Giuseppe D'Anna, Giuseppe Passafiume and Stefano Speciale of the
599 Istituto Nazionale di Geofisica e Vulcanologia (INGV) of Italy for assisting in the OBS
600 deployment ; to the Institute of Marine Science and Technology of the University of Izmir
601 for support with R/V Piri Reis; to Mireille Laigle of Géoazur of Sophia Antipolis
602 University for providing us the seismic profile SM 47 (e.g. Figure 4, by Bécel, A., et al,
603 2010) to COST_FLOWS (Action ES1301) for supporting a Short Term Scientific Mission
604 (STSM) for E. B.; to Bruno Marsset for his advices and encouragement; to Pascal Pelleau,
605 Mikaël Roudaut and Ronan Apprioual for their technical support; to Sylvain Bermell, for
606 drafting some of the figures; to Charline Guerin for providing us the grid of high
607 resolution bathymetry at 10 m; to professor Oguz Özel, for his support for using R/V
608 Yunuz of Istanbul University; to Jean Schmittbuhl, Hayrullah Karabulut and Jean-Robert
609 Grasso for their participation to the PhD Thesis committee. Intense use was made of
610 Global Mapping Tools (GMT) and ArcGIS. All the data used in this paper are available on
611 request to the authors.

References

612

613

614 Ambraseys, N.N. and Finkel, C., (1987). The Saros-Marmara earthquake of 9 August 1912,
615 *J. Earthq. Eng. Struct. Dyn.*, **15**, 189-211.

616

617 Ambraseys, N.N ands Finkel, C. (1995). The Seismicity of Turkey and adjacent areas. A
618 historical review, 1500-1800, *Istanbul: Eren Yayincilik*, 240 pp.

619

620 Aretusini, S., S. Mittempergher, O. Pl mper, E. Spagnuolo, A. F. Gualtieri, and G. Di Toro (2017),
621 Production of nanoparticles during experimental deformation of smectite and implications for
622 seismic slip, *Earth and Planetary Science Letters*, **463**, 221–231,
623 doi:10.1016/j.epsl.2017.01.048.

624

625 Armijo, R., Meyer B., Navarro, S., King, G., and Barka, A., (2002). Asymmetric slip
626 partitioning in the Sea of Marmara pull-apart: a clue to propagation process of the
627 North Anatolian Fault? *Terra Nova*, **14**, 80-86.

628

Armijo, R., Pondard, N., Meyer, B., Uçarkus, G., de Lepinay, B. M., Malavieille, J.,
Dominguez, S., Gustcher, M. A., Schmidt, S., Beck, C., et al, (2005). Submarine fault
scarps in the Sea of Marmara pull-apart (North Anatolian Fault): implications for
seismic hazard in Istanbul, *Geochem. Geophys. Geosyst.*, **6**, Q06009,
doi:10.1029/2004GC000896.

629

630 Bayrakci G., Laigle, M., Bécél, A., Hirn, A., Taymaz, T., Yolsal-Çevikbilen, S., and

27

631 SEISMARMARA team (2013). 3-D sediment-basement tomography of the
632 NorthernMarmara trough by a dense OBS network at the nodes of a grid of
633 controlled source profiles along the North Anatolian fault, *Geophys. J. Int.*, doi:
634 10.1093/gji/ggt211.

635

636 Bécél, A., (2006). Structure Sismique de la Faille Nord Anatolienne en Mer de Marmara,
637 Phd Thesis, Institut de Physique du Globe de Paris.

638

639 Bécél, A, Laigle, M., De Voogd, B., Hirn, A., Taymaz, T., Galvé, A., Shimamura, H.,
640 Murai, Y., Lépine, JC, Sapin, M. and Özalaybey, S. (2009). Moho, crustal architecture
641 and deep deformation under the North Marmara Trough, from the SEISMARMARA
642 Leg 1 offshore-onshore reflection-refraction survey, *Tectonophysics* **467**: 1-21.

643 Bécél, A., Laigle, M., De Voogd, B., Hirn, A., Taymaz, T., Yolsal-Cevikbilen, S., Shimamura,
644 H. (2010): North Marmara Trough architecture of basin infill, basement and faults,
645 from PDSM reflection and OBS refractions seismics, *Tectonophysics* **490**: 1-14.

646

647 Bourry, C., Chazallon, B., Charlou, JL, Donval, JP, Ruffine, L., Henry, P., Géli, L., Çagatay,
648 M., İnane, S. and Moreau, M. (2009). Free gas and gas hydrates from the Sea of
649 Marmara, Turkey: Chemical and structural characterization. *Chem. Geol.*,
650 doi:10.1016/j.chemgeo.2009.03.007.

651

652 Carton, H., Singh, S. C., Hirn, A., Bazin, B., de Voogd, B., Vigner, A., Ricolleau, A., Cetin, S.,
653 Oçakoglu, N., Karakoç, F., Sevligen, V., (2007), Seismic imaging of the three-dimensional

654 architecture of the Çınarcık Basin along the North Anatolian Fault, *J. Geophys. Res.*, **112**,
655 B06101, doi: 10.1029/2006JB004548.

656

657 Cros, E., and Géli, L. (2013). Characterization of microseismicity in the Western Sea of
658 Marmara: implications in terms of seismic monitoring, Project Report, Institut Carnot
659 Ifremer-Edrome, Abondement 2011, N°06/11/2013, 29 pages.

660

661 De Landro, G., Amoroso, O., Stabile, TA, Martullo, E., Lomax, A. and Zollo, A., (2015).
662 High precision Differential Earthquake Location in 3D models: Evidence for a
663 rheological barrier controlling the microseismicity at the Irpinia fault zone in
664 southern Apennines, *Geophys. J. Int.*, 203 (3): 1821-1831, doi: 10.1093/gji/ggv397

665

666 Dupré S., Scalabrin, C., Grall, C., Augustin, J-M, Henry, P., Sengor, A. M. C, Görür, N.,
667 Çağatay M. N., and Geli, L. (2015). Tectonic and sedimentary controls for widespread
668 gas emissions in the Sea of Marmara, Results from systematic, ship-borne multibeam
669 echosounder water column imageries, *J. Geophys. Res.*, doi: 10.1002/2014JB011617.

670

671 Faulkner, D. R., T. M. Mitchell, J. Behnsen, T. Hirose, and T. Shimamoto (2011), Stuck in the mud?
672 Earthquake nucleation and propagation through accretionary forearcs, *Geophys. Res. Lett.*, 38
673 (18), doi:10.1029/2011GL048552.

674

675 Géli, L., Henry, P., Zitter, T., Dupré, S., Tryon, M., Çağatay, M.N., Mercier de Lépinay,
676 B, Le Pichon, X., Şengör, A.M.C., Görür, N., et al, (2008). Gas emissions and active
677 tectonics within the submerged section of the North Anatolian Fault zone in the Sea

678 of Marmara. *Earth Planet. Sci. Lett.*, **274(1-2)**: 34-39.

679 Géli L., Çağatay, N., Gasperini, L., Favali, P., Henry P., and Çifçi, G., (2011). ESONET
680 WP4 – Demonstration Missions. Marmara-DM final report.

681

682 Géli, L., Piau, J. M., Dziak, R., Maury, V., Fitzenz, D., Coutellier, Q., and Henry, P. (2014),
683 Seismic Precursors linked to Highly Compressible Fluids at Oceanic Transform
684 Faults, *Nature Geoscience*, doi:10.1038/NGEO2244

685

686 Géli, L., Henry, P., Grall C., Tary, J.B., Lomax, A., C., Batsi E., Cros, E., Gürbüz C.,
687 Isik, S. E., Sengör A. M. C., et al, (2017). Gas related seismicity within the Istanbul
688 seismic gap, submitted to *Nature Scientific Reports* (submitted in October 2016).

689

690 Grall, C., Henry, P., Tezcan, D., Mercier de Lepinay, B., Bécel, A., Géli, L., Rudkiewicz,
691 J-L., Zitter, T., Harmegnies, F., (2012). Heat flow in the Sea of Marmara Central
692 Basin, possible implications for the tectonic evolution of the North Anatolian Fault,
693 *Geology*, **40:3-6**, doi:10.1130/G32192.32191.

694 Grall, C., Henry, P., Thomas, Y., Westbrook, G. K., . Çağatay, M. N, Marsset, B., Saritas,
695 H., Çifçi, G., and Géli, L., (2013). Slip rate estimation along the western segment of
696 the Main Marmara Fault over the last 330 ka by correlating Mass Transport De
697 posits, *Tectonics*, 10.1002/2012TC003255.

698

699 Gürbüz C., Aktar, M., Eyidogan, H., Cisternas, A., Haessler, H., Barka, A., Ergin, M.,
700 Türkelli, N., Polat, O., Üçer, S. B., Kuleli, S., et al, (2000). The seismotectonics of the

701 Marmara region (Turkey): results from a micro-seismic experiment. *Tectonophysics*
702 316, 1–17.
703
704 Gürbüz C., Isik S. E., Géli, L., Cross, E., (2013). High Resolution Micro Earthquake
705 Characterization, Deliverable D8_2, EU MARSITE PROJECT (New Directions in
706 Seismic Hazard Assessment through Focused Earth Observation in the Marmara
707 Supersite).
708
709 Hausmann, H., Hoyer, S., Schurr, B., Brückl, E., Houseman, G., and Stuart, G., (2010).
710 New seismic data improve earthquake location in the Vienna Basin area, Austria,
711 *Austrian Journal of Earth Sciences*, **103**, 2-14, Vienna.
712 Hardebeck, J.L. and Shearer, P.M., (2002). A new method for determining first- motion focal
713 mechanisms, *Bull. Seism. Soc. Am.*, **92**, 2264-2276.
714
715 Hardebeck, J.L. and Shearer, P.M., (2003). Using S/P Amplitude Ratios to Constrain the
716 Focal Mechanisms of Small Earthquakes, *Bull. Seism. Soc. Am*, **93**, 2434-2444.
717
718 Hardebeck, J.L. and Shearer, P.M., (2008). HASH: A Fortran program for computing
719 Earthquake First-Motion Focal Mechanisms -v1.2 – January 31
720
721 Helmstetter A., (2002). Is Earthquake Triggering Driven by Small Earthquakes, *Phys. Rev.*
722 *Lett.* **91**, 058501.
723
724 Husen, S., & Hardebeck J.L. (2010), Earthquake location accuracy, Community Online Resource

725 for Statistical Seismicity Analysis, doi:10.5078/corssa-55815573.

726

727 Imren, C., Le Pichon, X., Rangin, C., Demirbağ, E., Ecevitoglu, B., Görür, N., (2001). The
728 North Anatolian Fault within the Sea of Marmara: a new interpretation based on
729 multichannel seismic and multi-beam bathymetry data, *Earth Plan. Sci. Lett.*,
730 **186**,143–158, doi:10.1016/S0012-821X(01)00241-2.

731

732 Karabulut, H., Schmittbuhl, J., Özalaybey, S., Lengliné, O., Kömeç-Mutlu, A., Durand, V.,
733 Bouchon, M., Daniel, G., Bouin, M.P., (2011). Evolution of the seismicity in the east-
734 ern Marmara Sea a decade before and after the 17 August 1999 Izmit earthquake,
735 *Tectonophysics*, **510**, 17–27.

736

737 King G.C.P., Ross, S., Lin, J., (1994). Static stress changes and the triggering of earthquakes,
738 *Bull. Seism. Soc. Am.* **84**, 3, 935-953.

739

740 Kuscu, I., Okamura, M., Matsuoka, H., Gökaşan, E., Awata, Y., Tur, H., Şimşek and Keçer,
741 M. (2005). Seafloor gas seeps and sediment failures triggered by the August 17, 1999
742 earthquake in the Eastern part of the Gulf of Izmit, Sea of Marmara, NW Turkey. *Mar.*
743 *Geol.* **215**, 193–214.

744

745 Laigle M., Becel, A., De Voogd, B., Hirn, A., Taymaz, T., Ozalaybey, S. and Members of
746 SEISMARA Leg1 Team (2008). A first seismic survey in the Sea of Marmara: Deep
747 basins and whole crust architecture and evolution, *Earth Planet. Sci. Lett.*, **270**, 168-179.

748

749 Le Pichon, X., Sengör A.M.C., Demirbağ, E., Rangin, C., Imren, C., Armijo, R., Görür,
750 Çağatay, N., Mercier de Lepinay, B., et al, (2001), The active Main Marmara Fault,
751 *Earth Planet. Sci. Lett.*, **192**, 595–616.
752

753 Lomax, A., Michelini, A. and Curtis, A., (2009). Earthquake Location, Direct, Global-Search
754 Methods, in Complexity In *Encyclopedia of Complexity and System Science, Part 5*,
755 Springer, New York, pp. 2449-2473, doi:10.1007/978-0-387-30440-3.
756

757 Lomax, A., Satriano, C., and Vassallo, M., (2012). Automatic picker developments and
758 optimization : FilterPicker - a robust broadband picker for real - time seismic monitoring
759 and earthquake early - warning, *Seism. Res. Lett.*, **83**, 531-540, doi :
760 10.1785/gssrl.83.3.531.
761

762 Lomax, A., and Michelini, A., (2013). Users Guide for Early-est, Earthquake Rapid Location System
763 with Estimation of Tsunamigenesis, see link in « Data and Resources » section.
764

765 Lomax, A., (2014). Mise en oeuvre et support pour logiciels de traitement automatisé de
766 données sismologiques acquises dans le cadre du projet Européen FP7 Marsite, Contract
767 report, Reference CNRS, MA201301A.
768

769 Maurer, H., and U. Kradolfer (1996), Hypocentral parameters and velocity estimation in the western
770 Swiss Alps by simultaneous inversion of P- and S-wave data, *Bull. Seism. Soc. Am.*, **86**, 32-42.
771

772 Örgülü, G., (2011), Seismicity and source parameters for small-scale earthquakes along the splays

773 of the North Anatolian Fault (NAF) in the Marmara Sea, *Geophys. J. Int.* **184**, 385–404
774 doi:10.1111/j.1365-246X.2010.04844.x
775

776 Parson T., (2004). Recalculated probability of M>7 earthquakes beneath the Sea of Marmara.
777 *J. Geophys. Res.*, **109**, doi:10.1029/2003JB002667.
778

779 Pinar A., Kuge, K., Honkura, Y., (2003), Moment tensor inversion of recent small to moderate
780 sized earthquakes: implications for seismic hazard and active tectonics beneath the Sea of
781 Marmara, *Geophys. J. Int.*, **153**, 133–145
782

783 Pondard N., Armijjo, R., King, G.C.P., and Meyer, B., (2007). Fault interactions in the Sea
784 of Marmara pull-apart (North Anatolian Fault): earthquake clustering and propagating
785 earthquake sequences, *Geophys. J. Int.* (2007), **171**, 1185-1197, doi: 10.1111/j.1365-
786 246X.2007.03580.x.

Rangin, C., Demirbag, E., Imren., C., Crusson, A., Le Drezen, E., Le Bot, A., (2001).
Marine Atlas of the Sea of Marmara (Turkey). Data collected on board R.V Le Suroît,
September 2000, <http://archimer.ifremer.fr/doc/00279/39006/>

787

788 Rangin, C., Le Pichon, X., Demirbag, E., and Imren, C., (2004). Strain localization in the
789 Sea of Marmara: Propagation of the North Anatolian Fault in a now inactive pull-apart,
790 *Tectonics*, **23**, TC2014, doi:10.1029/2002TC001437.
791

792 Ruffine, L., Germain, Y., Polonia, A., De Prunelé, A., Croguennec, C., Donval, J-P., Pitel-
793 Roudaut, M., Ponzevera, E., Caprais, J-C., Brandily, C., (2015). Pore water

794 geochemistry at two seismogenic areas in the Sea of Marmara, *Geochem. Geophys.*
795 *Geosyst.*, **16**, 2038–2057, doi:10.1002/2015GC005798.

796

797 Ruffine, L., Fandino, O., Etoubleau, J., Chéron, S., Donval, J-P., Germain, Y., Ponzevera, E.,
798 Guyader, V., Dennielou, B., Etiope, et al, (2012). Geochemical dynamics of the natural-
799 gas hydrate system in the Sea of Marmara, offshore Turkey, *Advances in Natural Gas*
800 *Technology*, ISBN 978-953-51-0507-7, pp. 29-56.

801

802 Sakic, P., Piété, H., Ballu, V., Royer, J.-Y., Kopp, H., Lange, D., Petersen, F., Özeren, S., Ergintav,
803 S., Géli, L. Henry, P., Deschamps, A., (2016), No significant steady state surface creep along
804 the North Anatolian Fault offshore Istanbul: Results of 6 months of seafloor acoustic ranging,
805 *Geophys. Res. Lett.*, **43**, 6817–6825, doi:10.1002/2016GL069600.

806

807 Sato, T., Kasahara, J., Taymaz, T., Ito, M., Kamimura, A., Hayakawa, T., and Tan, O.,
808 (2004). A study of microearthquake seismicity and focal mechanisms within the Sea of
809 Marmara (NW Turkey) using ocean bottom seismometers (OBSs), *Tectonophysics*,
810 **391:303**, 314. doi:10.1016/j.tecto.2004.07.018.

811

812 Schmittbuhl, J., Karabulut, H., Lengliné, O., and Bouchon, M., (2015). Seismicity
813 distribution and locking depth along the Main Marmara Fault, Turkey, *Geochemistry,*
814 *Geophysics, Geosystems*, DOI 10.1002/2015GC006120.

815

816 Schmittbuhl, J., Karabulut, H., Lengliné, O., and Bouchon, M., (2016). Long-lasting seismic
817 repeaters in the Central Basin of the Main Marmara Fault, *Geophys. Res. Lett.*, **43**,
818 9527–9534, doi:10.1002/2016GL070505.

819

820 Shillington, D. J., Seeber L., Sorlien C. C., Steckler M. S., Kurt H., Dondurur D., Çifçi, G., İmren, C.,
821 Cormier M.-H., McHugh C.M.G., Gürçay S., Poyraz D., Okay, S., Atgın O., Diebold, J.B.;
822 Evidence for widespread creep on the flanks of the Sea of Marmara transform basin from
823 marine geophysical data. *Geology*; **40 (5)**: 439–442.

824

825 Şengör, A. M. C., Tüysüz, O., İmren, C., Sakıncı, M., Eyidoğan, H., Görür, N., Le Pichon,
826 X., and Rangin, C., (2005). The North Anatolian Fault: A new look, *Annu. Rev.*
827 *Earth Planet. Sci.*, **33**, 37–112, doi:10.1146/annurev.earth.32.101802.120415.

828

829 Şengör, A.M.C., Grall, C., Imren, C., Le Pichon, X., Görür, Henry, P., Karabulut, H., and
830 Siyako, M., (2014). The geometry of the North Anatolian transform fault in the Sea of
831 Marmara and its temporal evolution: Implications for the development of intra-
832 continental transform faults, *Can. J. Earth Sci.*, **51(3)**, 222–242, doi:10.1139/cjes-2013-
833 0160.

834

835 Steacy, S., Gomberg, J., and Cocco, M., (2005). Introduction to special section: Stress
836 transfer, earthquake triggering, and time-dependent seismic hazard, *J. Geophys. Res.*,
837 **110**, B05S01, doi:10.1029/2005JB003692.

838

839 Stein, R. S., Barka, A.A., and Dieterich, H., (1997). Progressive failure on the North Anatolian
840 fault since 1939 by earthquake stress triggering, *Geophys. J. Int.*, **128**, 594-604.

841

842 Tary, J.-B., Géli, L., Herny, P., Natalin, B., Gasperini, L., M. Çomoğlu, M., Çağatay, N.,
843 and Bardainne, T., (2011). Sea-Bottom Observations from the Western Escarpment of
844 the Sea of Marmara, *Bull. Seism. Soc. Am.*, **101** (2), 101, 775–791, doi:
845 10.1785/0120100014

846 Thomas, Y., Marsset, B., Westbrook, G., Grall, C., Géli, L., Cifci, G., Rochat, A., and
847 Sartas, H. (2012), Contribution of high-resolution 3D seismic near-seafloor imaging to
848 reservoir scale studies: application to the active north Anatolian Fault, Sea of Marmara,
849 *Near Surface Geophysics*, **10**, 291-301, doi:10.3997/1873-0604.2012019

850

851 Waldhauser, F., and Ellsworth, W.L., (2000), A double-difference earthquake location
852 algorithm: Method and application to the northern Hayward fault, *Bull. Seismol. Soc.*
853 *Am.*, **90**, 1353-1368

854

855 Yamamoto, Y., Takahashi, N., Pinar, A., Kalafat, D., Citak, S., Comoglu, M., Polata, R. and
856 Kaneda, Y. (2017): Geometry and segmentation of the North Anatolian Fault beneath
857 the Marmara Sea, Turkey, deduced from long-term ocean bottom seismographic
858 observations, *JGR*, doi:10.1002/2016JB013608

859

860

TABLES (1 to 8)**Table 1:** Table of coordinates and operation period of the temporary and permanent OBS stations of data-set

1.

OBS code	Latitude (°N)	Longitude (°E)	Depth (m)	Recording period
OBS-01	40.8848	27.6996017	1024	15 Apr. - 31 July
OBS-02	40.817055	27.7804433	652	15 Apr. - 30 June
OBS-03	40.750405	27.700185	516	15 Apr. - 31 July
OBS-04	40.8611483	28.580295	328	15 Apr. - 31 July
OBS-05	40.733415	27.920655	775	15 Apr. - 31 July
OBS-06	40.84155	27.9155833	906	15 Apr. - 31 July
OBS-07	40.786225	28.040535	1100	15 Apr. - 31 July
OBS-08	40.88608	28.0778767	1181	15 Apr. - 31 July
OBS-09	40.7344117	28.143615	634	15 Apr. - 31 July
OBS-10	40.8343517	28.2122183	720	15 Apr. - 31 July
KOERI-03	40.884783	27.975100	1204	permanent
KOERI-04	40.828184	27.535460	1144	permanent

862

863 *Where: OBS-01 to OBS-10 are the temporary OBS stations of Ifremer, during the 2011 recording period and KOERI-03 and KOERI-04:are the permanent*864 *OBS stations of KOERI used here*

865

Table 2: Table of coordinates and operation period of the temporary OBS stations of data-set 2

OBS code	Latitude (°N)	Longitude (°E)	Depth (m)	Recording period
OBS-01	40.91677	27.764366	443	19 Sep. - 14 Nov.
OBS-02	40.81528	27.7769	661	19 Sep. - 21 Sep.
OBS-03	40.71292	27.787066	481	19 Sep. - 14 Nov.
OBS-04	40.81267	27.7717	665	19 Sep. - 14 Nov.
OBS-05	40.77940	27.848133	918	19 Sep. - 14 Nov.
OBS-06	40.83143	27.947	1191	19 Sep. - 14 Nov.
OBS-07	40.77620	27.708516	598	19 Sep. - 14 Nov.
OBS-08	40.85125	27.708	1024	19 Sep. - 14 Nov.
OBS-09	40.81977	27.60506	1106	19 Sep. - 14 Nov.
OBS-10	40.84997	27.845516	401	19 Sep. - 23 Oct.
OBS-11	40.812946	27.768004	658	01 Nov. -14 Nov.
OBS-12	40.813015	27.768516	657	01 Nov. -14 Nov.
OBS-13	40.795116	27.83906	1016	06 Oct. 2013- 14 Nov. 2014

866

867 *Where: OBS-01 to OBS-12 are the temporary OBS stations of Ifremer, and OBS-13 is the temporary OBS station of INGV, during the 2014 recording*
868 *period*

869

870 **Table 3:** Results for synthetic tests on 1D-models, for Trials 1 and 2.

871

1D model	Trial 1			Trial 2		
	Latitude 1 (°)	Longitude 1 (°)	Depth 1 (km)	Latitude 2 (°)	Longitude 2 (°)	Depth 2 (km)
Initial location	40.80	28.00	12	40.80	28.00	2
1D – this study	40.7677	28.0008	15.2	40.7627	27.996	11.2
1D – Karabulut et al, 2011	40.7674	27.995	21.5	40.7611	27.9918	17.4

872

Table 4: Location results for triplet of case study 1.

Case study 1				Velocity Models								
No	Date-Time	OBS used	MI	1D – this study			3D – this study			3D – Yamamoto, Y., et al, 2017		
				Lat (°)	Long (°)	Depth bsf (km)	Lat (°)	Long (°)	Depth bsf (km)	Lat (°)	Long (°)	Depth bsf (km)
1	25 October 2014 01:46:52	01, 04, 05, 07, 13	1.50	40.8080	27.8032	10.77	40.8452	27.8120	6.21	40.8174	27.7668	18.62
2	25 October 2014 03:05:00	03, 04, 05, 06, 07, 08, 13	1.93	40.8036	27.7999	9.61	40.8484	27.8104	6.29	40.8171	27.7691	18.38
3	25 October 2014 04:21:38	01, 03, 04, 05, 07	1.54	40.8035	27.8039	10.52	40.8421	27.8096	6.59	40.8152	27.7667	18.61

873

Table 5: Location results for triplet of case study 2.

Case study 2				Velocity Models					
No	Date-Time	OBS used	MI	1D – this study			3D – this study		
				Lat (°)	Long (°)	Depth bsf (km)	Lat (°)	Long (°)	Depth bsf (km)
1	19 May 2011 04:44:05	01, 02, 05, 06, 07, 08, 09, 10	1.15	40.8159	28.0985	2.71	40.8277	28.1154	0.003
2	19 May 2011 05:05:38	07, 08, 10, 09	0.54	40.8377	28.0958	15.65	40.8340	28.1246	1.46
3	23 June 2011 20:25:11	07, 08, 10, 09	0.93	40.8558	28.1189	19.64	40.8361	28.1303	0.7

Where the relocation was obtained by the two velocity models (1D versus 3D).

40

Table 6: Location results for the 10-events cluster of case study 3.

Case study 3					Velocity Models					
No	Date-Time	OBS used	MI	1D – this study			3D – this study			
				Lat (°)	Long (°)	Depth bsf (km)	Lat (°)	Long (°)	Depth bsf (km)	
1	26 April 2011 16:12:09	02, 05, 06, 07, 08, 09, 10	0.98	40.7998	27.9829	12.09	40.8197	27.9867	11.89	
2	07 May 2011 04:14:26	01, 02, 03, 05, 06, 07, 08, 09, 10	1.40	40.8042	27.9827	14.49	40.8256	27.9889	14.77	
3	07 May 2011 17:27:49	01, 02, 03, 05, 06, 07, 08, 09, 10	2.16	40.8092	27.9763	14.05	40.8299	27.9819	13.89	
4	07 May 2011 17:46:15	02, 05, 06, 07, 08, 09, 10	1.51	40.8021	27.9860	12.55	40.8220	27.9903	12.36	
5	09 May 2011 14:00:02	02, 03, 05, 06, 07, 08, 09	1.51	40.7971	27.9895	12.60	40.8173	27.9945	12.48	
6	09 May 2011 23:08:07	01, 02, 03, 04, 05, 06, 07, 08, 09, 10	1.71	40.7946	27.9797	13.25	40.8165	27.9851	13.37	
7	12 May 2011 14:32:44	01, 02, 03, 05, 06, 07, 08, 09, 10	1.71	40.7995	27.9797	13.49	40.8207	27.9854	13.63	
8	13 May 2011 10:40:02	01, 02, 03, 05, 06, 07, 08, 09, 10	2.00	40.8020	27.9830	13.26	40.8226	27.9890	13.19	
9	17 May 2011 20:40:14	02, 05, 06, 07, 08, 09, 10	1.18	40.7999	27.9795	12.23	40.8202	27.9837	12.08	
10	18 May 2011 03:17:00	01, 02, 03, 05, 06, 07, 08, 09, 10	1.77	40.8093	27.9796	13.76	40.8294	27.9857	13.60	

Where the relocation was obtained by the two velocity models (1D versus 3D).

Table 7: Single (for $M > 3$) and composite (for $M < 2$) focal mechanisms solutions for selected earthquakes from the two data-sets.

No	Number of events used	Date-Time	Lat (°N)	Long (°E)	Depth (km) below seafloor	M_i	Strike(°)	Dip (°)	Rake (°)
S1	1	01 May 2011 08:36	40.8266	28.1355	14.2	3.3	312	63	135
S2	1	19 May 2011 04:38	40.8340	28.1442	4.3	3.1	70	20	-125
S3	1	25 July 2011 17:57	40.82	27.741	11.5	5.1	113	83	-148
S4	1	19 Sept 2014 10:52	40.837	27.8722	4.4	3.3	97	20	-86
C1	10	Aftershock Sequence See supplementary Information	40.82	27.75	2.5	1.2	300	34	-145
C2	10	See Case Study 3	40.82	27.98	13.1	1.5	78	58	151
C3	3	See Case Study 2	40.83	28.12	0.7	1.5	233	67	101
C4	3	See Case Study 1	40.84	27.81	6.4	1.65	190	59	-80

Where S1 to S4 and C1 to C4 correspond to single and composite focal mechanisms respectively.

874 **Table 8:** Common events used for comparison of locations from for this study (2014 period) and from *Yamamoto's et*
875 *al, 2017* and displayed in Figure 18.

876

877

No	Date-Time (2014)	This study				Yamamoto et al, 2017			
		Latitude (°)	Longitude (°)	Depth (km)	Mag	Latitude (°)	Longitude (°)	Depth (km)	Mag
1	26 September 06:02:55	40.8309	27.7308	5.25	0.9	40.8091	27.6466	15.46	1.7
2	01 October 14:44:49	40.8509	27.8905	3.55	0.7	40.8710	27.9218	10.00	1.3
3	03 October 21:40:22	40.8340	27.8769	5.59	0.7	40.8497	27.9223	18.2	1.7
4	04 October 11:58:34	40.8243	27.7265	7.00	1.9	40.8247	27.6696	14.54	2.2
5	12 October 04:58:34	40.7719	27.73	21.67	0.5	40.8167	27.7080	18.75	1.7
6	17 October 19:52:52	40.8295	27.8642	4.90	0.8	40.8041	27.8832	13.54	1.4
7	18 October 10:17:43	40.8471	27.8087	6.61	1.1	40.8310	27.8056	21.07	1.9
8	24 October 14:18:24	40.8356	27.7383	5.41	0.7	40.8241	27.6531	14.89	1.4
9	25 October 01:46:52	40.8452	27.812	6.21	0.9	40.8174	27.7668	18.62	1.5
10	25 October 03:05:00	40.8484	27.8104	6.29	1.7	40.8171	27.7691	18.38	1.9
11	25 October 04:21:38	40.8421	27.8096	6.59	0.9	40.8152	27.7667	18.61	1.5
12	25 October 09:28:57	40.8242	27.7754	5.22	0.5	40.8165	27.7706	18.19	1.6
13	25 October 04:21:38	40.8303	27.7331	5.19	0.9	40.8089	27.6489	15.46	1.6
14	26 October 07:41:51	40.8463	27.7379	6.68	0.7	40.8236	27.6907	20.28	2.0
15	27 October 21:22:10	40.8240	27.8023	4.59	0.7	40.8134	27.6734	20.52	1.4
16	05 November 23:31:49	40.7643	27.8128	11.69	0.9	40.8210	27.6969	19.92	1.6

878
879
880

881

882

883

FIGURE CAPTIONS (1 to 19)

884

885

886 **Figure 1:** (1a) General view of the SoM between the Black Sea and the Aegean Sea. Black lines indicate the
887 main structural features of the Marmara Fault System (e.g. [Sengör et al., 2005]). Black box correspond to Fig.
888 1b. Abbreviations: TB: Tekirdag basin; WH: Western high; CB: Central Basin; KB: Kumburgaz basin; CH: Central
889 High; ÇB: Çınarcık Basin.

890 (1b) Bathymetric map of the study area within the Western SoM, displaying the position of the OBSs used for
891 this study, along with the delimitation of the boxes shown in Figures 6b, 8b, and 9. Temporary seismic
892 networks of Ifremer in 2011 and 2014 are shown with yellow and red triangles, respectively, while the one of
893 INGV (in 2014) is represented by a purple triangle. The permanent OBS stations of KOERI (green triangles)
894 were operating in 2011 but not in 2014. Black lines are for active faults (e.g. Sengör et al. [2005]). Green
895 dots indicate acoustically detected gas emission sites, after [Dupré et al., 2015]. White circles show the centre of
896 the clusters of case study 1 (CS1), 2 (CS2) and 3 (CS3), respectively.

897

898 **Figure 2:** (2a) From [Géli and Cros, 2013]. See also Appendix 2 in [Géli et al., 2016]. Contours of the pre-
899 kinematic basement depth, from Figure 13a of [Bayrakci et al., 2013], are here super-imposed on the
900 bathymetric map of the Western SoM, based on the high resolution, 38m grid from [Le Pichon et al., 2001].
901 Red dots indicate grid nodes from the low-resolution ($6 \text{ km} \times 6 \text{ km} \times 2 \text{ km}$) grid of [Bayrakci et al., 2013].
902 Black dots indicate the nodes of the high-resolution grid ($0.75 \text{ km} \times 0.75 \text{ km} \times 0.2 \text{ km}$) used in this study.
903 Labels from 1 to 9 on the basement iso-depth contours indicate 9 different velocity domains: red dots within iso-
904 contour 1 share the same 1D-velocity profile within the pre-kinematic basement; so do all red dots located
905 between iso-contours 2 and 3, etc. The velocity profile below the pre-kinematic basement is based on [Bécel
906 et al., 2009], as described in [Géli and Cros, 2013]. Finally, the 1D velocity profile below each black dot is
907 obtained by interpolating the velocity profile from the surrounding red nodes.

908 (2b) 1D-velocity models used in previous studies of seismicity within the SoM (where blue, red and yellow lines
909 correspond to the models by [Tary et al., 2011], [Gürbüz et al., 2000] and [Karabulut et al., 2011] respectively), along
910 with the 1D-model used in this study (purple line) and described in [Géli and Cros, 2013].

911

912 **Figure 3:** Detailed bathymetric map of the Western High having a node spacing of 10 meters (contour interval :
913 100 m, see Data and Resource section). The bathymetric grid is still unpublished and available on request to the
914 authors (Courtesy of Charline Guérin, Ifremer). Dashed black line A2-08 is the 2D-high resolution seismic line
915 displayed in Figure 8. Black boxes correspond to Figures 6b, 16 and 17. Continuous black lines indicate the
916 main structural features of the Marmara Fault System. Temporary seismic networks of Ifremer in 2011 and
917 2014 are shown with yellow and red triangles, respectively, while the one of INGV (in 2014) is represented
918 by a purple triangle. The permanent OBS stations of KOERI (green triangles) were operating in 2011 but not
919 in 2014.

920

921 **Figure 4 :** Matrix of cross correlation for all events recorded during the 2014 deployment, by the central sta-
922 tion OBS04, on the vertical component . White arrows indicate highly correlated events, e.g. : the triplet (cc >
923 0.9) of 25th of October 2014, selected for case Study 1 (Figure 6).

924

925 **Figure 5:** Case study 1. Seismogram (vertical component) corresponding to the triplet (with cc>0.9) recorded by
926 the central OBS04 station of the 2014 network on the 25th of October.

927

928 **Figure 6:** Case study 1 (cont.) 6a) Distribution of OBSs (shown by triangles) used in this study for the location of
929 earthquake 2 of case study 1 (see seismogram in Figure 5). White star, circle and diamond indicate the 1D (this study),
930 the 3D (this study) and the [Yamamoto et al., 2017] locations, respectively. The distances (in kilometres) from the 3D lo-
931 cation of earthquake 2 to each OBS are indicated in red. Note that OBS10 (e.g. shown with a yellow cross) stopped
932 working 3 days before the occurrence of the events of case study 2. Note that paths to OBS4 necessarily cross-mud vol-
933 canoes and gas-prone sediment layers. Black box corresponds to Fig. 6b. Black lines indicate the main structural fea-
934 tures of the Marmara Fault System (e.g. [Sengör et al., 2005]). Green dots correspond to gas emissions sites, af-
935 ter [Dupré et al., 2015].

936 6b) Left panel indicates the relocated epicenters for the triplet shown in Figure 5, obtained using respectively the
937 1D (stars), the 3D (circles) velocity models of this study and the 3D velocity model by [Yamamoto et al.,
938 2017] (white diamonds). The right panel indicates the N-S cross-section with the relocated hypocenters. The prob-
939 abilistic, relative location uncertainties obtained by NLDiffLoc are displayed by black ellipsoids showing the pro-
940 jection of the 68% confidence ellipsoid for each earthquake with their PDF (probability density functions) in -

941 dicated by blue and red dots, for the 1D and 3D velocity models respectively. Red beachballs show the com -
942 posite focal mechanism solution calculated for the triplet events. Numbers 1 to 3 corresponds to the name of
943 each earthquake (see Table 5). Line A2-08 is the 2D-high resolution seismic lines displayed in Figure 12. Green
944 dots correspond to gas emissions sites, after [Dupré et al, 2015]. Note that OBS10 (e.g. shown with a yellow cross)
945 stopped working 3 days before the occurrence of the events of case study 2. See polarities and characteristics of com -
946 posite focal mechanisms of 3D locations in Supplementary Information.

947

948 **Figure 7:** Seismograms from earthquake 2 (25th of October, 2014) of case study 1 recorded at seafloor stations 1, 8, 4,
949 7, 5 and 3 of the 2014 OBS network. Dotted lines indicate t_p and t_s arrivals at each different OBS. The upper panel dis -
950 plays the vertical component (Figure 7a). The bottom panel is for Horizontal-1(Figure 7b) .

951 **Figure 8:** (a) 2D-high resolution seismic section along line A2-08 (see track line location in Figure 3) collected
952 in 2009 with Piri Reis. (b) Interpretation of seismic profile A2-08 (this study).

953

954 **Figure 9:** Case Study 2, presented for a triplet of highly correlated events ($cc > 0.8$) that occurred on the 19th of
955 May 2011 and on the 23rd of June 2011. 9a) Distribution of OBSs (shown by triangles) used in this study for the
956 location of earthquake 3 of case study 2 (see seismograms in Figure 10). White star and white dot indicate the 1D (this
957 study) and the 3D (this study) locations, respectively. Red lines indicate the distance of 3D location to each OBS sta -
958 tion. Dashed white line indicated the profile SM47 shot during the Seismarmara cruise in 2001 across the eastern side of
959 the Central Basin. Black box corresponds to figure Figure 8b. Black lines indicate the main structural features of the
960 Marmara Fault System (e.g. [Sengör et al., 2005]). Green dots correspond to gas emissions sites, after [Dupré et
961 al, 2015].

962 9b) Left panel indicates the relocated epicenters obtained using respectively the “this study 1D” (stars) vs the 3D
963 (circles) velocity models. Upper right panels indicate N-S cross-section with the relocated hypocenters. The proba -
964 bilistic, relative location uncertainties obtained by NLDiffLoc are displayed by black ellipsoids showing the projec -
965 tion of the 68% confidence ellipsoid for each earthquake with their PDF (probability density functions) indi -
966 cated by blue and red dots, for the “this study 1D” and 3D velocity models respectively. Events are numbered
967 from 1 to 3 (see Table 6). Red beachballs show the composite focal mechanism solution calculated for the triplet.
968 Green dots correspond to gas emissions sites, after [Dupré et al, 2015]. See polarities and characteristics of composite
969 focal mechanisms of 3D locations in Supplementary Information.

45

970 **Figure 10:** Seismograms for event 3 of case study 2, recorded at OBSs 7, 8, 9 and 10 on June 23, 2011. Horizontal ar-
971 rows indicate the t_s - t_p arrival at each different OBS. On OBS, a range is given for t_s - t_p . The upper panel displays the ver-
972 tical component (Figure 10a). The bottom panels is for Horizontal-1 component (Figure 10b).

973

974 **Figure 11** (after Figure 4, of Bécel et al, 2010): Hypocenters (orange dots) projected along the pre-stack depth
975 migrated section (Line SM47) shot during the Seismarmara cruise in 2001 across the eastern side of the Cen-
976 tral Basin. Line track and hypocenter locations are indicated in Figures 8 and 13. Interpretations (yellow, red
977 and brown lines) are from Bécel et al, 2010. Note that the shallowest (at depths < 3 km) hypocenters are
978 near or within to the positive flower structure underlined by the black box (see case study 2, Figure 9).

979

980 **Figure 12:** Case study 3. Left panel indicates the relocated epicenters of the cluster of events that occurred from
981 the 26th of April 2011 until the 18th of May 2011, obtained using respectively the “this study 1D” (stars) vs
982 the 3D (circles) velocity models. The right panel indicates the N-S cross-section with the relocated hypocenters.
983 The probabilistic, relative location uncertainties obtained by NLDiffLoc are displayed by black ellipsoids showing
984 the projection of the 68% confidence ellipsoid for each earthquake with their PDF (probability density func-
985 tions) indicated by blue and red dots, for the “this study 1D” and 3D velocity models respectively. Red
986 beachballs show the composite focal mechanism solution calculated for the cluster events. Numbers 1 to 10
987 correspond to the name of each earthquake (see Table 6). Green dots correspond to gas emissions sites, after
988 [Dupré et al, 2015]. See polarities and characteristics of composite focal mechanisms of 3D locations in Supplemen-
989 tary Information.

990

991

992 **Figure 13:** Comparison of RMS errors of absolute location (e.g. use of NonLinLoc) obtained for the case
993 studies 1 to 3, for the velocity models 1D (blue bins) and 3D (red bins) of this study. Event number for each
994 case study is indicated (see Tables 4, 5 and 6).

995

996

997

998 **Figure 14:** Upper left panel indicates the relocated epicenters (obtained using the 3D velocity model) for the
999 2011 recording period, including also the mainshock of the 25th of July and its sequence of aftershocks (e.g.
1000 15th of April until the 31st of July 2011). The lower left and upper right panels indicate E-W and N-S cross-sec-
1001 tions of the relocated hypocenters. Red beachballs show the focal mechanisms solutions, with white labels indicating
1002 the name, local magnitude and depth for each case (see tables 3 and 4). Yellow triangles show the temporary
1003 OBS stations of Ifremer during the 2011 recording. Green dots correspond to gas emissions sites, after [Dupré et
1004 al, 2015]. The size of the orange circles is proportional to their local magnitude (e.g. $0.5 < M < 5.1$). Red line
1005 corresponds to profile SM 47 (after Figure 4 of Bécel et al, 2010) and small black box to Fig. 8. Bathymet-
1006 ric map in upper left panel is with node spacing of 10 meters (see Data and Resource section). See polarities and
1007 characteristics of composite focal mechanisms of 3D locations in Supplementary Information.

1008

1009

1010 **Figure 15:** Upper left panel indicates the relocated epicenters (obtained using the 3D velocity model) for the
1011 recording period from September 19th to November 14th, 2014. The lower left and upper right panels indicate
1012 E-W and N-S cross-sections of the relocated hypocenters. Red beachballs show the focal mechanisms solu-
1013 tions with white labels indicating the name, local magnitude and depth for each case (see tables 3 and 4).
1014 Red and orange (OLD-OBS) triangles show the temporary OBS stations of Ifremer during the 2014 recording,
1015 while the purple triangle show the temporary OBS station of INGV. Green dots correspond to gas emissions
1016 sites, after [Dupré et al, 2015]. The size of the salmon circles is proportional to their local magnitude (e.g.
1017 $0.5 < M < 3.3$). Bathymetric map (upper left panel) with node spacing of 10 meters (see Data and Resource sec-
1018 tion). See polarities and characteristics of composite focal mechanisms of 3D locations in Supplementary Information.

1019

1020 **Figure 16:** Upper left panel presents a synthesis of the relocated epicenters (using our 3D velocity model)
1021 during the 2011 (orange circles) and 2014 (salmon circles) recording periods. The lower left and upper right
1022 panels indicate E-W and N-S cross-sections of the relocated hypocenters. Red triangles show the temporary
1023 OBS stations of Ifremer during the 2014 recording period. Green dots correspond to gas emissions sites, after
1024 [Dupré et al, 2015]. The bathymetric map in the upper left panel) of the Western High is with a node spacing of
1025 10 meters (see Data and Resource section). Black dashed line indicates seismic line A2-08 (see Figure 8).

1026

1027 **Figure 17:** Upper left panel presents the shallower (depth < 4 km), well constrained, relocated aftershocks
1028 (using our 3D velocity model) that followed the M5.1 earthquake of the 25th of July , 2011. The lower left
1029 and upper right panels indicate E-W and N-S cross-sections of the relocated hypocenters. Green dots correspond
1030 to gas emissions sites, after [Dupré et al, 2015]. Bathymetric map of upper left panel with a node spacing of
1031 10 meters and contour interval of 20 m (see Data and Resource section). See polarities and characteristics of com-
1032 posite focal mechanisms of 3D locations in Supplementary Information.

1033

1034 **Figure 18:** Comparison of location results for the common events, listed both in Yamamoto et al, 2017 (orange dots)
1035 and in this work (red dots), that occurred during the overlapping period, from September 19, to November 14, 2014. La-
1036 bels (from 1 to 16) correspond to the number of each individual event listed in Table 8. Green dots correspond to gas
1037 emissions sites, after [Dupré et al, 2015]. Bathymetric map of upper left panel with a node spacing of 10 me-
1038 ters and contour interval of 20 m (see Data and Resource section). Black lines indicate main structural features, af-
1039 ter [Sengör et al., 2005].

1040

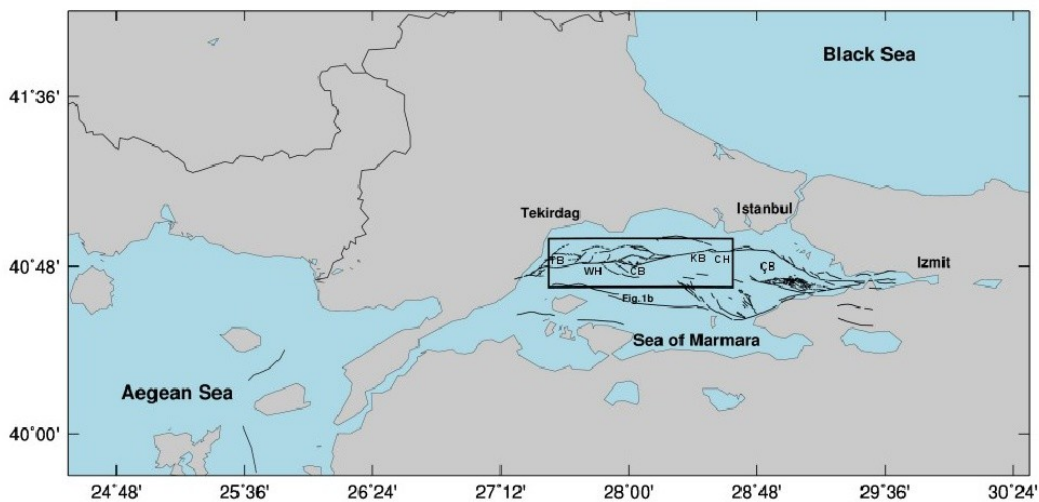
1041 **Figure 19:** Thresholded seismicity maps (between 2007 and 2012, after [Schmittbuhl et al, 2015]) displaying events
1042 of magnitude (M_1) above 2.0 (top); 2.6 (middle) and 3.0 (bottom), respectively. The “vertical” swarms of seismicity dis-
1043 appear for a threshold magnitude of $M_1 \sim 3$.

1044

FIGURES (1 to 19)

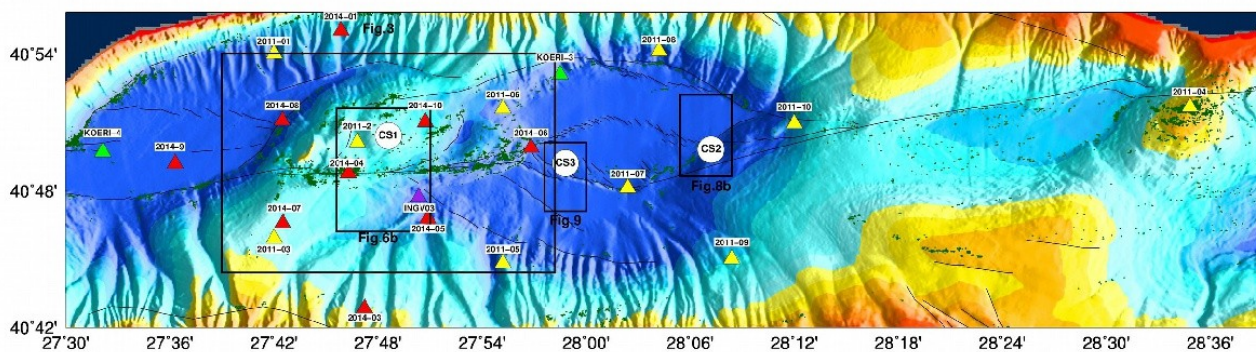
1

2 (a)



3

4 (b)



6

7

8

1

1

9 **Figure 1:** (1a) General view of the SoM between the Black Sea and the Aegean Sea. Black lines indicate the
10 main structural features of the Marmara Fault System (e.g. [Sengör et al., 2005]). Black box correspond to Fig. 1b.
11 Abbreviations: TB: Tekirdag basin; WH: Western high; CB: Central Basin; KB: Kumburgaz basin; CH: Central High; ÇB:
12 Çınarcık Basin.
13 (1b) Bathymetric map of the study area within the Western SoM, displaying the position of the OBSs used for
14 this study, along with the delimitation of the boxes shown in Figures 6b, 8b, and 9. Temporary seismic networks
15 of Ifremer in 2011 and 2014 are shown with yellow and red triangles, respectively, while the one of INGV (in
16 2014) is represented by a purple triangle. The permanent OBS stations of KOERI (green triangles) were operating
17 in 2011 but not in 2014. Black lines are for active faults (e.g. Sengör et al. [2005]). Green dots indicate
18 acoustically detected gas emission sites, after [Dupré et al, 2015]. White circles show the centre of the clusters of
19 case study 1 (CS1), 2 (CS2) and 3 (CS3), respectively.

20

21

22

23

24

25

26

27

28

29

30

31

32

33

34

35

36

37

2

2

38 (a)

39

40

41

42

43

44

45

46

47 (b)

48

49

50

51

52

53

54

55

56

57

58

59

60

61

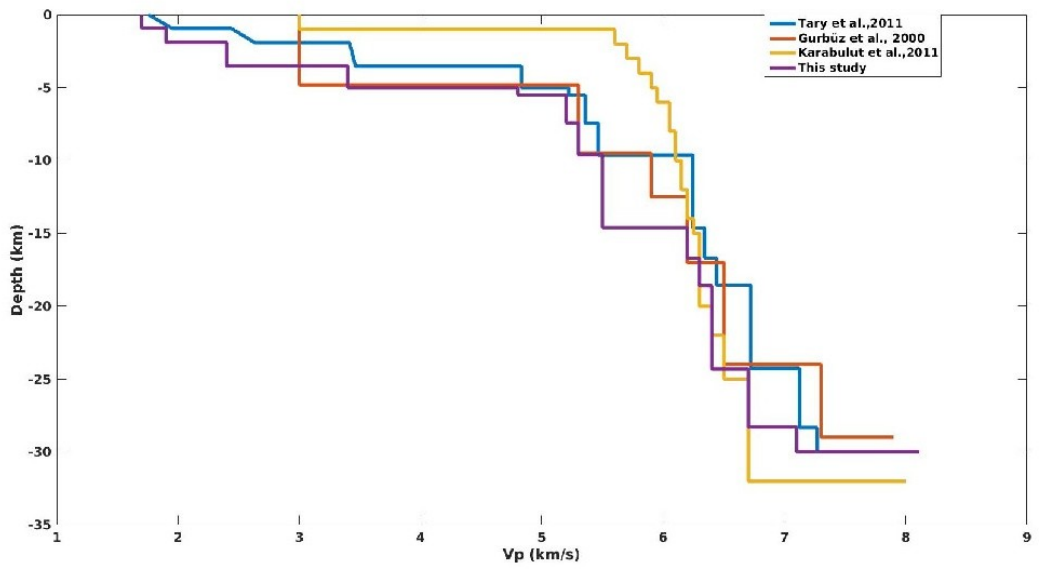
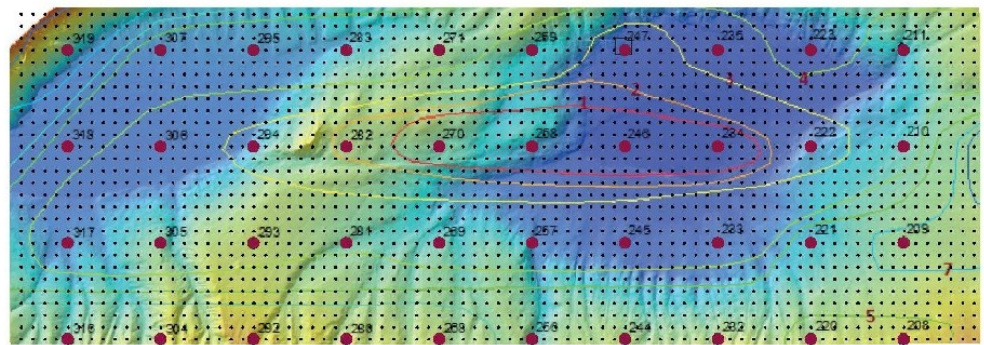
62

63

64

3

3



65

66 **Figure 2:** (a) From [Géli and Cros, 2013]. See also Appendix 2 in [Géli et al., 2016]. Contours of the pre-
67 kinematic basement depth, from Figure 13a of [Bayrakci et al, 2013], are here super-imposed on the bathymetric
68 map of the Western SoM, based on the high resolution, 38m grid from [Le Pichon et al, 2001]. Red dots
69 indicate grid nodes from the low-resolution ($6 \text{ km} \times 6 \text{ km} \times 2 \text{ km}$) grid of [Bayrakci et al, 2013]. Black dots
70 indicate the nodes of the high-resolution grid ($0.75 \text{ km} \times 0.75 \text{ km} \times 0.2 \text{ km}$) used in this study. Labels from 1 to 9
71 on the basement iso-depth contours indicate 9 different velocity domains: red dots within iso-contour 1 share the
72 same 1D-velocity profile within the pre-kinematic basement; so do all red dots located between iso-contours 2 and
73 3, etc. The velocity profile below the pre-kinematic basement is based on [Bécel et al, 2009], as described in
74 [Géli and Cros, 2013]. Finally, the 1D velocity profile below each black dot is obtained by interpolating the
75 velocity profile from the surrounding red nodes.

76 (2b) 1D-velocity models used in previous studies of seismicity within the SoM (where blue, red and yellow lines cor-
77 respond to the models by [Tary et al, 2011], [Gürbüz et al, 2000] and [Karabulut et al, 2011] respectively), along with
78 the 1D-model used in this study (purple line) and described in [Géli and Cros, 2013].

79

80

81

82

83

84

85

86

87

88

89

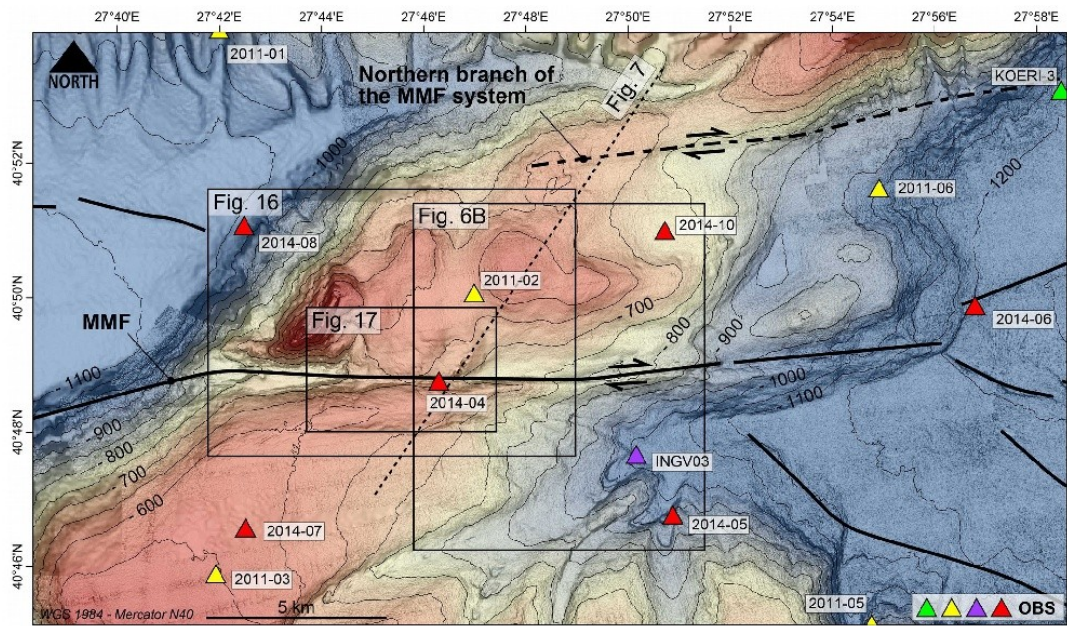
90

91

92

4

4

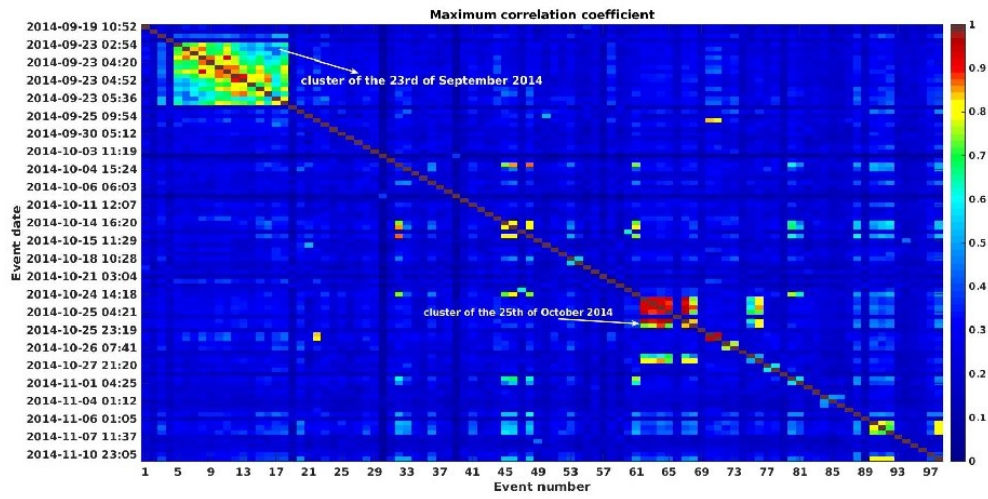


94 **Figure 3:** Detailed bathymetric map of the Western High having a node spacing of 10 meters (contour interval : 100
 95 m, see Data and Resource section). The bathymetric grid is still unpublished and available on request to the authors
 96 (Courtesy of Charline Guérin, Ifremer). Dashed black line A2-08 is the 2D-high resolution seismic line displayed in
 97 Figure 12. Black boxes correspond to Figures 6b, 16 and 17. Continuous black lines indicate the main structural
 98 features of the Marmara Fault System. Temporary seismic networks of Ifremer in 2011 and 2014 are shown with
 99 yellow and red triangles, respectively, while the one of INGV (in 2014) is represented by a purple triangle. The
 100 permanent OBS stations of KOERI (green triangles) were operating in 2011 but not in 2014.

101
 102
 103
 104
 105
 106
 107

5

5



108 **Figure 4:** Matrix of cross correlation for all events recorded during the 2014 deployment, by the central station
 109 OBS04, on the vertical component . White arrows indicate highly correlated events, e.g. : the triplet (cc > 0.9) of
 110 25th of October 2014, selected for case Study 1 (Figure 6).

111
 112
 113
 114
 115
 116
 117
 118
 119
 120
 121
 122
 123
 124

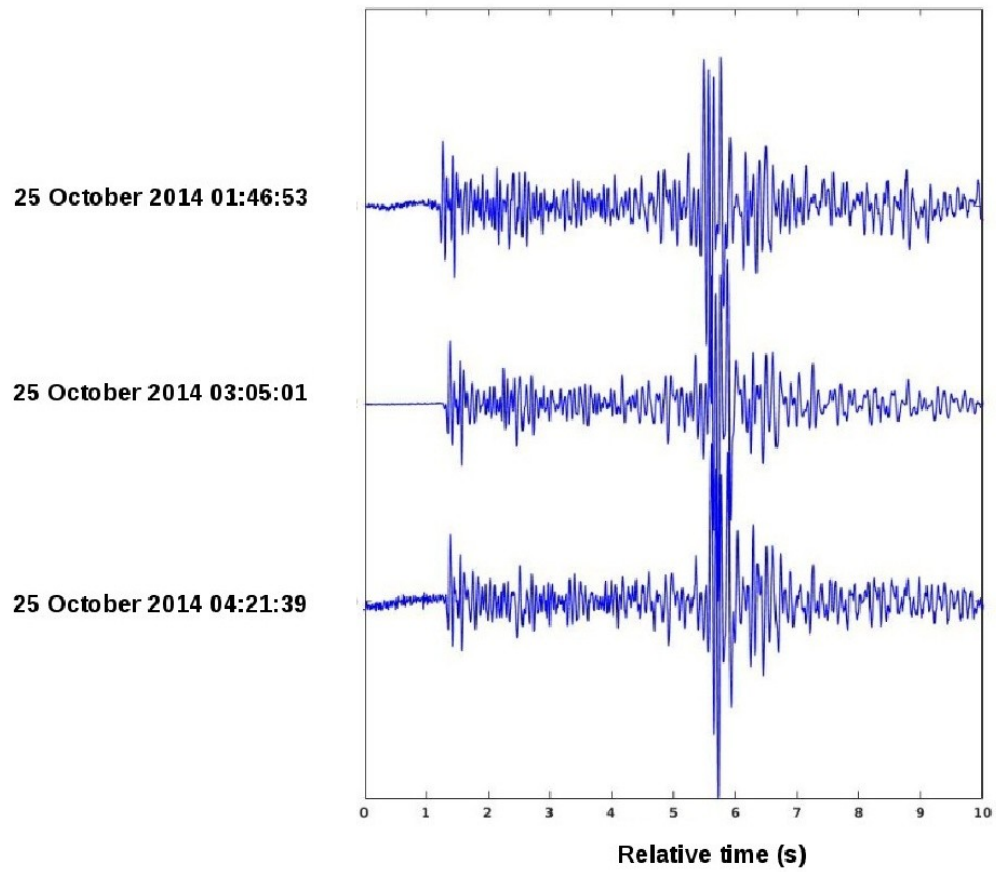
6

6

125

126 (a)

127



129

130

131

132

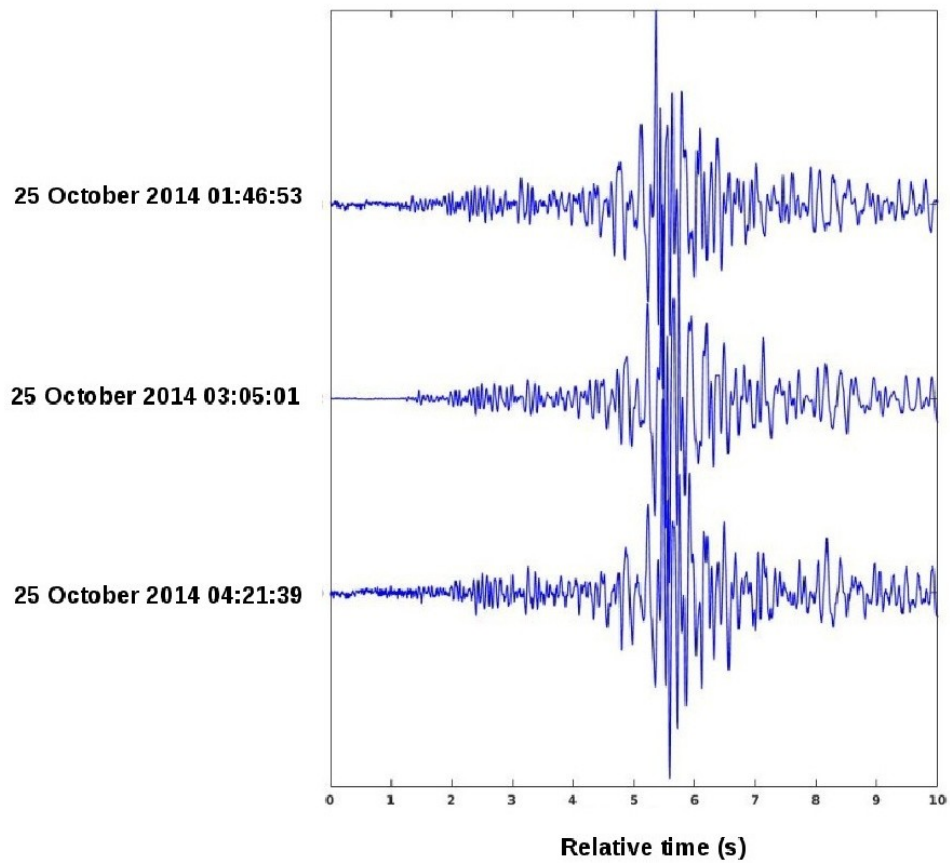
133

7

7

134

135 (b)



137

138

139

140

141

142

143

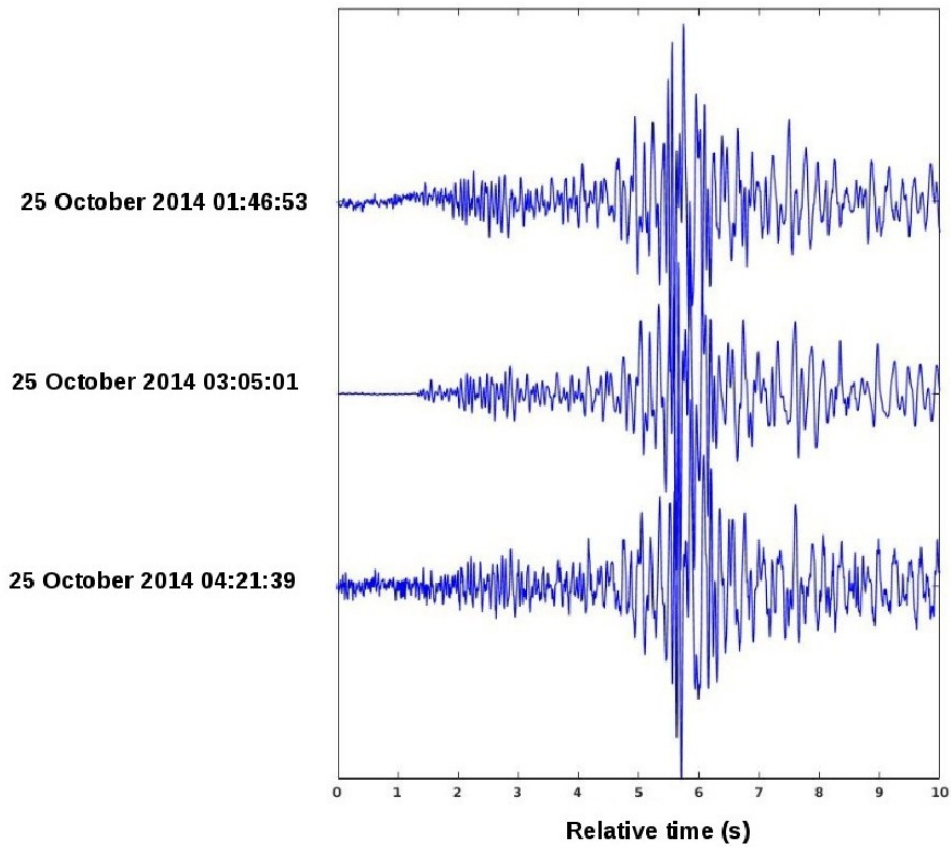
8

8

144

145 (c)

146



148

149

150 **Figure 5:** Case study 1. Seismograms from three components vertical (Figure 5a), horizontal 1 (Figure 5b) and horizontal
151 2 (Figure c) respectively corresponding to the triplet (with $cc>0.9$) recorded by the central OBS04 station of the 2014
152 network on 25th of October 2014.

153

9

9

154

155 (a)

156

157

158

159

160

161

162

163

164

165

166

167

168

169

170

171

172

173

174

175

176

177

178

179

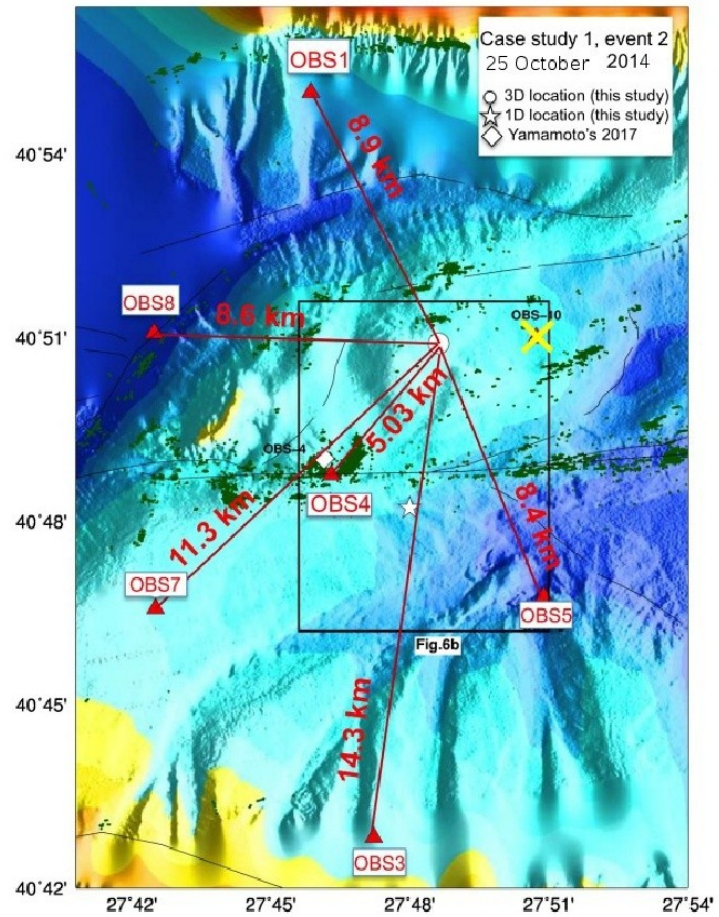
180

181

182

10

10

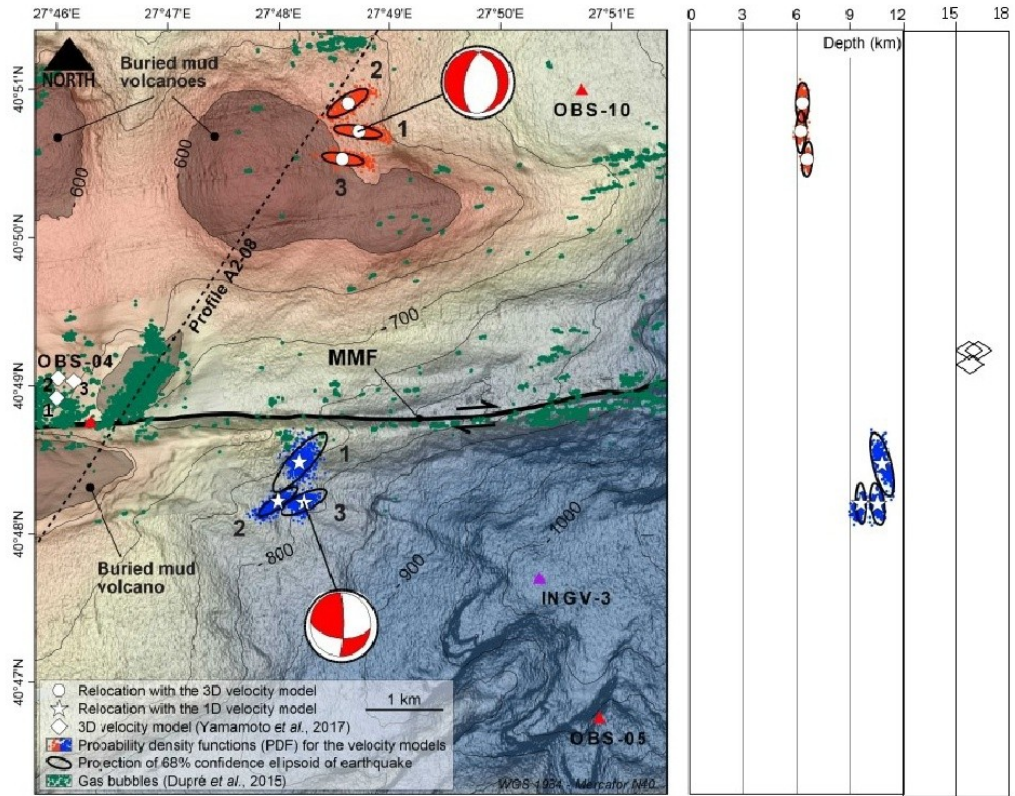


183

184 (b)

185

186



188

189

190

191

192

193

194

11

11

195 **Figure 6:** Case study 1 (cont.) (6a) Distribution of OBSs (shown by triangles) used in this study for the location of
196 earthquake 2 of case study 1 (see seismograms in Figure 5). White star, circle and diamond indicate the 1D (this study), the
197 3D (this study) and the [Yamamoto et al, 2017] locations, respectively. The distances (in kilometres) from the 3D location
198 of earthquake 2 to each OBS are indicated in red. Note that OBS10 (e.g. shown with a yellow cross) stopped working 3
199 days before the occurrence of the events of case study 2. Note that paths to OBS4 necessarily cross mud volcanoes and
200 gas-prone sediment layers. Black box corresponds to Fig. 6b. Black lines indicate the main structural features of the
201 Marmara Fault System (e.g. [Sengör et al., 2005]). Green dots correspond to gas emissions sites, after [Dupré et al,
202 2015].

203 (6b) Left panel indicates the relocated epicenters for the triplet shown in Figure 5, obtained using respectively the
204 1D (stars), the 3D (circles) velocity models of this study and the 3D velocity model by [Yamamoto et al, 2017]
205 (white diamonds). The right panel indicates the N-S cross-section with the relocated hypocenters. The probabilistic,
206 relative location uncertainties obtained by NLDiffLoc are displayed by black ellipsoids showing the projection of the
207 68% confidence ellipsoid for each earthquake with their PDF (probability density functions) indicated by blue and
208 red dots, for the 1D and 3D velocity models respectively. Red beachballs show the composite focal mechanism
209 solution calculated for the triplet events. Numbers 1 to 3 corresponds to the name of each earthquake (see Table
210 5). Line A2-08 is the 2D-high resolution seismic lines displayed in Figure 12. Green dots correspond to gas emissions
211 sites, after [Dupré et al, 2015]. Note that OBS10 (e.g. shown with a yellow cross) stopped working 3 days before the
212 occurrence of the events of case study 2. See polarities and characteristics of composite focal mechanisms of 3D locations
213 in Supplementary Information.

214

215

216

217

218

219

220

221

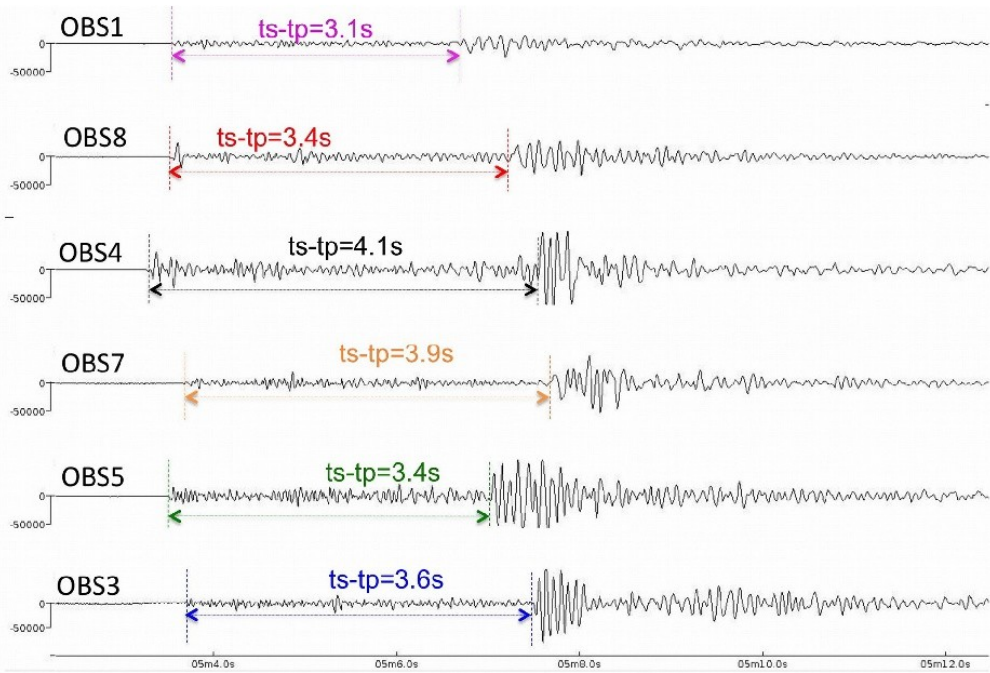
222

223

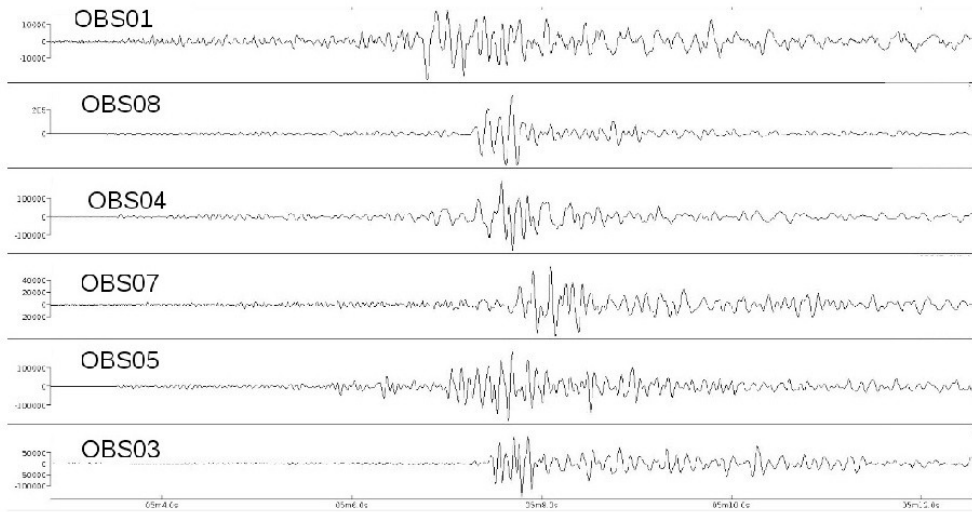
12

12

224 (a)



238 (b)



250

251

252

13

13

253 **Figure 7:** Seismograms from earthquake 2 (25th of October, 2014) of case study 1 recorded at seafloor stations 1, 8, 4, 7, 5
254 and 3 of the 2014 OBS network. Dotted lines indicate t_p and t_s arrivals at each different OBS. The upper panel displays the
255 vertical component (Figure 7a). The bottom panel is for Horizontal-1(Figure 7b).

256

257

258

259

260

261

262

263

264

265

266

267

268

269

270

271

272

273

274

275

276

277

278

279

280

281

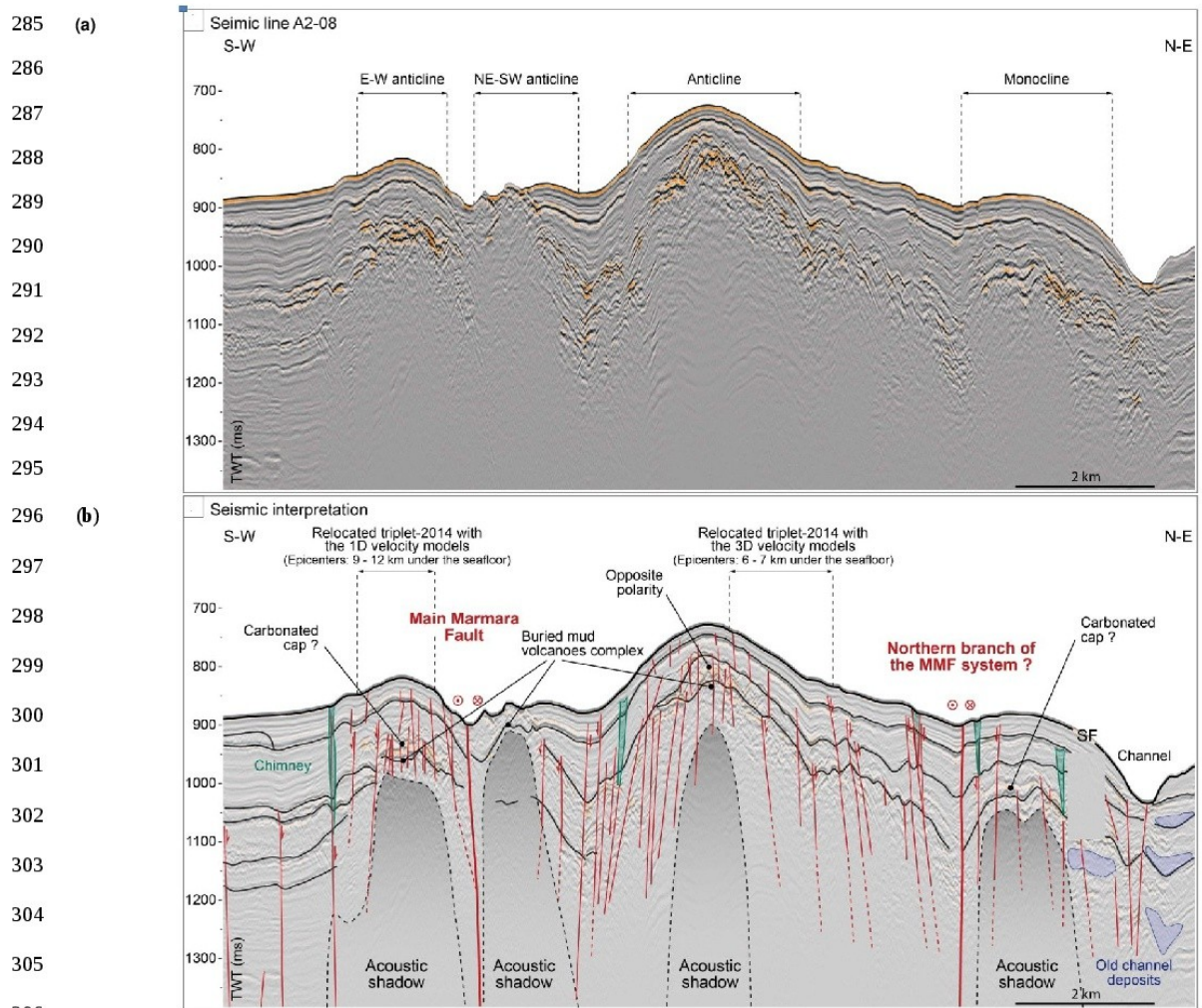
282

283

284

14

14



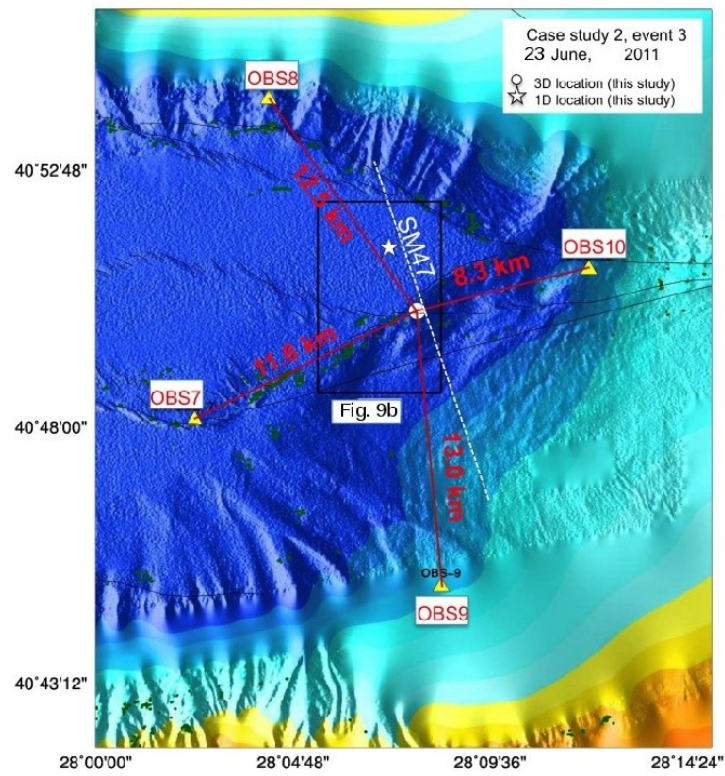
309 **Figure 8:** (a) 2D-high resolution seismic section along line A2-08 (see track line location in Figure 3) collected in
310 2009 with Piri Reis. (b) Interpretation of seismic profile A2-08 (this study).

311
312
313
314

15

15

315 (a)



317

318

319

320

321

322

323

324

325

326

327

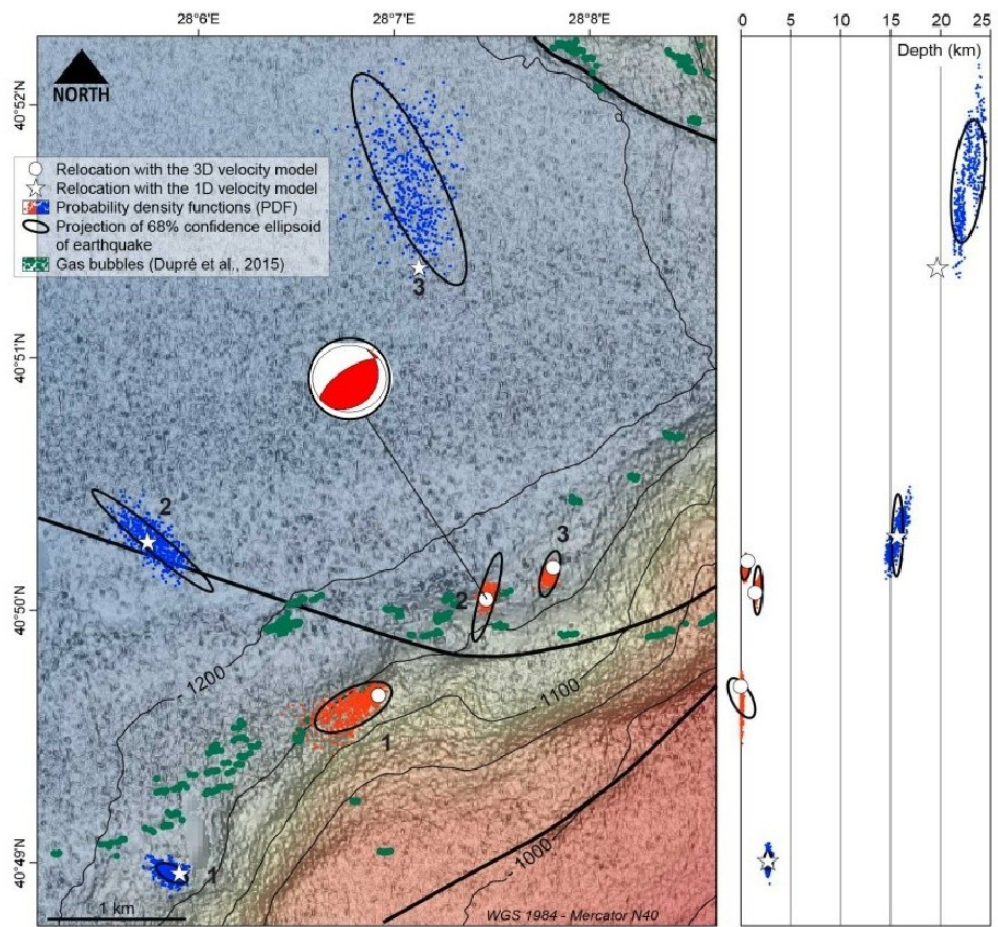
16

16

328

329

330 (b)



331

332

333

334

335

336

337

338

339

340

341

342

343

344

345

346

347

348

349

350

351

352

353

354

355

356

17

17

357

358 **Figure 9:** Case Study 2, presented for a triplet of highly correlated events ($cc > 0.8$) that occurred on the 19th of May
359 2011 and on the 23rd of June 2011. (9a) Distribution of OBSs (shown by triangles) used in this study for the location
360 of earthquake 3 of case study 2 (see seismograms in Figure 9). White star and white dot indicate the 1D (this study) and the
361 3D (this study) locations, respectively. Red lines indicate the distance of 3D location to each OBS station. Dashed white
362 line indicated the profile SM47 shot during the Seismarmara cruise in 2001 across the eastern side of the Central Basin.
363 Black box corresponds to figure Figure 8b. Black lines indicate the main structural features of the Marmara Fault Sys-
364 tem (e.g. [Sengör et al., 2005]). Green dots correspond to gas emissions sites, after [Dupré et al., 2015].
365 (9b) Left panel indicates the relocated epicenters obtained using respectively the “this study 1D” (stars) vs the 3D (cir-
366 cles) velocity models. Upper right panels indicate N-S cross-section with the relocated hypocenters. The probabilistic,
367 relative location uncertainties obtained by NLDiffLoc are displayed by black ellipsoids showing the projection of the
368 68% confidence ellipsoid for each earthquake with their PDF (probability density functions) indicated by blue and
369 red dots, for the “this study 1D” and 3D velocity models respectively. Events are numbered from 1 to 3 (see Ta-
370 ble 6). Red beachballs show the composite focal mechanism solution calculated for the triplet. Green dots correspond
371 to gas emissions sites, after [Dupré et al., 2015]. See polarities and characteristics of composite focal mechanisms of 3D
372 locations in Supplementary Information.

373

374

375

376

377

378

379

380

381

382

383

384

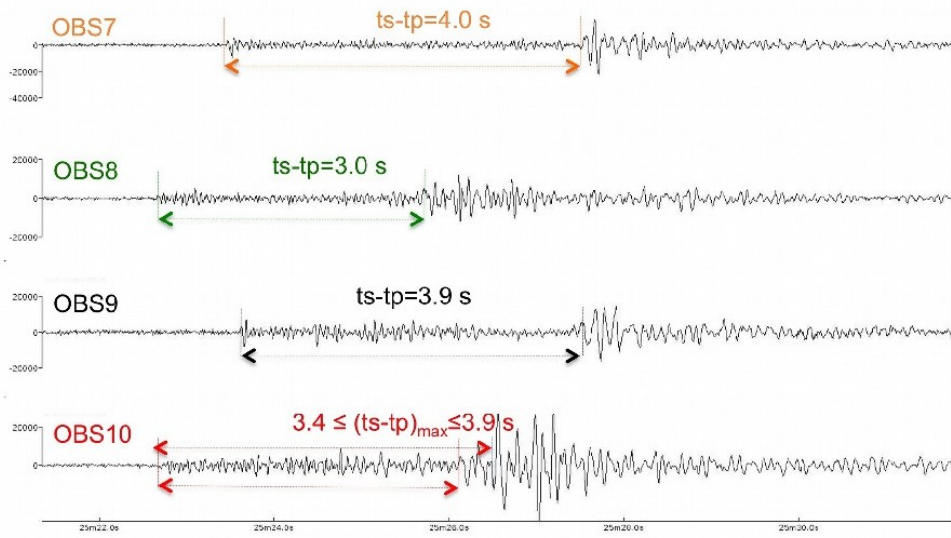
385

18

18

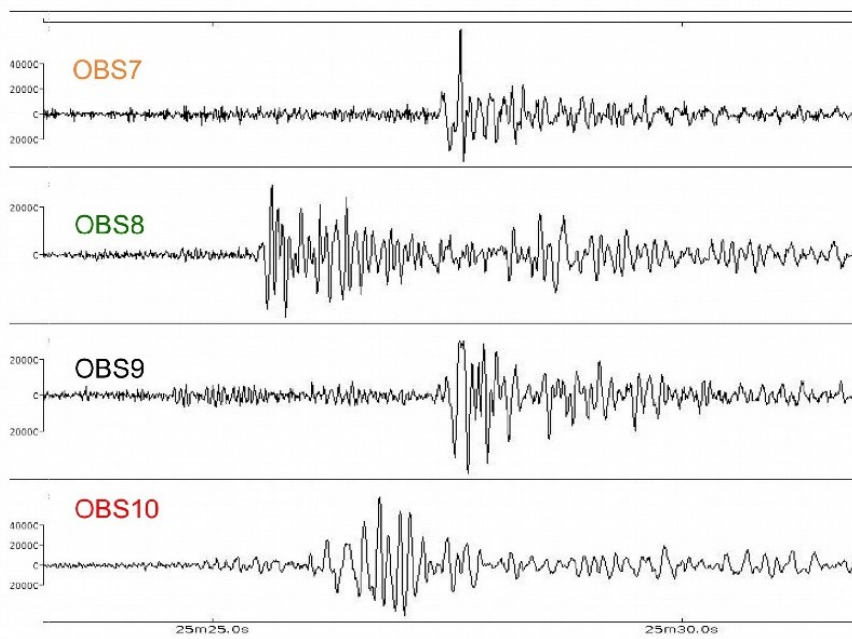
386

387 (a)



389

390 (b)



391

392

393

394

395

396

397

398

399

400

401

402

403

404

405

406

407

408

409

410

411

412

413

414

19

19

415

416 **Figure 10:** Seismograms for event 3 of case study 2, recorded at OBSs 7, 8, 9 and 10 on June 23, 2011. Horizontal arrows
417 indicate the t_s - t_p arrival at each different OBS. On OBS, a range is given for t_s - t_p . The upper panel displays the vertical com -
418 ponent (Figure 10a). The bottom panels is for Horizontal-1 component (Figure 10b).

419

420

421

422

423

424

425

426

427

428

429

430

431

432

433

434

435

436

437

438

439

440

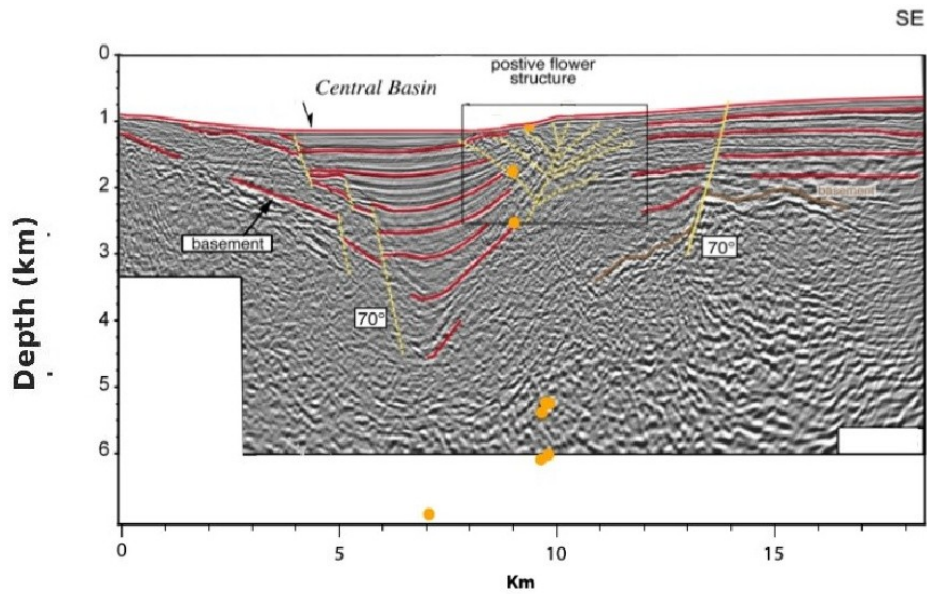
441

442

443

20

20



446 **Figure 11:** (after Figure 4, of Bécel et al, 2010): Hypocenters (orange dots) projected along the pre-stack depth
 447 migrated section (Line SM47) shot during the Seismarmara cruise in 2001 across the eastern side of the Central
 448 Basin. Line track and hypocenter locations are indicated in Figures 8 and 13. Interpretations (yellow, red and
 449 brown lines) are from Bécel et al, 2010. Note that the shallowest (at depths < 3 km) hypocenters are near or
 450 within to the positive flower structure underlined by the black box (see case study 2, Figure 9).

451

452

453

454

455

456

457

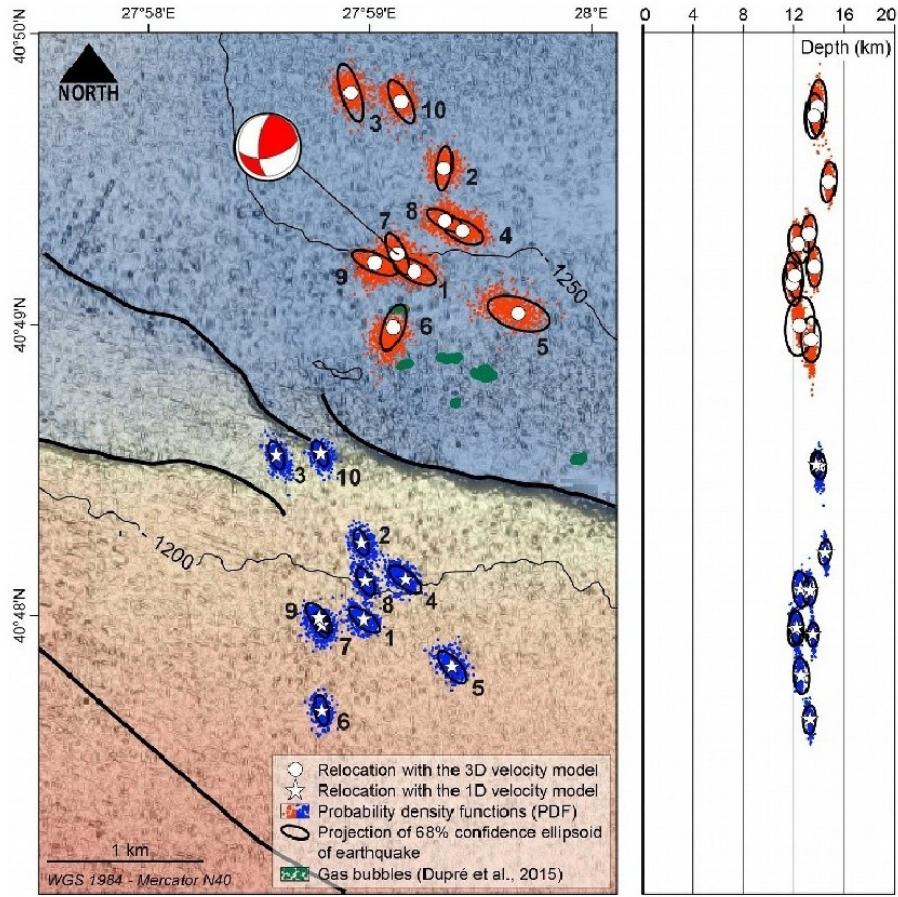
458

459

21

21

460
 461
 462
 463
 464
 465
 466
 467
 468
 469
 470
 471
 472
 473
 474
 475
 476
 477
 478
 479
 480
 481
 482
 483
 484
 485
 486
 487



22

22

488 **Figure 12:** Case study 3. Left panel indicates the relocated epicenters of the cluster of events that occurred from the
489 26th of April 2011 until the 18th of May 2011, obtained using respectively the “this study 1D” (stars) vs the 3D
490 (circles) velocity models. The right panel indicates the N-S cross-section with the relocated hypocenters. The proba-
491 bilistic, relative location uncertainties obtained by NLDiffLoc are displayed by black ellipsoids showing the projec-
492 tion of the 68% confidence ellipsoid for each earthquake with their PDF (probability density functions) indicated
493 by blue and red dots, for the “this study 1D” and 3D velocity models respectively. Red beachballs show the
494 composite focal mechanism solution calculated for the cluster events. Numbers 1 to 10 correspond to the name of
495 each earthquake (see Table 6). Green dots correspond to gas emissions sites, after [Dupré et al, 2015]. See polari-
496 ties and characteristics of composite focal mechanisms of 3D locations in Supplementary Information.

497

498

499

500

501

502

503

504

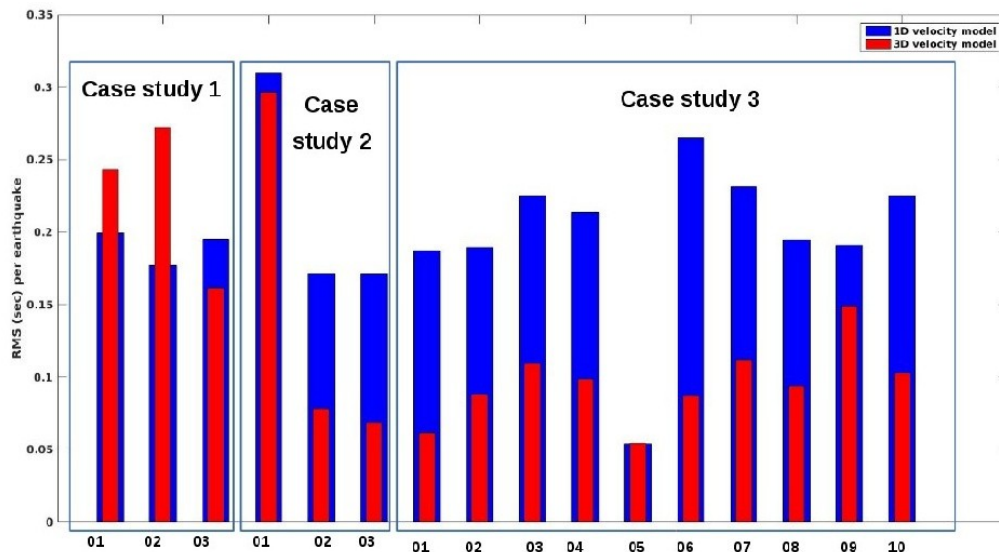
505

506

507

508

509



510 **Figure 13:** Comparison of RMS errors of absolute location (e.g. use of NonLinLoc) obtained for the case studies
 511 1 to 3, for the velocity models 1D (blue bins) and 3D (red bins) of this study. Event number for each case
 512 study is indicated (see Tables 5, 6 and 7).

513

514

515

516

517

518

519

520

521

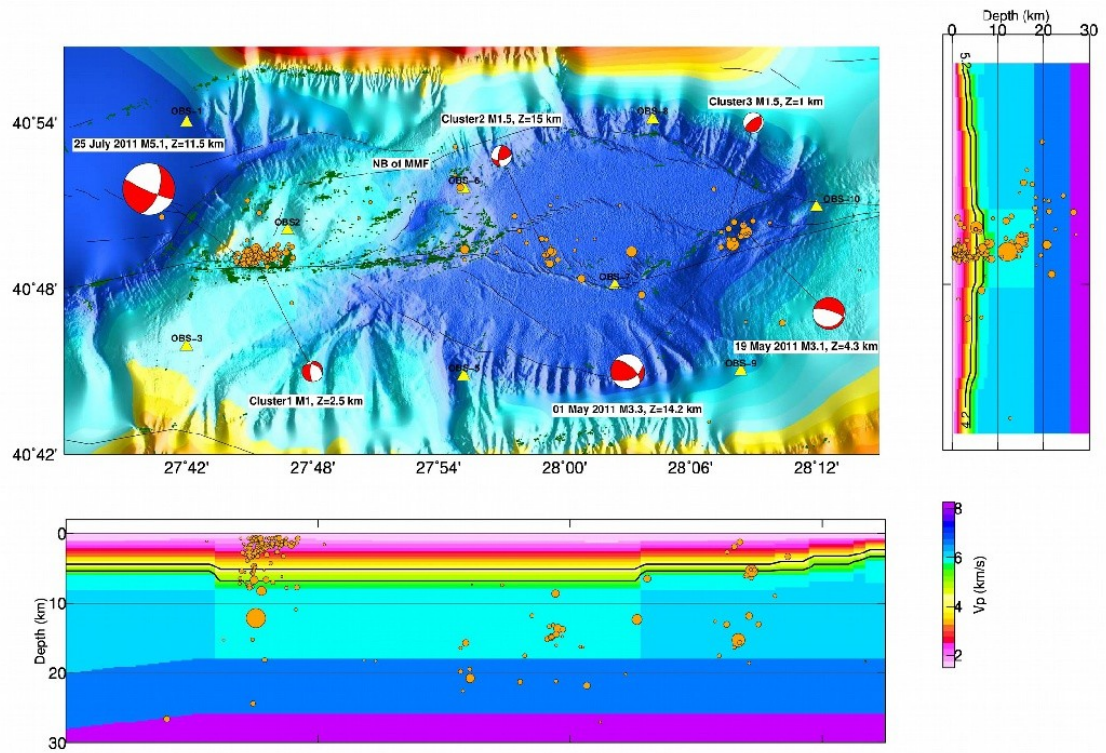
522

523

524

24

24



526

527

528

529

530

531

532

533

534

535

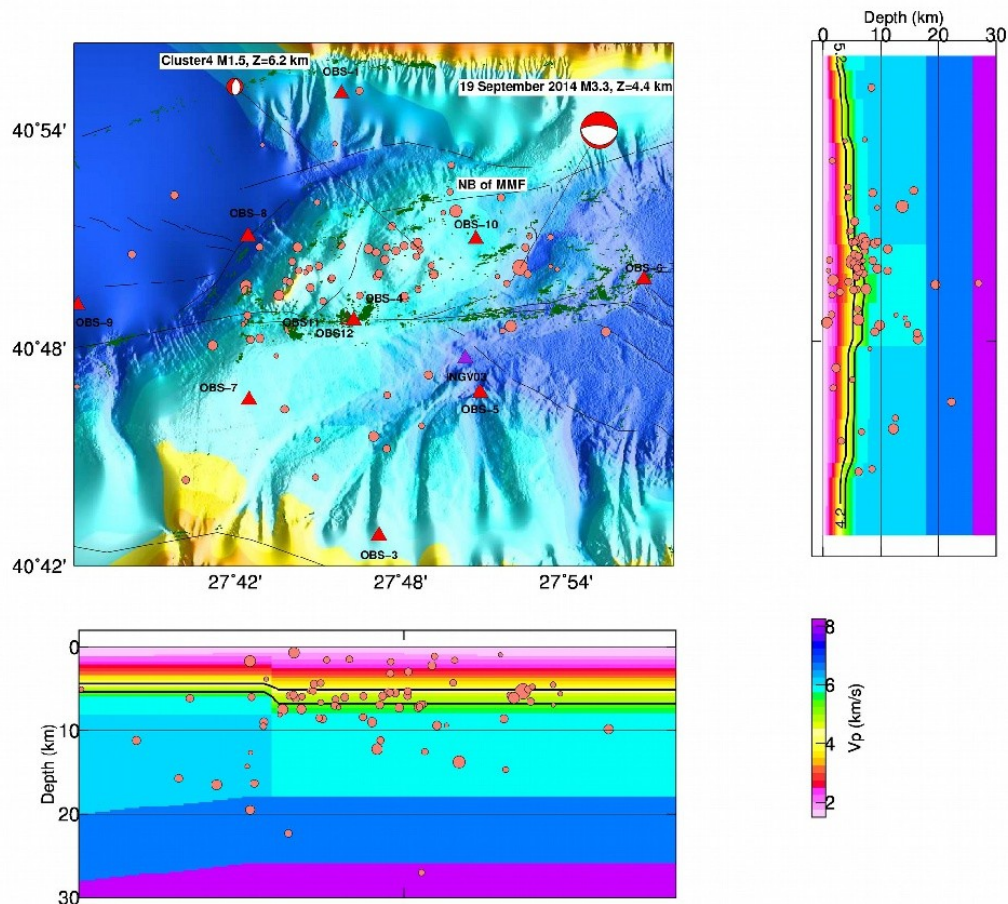
536

537

25

25

538 **Figure 14:** Upper left panel indicates the relocated epicenters (obtained using the 3D velocity model) for the 2011
539 recording period, including also the mainshock of the 25th of July and its sequence of aftershocks (e.g. 15th of
540 April until the 31st of July 2011). The lower left and upper right panels indicate E-W and N-S cross-sections of the
541 relocated hypocenters. Red beachballs show the focal mechanisms solutions, with white labels indicating the name, lo-
542 cal magnitude and depth for each case (see tables 3 and 4). Yellow triangles show the temporary OBS stations of
543 Ifremer during the 2011 recording. Green dots correspond to gas emissions sites, after [Dupré et al, 2015]. The size
544 of the orange circles is proportional to their local magnitude (e.g. $0.5 < M < 5.1$). Red line corresponds to profile
545 SM 47 (after Figure 4 of Bécel et al, 2010) and small black box to Fig. 8. Bathymetric map in upper left panel
546 is with node spacing of 10 meters (see Data and Resource section). See polarities and characteristics of composite focal
547 mechanisms of 3D locations in Supplementary Information.
548
549



559 **Figure 15:** Upper left panel indicates the relocated epicenters (obtained using the 3D velocity model) for the
 560 recording period from September 19th to November 14th, 2014. The lower left and upper right panels indicate E-
 561 W and N-S cross-sections of the relocated hypocenters. Red beachballs show the focal mechanisms solutions
 562 with white labels indicating the name, local magnitude and depth for each case (see tables 3 and 4). Red and
 563 orange (OLD-OBS) triangles show the temporary OBS stations of Ifremer during the 2014 recording, while the
 564 purple triangle show the temporary OBS station of INGV. Green dots correspond to gas emissions sites, after
 565 [Dupré et al., 2015]. The size of the salmon circles is proportional to their local magnitude (e.g. $0.5 < M < 3.3$).
 566 Bathymetric map (upper left panel) with node spacing of 10 meters (see Data and Resource section). See polarities
 567 and characteristics of composite focal mechanisms of 3D locations in Supplem entary Information.

27

27

568

569

570

571

572

573

574

575

576

577

578

579

580

581

582

583

584

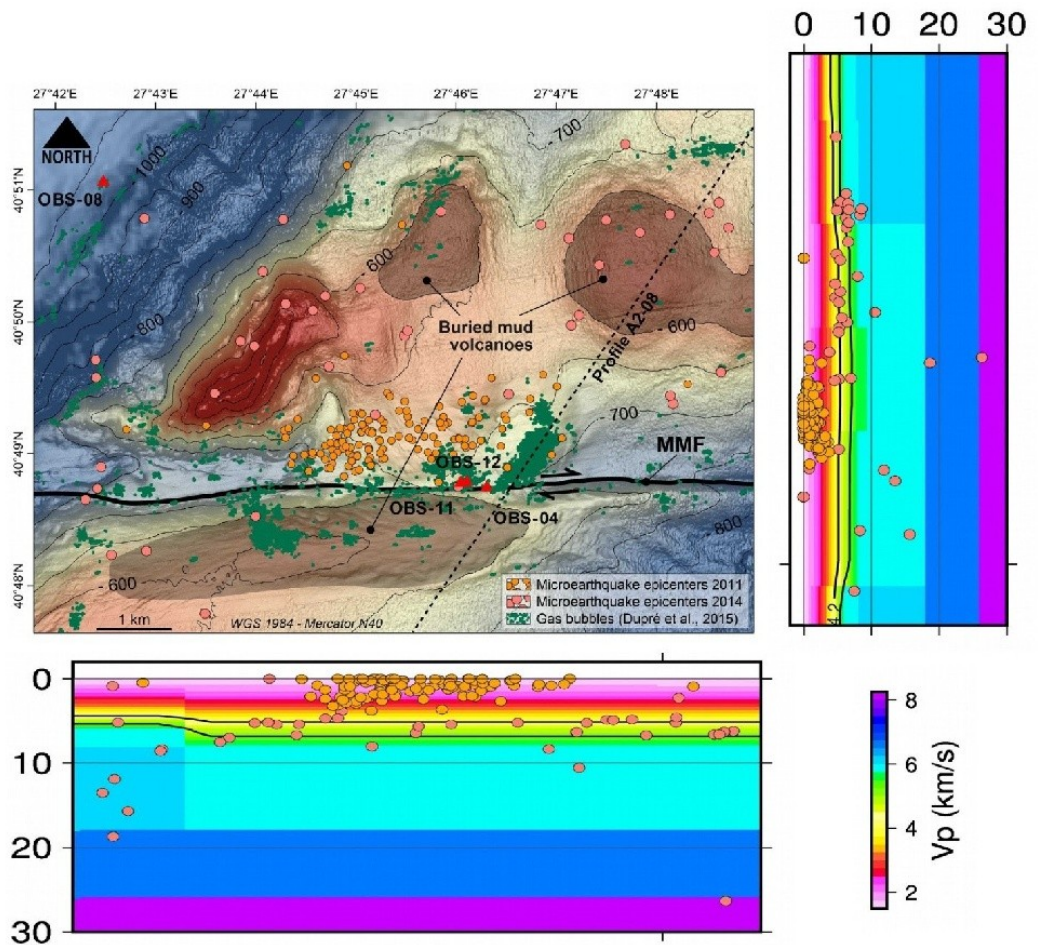
585

586

587

588

589



590 **Figure 16:** Upper left panel presents a synthesis of the relocated epicenters (using our 3D velocity model) during
591 the 2011 (orange circles) and 2014 (salmon circles) recording periods. The lower left and upper right panels indi-
592 cate E-W and N-S cross-sections of the relocated hypocenters. Red triangles show the temporary OBS stations of
593 Ifremer during the 2014 recording period. Green dots correspond to gas emissions sites, after [Dupré et al, 2015].
594 The bathymetric map in the upper left panel) of the Western High is with a node spacing of 10 meters (see Data and
595 Resource section). Black dashed line indicates seismic line A2-08 (see Figure 8).

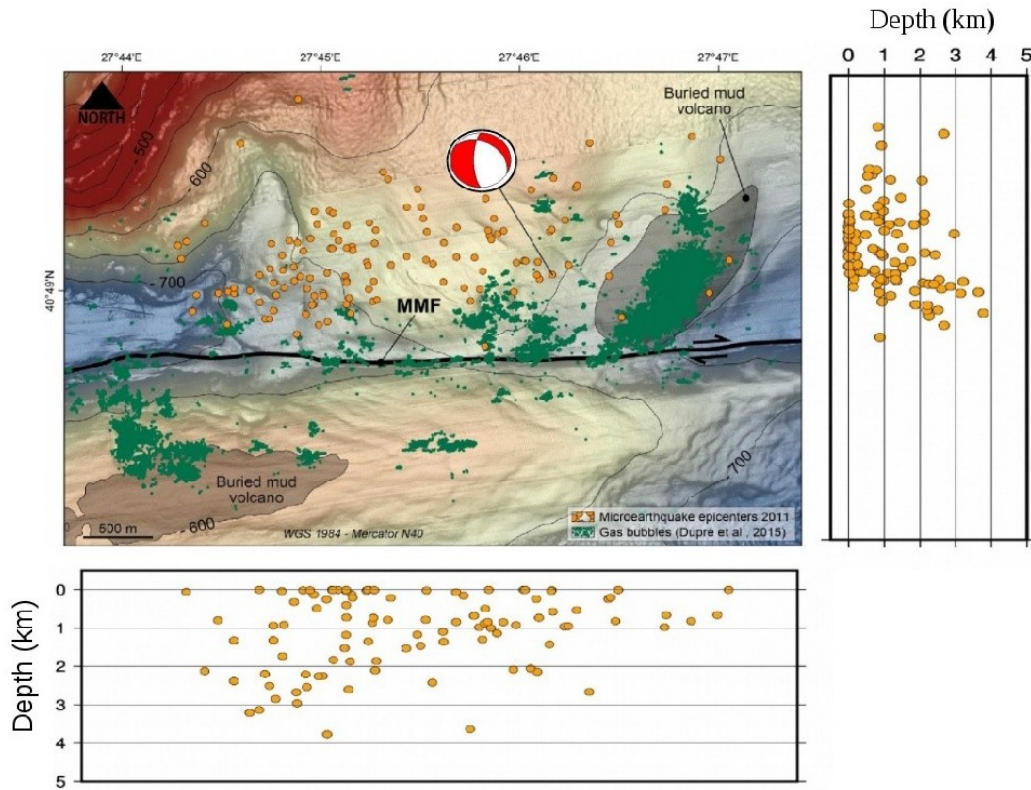
596

28

28

597

598



600 **Figure 17:** Upper left panel presents the shallower (depth < 4 km), well constrained, relocated aftershocks (using
601 our 3D velocity model) that followed the M5.1 earthquake of the 25th of July , 2011. The lower left and upper
602 right panels indicate E-W and N-S cross-sections of the relocated hypocenters. Green dots correspond to gas emis-
603 sions sites, after [Dupré et al, 2015]. Bathymetric map of upper left panel with a node spacing of 10 meters and
604 contour interval of 20 m (see Data and Resource section).

605

606

607

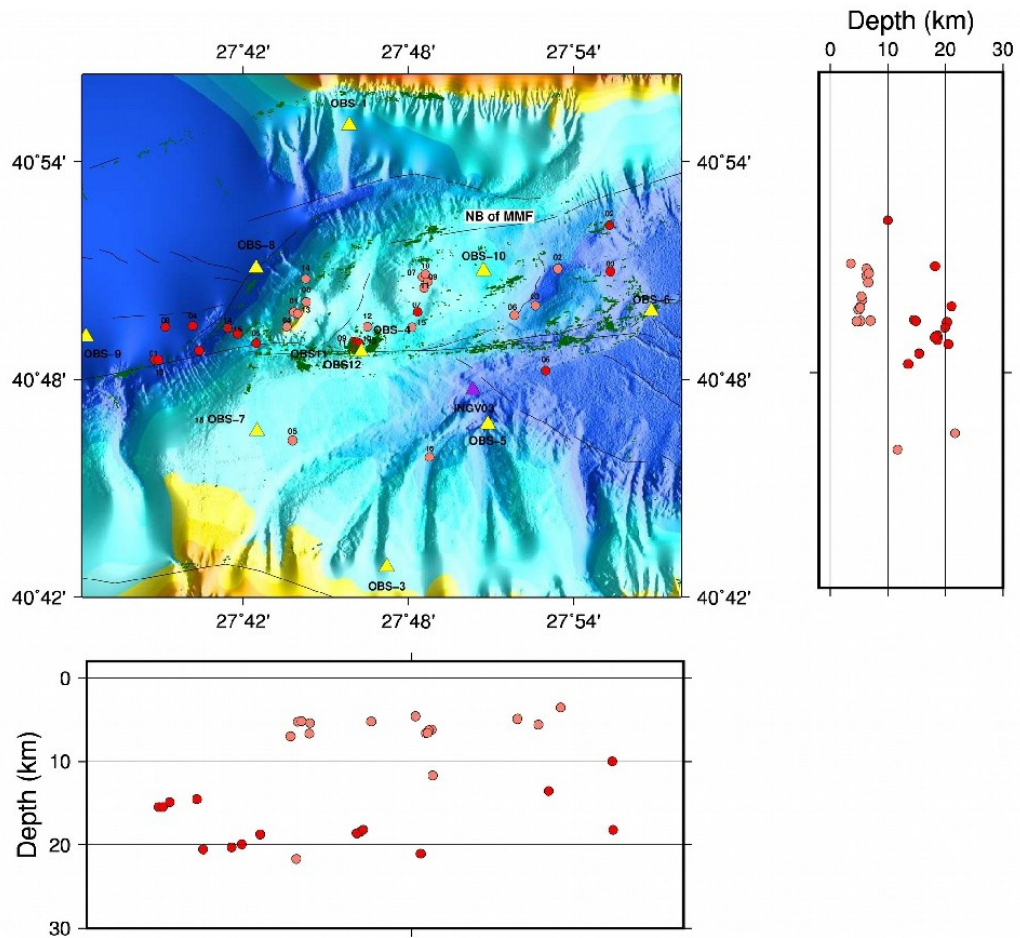
608

29

29

609

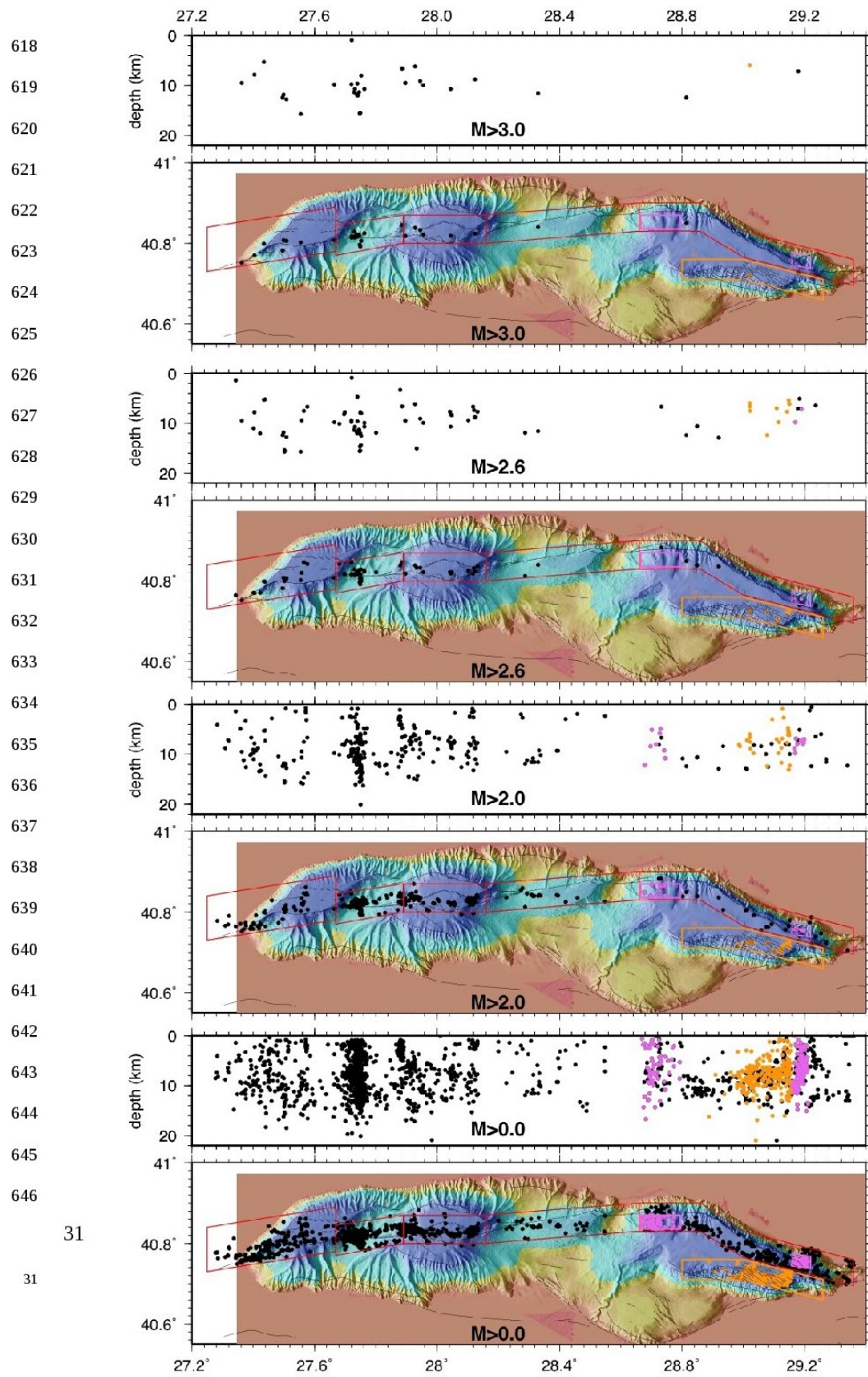
610



612 **Figure 18:** Comparison of location results for the common events, listed both in Yamamoto et al, 2017 (orange dots) and
613 in this work (red dots), that occurred during the overlapping period, from September 19, to November 14, 2014. Labels
614 (from 1 to 16) correspond to the number of each individual event listed in Table 8. Green dots correspond to gas emis-
615 sions sites, after [Dupré et al, 2015]. Bathymetric map of upper left panel with a node spacing of 10 meters and
616 contour interval of 20 m (see Data and Resource section). Black lines indicate main structural features, after [Sengör et
617 al., 2005].

30

30



647

648 **Figure 19:** Thresholded seismicity maps (between 2007 and 2012, after [Schmittbuhl *et al*, 2015]) displaying events of
649 magnitude (M_i) above 2.0 (top); 2.6 (middle) and 3.0 (bottom), respectively. The “vertical” swarms of seismicity disappear
650 for a threshold magnitude of $M_i \sim 3$.

32

32

28 **1. Catalogs of relocated events (Tables S1 to S4)**

29 **Table S1.** Catalogue of relocated events (Step 5: see main text) with statistics obtained with the NLDiffLoc, using the 1D velocity model of this study (2011 data set).

No	yy	mo	dd	hh	mm	ss	Lat	Long	Depth	Ml	Exx	Eyy	Ezz	RMS	Nph	Gap
							(°)	(°)	(km)		(km)	(km)	(km)	(sec)		(°)
1	2011	4	16	16	30	25	40.7995	28.0017	15.47	0.9	0.165	0.16	0.368	0.039	90	119
2	2011	4	20	5	4	49	40.8091	28.0051	14.82	0.6	0.08	0.075	0.155	0.046	127	107
3	2011	4	26	16	12	10	40.7998	27.9829	12.09	1	0.047	0.046	0.126	0.028	141	93
4	2011	4	29	4	58	40	40.7990	27.9446	3.74	0.8	0.049	0.056	0.081	0.076	130	78
5	2011	4	30	15	21	53	40.8112	27.9600	15.89	1.1	0.05	0.07	0.154	0.037	164	96
6	2011	5	1	8	36	17	40.8266	28.1355	13.69	3.3	0.057	0.064	0.093	0.027	187	115
7	2011	5	2	15	31	6	40.7147	28.1004	10.22	0.8	0.274	0.283	0.445	0.034	19	177
8	2011	5	4	5	3	19	40.8030	27.9136	19.28	0.7	0.143	0.326	0.771	0.072	97	78
9	2011	5	7	4	14	26	40.8042	27.9827	14.49	1.4	0.04	0.048	0.089	0.027	170	95
10	2011	5	7	17	27	50	40.8092	27.9763	14.05	2.2	0.036	0.049	0.097	0.029	182	97
11	2011	5	7	17	46	15	40.8021	27.9860	12.55	1.5	0.051	0.047	0.133	0.033	149	100
12	2011	5	9	14	0	3	40.7971	27.9895	12.6	0.9	0.046	0.05	0.134	0.035	140	98
13	2011	5	9	23	8	7	40.7946	27.9797	13.25	1.7	0.031	0.048	0.102	0.027	167	101
14	2011	5	12	14	32	44	40.7995	27.9797	13.49	1.7	0.034	0.045	0.088	0.028	176	93
15	2011	5	13	10	40	3	40.8020	27.9830	13.26	2	0.034	0.048	0.101	0.025	168	93
16	2011	5	14	15	23	24	40.7892	27.9927	8.74	0.5	0.048	0.055	0.112	0.058	124	103
17	2011	5	14	18	38	4	40.7927	27.9216	7.06	0.8	0.09	0.104	0.733	0.033	59	104
18	2011	5	15	3	39	1	40.8305	28.0294	18.48	1.1	0.273	0.209	0.372	0.076	45	111
19	2011	5	17	20	40	15	40.7999	27.9795	12.23	1.2	0.045	0.05	0.125	0.032	143	94
20	2011	5	18	3	17	0	40.8093	27.9796	13.76	1.8	0.033	0.042	0.089	0.029	180	104
21	2011	5	19	4	38	37	40.8251	28.1330	11.64	3.1	0.056	0.057	0.19	0.026	191	110
22	2011	5	19	4	44	7	40.8159	28.0985	2.71	1.1	0.061	0.045	0.129	0.075	168	95
23	2011	5	19	5	5	38	40.8377	28.0958	15.65	0.5	0.124	0.124	0.586	0.014	86	145
24	2011	5	22	22	39	26	40.8229	28.1370	11.12	2.3	0.067	0.061	0.198	0.024	174	106
25	2011	5	25	23	43	19	40.7918	27.9235	18.56	0.9	0.252	0.426	0.426	0.045	37	110
26	2011	5	29	7	24	20	40.8265	28.1468	13.62	1.1	0.066	0.076	0.106	0.022	170	108
27	2011	5	30	19	53	12	40.7872	27.9203	16.84	1.4	0.201	0.344	0.369	0.033	30	84
28	2011	6	9	20	43	27	40.8179	28.1227	10.65	1.8	0.039	0.043	0.123	0.021	185	96
29	2011	6	9	20	53	41	40.8194	28.1125	12.74	1.1	0.045	0.063	0.159	0.018	142	95
30	2011	6	10	3	54	24	40.8336	28.0822	15.22	0.6	0.12	0.13	0.281	0.023	65	135
31	2011	6	10	4	28	29	40.8202	28.1196	10.58	1.9	0.037	0.043	0.131	0.02	176	97
32	2011	6	10	5	52	19	40.7763	28.0507	4.94	1.4	0.127	0.147	0.115	0.139	61	109
33	2011	6	10	17	43	13	40.8205	28.1181	14.38	1.4	0.052	0.066	0.108	0.021	169	102
34	2011	6	12	6	9	29	40.8181	27.9563	18.93	0.9	0.081	0.105	0.29	0.044	168	101
35	2011	6	14	5	37	33	40.8229	28.1316	10.82	1.5	0.053	0.05	0.166	0.022	181	105
36	2011	6	23	20	25	11	40.8558	28.1189	19.64	0.9	0.181	0.324	0.87	0.018	71	137
37	2011	6	24	12	37	45	40.8439	27.9134	16.17	1.2	0.19	0.249	0.542	0.027	29	146
38	2011	6	24	12	58	48	40.8557	27.9150	19.48	1.7	0.192	0.292	0.807	0.014	22	152
39	2011	6	24	13	20	26	40.8369	27.9171	15.7	1	0.105	0.188	0.393	0.041	56	98
40	2011	7	2	3	30	53	40.8256	27.8485	12.45	1	0.198	0.298	0.894	0.021	19	143
41	2011	7	6	12	45	53	40.8254	27.9805	19.28	0.7	0.071	0.071	0.153	0.029	130	115
42	2011	7	7	9	42	35	40.8021	28.0094	22.49	0.7	0.093	0.075	0.387	0.033	109	95
43	2011	7	10	10	11	39	40.7531	28.1297	10.56	0.6	0.184	0.321	0.564	0.058	59	136
44	2011	7	14	9	15	41	40.7771	28.0119	18.43	1.6	0.124	0.103	0.335	0.036	100	118
45	2011	7	22	15	16	12	40.8062	28.0953	15.28	1.1	0.07	0.09	0.145	0.032	148	87
46	2011	7	23	5	14	59	40.8050	28.0950	12.68	1.5	0.087	0.102	0.475	0.029	126	91

31 Where: yy, mo, dd, hh, mm,ss, lat, lon stand for year, month, day, hour, minute, second, latitude, longitude
32 Exx, eyy, ezz, Nph for horizontal1, horizontal2, vertical location errors, respectively, and number of phases used
33 **Table S2.** Catalogue of relocated events (Step 5: see main text) with statistics obtained with the NLDiffLoc, using the
34 3D velocity model of this study after applying station corrections (2011 data set).
35

No	yy	mo	dd	hh	mm	ss	Lat	Long	Depth	MI	Exx	Eyy	Ezz	RMS	Nphs	Gap
							(°)	(°)	(km)		(km)	(km)	(km)	(sec)		(°)
1	2011	4	16	16	30	25	40.7995	28.0017	15.47	0.9	0.165	0.16	0.368	0.039	90	119
2	2011	4	20	5	4	49	40.8091	28.0051	14.82	0.6	0.08	0.075	0.155	0.046	127	107
3	2011	4	26	16	12	10	40.7998	27.9829	12.09	1	0.047	0.046	0.126	0.028	141	93
4	2011	4	29	4	58	40	40.7990	27.9446	3.74	0.8	0.049	0.056	0.081	0.076	130	78
5	2011	4	30	15	21	53	40.8112	27.9600	15.89	1.1	0.05	0.07	0.154	0.037	164	96
6	2011	5	1	8	36	17	40.8266	28.1355	13.69	3.3	0.057	0.064	0.093	0.027	187	115
7	2011	5	2	15	31	6	40.7147	28.1004	10.22	0.8	0.274	0.283	0.445	0.034	19	177
8	2011	5	4	5	3	19	40.8030	27.9136	19.28	0.7	0.143	0.326	0.771	0.072	97	78
9	2011	5	7	4	14	26	40.8042	27.9827	14.49	1.4	0.04	0.048	0.089	0.027	170	95
10	2011	5	7	17	27	50	40.8092	27.9763	14.05	2.2	0.036	0.049	0.097	0.029	182	97
11	2011	5	7	17	46	15	40.8021	27.9860	12.55	1.5	0.051	0.047	0.133	0.033	149	100
12	2011	5	9	14	0	3	40.7971	27.9895	12.6	0.9	0.046	0.05	0.134	0.035	140	98
13	2011	5	9	23	8	7	40.7946	27.9797	13.25	1.7	0.031	0.048	0.102	0.027	167	101
14	2011	5	12	14	32	44	40.7995	27.9797	13.49	1.7	0.034	0.045	0.088	0.028	176	93
15	2011	5	13	10	40	3	40.8020	27.9830	13.26	2	0.034	0.048	0.101	0.025	168	93
16	2011	5	14	15	23	24	40.7892	27.9927	8.74	0.5	0.048	0.055	0.112	0.058	124	103
17	2011	5	14	18	38	4	40.7927	27.9216	7.06	0.8	0.09	0.104	0.733	0.033	59	104
18	2011	5	15	3	39	1	40.8305	28.0294	18.48	1.1	0.273	0.209	0.372	0.076	45	111
19	2011	5	17	20	40	15	40.7999	27.9795	12.23	1.2	0.045	0.05	0.125	0.032	143	94
20	2011	5	18	3	17	0	40.8093	27.9796	13.76	1.8	0.033	0.042	0.089	0.029	180	104
21	2011	5	19	4	38	37	40.8251	28.1330	11.64	3.1	0.056	0.057	0.19	0.026	191	110
22	2011	5	19	4	44	7	40.8159	28.0985	2.71	1.1	0.061	0.045	0.129	0.075	168	95
23	2011	5	19	5	5	38	40.8377	28.0958	15.65	0.5	0.124	0.124	0.586	0.014	86	145
24	2011	5	22	22	39	26	40.8229	28.1370	11.12	2.3	0.067	0.061	0.198	0.024	174	106
25	2011	5	25	23	43	19	40.7918	27.9235	18.56	0.9	0.252	0.426	0.426	0.045	37	110
26	2011	5	29	7	24	20	40.8265	28.1468	13.62	1.1	0.066	0.076	0.106	0.022	170	108
27	2011	5	30	19	53	12	40.7872	27.9203	16.84	1.4	0.201	0.344	0.369	0.033	30	84
28	2011	6	9	20	43	27	40.8179	28.1227	10.65	1.8	0.039	0.043	0.123	0.021	185	96
29	2011	6	9	20	53	41	40.8194	28.1125	12.74	1.1	0.045	0.063	0.159	0.018	142	95
30	2011	6	10	3	54	24	40.8336	28.0822	15.22	0.6	0.12	0.13	0.281	0.023	65	135
31	2011	6	10	4	28	29	40.8202	28.1196	10.58	1.9	0.037	0.043	0.131	0.02	176	97
32	2011	6	10	5	52	19	40.7763	28.0507	4.94	1.4	0.127	0.147	0.115	0.139	61	109
33	2011	6	10	17	43	13	40.8205	28.1181	14.38	1.4	0.052	0.066	0.108	0.021	169	102
34	2011	6	12	6	9	29	40.8181	27.9563	18.93	0.9	0.081	0.105	0.29	0.044	168	101
35	2011	6	14	5	37	33	40.8229	28.1316	10.82	1.5	0.053	0.05	0.166	0.022	181	105
36	2011	6	23	20	25	11	40.8558	28.1189	19.64	0.9	0.181	0.324	0.87	0.018	71	137
37	2011	6	24	12	37	45	40.8439	27.9134	16.17	1.2	0.19	0.249	0.542	0.027	29	146
38	2011	6	24	12	58	48	40.8557	27.9150	19.48	1.7	0.192	0.292	0.807	0.014	22	152
39	2011	6	24	13	20	26	40.8369	27.9171	15.7	1	0.105	0.188	0.393	0.041	56	98
40	2011	7	2	3	30	53	40.8256	27.8485	12.45	1	0.198	0.298	0.894	0.021	19	143
41	2011	7	6	12	45	53	40.8254	27.9805	19.28	0.7	0.071	0.071	0.153	0.029	130	115
42	2011	7	7	9	42	35	40.8021	28.0094	22.49	0.7	0.093	0.075	0.387	0.033	109	95
43	2011	7	10	10	11	39	40.7531	28.1297	10.56	0.6	0.184	0.321	0.564	0.058	59	136
44	2011	7	14	9	15	41	40.7771	28.0119	18.43	1.6	0.124	0.103	0.335	0.036	100	118
45	2011	7	22	15	16	12	40.8062	28.0953	15.28	1.1	0.07	0.09	0.145	0.032	148	87
46	2011	7	23	5	14	59	40.8050	28.0950	12.68	1.5	0.087	0.102	0.475	0.029	126	91

36 Where: yy, mo, dd, hh, mm,ss, lat, lon stand for year, month, day, hour, minute, second, latitude, longitude
37 Exx, eyy, ezz, Nph for horizontal1, horizontal2, vertical location errors, respectively, and number of phases used

38 **Table S3.** Catalogue of relocated events (Step 5: see main text) with statistics obtained with the NLDiffLoc, using the
 40 1D velocity model of this study (2014 data set).

No	yy	mo	dd	hh	mm	ss	Lat (°)	Long (°)	Depth (km)	Ml	Exx (km)	Eyy (km)	Ezz (km)	RMS (sec)	Nph	Gap (°)
1	2014	9	21	4	35	29	40.8279	27.8751	3.7	1.7				0.081	42	133
2	2014	9	23	4	15	39	40.8054	27.7898	10.0	1.8	0.091	0.063	0.148	0.044	147	86
3	2014	9	23	4	43	18	40.7996	27.7948	11.4	1.7	0.148	0.531	0.646	0.02	97	90
4	2014	9	23	5	6	21	40.8067	27.7975	9.5	2	0.07	0.038	0.086	0.015	124	68
5	2014	9	23	5	34	36	40.8055	27.7925	10.2	1.9	0.088	0.051	0.24	0.043	141	73
6	2014	9	25	6	54	60	40.8000	27.7356	7.9	1.7	0.129	0.151	0.477	0.026	39	167
7	2014	9	26	6	2	54	40.7888	27.7165	9.4	1.7	0.2	0.301	0.229	0.04	126	99
8	2014	9	27	8	50	14	40.8107	27.9007	3.3	1	0.212	0.22	0.515	0.05	21	174
9	2014	9	30	12	34	16	40.8169	27.7222	4.7	1.7	0.052	0.045	0.07	0.025	72	139
10	2014	10	1	14	44	50	40.8325	27.8917	3.9	1.3	0.152	0.208	0.277	0.074	31	152
11	2014	10	3	11	19	24	40.8628	27.8552	10.1	1.3	0.265	0.531	0.841	0.124	38	155
12	2014	10	3	21	40	19	40.7219	27.7818	25.4	1.7	0.297	0.401	0.625	0.111	90	132
13	2014	10	4	11	58	35	40.8360	27.7524	3.0	2.2	0.063	0.122	0.192	0.028	84	136
14	2014	10	4	17	31	45	40.8395	27.7928	4.5	1.8	0.16	0.314	0.715	0.022	62	175
15	2014	10	5	14	48	4	40.8130	27.7243	3.6	1.6	0.167	0.225	0.042	0.009	68	114
16	2014	10	6	11	4	57	40.8121	27.7676	6.5	1.7	0.672	0.408	0.391	0.002	63	125
17	2014	10	8	3	11	44	40.7878	27.6762	10.4	1.5	0.423	0.182	0.464	0.032	46	119
18	2014	10	11	6	42	58	40.7227	27.7705	10.7	2.3	0.183	0.429	0.766	0.059	49	178
19	2014	10	11	12	7	0	40.7394	27.8128	0.0	1.6	0.328	0.104	0.116	0.185	47	146
20	2014	10	12	4	58	26	40.8390	27.7662	3.5	1.7	0.07	0.054	0.125	0.047	125	140
21	2014	10	12	22	8	19	40.8349	27.7715	13.9	1.5	0.7	0.151	0.553	0.009	43	138
22	2014	10	17	8	44	29	40.7140	27.7370	5.1	1.5	0.185	0.332	0.349	0.054	40	174
23	2014	10	18	5	25	50	40.8329	27.7483	17.2	1	0.715	0.594	0.395	0.009	24	116
24	2014	10	18	10	17	42	40.8093	27.8204	13.1	1.9	0.137	0.08	0.322	0.034	70	151
25	2014	10	19	23	49	33	40.8230	27.7435	11.5	1.7	0.569	0.465	0.6	0.003	35	169
26	2014	10	20	3	48	37	40.8145	27.7890	6.9	1.5	0.054	0.08	0.116	0.038	132	81
27	2014	10	22	6	7	16	40.8151	27.8222	12.4	1.4	0.319	0.739	0.555	0.028	15	180
28	2014	10	22	17	11	35	40.7576	27.8581	5.1	2.4	1.083	0.199	0.629	0.053	54	154
29	2014	10	23	0	9	42	40.7515	27.6776	12.4	2.2	0.352	0.635	0.603	0.044	39	134
30	2014	10	23	16	29	40	40.7483	27.8410	4.2	1.8	0.807	0.536	0.735	0.105	36	176
31	2014	10	25	1	46	52	40.8080	27.8032	10.8	1.5	0.094	0.128	0.246	0.032	83	92
32	2014	10	25	3	5	1	40.8036	27.7999	9.6	1.9	0.096	0.07	0.147	0.038	136	112
33	2014	10	25	4	21	39	40.8035	27.8039	10.5	1.5	0.08	0.061	0.165	0.015	92	126
34	2014	10	25	15	9	6	40.8165	27.6666	19.4	1.7	0.398	1.081	0.403	0.017	12	128
35	2014	10	26	3	21	34	40.8042	27.7308	7.3	1.6	0.07	0.059	0.192	0.051	93	120
36	2014	10	26	7	41	51	40.8046	27.7344	15.5	2	0.175	0.148	0.657	0.006	56	134
37	2014	10	26	19	24	37	40.8066	27.8076	10.5	1.9	0.131	0.054	0.137	0.01	83	152
38	2014	10	27	21	22	10	40.7717	27.7855	0.0	1.6	0.024	0.026	0.237	0.027	90	93
39	2014	11	2	22	1	31	40.8868	27.6170	5.2	1.7	0.693	0.19	0.559	0.001	17	168
40	2014	11	5	5	56	5	40.7965	27.8383	5.1	1.4	0.221	0.138	0.641	0.025	77	140
41	2014	11	5	23	31	48	40.7292	27.9154	6.5	1.4	0.833	0.594	0.714	0.001	20	119
42	2014	11	7	0	38	38	40.8883	27.7666	14.3	1	0.294	0.257	0.684	0.024	45	130
43	2014	11	10	6	17	38	40.7930	27.8438	0.2	1.8	0.118	0.079	0.113	0.089	47	135
44	2014	11	13	4	26	15	40.8136	27.7386	4.9	1.5	0.081	0.053	0.129	0.037	93	71
45	2014	11	13	15	51	32	40.7787	27.7423	19.7	1.7	0.564	0.233	0.609	0.014	70	115

41
 42
 43
 44
 45

Where: yy, mo, dd, hh, mm,ss, lat, lon stand for year, month, day, hour, minute, second, latitude, longitude
 Exx, eyy, ezz, Nph for horizontal1, horizontal2, vertical location errors, respectively, and number of phases used

46 **Table S4.** Catalogue of relocated events (Step 5: see main text) with statistics obtained with the NLDiffLoc, using the
 48 3D velocity model of this study after applying station corrections (2014 data set).

No	yy	mo	dd	hh	mm	ss	Lat	Long	Depth	Ml	Exx	Eyy	Ezz	RMS	Nph	Gap
							(°)	(°)	(km)		(km)	(km)	(km)	(sec)		(°)
1	2014	9	21	4	35	28	40.8462	27.8754	4.16	1.7	0.046	0.064	0.067	0.05	57	156
2	2014	9	23	4	15	40	40.8439	27.7854	6.33	1.8	0.218	0.085	0.113	0.059	116	101
3	2014	9	23	4	43	18	40.8469	27.8022	5.22	1.7	1.178	0.842	0.584	0.094	68	153
4	2014	9	23	5	34	36	40.8405	27.7905	4.89	2	0.055	0.032	0.138	0.035	113	87
5	2014	9	25	6	54	60	40.8376	27.7507	8.01	1.9	0.074	0.061	0.133	0.02	104	154
6	2014	9	26	6	2	55	40.8309	27.7308	5.25	1.7	0.076	0.041	0.132	0.04	159	76
7	2014	9	27	8	50	14	40.8361	27.8948	4.71	1.7	0.052	0.062	0.134	0.048	56	149
8	2014	9	30	12	34	16	40.8397	27.7345	5.42	1	0.226	0.076	0.319	0.021	143	84
9	2014	10	1	14	44	49	40.8509	27.8905	3.55	1.7	0.043	0.141	0.136	0.057	53	154
10	2014	10	3	11	19	25	40.8514	27.8779	3.88	1.3	0.046	0.077	0.086	0.024	48	163
11	2014	10	3	21	40	22	40.8340	27.8769	5.59	1.3	0.054	0.057	0.116	0.016	50	140
12	2014	10	4	11	58	35	40.8243	27.7265	7	1.7	0.39	0.42	0.446	0.006	111	130
13	2014	10	4	17	31	44	40.8558	27.7948	4.83	2.2	0.187	0.139	0.686	0.004	71	151
14	2014	10	5	14	48	4	40.8150	27.7076	5.21	1.8	0.057	0.026	0.081	0.002	77	173
15	2014	10	6	11	4	58	40.8277	27.7455	3.83	1.6	0.68	0.683	0.582	0.011	53	174
16	2014	10	8	3	11	44	40.8216	27.7532	0.92	1.7	0.05	0.02	0.104	0.021	83	102
17	2014	10	11	6	42	59	40.7594	27.7838	11.43	1.5	0.445	0.316	0.809	0.083	28	161
18	2014	10	11	12	7	1	40.7538	27.7917	2.44	2.3	0.578	0.535	0.691	0.088	21	123
19	2014	10	12	4	45	29	40.8109	27.7050	13.52	1.6	0.241	0.075	0.439	0.046	93	169
20	2014	10	12	22	8	19	40.8669	27.7496	3.47	1.7	0.167	0.063	0.48	0.002	72	132
21	2014	10	17	8	44	30	40.7406	27.7486	7.91	1.5	0.222	0.236	0.464	0.028	25	143
22	2014	10	17	19	52	53	40.8295	27.8642	4.9	1.5	0.052	0.057	0.125	0.056	72	121
23	2014	10	18	5	25	52	40.8932	27.7166	2.87	1	0.626	0.4	0.548	0.005	57	146
24	2014	10	18	10	17	43	40.8471	27.8087	6.61	1.9	0.102	0.094	0.247	0.042	72	101
25	2014	10	19	23	49	32	40.8230	27.8027	2.27	1.7	0.176	0.435	0.564	0.005	63	163
26	2014	10	20	3	48	37	40.8462	27.7916	4.91	1.5	0.063	0.051	0.062	0.064	108	103
27	2014	10	22	6	7	16	40.8717	27.8299	3.61	1.4	0.432	0.124	1.165	0.047	31	168
28	2014	10	22	17	11	36	40.8101	27.8667	5.14	2.4	0.79	0.817	0.31	0.024	17	98
29	2014	10	23	0	9	43	40.8012	27.6865	15.73	2.2	0.565	0.928	1.305	0.048	9	180
30	2014	10	23	16	29	41	40.8430	27.6378	10.08	1.8	0.678	0.095	0.175	0.004	106	114
31	2014	10	25	1	46	53	40.8452	27.8120	6.21	1.5	0.154	0.044	0.131	0.02	73	166
32	2014	10	25	3	5	1	40.8484	27.8104	6.29	1.9	0.132	0.094	0.107	0.027	88	168
33	2014	10	25	4	21	39	40.8421	27.8096	6.59	1.5	0.136	0.045	0.095	0.02	75	175
34	2014	10	25	15	9	8	40.7394	27.6703	5.68	1.7	0.46	1.457	1.625	0.12	10	125
35	2014	10	26	3	21	34	40.8303	27.7331	5.19	1.6	0.034	0.021	0.034	0.02	125	113
36	2014	10	26	7	41	52	40.8463	27.7379	6.68	2	0.229	0.656	0.248	0.034	91	108
37	2014	10	26	19	24	37	40.8446	27.7972	6.7	1.9	0.069	0.054	0.173	0.013	105	149
38	2014	10	27	21	20	29	40.8263	27.7068	18.68	1.6	0.537	0.362	1.326	0.002	92	162
39	2014	11	2	22	1	31	40.8702	27.6634	14.65	1.7	1.539	0.716	0.702	0.001	53	156
40	2014	11	5	5	56	4	40.8378	27.8186	0.53	1.4	0.076	0.065	0.176	0.027	84	163
41	2014	11	5	23	31	50	40.7643	27.8128	11.69	1.4	0.885	0.578	0.981	0.004	9	112
42	2014	11	7	0	38	39	40.8938	27.7604	6.31	1	0.312	0.212	0.514	0.003	15	123
43	2014	11	10	6	17	38	40.7877	27.8170	1.31	1.8	0.632	0.623	0.31	0.014	14	130
44	2014	11	13	4	26	15	40.8366	27.7449	4.68	1.5	0.079	0.026	0.086	0.027	109	98
45	2014	11	13	15	51	33	40.8343	27.7871	5.23	1.7	0.188	0.101	0.89	0.015	78	134

49
 50
 51
 52
 53

Where: yy, mo, dd, hh, mm,ss, lat, lon stand for year, month, day, hour, minute, second, latitude, longitude
 Exx, eyy, ezz, Nph for horizontal1, horizontal2, vertical location errors, respectively, and number of phases used

54 **2. Comparison of 1D vs 3D time delays for selected events (Table S5 and Figure S1)**

55

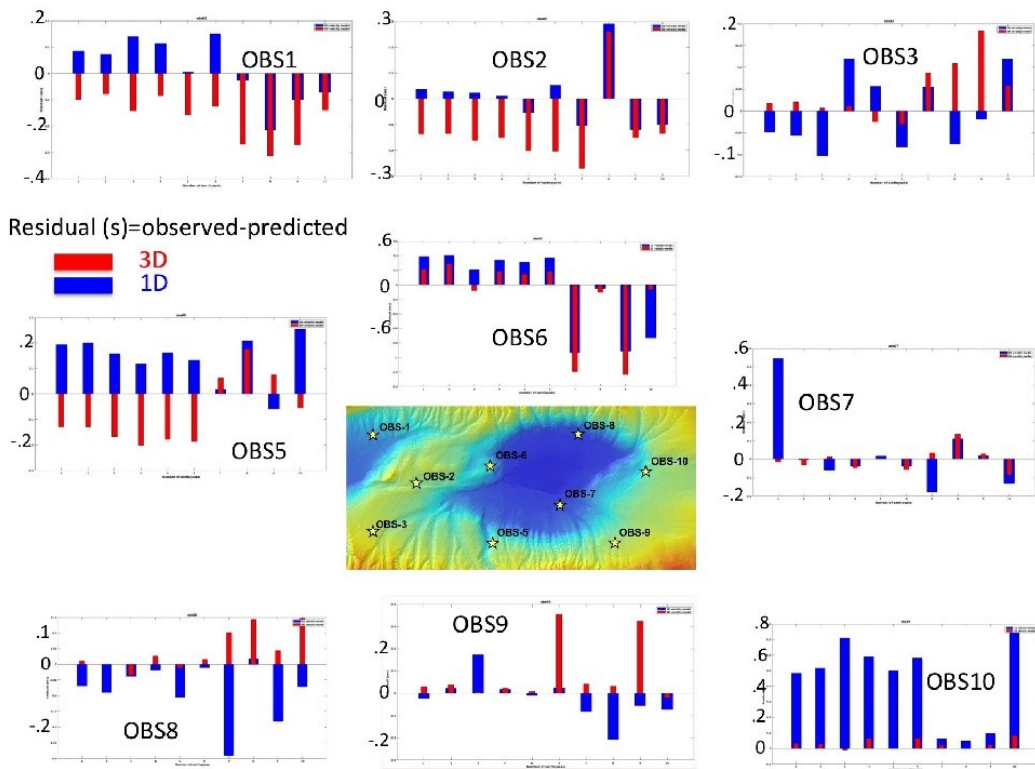
56 **Table S5:** List of selected events detected by all 10 OBSs (2011 dataset), displayed in FigureS1.

Nº	year	month	day	hh	mm	ss	Lat (3D absolute location)	Long (3D absolute location)	Depth (3D absolute location)	Average RMS-1D (seconds)	Average RMS-3D (seconds)
1	2011	5	7	4	14	26	40.8291	27.9908	12.9	0.18	0.08
2	2011	5	7	17	27	50	40.8332	27.9835	12.3	0.22	0.10
3	2011	5	9	23	8	8	40.8187	27.9872	11.2	0.26	0.08
4	2011	5	12	14	32	44	40.8263	27.9889	12.3	0.23	0.11
5	2011	5	13	10	40	3	40.8256	27.992	10.9	0.19	0.09
6	2011	5	18	3	17	1	40.8338	27.9905	12.3	0.22	0.10
7	2011	5	19	4	38	36	40.834	28.136	2.2	0.24	0.18
8	2011	5	19	20	0	34	40.8198	28.1902	13.5	0.27	0.14
9	2011	6	9	20	43	27	40.8296	28.1321	2.4	0.20	0.20
10	2011	6	12	6	9	29	40.8371	27.9656	20.7	0.20	0.21

57

58 Where hh, mm,ss stand for hour, minute, second

59
60



61
62
63
64
65
66
67

Figure S1: P-wave travel-time residuals (observed-predicted) in seconds at 10 OBS (of 2011) for 1D (blue) and 3D (red) locations of 10 selected events (see Table S5).

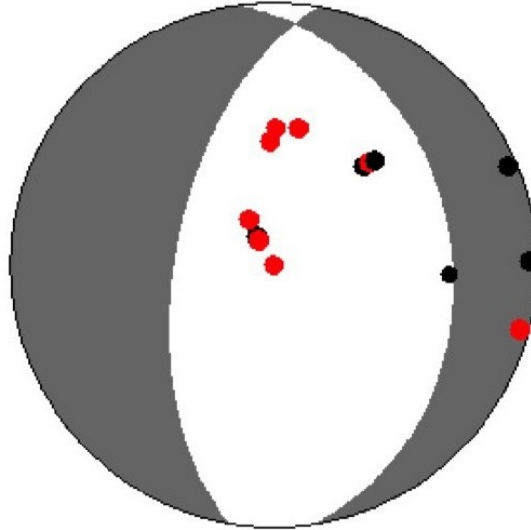
7

7

68

69 **3. Characteristics of Focal Mechanisms (Table S6 and Figures S2 to S5)**

70



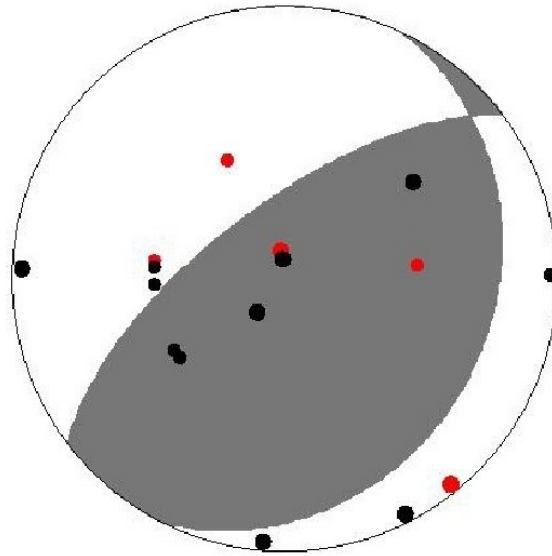
71

72

73 **Figure S2:** Composite focal mechanism of case study 1, computed with HASH software
74 (Hardebeck and Shearer, 2008), with the measured polarities represented with red and black circles,
75 down and up motions respectively, calculated with the 3D velocity model of this study. Resulting
76 focal mechanism: Strike/Dip/rake=190°/59°/-80°.

77

78



79

80

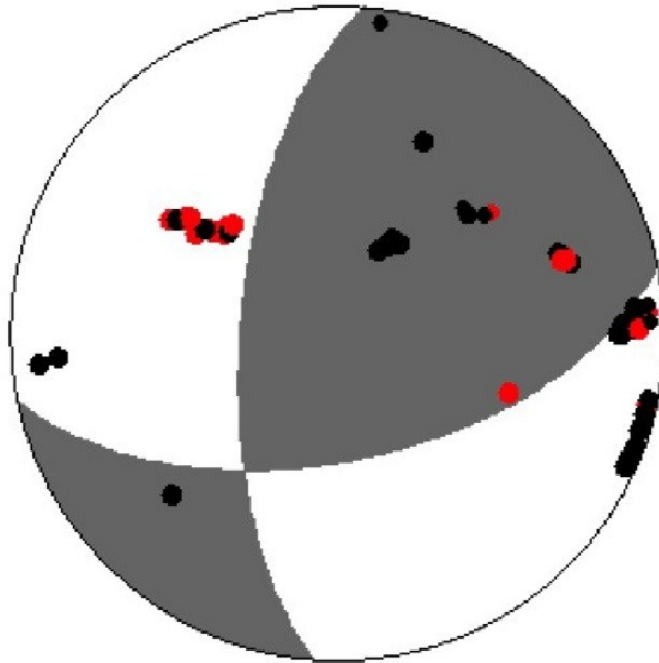
81 **Figure S3:** Composite focal mechanism of case study 2, computed with HASH software
82 (Hardebeck and Shearer, 2008), with the measured polarities represented with red and black circles,
83 down and up motions respectively, calculated with the 3D velocity model of this study. Resulting
84 focal mechanism: Strike/Dip/rake=233°/67°/101°.

85

9

9

86



87

88

89 **Figure S4:** Composite focal mechanism of case study 3, computed with HASH software
90 (Hardebeck and Shearer, 2008), with the measured polarities represented with red and black circles,
91 down and up motions respectively, calculated with the 3D velocity model of this study. Resulting
92 focal mechanism: Strike/Dip/rake= $78^{\circ}/58^{\circ}/151^{\circ}$.

93

94

95

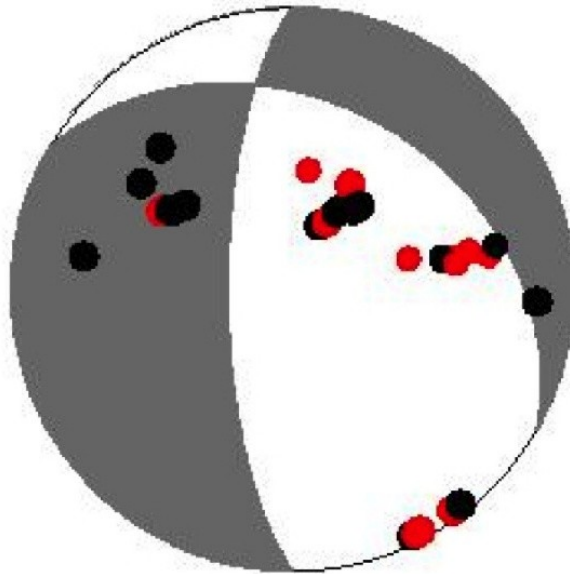
96

97

98

10

10



100

101

102 **Figure S5:** Composite focal mechanism computed for 10 events triggered by the M 5.1 earthquake
 103 of the 25th of July, 2011 (see Table S6). Computation with HASH software (Hardebeck and Shearer,
 104 2008), with the measured polarities represented with red and black circles, down and up motions
 105 respectively, calculated with the 3D velocity model of this study. Resulting focal mechanism:
 106 Strike/Dip/rake=300°/34°/-145°.

107

108

109

110 **Reference:**

111

112 Hardebeck, J.L. and Shearer, P.M., (2008). HASH: A Fortran program for computing

113 Earthquake First-Motion Focal Mechanisms -v1.2 – January 31

114

115

12

12

Bulletin of the Seismological Society of America

COPYRIGHT/PUBLICATION CHARGES FORM

PLEASE FILL OUT AND SUBMIT THIS FORM ONLINE WHEN SUBMITTING YOUR PAPER

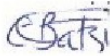
Manuscript Number: BSSA-D-

[leave blank for new submissions]

Title: A new view of the micro-seismicity along the Western Main Marmara Fault based on a high-resolution studyAuthors: Evangelia Batsi, Anthony Lomax, Jean-Baptiste Tary, Frauke Klingelhoefer, Vincent Riboulot, Shane Murphy, Pierre Henry,Stephen Monna, Nurcan Meral Özel, Dogan Kalafat, Hakan Saritas, Günay Cifçi, Namik Çagatay, Luca Gasperini, Louis Géli
COPYRIGHT

In accordance with Public Law 94-533, copyright to the article listed above is hereby transferred to the Seismological Society of America (for U.S. Government employees, to the extent transferable) effective if and when the article is accepted for publication in the *Bulletin of the Seismological Society of America*. The authors reserve the right to use all or part of the article in future works of their own. In addition, the authors affirm that the article has not been copyrighted and that it is not being submitted for publication elsewhere.

To be signed by at least one of the authors (who agrees to inform the others, if any) or, in the case of "work made for hire," by the employer.



08/09/2017

Authorized Signature for Copyright

Print Name (and title, if not author)

Date

PUBLICATION CHARGES

The Seismological Society of America requests that institutions supporting research share in the cost of publicizing the results of that research. The Editor has the discretion of waiving publication charges for authors who do not have institutional support. If pages are paid for by SSA, then no further page charge waivers can be requested for two years by any author listed on the paper. Page charges for waived papers cannot exceed 12 printed pages. Rejected papers in which a page waiver was requested will be considered toward the limit of one request per two years. In addition to regular publication charges there is a nominal fee for publishing electronic supplements, which will not be waived. Current rates are available at <http://www.seismosoc.org/publications/journal-publication-charges/>.

Color options: Color figures can be published (1) in color both in the online journal and in the printed journal, or (2) in color online and gray scale in print. Online color is free; authors will be charged for color in print. You must choose one option for all of the color figures within a paper; that is, you cannot choose option (1) for one color figure and option (2) for another color figure. You cannot submit two versions of the same figure, one for color and one for gray scale. You are responsible for ensuring that color figures are understandable when converted to gray scale, and that text references and captions are appropriate for both online and print versions. Color figures must be submitted before the paper is accepted for publication.

Art guidelines are at <http://www.seismosoc.org/publications/bssa/bssa-art-submission-guidelines/>

Will publication charges be paid? Check one:

BOTH PUBLICATION CHARGES AND COLOR CHARGES WILL BE PAID, and all color figures for this paper will be color both online and in print. This option requires full payment of publication & color charges.

ONLY PUBLICATION CHARGES WILL BE PAID, and all figures for this paper will be gray scale in print. Color figures, if any, will be color online.

REQUEST A REDUCTION IN PUBLICATION CHARGES. Send a letter of request and explanation to the Editor-in-Chief at BSSAeditor@seismosoc.org. Color figures, if any, will be color online but gray scale in print.

Send Invoice to: Bruno Ragueneas, Centre Bretagne - ZI de la Pointe du Diable - CS 10070 - 29280 Plouzané,
Bruno.Ragueneas@ifremer.fr

If your paper is accepted for publication, SSA requires that you fill out and submit your final files.

Questions regarding billing should be directed to the SSA Business Office,
400 Evelyn Avenue, Suite 201 Albany, CA 94706 USA Phone 510 525-5474 Fax 510 525-7204

Rev. 2016-06-01

1st of December 2017

**Response to the editor and to the reviewers ,
Manuscript BSSA MS# BSSA-D-17-00258
By Batsi et al, "A new view of the micro-seismicity along the Western Marmara Fault, based on a high
resolution study"**

Reply to the Editor

Recommendation of the editor. Both reviews are skeptical of parts of the work, and both feel that parts of the paper need clarification or more explanation. As reviewer 1 states in the comments to the editor: "This one is hard because they have essentially done the best they could with the data they have. While there is some missing technical detail I would want to see, like my comments above about S-quality and differential catalog quality, it is not clear to me that improvements to the manuscript will fix the problems or allow one be sure there are shallow (<2 km) earthquakes here. I would like to see synthetic full catalog location in a range of 3D velocity models - but that is an entirely new study. **Perhaps the best course is to suggest they more thoroughly acknowledge the uncertainty for the shallowest earthquakes and leave resolving the depth of the shallow seismicity for future work.**"

Reply. We are fully aware that resolving the depth of shallow earthquakes requires a network of OBSs with source-receiver distance of the order of hypocentral depths. Hence, as suggested in the above bolded sentence, the MS was modified in order to take into account the recommendation of the editor:

- The following sentence was added to the abstract: "Because our results are significantly different from those of previous workers (e.g. Schimttbul 2015 and Yamamoto et al 2017), it is important to acknowledge the uncertainty for the shallowest earthquakes. Resolving the depth of the shallow seismicity is left for future studies using adequate experimental design ensuring source-receiver distances of the same order as hypocentral depths."
- The title was changed: "An alternative view of the micro-seismicity along the Western Main Marmara Fault" instead of "A new view of..."
- The wording was changed, in order to make it more modest and to avoid over-statements (such as "an unprecedented view", etc)
- A new chapter was added on "the limitations of the present work and perspectives for future research"
- A new paragraph was included in the discussion on the comparison with Yamamoto's results.
- All focal mechanisms were re-calculated. Polarities are shown in the supplementary material.

Reply to Reviewer #1 (R1)

Comment R1.1: I will first focus on phase onsets and differential time data. My understanding is that IFREMER short-period OBS, which make up most of the stations in the study, are 3-component. All of the waveforms shown in the manuscript are vertical component, and there is no indication if horizontal components were used S-wave phase onsets. This becomes an issue because strong velocity contrasts in areas with shallow sediments can generate converted phases and therefore there may be danger in identification of S-onsets on vertical channels. And ultimately since few of the OBS are within a focal depth of 2 km depth earthquakes and the Vp/Vs structure is so important, showing/discussing S onset is accuracy is necessary. This could simply be a couple of sentences and a revision to the waveform figures.

Reply: Ifremer's instruments are indeed 4-components OBSs, including one vertical (z), two horizontal, NON-ORIENTED, geophones (x, y), and one hydrophone (H). It must be clear that ALL 4 COMPONENTS WERE USED FOR THE ANALYSIS. For the picking, the horizontal components were primarily used, particularly for S-wave phase onsets, while P-phases were preferentially considered on the vertical components. Note that all picks were controlled visually and -when necessary- modified manually. Following the reviewer's recommendations, additional figures are presented in the revised version, to display the two horizontal components (see Figures 5, 7 and 9 of the revised version, and also below, Figures R1, R2 and R3 of the current document). The procedure that was followed is now better explained in Data and Methodology paragraph.

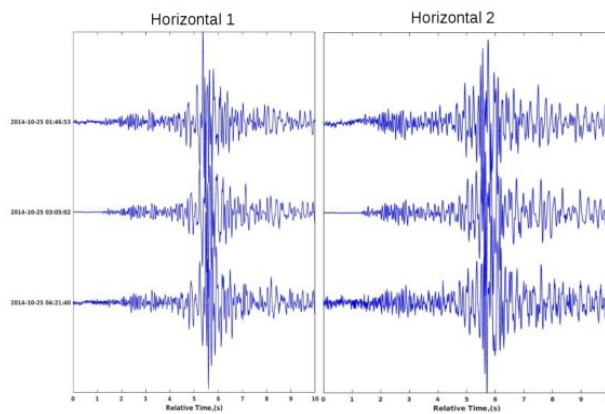


Figure R1: (Figure 5 of the revised version). Case study 1. Seismograms on the two not-oriented horizontal components (e.g. left: horizontal 1 and right: horizontal 2), corresponding to the triplet (with $c > 0.9$) recorded by the central station OBS04, on 25th, October 2014.

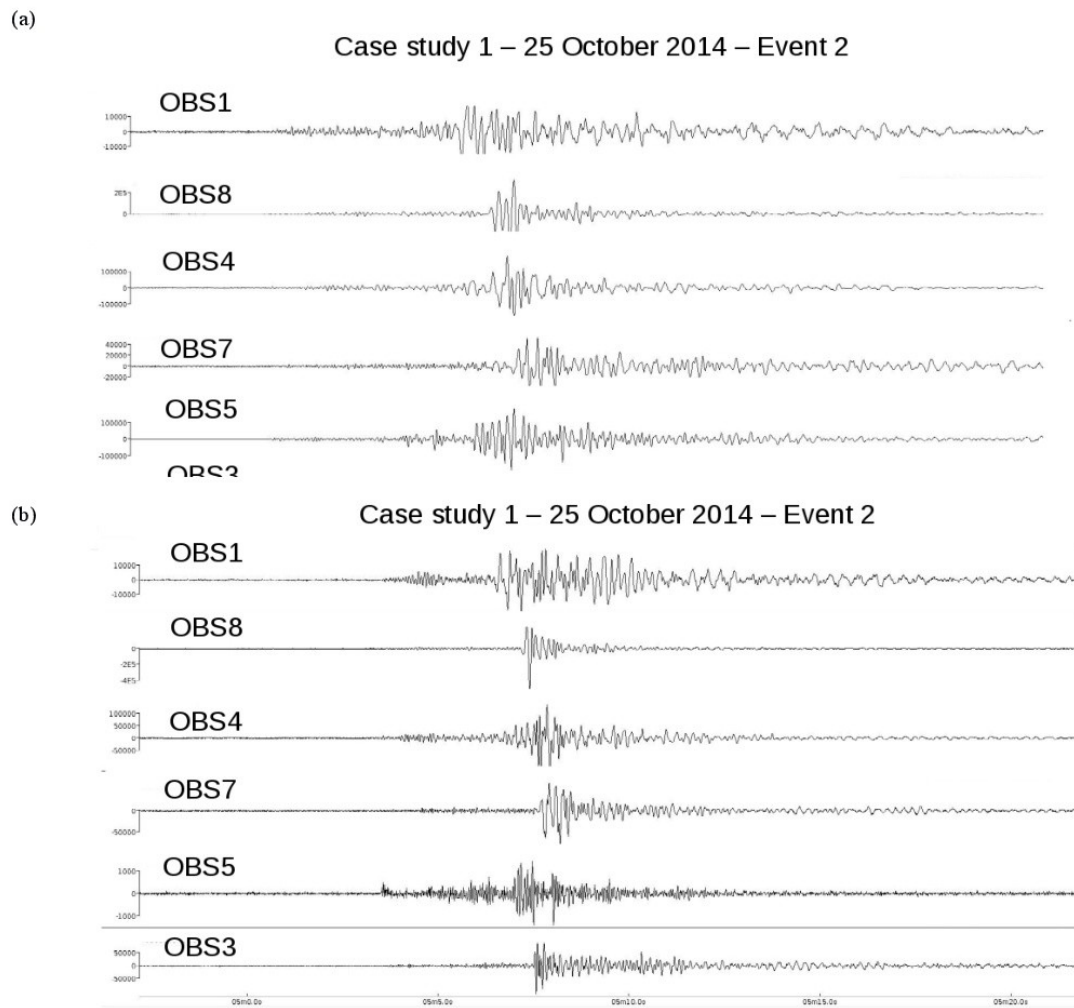


Figure R2: (Figure 7 of the revised version). Seismogram from earthquake 2 (25th of October 2014) of case study 1 recorded at the seafloor stations 1, 8, 4, 7, 5 and 3 of the 2014 OBS network on the two not-oriented horizontal components. Panels (a) and (b) correspond to horizontal components 1 and 2 respectively.

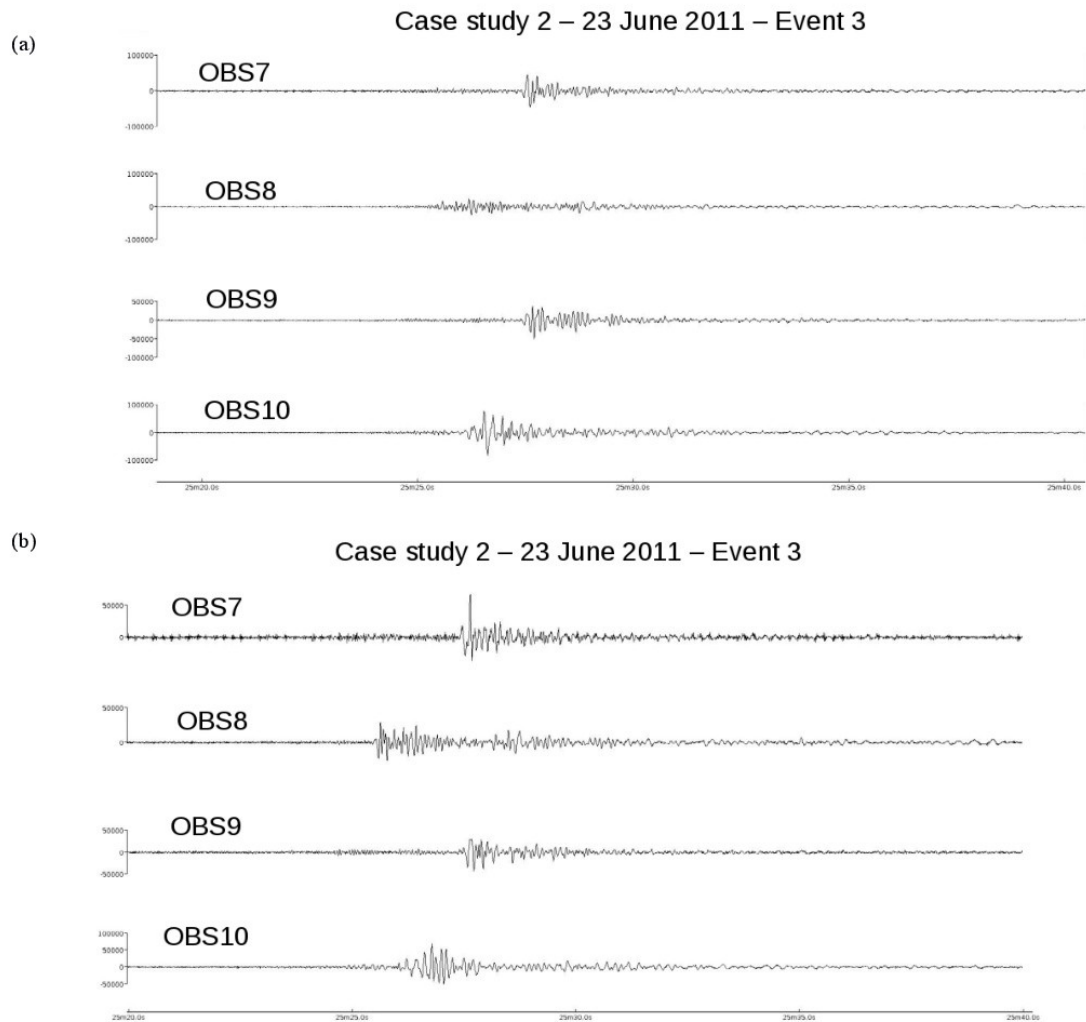


Figure R3: (Figure 9 of the revised version). Seismogram from earthquake 2 (23rd of June 2011) of case study 2 recorded at the seafloor stations 7, 8, 9 and 10 of the 2011 OBS network on the two not-oriented horizontal components. Panels (a) and (b) correspond to horizontal components 1 and 2 respectively.

Comment R1.2: Similarly, I was a bit confused about how a full waveform cross-correlation (P & S) produced "the best results" for the differential time dataset than a separate P and S cross-correlation [line 248]. I would personally prefer to see a more thorough discussion of the differential time dataset used in NLDiffLoc. GISMO can be optimized to recognize clusters of similar earthquakes or high-resolution differential times. I tend to think of full waveform correlation being best for recognizing event clusters but at the cost to the accuracy for the S-differential times in particular. Again, these issues could be easily addressed with the addition of a paragraph focused on the differential time dataset.

Reply: (i) **Cross-correlations:** The cross-correlation used for the current analysis were obtained by using all three components of the geophone. Specifically for each component different tests were applied: by using (i) only P-wave, (ii) only S-wave and (iii) both P and S wave trains. The best results on the vertical component were obtained in case (iii). In contrast, on the horizontal components the best results were obtained by the S phases individually. However, in practise, we have found that the phases were easier to identify on the vertical components compared to the horizontal components. Therefore our choice for event correlation, was to work on the vertical components. We fully agree with the reviewer's remark: 'I tend to think of full waveform correlation being best for recognizing event clusters but at the cost to the accuracy for the S-differential times in particular'. We arrive at the same conclusion.

(ii) **Differential time dataset of NLDiffloc:** NLDiffLoc performs a differential earthquake location based on the double difference equation from [Waldhauser and Ellsworth, 2000]. Two files are used as input for the double difference code: (i) initial absolute locations (e.g. derived from NLLoc) and (ii) differential traveltimes (e.g. derived from Loc2ddct tool) which are calculated for a specified maximum distance between event couples. The relative coordinates (e.g. x, y, z and t) are optimized for a set of hypocenters given a set of differential phase arrival time measures at each station for multiple hypocenters. This is achieved by using a non-linearized global search (e.g. a Metropolis random walk, [Lomax et al, 2009]), which maximizes the probabilistic solution likelihood as the hypocenter coordinates are perturbed. A double-difference equation from [Waldhauser and Ellsworth, 2000] is then evaluated for determining the misfit and the solution likelihood by using an L1 norm which more robust with outlier data (e.g. in contrast to L2 norm which is equivalent to what HypoDD is using).

Comment R1.3: The velocity model issues form the core set of problems with the earthquake location, and with previously published earthquake catalogs. There are 1D models and 3D P-wave models available for the area. And those models in turn use constant V_p/V_s with depth or gradient V_p/V_s with depth. The 3D models range from lower resolution tomography models used in studies by other authors or the a priori 3D P-wave model used in this study based on combining bathymetry and 3D- and 2D seismic data. The basic argument here is that, of the 1D models, 1D models with slow shallow velocities and gradient V_p/V_s fit the seismic data best. The interpretation is that the shallow sediments are essentially mudrocks. The equivalent V_p/V_s to the empirical relationship on line 176 is ~ 1.58 , much lower than the constant V_p/V_s of 1.78 used with the a priori 3D velocity model in this study. While it is not explicitly discussed, I assume that the authors assume that the station corrections (P and S, again I presume because it is not specified and not included in the tables) calculated in Step 3 (lines 180-183) account for the travel time difference between V_p/V_s of 1.58 vs 1.78. No earthquake catalog exists independent of velocity model and associated station corrections, so for reproducibility, I prefer to see the catalog, corrections and model archived in electronic data supplements. I also think a discussion of the station corrections are warranted, even if they authors don't seem to believe them [??? Line 223-229].

Reply: 1D Velocity model. The 1D model that we have used in Step 2 of the location procedure is shown in green in Figure R4 below. The Castagna formula (red curve) **WAS ACTUALLY NOT USED** in our work. This formula may yield estimations that fit with our VS velocity model at depth of $\sim 4 \pm 1$ km. However, Castagna's velocity model is too low at depth < 3 km and too high at depth > 5 km (see Figure R4 below). Hence, references to Castagna's formula and the analogy to mudrock were removed from the revised version, as they are not useful, in order to avoid any confusion.

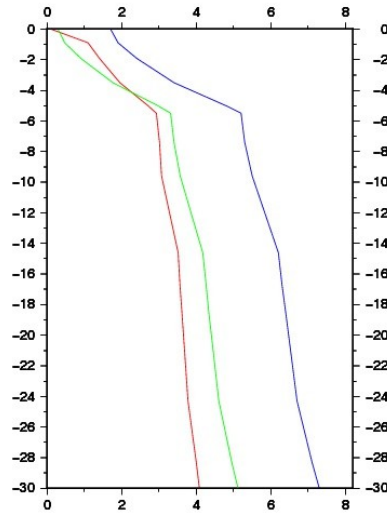


Figure R4. Blue and green curves are 1D velocity model for VP and VS respectively, used in the 2 first steps of our location procedure, based on Cros and Géli [2013] (see also [Lomax, 2014]). The red curve is for Castagna's model.

Station corrections. The earthquake catalog, corrections and model are now archived in the electronic supplements. Regarding the station corrections, we agree with the reviewer and have modified the manuscript accordingly. Station corrections are robust, and certainly useful for reducing the effects of algorithm's errors, velocity model errors, picking errors, etc, and producing in this way more precise (not necessarily more accurate) locations¹. Station corrections provide bulk estimates that represent the integral of all these effects. The basic idea of station corrections is that with any model, including 3D, there are simplifications and smoothing so that not all real velocity variations are taken into account. In particular, shallow, near-station, smaller scale and potentially low velocity structures cannot or are not modelled. In 3D tomography, these would be the remaining station residuals after inversion. It is a tautology to say that “the more accurate the velocity model, the less necessary the station corrections”.

Comment RI.4: The 1D synthetics are nicely illustrative of the limits of 1D models, it is seems the limits of the 3D models are more at issue. I would be curious how synthetic travel times for shallow and crustal earthquake depths computed in the 3D P-model with V_p/V_s of 1.78 and a variable V_p/V_s , with noise added, were relocated. Were synthetic differential times computed?

Reply: The objective of the test presented in the manuscript was to compare 1D models (off-shore derived 1D-model vs onshore 1D-model). As a starting point, we computed synthetic travel times from two given earthquakes (one shallow and one deep) to the OBS sites, using NonLinLoc and our 3D-velocity model. The resulting travel-times were then considered as real data. Then we relocated the position of the two earthquakes, using two 1D-models: one on-shore derived 1D-model (Karabulut's), and one off-shore derived 1D-model taking into account the sharp velocity variations in the upper sediment layers. A constant V_p/V_s of 1.78 was used for steps 3, 4, 5 of the relocation procedure. For the 3D velocity model no synthetic tests were computed to test the dependence of the location results to small variations in the 3D-velocity model or to V_p/V_s variations. We agree with the reviewer's remark that such tests should be done, but at this stage we have no choice than to leave this to future workers. The possibility of using a variable V_p/V_s during relocation procedure is undoubtedly necessary for improving the location results; it is therefore going to be considered for future work.

¹ For differences between precision and accuracy, see: <https://www.thoughtco.com/difference-between-accuracy-and-precision-609328>

Comment RI.5: Does the NLDiffLoc program use the absolute data, or like hypoDD, does it only modify relative location once the initial absolute distribution is set. What does "reasonably confident" mean in a scientific publication - I would rather see some degree of quantification.

Reply: NLDiffLoc program is quite similar with hypoDD program, that means that is taking as input data: (i) the initial absolute locations that have been calculated by NonLinLoc and (ii) differential traveltimes (e.g. derived from Loc2ddct tool) which are calculated for a specified maximum distance between event couples. For more details, see Reply to R1.2.

The expression "reasonably confident" was removed from the revised version. Our preference for the location results we obtain using the 3D-velocity model (compared to both Yamamoto's and 1D location results) is based on 2 quantitative criteria and on geology:

- i) In general RMS errors in travel time differences (measured-calculated) are smaller for 3D locations.
- ii) The computed probability density functions (pdf) indicate that 3D locations have smaller confidence ellipsoids for each event
- iii) 3D locations are consistent with geology. Particularly deep-events ($d > 10$ km) are characterized by a dominantly strike-slip fault mechanism, while most shallow-events ($d < 6$ km) have a dominantly normal fault mechanism, except for the events of case study 2 that are characterized by thrust faulting.

Intellectually, the latter point (iii) is as much important as points i) and ii).

Comment RI.6: Why wasn't the Yamamoto et al model used for Case Study 2 and 3 also used to assess different 3D models?

Reply: The paper of Yamamoto was published on line on March 2017, after the first submission of our paper (in February 2017). Because we were tight by different time constraints, we had no time to run new locations with Yamamoto's model. In addition, case studies 2 and 3 concern earthquakes recorded in 2011 (data set 1), while Yamamoto's study is based on data records from September 2014 to June 2015; hence, we did not realize the interest of running new computations with Yamamoto's model. Today, we agree with reviewer 1, that this should be done in the future.

Comment RI.7: I would prefer a clearer organization between Methods, Synthetic Tests to Establish Uncertainty and Discussion. There are many tables, with captions! Captions should be points of discussion in the main text. Table 1 could be an electronic supplement and have station corrections added. Mechanisms could be a single table.

Reply: Following the reviewer's recommendations, we have revised the MS in such a way as to propose a clearer organization between methods, synthetic tests and discussion. The paragraph on « data and methodology » has been split into two separate paragraphs. Table Captions have been also simplified. The electronic supplements have been enriched, with travel-time residuals and details on the computation of focal mechanisms.

Comment RI.8: I am not surprised to see use of a 3D velocity model make such a difference but it is harder to understand what aspects of the various 3D models (this study versus Yamamoto et al. for instance) are leading to the variation.

Reply: This question is fully addressed in the manuscript. Let us here recall the following differences between this study versus Yamamoto et al, 2017:

- i) The structure of the Marmara Trough. Based on deep, multichannel seismic soundings (cf Laigle et al, 2008, Bécel et al, 2009 and 2010), the Main Marmara Fault is known to be located within a deep trough, filled with Plio-Quaternary, slow velocity sediments. The central part of the trough, where most of our locations are found, is ~ 7 km deep and ~ 10 km wide. At the deeper base of the trough, there are sharp heterogeneities, that occur horizontally within less than ~ 12 km. In addition, seafloor topography induces sharp velocity variations within a few hundreds of meters. 3D velocity grids of 10 km (like Yamamoto's, for instance) are inadequate to take into account the scale of horizontal (and also vertical) heterogeneities.
- ii) Network geometry and number of OBSs: Within this study our OBS network was specifically designed for high resolution locations within Western Sea of Marmara. A first OBS deployment in 2011 was hampered by the loss of the OBS located at the center of the network. Hence, a new experiment specifically targeted on the

Western High was made in 2014. To meet our objectives, we used a network including more than 9 OBS, evenly distributed within a circle having a radius of less than 10 km, centered on the Western High. In contrast, Yamamoto et al, 2017, have used an elongated network, with 10 OBS stations in September 2014 and 5 more were added in March 2015. As a result, the OBS were unevenly distributed along the Main Marmara Fault². In Yamamoto's paper, our study area is covered by only 4 OBS.

- iii) Velocity models: in our study, we have used a 3D high resolution velocity model with a grid node spacing of 750 m x 750 m x 750 m, that was specifically developed for the western part of the Sea of Marmara in order to take into account the velocity contrast at the seafloor interface and the sharp geometry of the basins. In contrast, Yamamoto et al (2017) use a 3D-velocity model having a mesh size of 10 km x 10 km, which is well above the size of the heterogeneities within the deep basins. Yamamoto's 3D-velocity model does not actually account for the small-scale, across-strike heterogeneities of the velocity structure.
- iv) Initial velocity model: We have used an initial 3D velocity model, while Yamamoto *et al* (2017) use a 1D, initial velocity model (see details on our location procedure in the *ad hoc* section).

Consequently, our results and Yamamoto's should not be compared, but considered separately and used positively for the new insights they provide. Yamamoto *et al* (2017) give a new picture of the deep crustal structure, with a clear deepening of the Moho below the Western High. In contrast, we focus on the existence of shallow (< 6 km) seismicity.

Comment R1.9: It is also difficult to assess if the really shallow events (<2 km) are well located because of the discrepancy between the geologically reasonable and low Vp/Vs and the higher Vp/Vs paired with the 3D velocity model. The synthetics are useful but I am not sure are sufficient to solve the fundamental issue of network-source geometry.

Reply:

- i) General consideration. We definitely agree with the reviewer that the network-source geometry is a fundamental issue that is not solved. The bullet proof will be obtained with a specific deployment designed to locate ultra-shallow earthquakes at depths < 2 km, e.g. with an OBS spacing of < 2 km. We leave this to future workers. Here, we present the results that we have obtained with the available datasets: the methods are explained, the data and the velocity model are available to the scientific community, etc. Scientific results obtained with a given dataset are meant to evolve as new data are collected.
- ii) On the physics of ultra-shallow seismicity. Indeed a great number of events occurred at shallow depths. In general is considered that soft marine sediments (with velocities < 2 to 3 km/s) are expected to behave aseismically. However, recent results from laboratory experiments on clays at high slip-rates (i.e. > 2 m/s) [Faulkner et al., 2011³; Aretusini et al., 2017⁴] suggest that clays can react seismically to rupture that propagates into them. This was actually the case of the 2011 Tohoku earthquake where 30 m of slip is estimated to have occurred in clay like material [Romano et al., 2014⁵]. A similar scenario could apply to explain the ultra-shallow events that occurred at depths of less than a few hundred meters. Note that this question of ultra-shallow seismicity is fully addressed in a paper in preparation by *Batsi et al*, based on high-resolution 3D seismic data, showing that these ultra-shallow earthquakes are mostly located on normal faults cutting through the upper sediment layers (see Figures R5 and R6).
- iii) Why Yamamoto et al, 2017 did not report shallow seismicity (< 2 km)? As suggested by Figure R7 (from *Géli et al, 2017*, in review in *Scientific Reports*), vertically swarms of seismicity (including ultra-shallow seismicity) occur as aftershocks following earthquakes of intermediate magnitude ($M_i > 4.5$), in areas where gas emissions have been detected. Hence it is hypothesized that ultra-shallow seismicity likely result from gas induced processes, likely triggered by moderate earthquakes along

² For information to the reviewers and editor, let us here mention that in 2009, Ifremer deployed a network of OBSs having a similar geometry as Yamamoto's. We realized that this geometry was not satisfying and results were not published. Hence, Ifremer did a second experiment focused on the Western SoM and a 3rd experiment in 2014, centred on the Western High.

³ Aretusini, S., et al (2017), Production of nanoparticles during experimental deformation of smectite and implications for seismic slip, *Earth and Planetary Science Letters*, 463, 221–231, doi:10.1016/j.epsl.2017.01.048.

⁴ Faulkner, D. R., et al, Stuck in the mud? Earthquake nucleation and propagation through accretionary forearcs, *Geophys. Res. Lett.*, 38(18), doi:10.1029/2011GL048552.

⁵ Romano, F., et al (2014), Structural control on the Tohoku earthquake rupture process investigated by 3D FEM, tsunami and geodetic data, *Sci. Rep.*, 4, doi:10.1038/srep05631.

the MMF. It is important to note that, during the recording period of Yamamoto (e.g. from September 2014 to June 2015), no event of magnitude $M > 3.2$ occurred in the study area. This may explain why no shallow seismicity was reported by Yamamoto *et al* (2017).

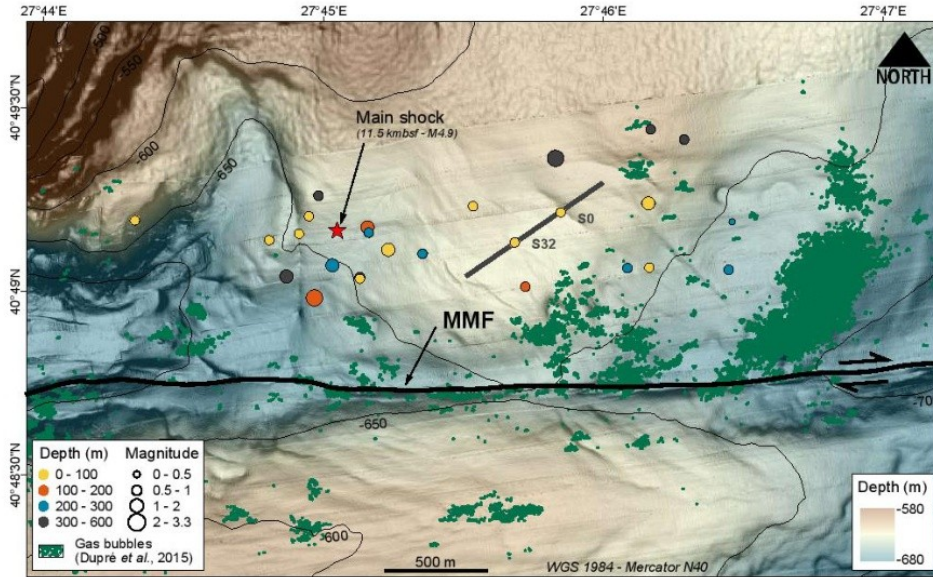


Figure R5: Bathymetric map showing ultra-shallow earthquakes used (e.g. different colors correspond to depth range and circles are proportional to magnitude). Red star indicates the M5.1 mainshock of the 25th of July, 2011, whereas green dots show the gas emission sites that were acoustically detected during the Marmesonet cruise in 2009 (from Duprè *et al*, 2015), from Batsi *et al*, in preparation.

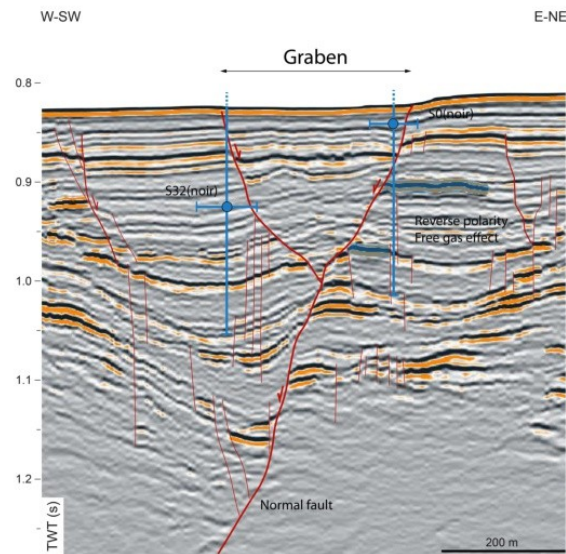


Figure R6: Example of localization of some shallow earthquakes on the 3D seismics. Red and blue lines indicate normal faulting and horizontal-vertical uncertainties of the earthquake location, respectively. From Batsi *et al*, in preparation.

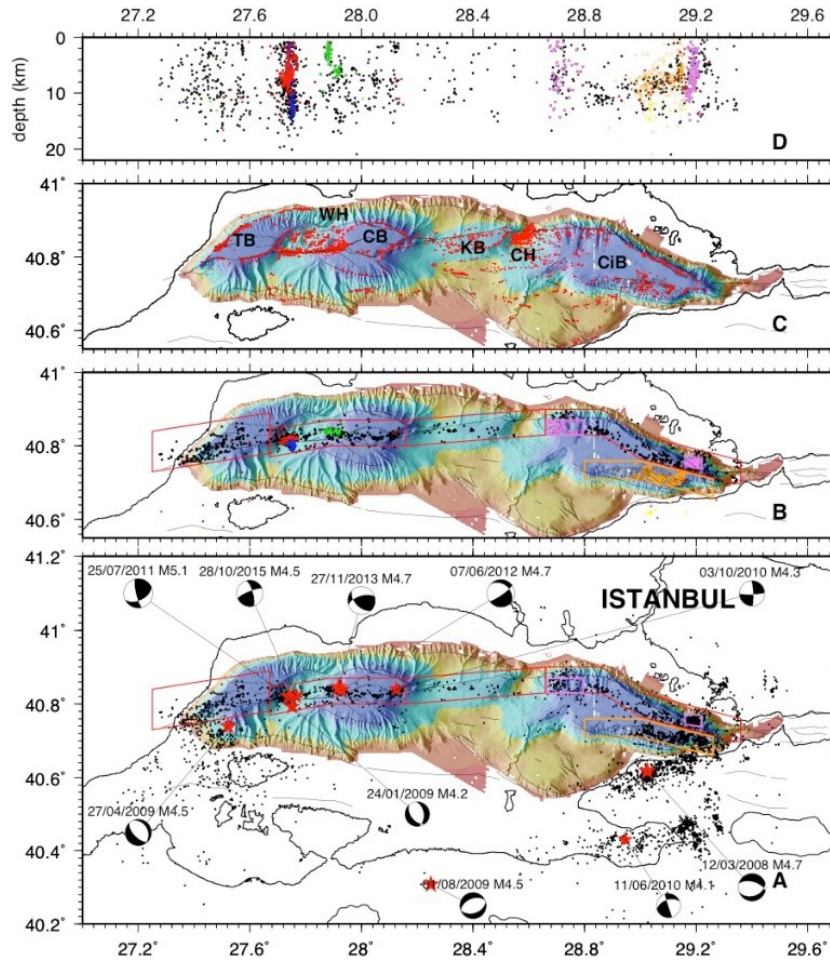


Figure R7, from Géhi et al, Sci Rep., 2017, in review. Seismicity and gas emissions within the Sea of Marmara. A) Full seismicity map from 2007 to 2012 based on the recordings from 132 land stations, as well as from temporary seabottom networks, including 5 cabled observatories from 2009 to 2011 and 10 autonomous stations deployed by Ifremer from april 2011 to july 2011 (see location of stations in after Schmittbuhl et al, 2016). The Western Sea of Marmara is regularly affected by earthquakes of magnitude > 4.5. The two earthquakes of magnitude > 4.0 which occurred in 2013 and 2015 were therefore added to complete the general pattern of seismicity in this area (locations from KOERI catalog). For all maps, thin black lines indicate major structural features, from Reference3. B) Selected micro-earthquakes with epicentres located within the boxes shown in panel A, respectively centered along the MMF and within the southern part of the Cinarçik Basin. Coloured dots indicate those aftershocks that occurred within the Western Sea of Marmara, 7 days after the earthquakes of magnitude > 4 (years 2007 to 2012 only). Blue: 27/04/2009; pink: 03/10/2010; red: 25/07/2011; green: 07/06/2012. C) Sites of acoustically detected gas emissions (red dots), from Reference 22. TB: Tekirdag Basin. WH: Western High; KB: Kumburgas Basin; CH: Central High; CiB: Cinarçik Basin. Note that in the Central High and the in the Kumburgas basins, gas is not found within the Main Marmara Fault Valley, nor along the Fault trace, but on top of adjacent structures or at the edge of basins (see references 21 and 22). D) Depth of selected earthquakes plotted versus longitude, with events from aftershock sequences represented using the same colour code as in panel B. Orange dots indicate events from the area delineated by the orange box (Panel B) in the South Cinarçik Basin; Violet dots are for events from the area delineated by the 2 violet boxes shown in Panel B.

Reply to Reviewer #2 (R2)

Comment R2.1: In Case Study 1, Yamamoto et al., 2017 and this study uses 3D velocity model. However, this study finds the triplet at shallower depths (~6km) while the former one constrains them at depths of 18km.

The authors observe travel time differences in P- and S-waves at OBS stations to the north and to the south of the Main Marmara Fault (MMF). Travel time differences ($t_s - t_p$) at OBS stations located on the northern side of the MMF are less. This observation is explained by heterogeneity in 3D velocity model in the Marmara Sea. Thus, they infer that seismic velocities are faster to the north of the MMF, slower to its south. This difference is not obvious in the cross sections in figures 14 and 15.

Based on these observations, does not Yamamoto's 3D velocity model include this heterogeneity to the north and south of the MMF? If it includes this velocity difference, why is this triplet constrained at two different depths?

Besides, it seems that the S-wave arrival time on OBS 4 recording (Figure 7) may be wrongly picked. I am not sure, but there is a possibility to identify an earlier phase as an S-wave arrival (as in the case of OBS 9 recording in Figure 10, where the smaller-amplitude phase preceding the larger phase is picked). If you choose this phase as an S-wave arrival, how much does it influence the hypocenter of this event in the triplet?

Reply:

i) Reminder about our 3D velocity model. The main differences between our velocity model and Yamamoto's are recalled in reply to R1.8 (reply to Reviewer 1). Let us here remind the main points of our 3D-model:

- The construction of the 3D-velocity model is detailed in Cros and Géli (2013) and in Gürbüz et al. (2013). First, it is important to remind that we use a 750 m x 750 m x 200 m grid spacing in our 3D-velocity model in order to properly account for the bathymetry, the water depth at each grid node being inferred from the High-Resolution (38 m) bathymetric grid of [Le Pichon et al, *EPSL*, **192**, 595–616, 2001].
- Second, for the velocities within the upper 2 kilometers of sediments, we have interpolated between 1515 m/s at the seafloor and the velocity at 2 km below seafloor inferred from the model of [Bayrakci et al, 2013]. Velocities from [Bayrakci et al, 2013] are themselves based on those reported in [Laigle et al, *EPSL*, **270** (2008) 168–179], (page 171) from the analysis of deep-penetration, multi-channel data: "The P-wave velocities are very low for the sea-bottom deposits, especially in the deep bathymetric troughs (1.6 to 1.8 km/s), and are gradually increasing from sea-bottom down to the pre-kinematic basement where they can reach values of 4 to 4.2 km/s. These values are consistent with the joint modeling of the shots recorded by the OBS array".
- These velocities within the uppermost sediment layers (depth < 2 km) are consistent with those that we have ourselves measured directly using OBSs deployed in 2007 and wide-angle reflection and refraction techniques: see Figure R5a below and details in Appendix A of [Tary et al, 2011, *BSSA*, **101**, pp. 775–791, doi: 10.1785/0120100014].
- More details for the velocity within the upper 300 m of sediments are also provided by [Thomas et al, 2012]⁶, page 295, section « Data set and processing » : «The [High-Resolution] data set allowed the velocity of the upper sedimentary cover to be assessed with a relatively low mean interval velocity of 1650 m/s. A three-layer velocity model, 1515 m/s for the water column, 1650 m/s for the upper sedimentary cover, and a constant gradient of 500 m/s km⁻¹ for the underlying sediments was then employed to perform 3D stacking prior to constant velocity two-pass Stolt migration.»

⁶ Thomas, Y., Marsset, B., Westbrook, G. K., Grall, C., Géli, L., Henry, P., Cifçi, C., Rochat, A., and Saritas, H., (2012), Contribution of high-resolution 3D seismic near-seafloor imaging to réservoir scale studies: application to the active north Anatolian Fault, Sea of Marmara, *Near Surface Geophysics*, 10, 291-301, doi:10.3997/1873-0604.2012019. Paper available on Research Gate.

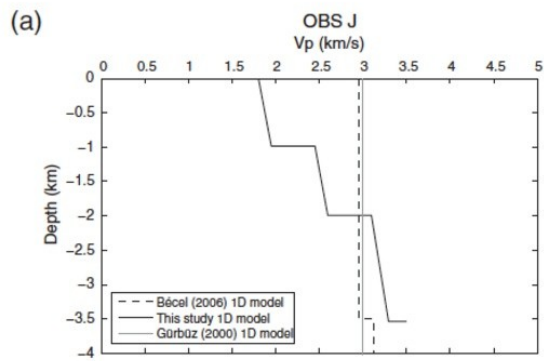


Figure R8 After [Tary et al, 2011, BSSA, **101**, pp. 775–791, doi: 10.1785/0120100014]. Velocities within the uppermost sediment layers (depth < 3.5 km), directly measured using OBSs and wide-angle reflection and refraction techniques.

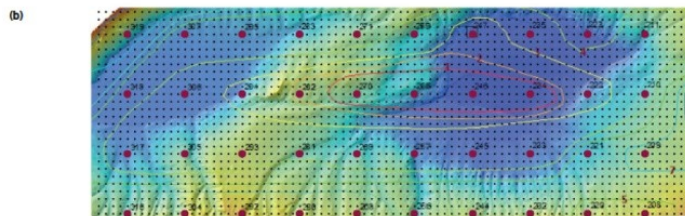
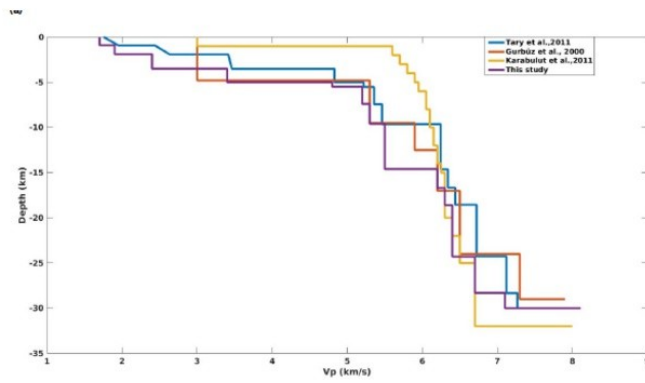


Figure R9 After Batsi et al, 2017, BSSA, in review. The above panel indicates different 1D velocity profiles use by different authors for earthquake location in the Sea of Marmara. The 1D velocity profile at the center of our high-resolution, 3D grid is in mauve colour, indicated as “this study”.

- i) **Travel time differences in P- and S-waves and heterogeneity in 3D velocity model:** The reviewer mentions that “travel time differences (ts-tp) at OBS stations located on the northern side of the MMF are less”. However, this is not what we write, neither what we see in the dataset. In case study 1, travel time differences (ts-tp) are anomalous high when the source to receiver path crosses the mud volcano area. In addition, we do not infer that “seismic velocities are faster to the north of the MMF, slower to its south”. Based on what we know from the geology of the Western High, **the major difficulty for earthquake location, is due to the presence of gas, both within the deep gas sources, within the sediment layers and below the mud volcanoes.** For technical reasons, our 3D velocity model does not take into account the finest-scale heterogeneities due to the presence of gas.
- ii) **Representation of horizontal components and use of S-wave arrival times:** In the location process, we have used both the S- and P- arrivals, although only the S-phases were presented in the previous version of the manuscript. In the revised version, the components of the two non-oriented horizontal components are also presented. In our approach we have used all geophone's components for picking. Preferentially, the vertical component was used for the detection of P-wave arrivals while the horizontal ones were used for the S-wave onsets. Because strong velocity contrasts in areas with shallow sediments could generate converted phases, the phase identification on vertical channels could be misleading. Therefore, horizontal components were preferentially used for S arrivals.

Comment R2.2: *A moderate size earthquake (Ml 5.1) occurred in the Western High (WH), on July 25, 2011. This event occurred at a depth of 11km, its focal mechanism solution gave a strike-slip focal mechanism, associated with the MMF in the WH. This event produced aftershocks, but these aftershocks did not occur at the depth where the mainshock occurred, they were located shallower (<6m), especially in a gas prone sediment layer seated at depths of about ~1-2km. They state that this sediment is aseismic layer, and does not produce any weak motion. They also state that this mainshock changes the aseismic response of this sediment to a seismic one. For a vertical strike slip event on an east-west trending fault, the Coulomb stress increases at the ends of this fault while off-fault lobes are observed over most of its length where the Coulomb stress is reduced. Aftershock distribution is consistent with these patterns. Increases in the Coulomb stress triggers aftershocks while the Coulomb stress reductions suppress them. However, aftershocks that the Ml 5.1 earthquake triggers are located to the north of the MMF where the Coulomb stress is reduced and aftershock distribution is not expected. Besides, aftershocks were not produced at the depths where the mainshock occurred. It is interpreted that the mainshock triggers aftershocks located at shallower depths, especially in a sedimentary layer with a thickness of ~1-2km based on rock physics experiments. But, this interpretation is not consistent with Coulomb stress distribution.*

Reply:

(i) **Seismic sequence following the M5.1 mainshock:** First of all, it is worth noting that for our approach only 112 out of 550 events of the sequence are used for the analysis. Specifically, events located 1) either within the water column, 2) either outside the area delineated by the 2011 seismic network-source and 3) not following the criteria that were set up, were removed from the catalog. Hence, only well constrained events were considered for the analysis. Most of the remaining events are not observed to be in the direct vicinity of the mainshock rupture zone, probably due to the presence of over-pressurized gas in the area. These events should not be called “aftershocks”, but “triggered events”.

(ii) **Triggered seismicity:** This question is fully addressed within the paper in preparation by Tary et al., entitled “Improved detection of gas-related seismicity triggered by dynamic stresses in the Sea of Marmara” Our study deals with the neither dynamic nor static Coulomb stress transfer induced by the M_l5.1 mainshock do not exceed tens of kPa. The positions of the shallow clusters correspond to the positive lobes for Coulomb stress transfer. Dynamic stresses variations may reach values of at most $\sim \pm 50$ kPa (depending on the rise time considered), but cannot last more than 30 seconds after the mainshock. Static stress variations range from 2 to 10 kPa while the corresponding changes in pore pressure range within ± 5 kPa (assuming undrained conditions). Even though shallow faults in the western Sea of Marmara were close to failure due to the presence of high fluid pressures, the duration (3 to 4 days after the mainshock) of the sequence of shallow clusters suggest that other processes than Coulomb stress transfer triggered the shallow clusters. From this study, we conclude that these earthquakes were likely triggered by over pressurized gas.

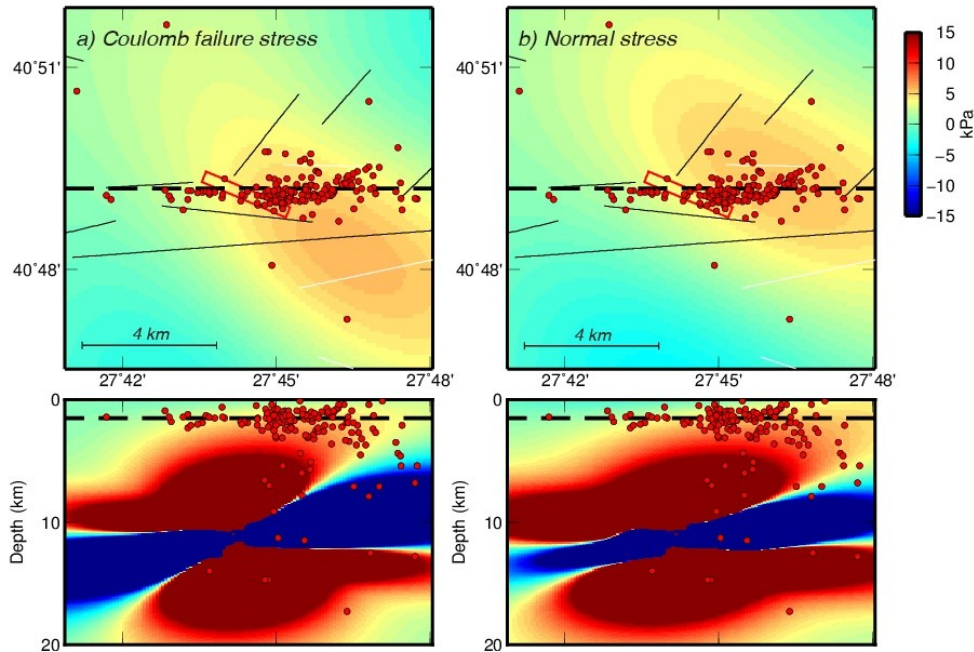


Figure R10, from Tary et al, EPSL, in preparation. Coulomb failure stress and normal stress changes calculated on faults oriented with strike=310, dip=55, and rake=126 corresponding to the composite focal mechanism of the superficial events of Batsi et al., 2017.

Comment R2.3: In cross sections of this study, I do not observe any alignment in terms of depth. Most of the events occur at similar depth ranges (e.g., case study 3 in Figure 10). These events are clustered in a small area. Probably, they result from the same faulting. The composite focal mechanism solution gives a strike slip faulting. But, the depth view of the seismicity is not compatible with nodal planes of the retrieved mechanism. Most of these events occur at depths of 12 km. Is it coincidence or related to the velocity model that is accepted in this study? This discrepancy between the strike-slip focal mechanism and the horizontal distribution of locations of the earthquakes needs discussion.

Reply: The events shown in case study 3 occur at depths >12 km below the Central Basin, close to the area where [Schmittbuhl et al, 2016] and [Bohnoff et al 2017] identified the occurrence of deep, seismic repeaters based on the analysis of a larger data set. Deep multichannel seismics indicate that the Central Basin is cut by different E-W trending, normal faults that, most likely converge to form a strike slip structures at crustal depths (see figure 15 in [Bécel et al, 2009] and figures 2, 5, 6 in [Bécel et al, 2010]). The deep events of case study 3 could thus well occur along very close E-W trending, strike-slip faults. Therefore, the highly correlated, repeating events may (hypothesis 1) constantly activate the same patch of an active fault portion (e.g. indicator for identifying and evaluating the amount of creeping), or alternatively, these events may occur along very closely spaced faults. A specific, high resolution survey with loosely-spaced OBSs is needed to test either two hypotheses.

Note that all focal mechanisms have been derived by using the 3D velocity of this study. The lack of data (e.g. a limited number of OBS stations were used, only P-wave first polarities were considered, etc) could result in a poor quality of the focal mechanism solution. However, for all cases the derived focal mechanism are systematically consistent with the geological background of the area.

Comment R2.4: The authors state that a significant number of earthquakes occur along the axis of the Main Marmara Fault where the vertical seismic alignment will be expected, but also off-axis along the secondary faults in the Marmara Sea. The Ml 5.1 earthquake is associated with the main fault (MMF) in the Western High. Its focal mechanism gives a strike-slip faulting consistent with the strike of the MMF at this locality. Vertical alignment in seismicity is expected for the Ml 5.1 earthquake activity. Unfortunately, the mainshock and aftershocks are not related to the same tectonic structure. While the mainshock results from the MMF in strike slip character, the aftershocks are associated with faulting structures in shallower sediment (~1 or 2 km), generally involved with normal (or reverse) faults. This needs discussion and explanation.

Reply: In a companion paper, Géli et al, 2017 (in review in Scientific Reports) demonstrate that the sequence of aftershocks that followed the Ml 5.1 earthquake of July 25th occurred within a zone of gas generation and fluid over-pressuring in the 1.5-5 km depth range, from where pressurized gas is expected to migrate along the MMF, up to the surface sediment layers. Their argumentation is based on seismological data, but also on evidence from multi-channel seismic, geochemistry and heat flow data. See for instance in Figure R11, the distribution of the triggered seismicity, super-imposed on a multi-channel seismic line crossing the western high.

The question of “ultra-shallow seismicity” is also addressed in a companion paper in preparation by Batsi et al, showing that the well-constrained ultra-shallow earthquakes occur along normal faults curving through gas prone sediment layers. See Figures R5 and R6 and replies to comments R1.9 and R2.2.

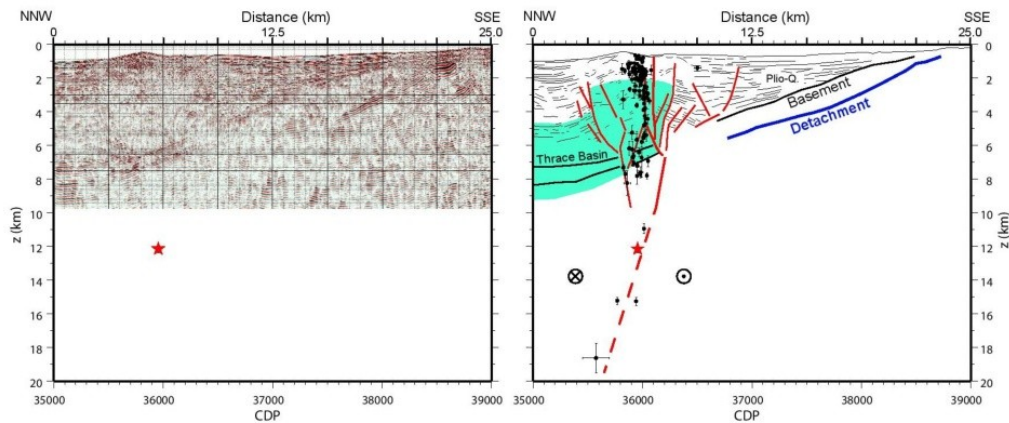


Figure R11: From Géli et al, in revision in *Scientific Reports*. Left panel displays the hypocenters of the aftershock sequence, superimposed on the Post-Stack Depth Migrated seismic section (see track line in Figure 2) that was shot during the Seismamara cruise in 2001 in the Western High area (courtesy of Mireille Laigle and Anne Bécel). Right panel displays the line-drawing along with the locations of the aftershocks that followed the M5.1 earthquake of July, 25, 2011. Continuous red line indicates the MMF. The dotted line within the sedimentary basin indicates the east-west oriented, secondary fault.

Comment R2.5: *Based on the micro-seismicity with high resolution and single/composite focal mechanism solutions obtained in this study, the authors do not discuss tectonic structure in the Western High and/or Central Basin. I think that the discussion part is too weak. Most of the seismicity is distributed over off-fault secondary faults.*

Reply: The focal mechanisms have been recomputed and the discussion part has been developed.

Comment R2.6: *Previous studies discussing seismicity and present-day tectonics in the Marmara Sea are not referenced in the manuscript. The following references should be added.*

- Pinar A, Kuge K, Honkura Y (2003) Moment tensor inversion of recent small to moderate sized earthquakes: implications for seismic hazard and active tectonics beneath the Sea of Marmara, *Geophys J Int* 153:133-145
- Orgulu, G., 2011. Seismicity and source parameters for small-scale earthquakes along the splays of the North Anatolian Fault (NAF) in the Marmara Sea, *Geophys. J. Int.*, 184, 385-404.

Reply: We thank the reviewer for this remark. The two missing references are now used in the discussion and included in the list of references.

Minor revisions of R2: 1) In line 102, number of basins in the Marmara Sea is given as 3, but they give names of four basins. 2) Some references are not defined in the manuscript such as Gürbüz et al., 2000 and Sato et al., 2004

Reply: Both revisions were taken into account.

Reply to Reviewer #3

Comment R3.1: The empirical relationship between v_p and v_s should be used to show V_s velocities as well as V_p/V_s in Figure 1. Values of V_p/V_s should be commented.

Reply: See Reply to comment R1.3. "The 1D model that we have used in Step 2 of the location procedure is shown in green in Figure R4. It includes a non-constant V_p/V_s ratio. The Castagna formula (red curve) WAS ACTUALLY NOT USED in our work. This formula may yield estimations that fit with our V_s velocity model at depth of $\sim 4 \pm 1$ km. However, Castagna's velocity model is too low at depth < 3 km and too high at depth > 5 km. Hence, references to Castagna's formula and the analogy to mudrock were removed from the revised version, as they are not useful ».

We agree with the reviewer comment that using a non-constant V_p/V_s ratio in steps 3 to 5 of the location procedure could lead to location bias (e.g. [Maurer and Kradolfer 1996]). Using not constant V_p/V_s (as shown in Figure R13, for instance) would certainly improve the location accuracy, but not fundamentally change our main results, regarding the well constrained events (e.g. those that comply with the seismological criteria that were set up during the location process). Hence, due to deadline constraints, we leave the issue to future workers.

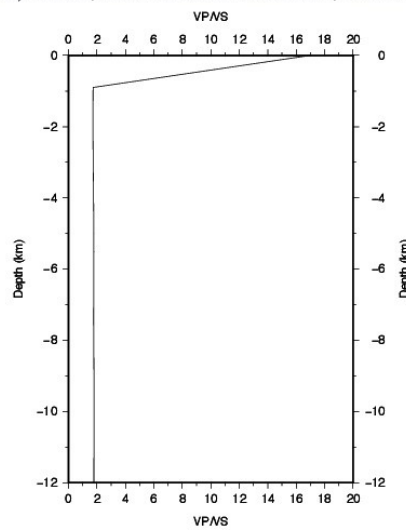


Figure R12. V_p/V_s ratio used in Steps 1 and 2 of the location process, based on Géli and Cros (2013) and Lomax (2014).

Comment R3.2. The P and S phases have the same weight for the localization. Is this choice consistent with their final respective residuals? One usually considers that the S wave velocity is less constrained and more variable than P wave velocities in soft sediments, where v_p/v_s significantly differs from 1.8; this would not be the case here? (see also previous question)

Reply. This has been clarified in the revised manuscript. Let us first recall that all picks recovered from the Picker algorithm of Lomax were systematically checked visually and modified manually. Individual weights were systematically assigned for P and S wave phases. Hence different weights have been manually assigned and considered for P and S phases by using the 3 components of the geophone. In most cases, weaker weights have been given to S waves (e.g. hardest to be picked with regard the P phases). See also reply to comment R1.1: the vertical component was used for the detection of P -wave arrivals while the two not-oriented horizontal components were used for the S -wave onsets (e.g. strong velocity contrasts in areas with shallow sediments could generate converted phases, hence their identification on vertical channels could be misleading)

Comment R3.3: For the case studies, the authors selected events with well correlated waveforms, in order to benefit from their a priori close proximity. This also allows to work with double difference techniques for a better relocation. The correlation between waveforms for two nearby events at two different stations can be used to estimate the local ratio V_s/V_p , taking the ratio of the double differences P over S? Would this be accurate enough to get more information on the velocity structure?

Reply: Yes indeed, this could be an efficient way for getting further information on the velocity structure of the western part of the SoM. This is particularly true in the area below the mud volcano, where the presence of gas likely results in short scale heterogeneities in the velocity structure. Therefore, the procedure suggested by Reviewer 3 is expected to be the most efficient for the well correlated events that followed the Ml 5.1 earthquake of July 2011. Unfortunately, the central OBS did not work, so that no station was available in the mud volcano area, and the benefit of the suggested procedure should likely be less than expected. Consequently, due to deadline constraints, we leave this for future work. This again could be considered for future work.

Comment R3.4: The authors write that the best results for the relocation are obtained when the delay between seismograms is calculated over the whole (P+S) time window, contrary to what is usually done, separating P and S correlation operations. This approach and the result require some explanation.

Reply: This comment R3.4 is the same as Comment R.1.2. Thus, see reply to Comment R1.2.

Comment R3.5: The composite focal mechanisms should be presented in a Schmitt diagram with their measured polarities.

Reply: See below, figure S5 of Supplementary Information.

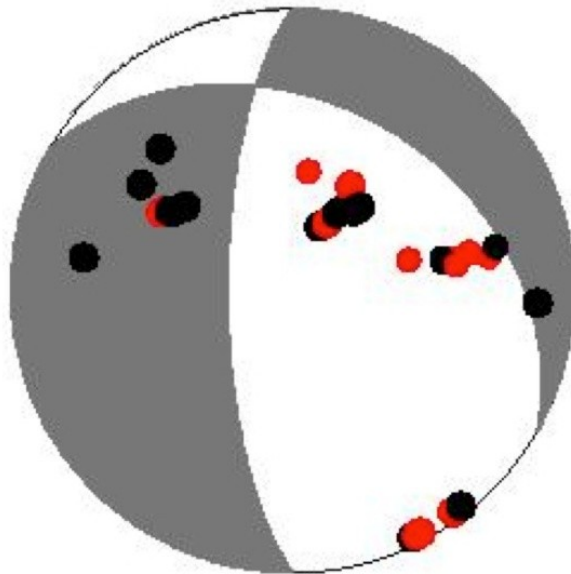


Figure S5: Composite focal mechanism computed for 10 events triggered by the M 5.1 earthquake of the 25th of July, 2011 (see Table S6). Computation with HASH software (Hardebeck and Shearer, 2008), with the measured polarities represented with red and black circles, down and up motions respectively, calculated with the 3D velocity model of this study. Resulting focal mechanism: Strike/Dip/rake=300°/34°/-145°.

Comment R3.6: For the calculations of the focal mechanisms, the incidence angle of the P wave at the source is strongly dependent on the local velocity and on the depth. Can one estimate the related uncertainties in this angle, and the resulting uncertainties on the final mechanism?

Reply: We fully agree with Reviewer 3 that the incidence angle of the P wave at the source is strongly dependent on the local velocity and on the depth. We have recalculated the focal mechanisms. For case study 1, we find now two different focal mechanisms depending on the velocity model (see below, figure 6b of the present, revised manuscript):

- deep location and strike-slip for 1D location
- shallow location and normal faulting for 3D location.

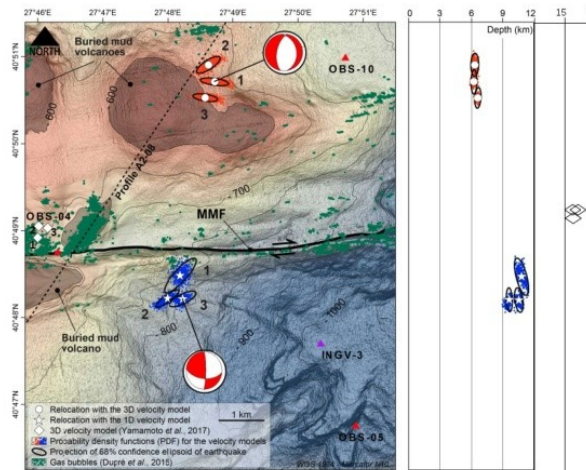


Figure 6b of the present, revised manuscript

Comment R3.7 (Case study 1). The authors write that if the event was located just beneath OBS04, as in Yamamoto 2017, the $t_s - t_p$ delay would be minimal at this station. This is not necessarily true, as it depends on the velocity model and on lateral heterogeneities.

Reply: What we observe at OBS04 is that the $t_s - t_p$ delay is maximum AND t_p is minimum. From the observation that the P-wave arrives first at OBS04, we infer that, if the event was located just beneath OBS04, as stated by Yamamoto et al (2017), the $t_s - t_p$ delay would be minimal at this station. We have corrected the text accordingly. This example strongly suggests that the S-velocity is likely very slow below the Western, due to the presence of gas in over-pressurized gas sources in the 1.5 – 5 km depth range and in the uppermost sediments.

Comment R3.8 (Case study 1). The discussion on the arrival times is done on the comparison between ($t_s - t_p$) for the different OBS. But as the S velocities are less reliable, a first discussion and comment on the P wave arrival times would be more appropriate.

Reply: Due to the presence of gas below the Western High, it is expected that, for shallow earthquakes, first P-wave arrivals come from grazing rays propagating in the shallow layers having low P- and low S-velocity layers. As a result, $t_s - t_p$ may be very large, due to both small P and small S velocities. This is well illustrated in the 2D ray-tracing displayed in Figure R13 (see reply to Comment R3.10).

Comment R3.9 (Case study 1). The composite focal mechanisms should be presented in a Schmitt diagram with their measured polarities.

Reply: The composite focal mechanism with polarities is shown below (Figure S2 of Supplementary material).

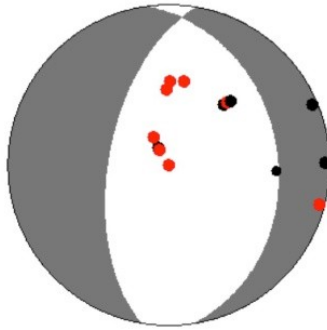


Figure S2: Composite focal mechanism of case study 1, computed with HASH software (Hardebeck and Shearer, 2008), with the measured polarities represented with red and black circles, down and up motions respectively, calculated with the 3D velocity model of this study. Resulting focal mechanism: Strike/Dip/rake=190°/59°/-80°.

Comment R3.10 Case study 2). It is surprising that earthquakes with well correlated waveforms ($C > 0.8$) could provide such different localization (from 3 to 20 km in depth) : indeed, one would expect very similar $t_s - t_p$ delays. This requires some explanation and comment.

Reply:

To address the reviewer's concerns, it is important to understand that, for shallow earthquakes, the situation is similar to what is observed in refraction seismics. For short (below critical) source-receiver offsets, first P-wave arrivals come from grazing rays propagating in the shallow, low-velocity layers. Similarly, for shallow earthquakes, first P-arrivals have preferentially propagated within shallow layers. As a result, $t_s - t_p$ may be very large at small source-receiver offsets, due to both small P and small S velocities.

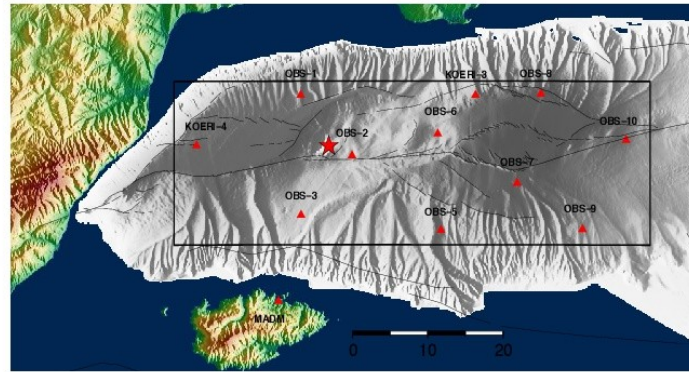


Figure R3-10-1 Red triangles indicate seismic stations, respectively: cabled, permanent Broad-Band Observatories operated by KOERI, from 2009 to 2012; OBSs deployed by Ifremer from April 15th to July 31st, 2011; and MADM installed on Marmara Island [Karabulut et al, 2014]. The black rectangle delineates the area covered by the 3D, high-resolution P-wave velocity model.

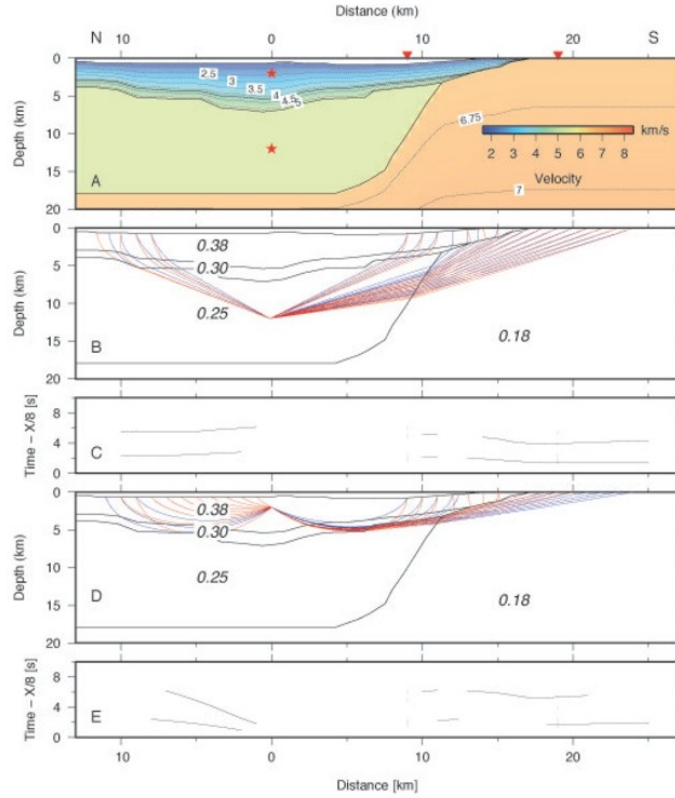


Figure R3.10-2: A. P-wave velocity model used in the present calculation. Red triangles at source-receiver distance of 9.3 km and 20.5 km indicate the position of OBS03 and MADM, respectively. In the basin, velocities are derived from the high-resolution velocity model described in Appendix 2. Velocities in the Marmara Island area (right part of the figure) are hypothesized, based on Altinok and Alpar [2005] and on Le Pichon et al [2016]. B. Ray tracing computed using Raylnvr [Zelt and Smith, 1992], assuming that the clustered events are located at a depth of 12 km below seafloor. Numbers indicate Poisson Ratio values assigned to each layer. C. computed travel times. Calculated and measured values of $ts-tp$ at OBS03 and MADM station are indicated in the table below.

		OBS03	MADM
Observation	clustered events	$(ts-tp)_{mes}=3.83$ s	$(ts-tp)_{mes}=2.95$ s
	mainshock	$(ts-tp)_{mes}= \text{NaN}$ (OBS saturation)	$(ts-tp)_{mes}= 2.65$ s
Best Fit Model	Shallow source ~ 2 km	$(ts-tp)_{obs}=3.85$ s	$(ts-tp)_{obs}=3.55$ s
	Deep Source ~ 12 km	$(ts-tp)_{obs}=2.5$ s	$(ts-tp)_{obs}=2.85$ s

Table 4: S- to P-wave arrival time difference ($ts-tp$), measured and modelled at OBS03 and MADM, respectively.

Comment R3.11 (Case study 2). The composite focal mechanisms should be presented in a Schmitt diagram with their measured polarities.

Reply: The composite focal mechanism with polarities is shown below (Figure S3 of Supplementary material).

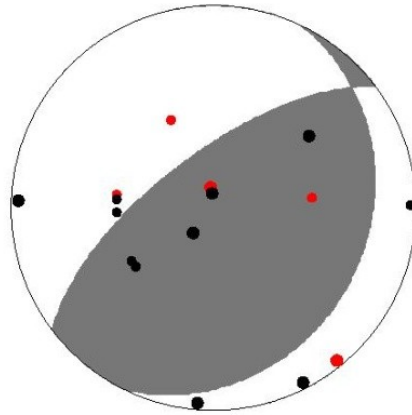


Figure S3: Composite focal mechanism of case study 2, computed with HASH software (Hardebeck and Shearer, 2008), with the measured polarities represented with red and black circles, down and up motions respectively, calculated with the 3D velocity model of this study. Resulting focal mechanism: Strike/Dip/rake= $233^{\circ}/67^{\circ}/101^{\circ}$.

Comment R3.12 (Case study 3). The composite focal mechanisms should be presented in a Schmitt diagram with their measured polarities.

Reply: The composite focal mechanism with polarities is shown below (Figure S4 of Supplementary material).

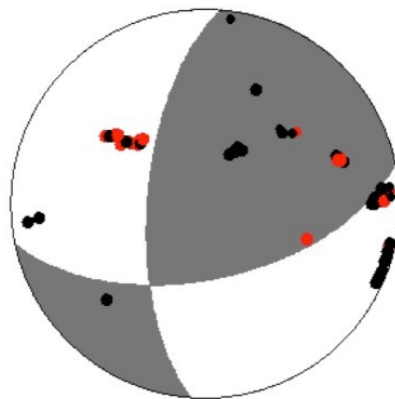


Figure S4: Composite focal mechanism of case study 3, computed with HASH software (Hardebeck and Shearer, 2008), with the measured polarities represented with red and black circles, down and up motions respectively, calculated with the 3D velocity model of this study. Resulting focal mechanism: Strike/Dip/rake= $78^{\circ}/58^{\circ}/151^{\circ}$.

Comment R3.13: *It is written that the ultra shallow earthquakes of 2011 and 2014 belong to the same aftershock sequence (line 388). This seems inappropriate, as 3 years is too long for a single aftershock sequence, and there is no mention of another triggering events for the 2014 swarm... What do the authors mean ?*

Reply: This was corrected. The shallow earthquakes of the two different recording periods do not correspond to the same aftershock sequence.

Comment R3.14: *The discussion of the localizations, in comparison with those of Yamamoto 2017 (for the 2011 period) and of Schmittbuhl et al 2015 (for 2014), is a bit confusing. It should be clarified by a comparative study of the catalogues: some events are common to all catalogues, some only in the present study, and some others only in the other catalogues... Their inventory should be presented, with their respective magnitudes and localizations, and related uncertainties.*

Reply:

Yamamoto's: The comparison between our location results and Yamamoto's (for the 2014 period) has been included in the revised version. Figure R15 displays the location of the events that were detected in common in this work and in Yamamoto's, during the overlapping period (from September 19th to November 14th, 2014). The location results provide very different views (Figure R13). West of 27°50'E, Yamamoto et al, 2017 find systematically deep, strike-slip events occurring along the MMF and along EW striking associated structures. These locations are consistent with pure strike-slip motion along the MMF. In contrast our locations suggest normal faulting along SW-NE striking features north of the MMF. The differences in the two sets of locations result in differences in:

- The location method: linear versus non linear.
- The network geometry: we used a network of more than 9 OBS evenly distributed within a circle of less than 10 km centred on the Western High; Yamamoto et al, 2017, used an elongated network of 10 OBS stations distributed all along the MMF.
- The 3D velocity model (see § on the Construction of the 3D Western Marmara Fault).

Besides the limitations of our work, we consider that the network geometry and the 3D-velocity model that we use are more appropriate to take into account the heterogeneity of the Marmara Trough.

Schmittbuhl's. The main points of the comparison between our results and those of Schmittbuhl (for the 2011 period) are summarized hereafter:

- In Schmittbuhl (2016)'s catalog, hypocentral depths are highly dispersed for the low-magnitude ($\sim M_1 < 3$) aftershocks that followed the M 5.1 earthquake. The dispersion appears to depend on magnitude and is significantly reduced for earthquakes of magnitude $M_1 > 3$ (see also Figure R14 below).
- In the REAKT Project report (Deliverable D2.2), Karabulut and Aktar (2013)⁷ published the seismograms of highly correlated events (yellow dots in Figure R17, recorded by an on-shore station installed on the Marmara Island (see Figures R15 and R16). These well correlated events are found to occur within the sedimentary basin below the Western High.
- in our location results, the hypocenters of these common are systematically 2 to 4 km shallower, within the pressurized gas source layer (Figure R17).
- In conclusion: event though, following the editor's recommendation, we do "**acknowledge the uncertainty for the shallowest earthquakes and leave resolving the depth of the shallow seismicity for future work** », our results do confirm that the clusters documented by Karabulut and Aktar (2013) occurred within the thick sedimentary sequence and not at crustal depths.

⁷ Karabulut, H., Aktar, M., (2012), REAKT-Project Deliverable D2.2, <http://www.reaktproject.eu/deliverables/REAKT-D2.2.pdf>

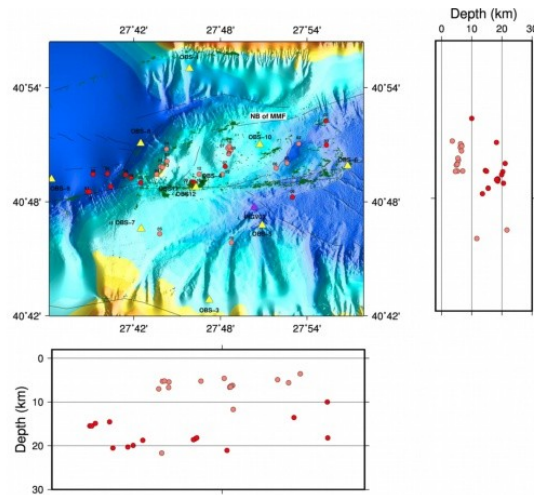


Figure R13: Comparison of location results for the common events, listed both in Yamamoto et al, 2017 (orange dots) and in this work (red dots), that occurred during the overlapping period, from September 19, to November 14, 2014. Labels (from 1 to 16) correspond to the number of each individual event listed in Table below (see Table 8 in main text). Green dots correspond to gas emissions sites, after [Dupré et al, 2015]. Bathymetric map of upper left panel with a node spacing of 10 meters and contour interval of 20 m (see Data and Resource section). Black lines indicate main structural features, after [Sengör et al., 2005].

No	Date-Time	This study				Yamamoto et al, 2017			
		Latitude (°)	Longitude (°)	Depth (km)	Mag	Latitude (°)	Longitude (°)	Depth (km)	Mag
1	26 September 06:02:55	40.8309	27.7308	5.25	0.9	40.8091	27.6466	15.46	1.7
2	01 October 14:44:49	40.8509	27.8905	3.55	0.7	40.8710	27.9218	10.00	1.3
3	03 October 21:40:22	40.8340	27.8769	5.59	0.7	40.8497	27.9223	18.2	1.7
4	04 October 11:58:34	40.8243	27.7265	7.00	1.9	40.8247	27.6696	14.54	2.2
5	12 October 04:58:34	40.7719	27.73	21.67	0.5	40.8167	27.7080	18.75	1.7
6	17 October 19:52:52	40.8295	27.8642	4.90	0.8	40.8041	27.8832	13.54	1.4
7	18 October 10:17:43	40.8471	27.8087	6.61	1.1	40.8310	27.8056	21.07	1.9
8	24 October 14:18:24	40.8356	27.7383	5.41	0.7	40.8241	27.6531	14.89	1.4
9	25 October 01:46:52	40.8452	27.812	6.21	0.9	40.8174	27.7668	18.62	1.5
10	25 October 03:05:00	40.8484	27.8104	6.29	1.7	40.8171	27.7691	18.38	1.9
11	25 October 04:21:38	40.8421	27.8096	6.59	0.9	40.8152	27.7667	18.61	1.5
12	25 October 09:28:57	40.8242	27.7754	5.22	0.5	40.8165	27.7706	18.19	1.6
13	25 October 04:21:38	40.8303	27.7331	5.19	0.9	40.8089	27.6489	15.46	1.6
14	26 October 07:41:51	40.8463	27.7379	6.68	0.7	40.8236	27.6907	20.28	2.0
15	27 October 21:22:10	40.8240	27.8023	4.59	0.7	40.8134	27.6734	20.52	1.4
16	05 November 23:31:49	40.7643	27.8128	11.69	0.9	40.8210	27.6969	19.92	1.6

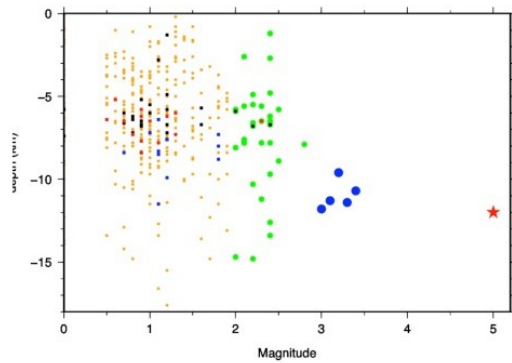


Figure R14. Depths of the aftershocks that followed the M 5.1 event of July, 25, 2011 (based on 1D-locations after *Schmittbuhl et al, 2016*) plotted versus magnitude. Blue, green and brown dots represent events of magnitude M_1 lower than 2, comprised between 2 and 3 and greater than 3, respectively. Highly correlated events are plotted as squares (see Figures R17).

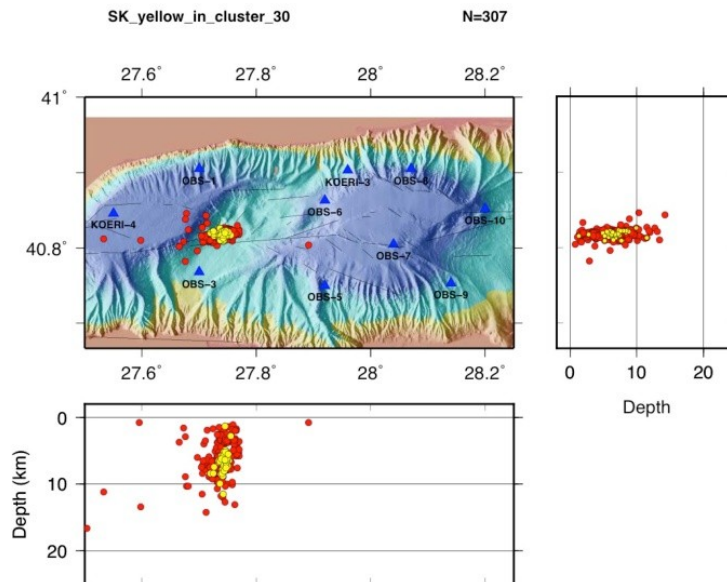


Figure R15. 1D-Location of the aftershocks that followed the M 5.1 event of July, 25, 2011, after *Schmittbuhl et al, 2016*. Yellow dots represent the locations of the highly correlated events displayed in Figures R18a, R18b and R18c.

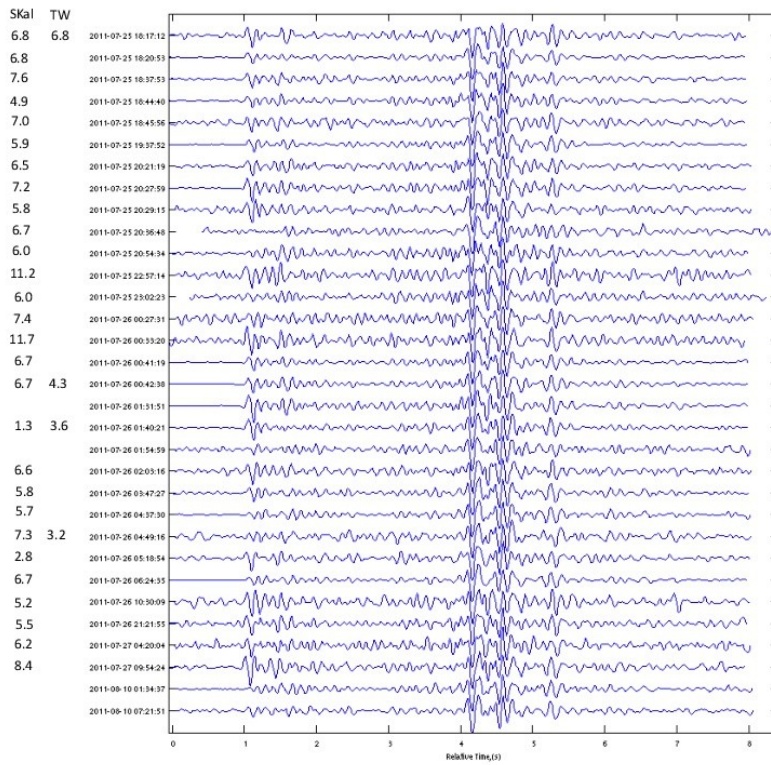


Figure R16. After Aktar & Karabulut et al, [2013]. Clustered events with correlation coefficient > 0.7 recorded at MADM station, onshore Marmara Island for the sequence that followed the M.1 earthquake of July, 25, 2011. SKal are depth estimates by Schmittbuhl et al (2015). TW are for "This Work" (results obtained by NonLinLoc for absolute locations and HypoDD-3D for relative locations).

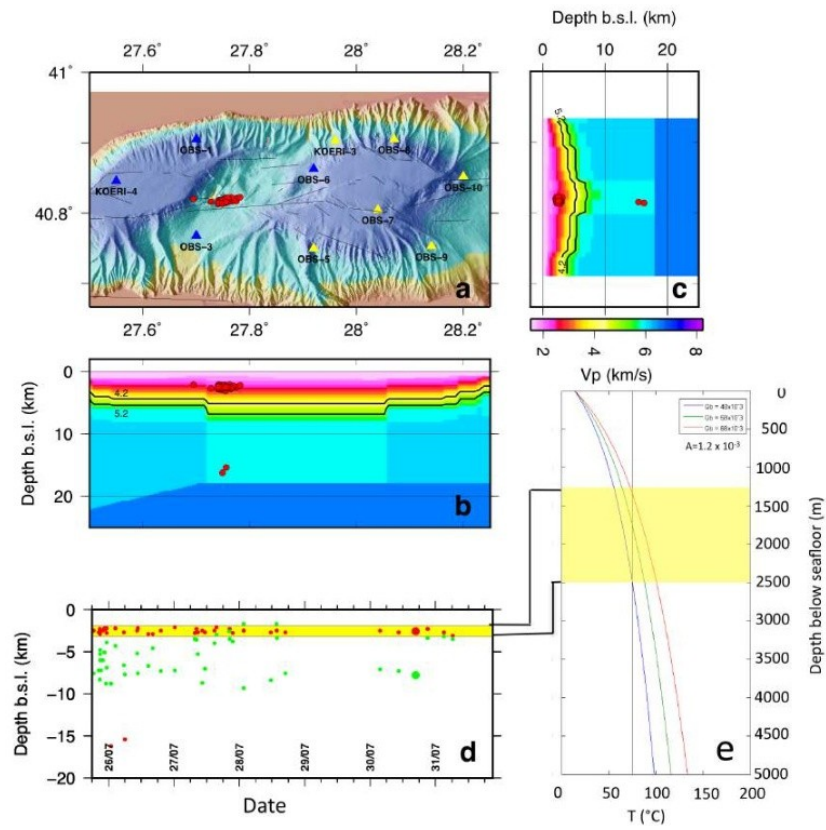


Figure R17: Red dots in panels a-b-c-d correspond to selected, well correlated ($C > 0.7$) events from the sequence that followed the M.1 earthquake of July, 25, 2011 (locations obtained by NonLinLoc for absolute locations and HypoDD-3D for relative locations). Green dots in panel d are the corresponding locations by Schmittbuhl et al (2015), which are systematically 2 to 4 km deeper than those of this work. The yellow stripe in Panel e indicates the depth range of the pressurized gas sources, based on geochemical and thermal data.

Comment R3.15: The possibility of creep of the deep part of the fault, beneath the western high, as proposed by Schmittbuhl et al. 2015, should be better discussed here : how could the gas seepage and the ultra-shallow seismicity be linked, directly or indirectly, to this deep creeping ?

Reply: By considering that: (1) the western segment of the MMF is creeping following Schmittbuhl et al (2015); and (2) that the central segment -where no gas emissions are observed- is locked, based on the absence of historical, large earthquakes since 1766 and based on Sakic et al (2016), it can be proposed that a causal relation exists between i) creeping at crustal levels, ii) increase in sediment permeability within the fault zone and iii) gas emissions.

The following scenario may indeed be proposed: Creeping at crustal levels likely induces deformation within the upper, sediment layers, which in turn contribute to maintain high permeability within the damage zone, which in turn may enhance gas migration up to the surface. In addition, the repeated earthquakes of intermediate magnitude that frequently occur along the western segments of the Main Marmara Fault, may trigger aftershocks in relation to the presence of gas, within the gas source (at depths ranging from ~1.5 to 5 km) and within the uppermost, gas-prone, sediment layers, which may result in gas emissions from the seafloor.

For information to the reviewer, let us here quote the abstract presented by Pierre Henry at the MARFLUID Symposium, held in Brest from October 16-19, 2017.

Creep and seep: the North Anatolian Fault in the Sea of Marmara
Pierre Henry
Aix-Marseille Université, CNRS, Coll. France, IRD, CEREGE, Aix-en-Provence

« Since the 1999 İzmit-Kocaeli earthquake, the offshore segments of the North Anatolian Fault system in the Sea of Marmara have been considered at an imminent risk for a large earthquake. The expected earthquake has not happened yet and studies based on land geodesy could not detect interseismic loading on the fault segment that directly menaces Istanbul. The need to clarify the slip rate and locking state of the offshore faults is motivating current studies and seafloor monitoring projects. An acoustic ranging experiment is ongoing in the framework of EMSO and early results indicate that the Istanbul segment is not creeping at the seafloor at a significant rate. Other recent results include new estimations of the geological slip rate on the main strike slip fault branch and of the amount and timing of extension, assessment of earthquake recurrence intervals and segmentation based on turbidite/homogeneous records, mapping of fluid and gas emissions at the seafloor and of their relationships with active faults and sedimentary structures. Overall, the slip rate on the MMF represents 2/3 to 3/4 of the Eurasia-Anatolia plate motion. Creep on this fault appears to influence seismogenesis, and may locally take up a significant part of the plate motion. A relation is found between the distribution of gas emissions along the faults and occurrence of background seismicity and creep. This may be explained if sediment deformation around a moving fault favor fluid migration through the sediment. Segments remaining fully locked for long periods of time would thus be comparatively less favorable for fluid expulsion at the seafloor than segments with creep or frequent moderate size earthquakes. Temporal variations of gas emission along the fault and of microseismicity rates both appear as potential indicators of strain rate variations and should be considered in an integrative monitoring strategy. »

References:

- Aretusini, S., S. Mittempergher, O. Plumper, E. Spagnuolo, A. F. Gualtieri, and G. Di Toro (2017), Production of nanoparticles during experimental deformation of smectite and implications for seismic slip, *Earth and Planetary Science Letters*, 463, 221–231, doi:10.1016/j.epsl.2017.01.048.
- Bécel, A., Laigle, M., De Voogd, B., Hirn, A., Taymaz, T., Galvé, A., Shimamura, H., Murai, Y., Lépine, J.C., Sapin, M., and Özalaybey, S. (2009). Moho, crustal architecture and deep deformation under the North Marmara Trough, from the SEISMARMARA Leg 1 offshore- onshore reflection-refraction survey, *Tectonophysics* 467: 1-21.
- Bécel, A., Laigle, M., De Voogd, B., Hirn, A., Taymaz, T., Yolsal-Cevikbilen, S., Shimamura, H. (2010): North Marmara Trough architecture of basin infill, basement and faults, from PSDM 490: 1-14.
- Dupré S., et al. (2015). Tectonic and sedimentary controls for widespread gas emissions in the Sea of Marmara. Results from systematic, ship-borne multibeam echosounder water column imageries, *J. Geophys. Res., Solid Earth*, 120, doi:10.1002/2014JB011617.
- Bonhoff, M., et al. (2017), Repeating Marmara Sea Earthquakes: Indications for fault creep, *Geophysical Journal International*, 210, 332-339, doi.org/10.1093/gji/ggx169 .
- Husen, S., E. Kissling, N. Deichmann, S. Wiemer, Giardini, D., Baer M. (2003), Probabilistic earthquake location in complex three-dimensional velocity models: Application to Switzerland, *J. Geophys. Res.*, 108, doi: 10.1029/2002JB001778
- Faulkner, D. R., T. M. Mitchell, J. Behn, T. Hirose, and T. Shimamoto (2011), Stuck in the mud? Earthquake nucleation and propagation through accretionary forearcs, *Geophys. Res. Lett.*, 38(18), doi:10.1029/2011GL048552.
- Karabulut, H., Schmittbuhl, J., Özalaybey, S., Lengliné, O., Kömeç-Mutlu, A., Durand, V., Bouchon, M., Daniel, G., Bouin, M.P., (2011). Evolution of the seismicity in the eastern Marmara Sea a decade before and after the 17 August 1999 Izmit earthquake, *Tectonophysics*, 510, 17–27.
- Lomax, A., A. Michelini, and A. Curtis (2008). Earthquake location, direct, global-search methods. In *Encyclopedia of Complexity and System Science*, pp. 2449-2473, ed. Meyers, R. A. Springer, New York.
- Maurer, H., and U. Kradolfer (1996), Hypocentral parameters and velocity estimation in the western Swiss Alps by simultaneous inversion of P- and S-wave data, *Bull. Seism. Soc. Am.*, 86, 32-42.
- Romano, F., E. Trasatti, S. Lorito, C. Piromallo, A. Piatanesi, Y. Ito, D. Zhao, K. Hirata, P. Lanucara, and M. Cocco (2014), Structural control on the Tohoku earthquake rupture process investigated by 3D FEM, tsunami and geodetic data, *Sci. Rep.*, 4, doi:10.1038/srep05631.
- Sakic, P., Piété, H., Ballu, V., Royer, J.-Y., Kopp, H., Lange, D., Petersen, F., Özeren, S., Ergintav, S., Géli, L. Henry, P., Deschamps, A., (2016), No significant steady state surface creep along the North Anatolian Fault offshore Istanbul: Results of 6 months of seafloor acoustic ranging, *Geophys. Res. Lett.*, 43, 6817–6825, doi:10.1002/2016GL069600.
- Schmittbuhl, J., Karabulut, H., Lengliné, O., and Bouchon, M., (2016). Long-lasting seismic repeaters in the Central Basin of the Main Marmara Fault, *Geophys. Res. Lett.*, 43, 9527–9534, doi:10.1002/2016GL070505

III.1.3 Implications not discussed in the BSSA Paper

III.1.3.1 On the use of b-values

Using b-values as indicator of creeping is subject to debate. For instance, [Schorlemmer and Wiemer, 2005] consider that the low b-values obtained for the different segments of the San Andreas Fault, provide indications on the presence of highly stressed patches. In contrast, Schmittbuhl et al, [2015] interpreted the low b-values that characterize the western segments of the MMF as indicators of creeping.

Besides this debate, we believe that the b-values computed by Schmittbuhl et al, [2015]) are questionable *per se*, for at least two reasons:

- our results show that a great number of low-magnitude earthquakes are shallow and not crustal ; as a result, these events do not reflect crustal creeping.
- Also, a great number of events are located on secondary, normal faults, off the axis of the MMF; these events do not reflect strike slip motion *stricto sensu* along the MMF.

III.1.3.2 On possible triggering effects

Two puzzling observations need to be noted:

- On September 23rd of 2014 at 01:37 GMT, an earthquake of magnitude M_l 3.5, occurred on the offshore sector of the Limnos island, along the Ganos fault, which prolongates the NAF to the west of the Sea of Marmara. After 1 hour and 17 minutes, a small crisis of 17, low magnitude ($1.64 < M_l < 2.2$) earthquakes occurred below the Western High, within a distance of ~ 234 km (see Figure III.1.3.2.1). The crisis lasted about 3 hours (from 02:54 until 05:39 GMT). After relocation, the “well-correlated” events ($cc > 0.8$) were found to occur ~ 6 km below sealevel, ~ 4 km to the north of the MMF, along E-W trending, normal faults. One

possible hypothesis (yet to be tested) is that the September 23rd crisis may have been remotely triggered by the M_l 3.5 earthquake which ruptured the Ganos Fault on the same day. This crisis originated in the same area as the cluster which occurred on October 25th 2014, however no triggering candidate event is found to explain the events of October 25th, 2014 (see § III.1.2).

- On April 22nd 2011 at 07:50 GMT, an earthquake of magnitude M_l 4.3, occurred along the Ganos Fault, about 37 km to the NNW of Limnos island. Some days afterwards, from April 26th until May 18th, a series of 10, low-magnitude ($M_l < 2$) earthquakes with a strike-slip focal mechanism occurred within the crust below the Central Basin, ~ 13 km below sea level. It is interesting to note that these events are located within 6 km distance from the 9 long-lasting, strike-slip seismic repeaters that were documented by [Schmittbuhl *et al*, 2016] for the period between 2008 and 2015 (see Figure III.1.3.2.1).

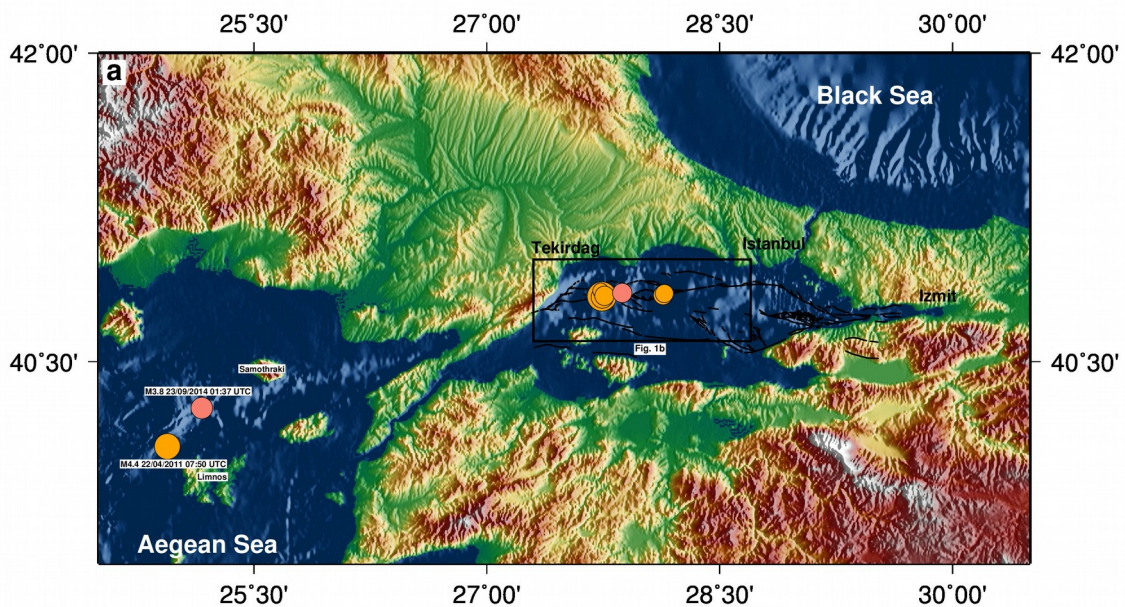


Figure III.1.3.2.1: General view of the SoM between the Black Sea and the Aegean Sea. Black lines indicate the main structural features of the Marmara Fault system ([Sengör *et al*, 2014]). Note the continuation of the Ganos Fault. Orange and magenta circles for local and remote (along the Ganos Fault) seismicity in 2011 and 2014 respectively.

Previous studies have shown that an earthquake may be followed by nearby or even distant events, that have been presumably triggered by stress changes of less than 1 bar (e.g. [King et al,1994], [Helmstetter et al, 2002]). Earthquakes occurring along the Ganos fault may well remotely trigger micro-earthquakes along the Ganos-MMF system, but further modelling work is needed to confirm our hypothesis, by using stress transfer theory (dynamic versus static).

III.2 Deciphering the origin of the ultra-shallow (< 1 km) micro-seismicity

III.2.1 General considerations

Progress in high-resolution seismics and acoustic imagery in the water column have revealed that gas -may it be as free gas or gas hydrates- is of common occurrence in sub-seafloor, marine sediments. The role of gas hydrates on geohazards has been widely studied, and the destabilization of gas hydrates is now recognized to be a major cause of gravity slope instabilities, as well as a potential hazard for the earth climate. In contrast, the relations between shallow seismicity and gas occurrence in near-surface sediments has been hardly documented. The major reason for this is that, due to the difficulties of observation in submarine environments, the existence of “ultra-shallow” seismicity has been hardly recognized (in general, when referring to “shallow earthquake”s in seismology, one mostly refers to events at depths < 10 km; here we will use the term “ultra-shallow” to refer to earthquakes at depths < 1 km).

In continental environments, cases of shallow earthquakes are documented for mines and gas fields, in depleted layers at depths of a few hundred meters. Other cases of shallow seismicity have been reported, like for instance (i) in Tricastin, lower Rhone Valley, France, (e.g. Thouvenot et al, 2009)

where a cluster of events was found to occur within 200 m from the surface, probably due to flooding (e.g. seasonal groundwater recharge and rainfall), (ii) at Vulcano Island in Italy, where they have recorded ultra micro-earthquakes of $M < 2$ at depths < 1.5 km, probably associated with both fracturing and degassing mechanisms (Gambino, et al, 2009), (iii) in California, at the Geysers Geothermal field, where micro-earthquakes were found to occur near the surface mainly above the reservoir at depths ranging from 220 to 1000 m (e.g. Rutledge, et al, 2002), (iv) in SE Brazil where a very shallow cluster of small events was found to occur within 1 km from the surface, induced by water percolation (e.g. [Agurto-Detzel, et al, 2017]), etc. In most cases, the seismicity seems to have been triggered or induced by fluid-related process, which have been shown to control, under certain circumstances, the nucleation, arrest and recurrence of earthquake rupture (e.g. [Rice and Cleary, 1976]).

For submarine environments, in contrast, no documented example of ultra-shallow seismicity has come to our knowledge. In addition to the monitoring difficulties that hamper the depth determination of shallow events, the common belief is that soft, marine clays, which normally exhibit ductile behaviors, cannot sustain the differential stress required for producing earthquakes. Therefore, we hereafter consider in further detail the sequence of ultra-shallow cluster of aftershocks that occurred in the upper-most sediment layers (at depths < 600 m), following the $M_w 5.1$ strike-slip earthquake of July 25th, 2011 (see Figures III.2.1.1 and III.2.1.2).

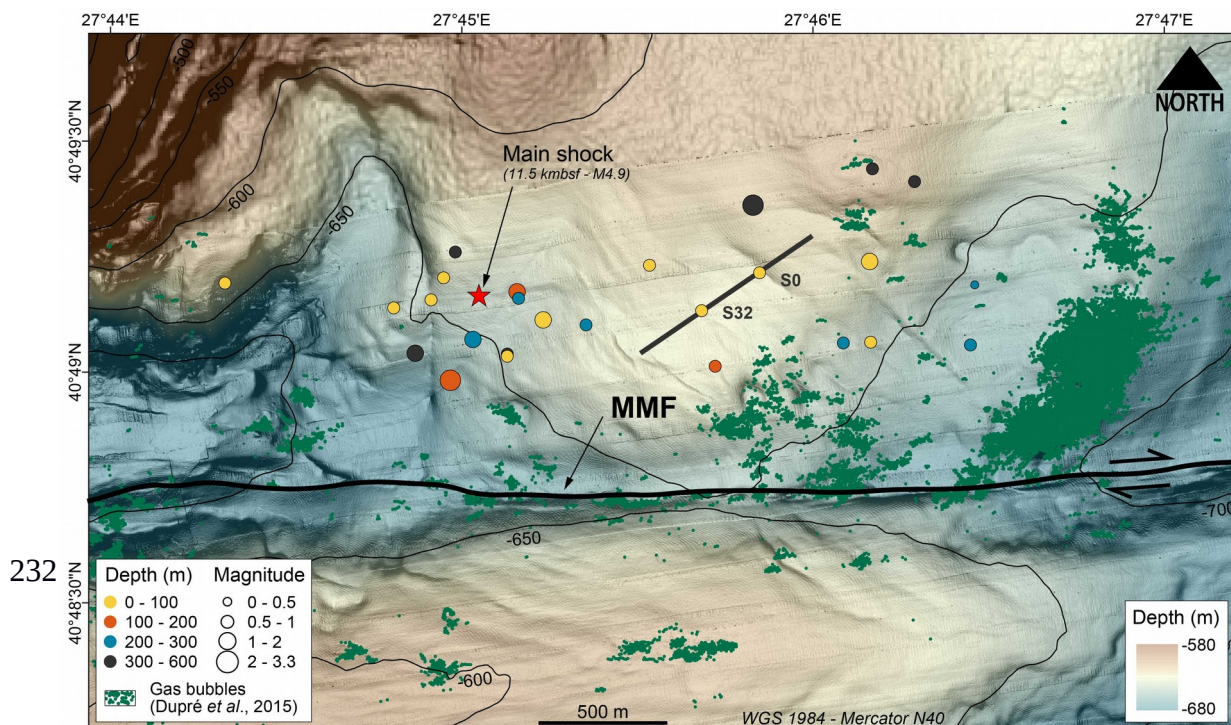
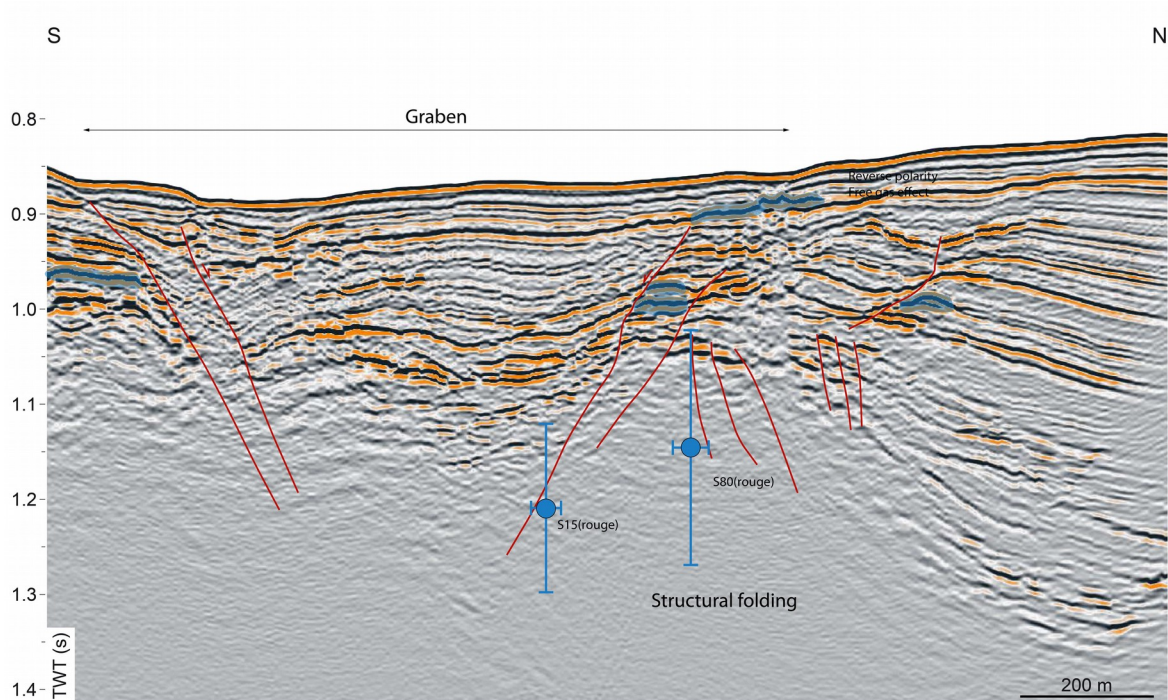


Figure III.2.1.1: Bathymetric map showing the ultra shallow earthquakes used for this study (e.g. different colors correspond to depth range and circles are proportional to magnitude). The red star indicates the mainshock, whereas the green dots show gas emission sites that were acoustically detected using the shipboard multibeam echosounder system of R/V Le Suroit during the Marmesonet cruise in 2009, e.g. 2 years before the M5.1 earthquake that ruptured the Main Marmara Fault on July 25th, 2011 (from [Dupré et al., 2015]). Add inset showing the map location within the SoM.



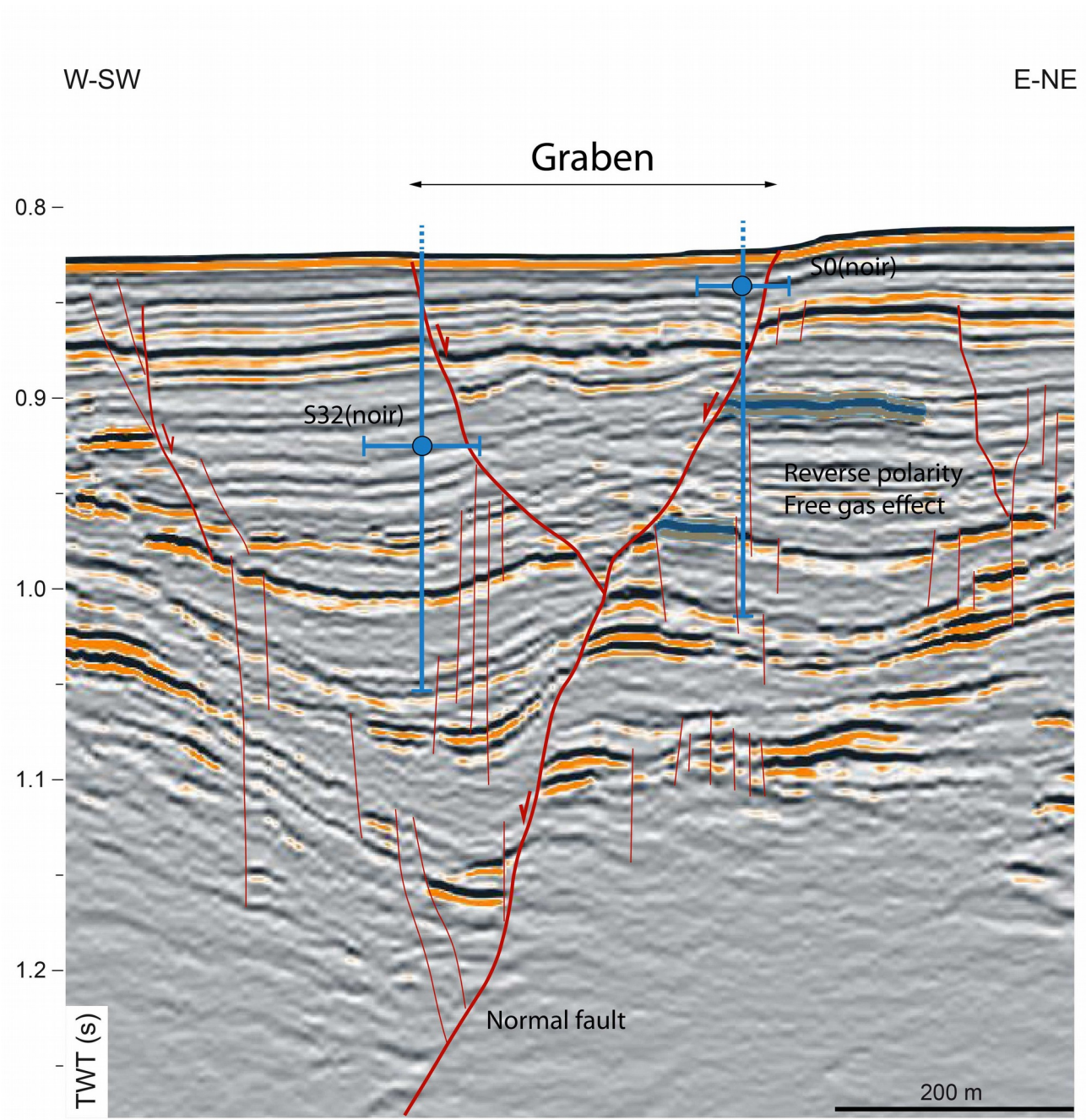


Figure III.2.1.2: Examples of ultra-shallow earthquakes, shown with blue dots localised on 3D seismics (upper and bottom figures). Blue vertical lines indicate the horizontal and vertical uncertainties of the earthquake location of each aftershock. Red lines indicate faults.

III.2.2 Gas-related “ultra-shallow” seismicity

Very shallow sediment is not expected to be able to host earthquakes as they have been observed to be aseismic in nature. Laboratory experiments on clays have shown them to exhibit velocity strengthening behaviour at low slip rates making earthquake nucleation difficult in such material [Saffer *et al*, 2012]. However experiments at high slip-rates (i.e. > 2 m/s) have shown clays switching to velocity weakening behaviour [Faulkner *et al.*, 2011; Aretusini *et al*, 2017]. With the very low strength of clays, clay material can react seismically to rupture that propagates into it, one such example being the 2011 Tohoku earthquake where 30m of slip is estimated to have occurred in clay like material [Romano *et al.*, 2014]. However, the location of ultra-shallow earthquakes implies that a fault-value mechanism is occurring [Sibson and Xie, 1998]. That is, the normal faults fail when the effective normal stress in the layer reaches the failure criterion of the fault.

Computations [Jean-Baptiste Tary, *personnal communication*] indicate that all the “ultra-shallow aftershocks” occur within zones of increase of dynamic and static Coulomb stress criterion. Even though both stress perturbations could contribute to the triggering, dynamic stresses show variations 2-3 times larger ($\sim \pm 50$ kPa depending on the rise time considered) than maximum static stress variations (2-8 kPa), based on reasonable hypotheses. However, the dynamic effects lasted only for about 1-2 minutes. It is therefore rather unlikely that the Coulomb stress transfer alone triggered the observed sequence of “ultra-shallow earthquakes”, which lasted over more than 4 days. In addition, gas, relative to a fluid is highly compressible [Jaeger *et al.*, 2007] meaning that the Skempton coefficient approaches zero as the amount of gas relative to fluid increases. Therefore, the main shock would have a minimal effect on pore pressure changes in gas filled layers.

Consequently, it is proposed that the mainshock caused the fault diffusivity to increase, triggering

pressurized gas to migrate from the different, multiple gas sources into the faults located above. As a result, the fluid pressure p_f within a given fault F material progressively increased with time t after the mainshock. The Coulomb failure criterion $C_F(t)$ fault F also evolved with t as written below:

$$C_f(t) = \tau_0 - \mu(\sigma_{n0} - p_0) + \Delta\tau_c - \mu(\Delta\sigma_{nc} - \Delta p_c) - \mu \Delta p_f(t) \quad (1)$$

where μ is the friction coefficient; τ_0 , σ_{n0} , p_0 are the initial shear stress, normal stress and pore pressure on a given fault plane, respectively ; $\Delta\tau_c$, $\Delta\sigma_{nc}$, Δp_c are the respective changes in shear and normal stresses induced by Coulomb stress transfer, and $\Delta p_f(t)$ is the increase in pore pressure induced by the migration of pressurized gas into the representative elementary volume. Failure occurs when $C_f(t)=0$, e.g. when the increase in pore pressure ($\Delta p_f(t)$) reaches a critical value $\Delta p_{f,crit}$ equal to the sum of the initial Coulomb stress and the transferred Coulomb stress divided by m :

$$\mu \Delta p_{f,crit} = \tau_0 - \mu(\sigma_{n0} - p_0) + \Delta\tau_c - \mu(\Delta\sigma_{nc} - \Delta p_c) \quad (2)$$

Because the Coulomb stress transfer is less than a few tens of kPa, the triggering essentially depends on how close the fault was initially from rupture and on the quantity of pressurized gas injected in the fault. Gas migrating from depth z_1 into the fault at depth z_2 pressurizes the fault by:

$$\Delta p = \rho_w g(z_1 - z_2) \quad (3)$$

This process may yield enormous overpressure, able to trigger rupture on the superficial faults. Gas migration over a height of 10 m, from the gas source in to the fault located immediately above would result in an overpressure of 100 kPa. The excess pressure is released co-seismically as the “ultra-shallow aftershock” occurs, along with the excess gas. The released gas may or may not

reach the sediment surface, depending on the permeability of the conduit network. The presence of gas emissions at the seafloor highlights the location of the active faults systems that are being used by over pressurized layers to decompress (see Figure III.2.2.1).

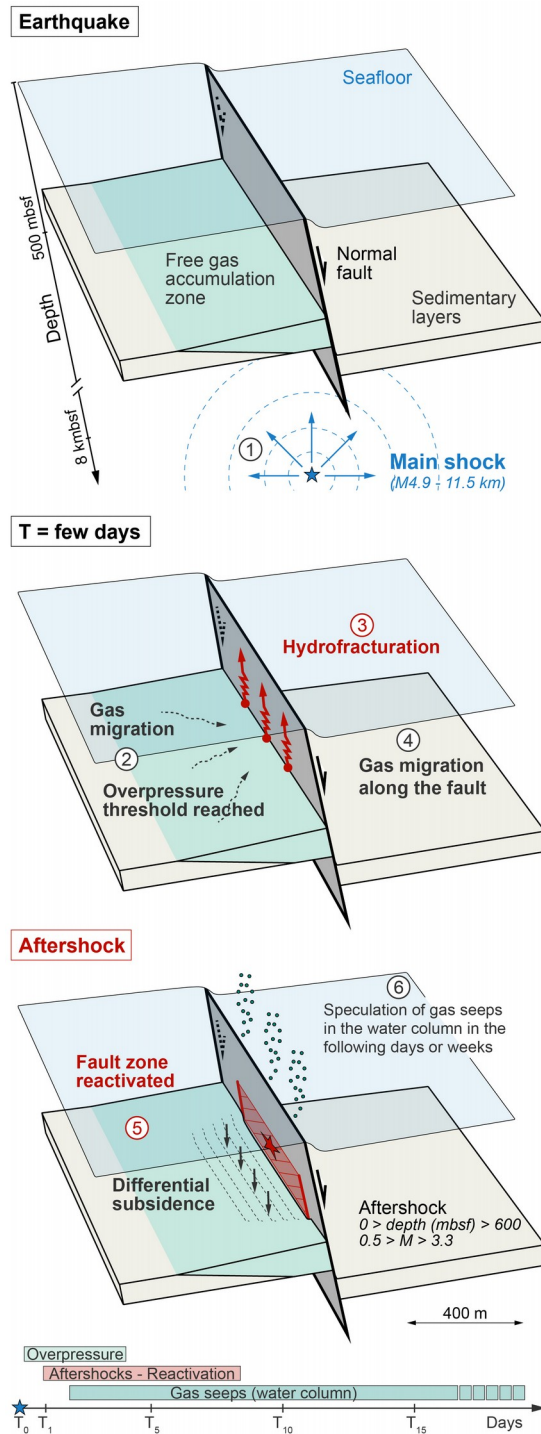


Figure III.2.2.1: Proposed scenario explaining the mechanism that triggered the aftershocks within the upper-most shallow sediments.

More generally, it is observed [Géli et al, 2018] that the events of intermediate magnitude (greater than ~ 4.2) that regularly occur in the Western SoM generate large sequences of aftershocks with numerous “ultra-shallow” events below sites of gas emission, while our analysis of the OBS dataset of 2014 suggests that “ultra-shallow” earthquakes are not so common in absence of intermediate ($M_w > 4$) earthquakes. We hence infer that the combined effect of the mainshock and of the resulting gas pressurization likely induces the observed “ultra-shallow” seismicity. Continuous deep seafloor exploration over the last decades has shown that gas is commonly found in shallow sediment layers. Hence, it is reasonable to expect that such ultra-shallow, low-magnitude earthquakes may also occur in other tectonically active settings (e.g. at subduction zones, for instance), wherever gas is present in shallow layers.

IV. Analysis of non-conventional signals

IV.1 Foreword

Tary et al [2012] reported the existence of Short Duration Events (SDE) recorded by OBSs deployed in the western SoM. According to these authors, SDEs are characterized by durations of less than 0.8 s, by frequencies ranging between 4 and 30 Hz, and by highly variable amplitudes. They also mentioned, that SDE were recorded by the geophones, but generally not by the hydrophones, except when the hydrophone is located less than a few tens of centimetres above the seafloor. The presence of gas within the upper sediments layers in the Tekirdag Basin, along with analogies with laboratory experiments, lead the authors to propose that gas migration followed by the collapse of fluid-filled cavities or conduits could be the source of the observed microevents. However, there is no bullet proof to confirm this hypothesis.

It is now realized that SDEs are systematically recorded by OBSs deployed on the seafloor, not only the Sea of Marmara, but also in a large variety of environments: in the Gulf of Guinea [Sultan et al, 2011]; off Svalbard [Franek et al, 2014]; off Antarctica [e.g. Bowman and Wilcock, 2014], in Marsili, Tyrrhenian Sea [e.g. D'Alessandro, et al, 2009], etc. SDEs may result from many different causes: bioturbation; cavity collapse in response to fluid (including gas) emission from the seafloor; activity of marine mammals; etc.

Therefore, studying SDEs may be an important issue to better understand deep seafloor processes. A systematic study was thus conducted using the OBS data recorded in 2011. The results of this study are presented in the following paragraph.

IV.2 New outcomes from the study of Short Duration Events (SDE) in the western SoM

The revised version of the paper presented here below was resubmitted after major revision in *Deep-Sea Research Part II: Topical Studies in Oceanography (DSRII)* on November 23rd 2017, by [Batsi et al, 2017], in October, under the title “*Non-conventional signals detected in the western part of the Sea of Marmara: hypotheses based on the analysis of Ocean Bottom Seismometer data*”. The analysis of the OBS data collected from April 15th to July 31st, 2011, reveals the existence of at least two different families of SDEs in the western part of the SoM:

- i. *Background SDEs*: occurring in a permanent basis, at a rate of a few hundred times per day and are most probably related to local deep seafloor processes, like for example micro-degassing phenomena at the seafloor, biological activity near the seabed, etc.
- ii. Two sub-families of *Swarmed SDEs*: where the 1st sub-family is recorded only by the geophone, while the 2nd is recorded by both the geophone and hydrophone with a periodicity

of ~ 1.6 to 2 seconds. Periodic SDEs, could be due to several external uses such as anthropogenic causes, marine mammals, gas emissions, etc.

ARTICLE

“Non-conventional signals detected in the western part of the Sea of Marmara: hypotheses based on the analysis of Ocean Bottom Seismometer data”, by Batsi et al, [2017]

DSRII (in review)

Non-conventional, unexplained signals detected by 4-components Ocean Bottom Seismometers deployed in the western Sea of Marmara: what insights for deep sea processes ?

Evangelia Batsi¹, Gaye Bayrakci², Achille Casellato¹, Jean-Baptiste Tary³ & Louis Géli¹

¹Ifremer, Marine Geosciences, CS 10070 - 29280 Plouzané, France

²Geology and Geophysics Group within Ocean and Earth Sciences, University of Southampton, University Road, Southampton SO17 1BJ, UK

³Universidad de los Andes, Facultad de Ciencias, Departamento de Geociencias, Carrera 1ª No 18-A-10, Bogota, Colombia

Abstract

Ocean Bottom Seismometers (OBSs) commonly record Short Duration Events (SDEs) characterized by durations of less than 1.0 s; by highly variable amplitudes; and generally, by one single wavetrain, e.g. with undistinguishable P- and S-arrivals. Based on the analysis of data recorded by ten, short-period (4.5 Hz), 4-components OBSs (3 geophones + 1 hydrophone) deployed in the western part of the Sea of Marmara (SoM) in Western Turkey, from mid of April until the end of July, 2011, we here report the existence of at least two families of SDEs. These families are differentiated based on their mode of occurrence only; we have not tried to classify these two families based on waveform, amplitude or frequency. Family 1 consists in "background SDEs", occurring on a permanent, but irregular basis at a rate of few tens to a few hundreds times per day. "Background SDEs" are likely related to local, deep seafloor processes known to be at work in the SoM, such as natural degassing from the seafloor, biological activity near the seabed (including fish bumps), bioturbation, etc. In contrast, Family 2 consists in "swarmed SDEs", which generally occur more or less by sequences of a few hours. Two sub-families of "swarmed SDEs" have been identified: those that are recorded only by the geophone, composed by "packets" of SDEs lasting some minutes (~ 5 to 10 minutes), followed by a short period of quiescence of roughly 5 minutes; and those that are recorded by the hydrophones and by the geophones, composed by "packets" of pulses of SDEs, occurring periodically, ~ every 1.6 to 2 seconds, each packet lasting 20 to 30 minutes and being followed by a period of quiescence of a ~ 10 to 20 minutes. Swarms of SDEs of sub-family 2a, generally occur not simultaneously at distant OBSs, in contrast with sub-family 2b, where swarms of SDEs occur more or less synchronously at distant OBSs, suggesting that they could result from a remote cause capable to emit signals recordable at the scale of the whole Sea of Marmara. Many different causes may be listed, such as: anthropogenic causes (e.g. submarines); marine mammals; degassing events from gas prone sedimentary layers; tremors from the North Anatolian Fault; etc. The correlation between these puzzling "periodic SDEs" and seismicity cannot be precluded at this stage. Further work including systematic statistics and numerical modelling is needed to investigate the different causes that may be responsible for the observed SDEs.

1

I. Introduction

Ocean Bottom Seismometers (OBSs) are ultra-sensitive instruments meant to measure seafloor motion velocity. OBSs were initially designed to study earthquakes. OBSs also record atypical signals of short duration (< 1 s), hereafter called Short Duration Events (SDEs), having different characteristics from those of tectonic earthquakes. Because SDEs reflect perturbations affecting the seafloor sediments and occur in a large variety of geological environments, it is now realized that studying SDEs could usefully contribute to a better understanding of deep seafloor processes.

SDEs were first reported from the Pacific by [Buskirk et al, 1981]. Since then, SDEs were recorded by OBSs in different geological environments, e.g. in the North Atlantic Ocean [e.g. Diaz et al, 2007]; at Deception Island in Antarctica [e.g. Bowman and Wilcock, 2014]; offshore Ecuador [e.g. Pontoise and Hello, 2002]; in Marsili, Tyrrhenian Sea [e.g. D'Alessandro, et al, 2009]; in South-China Sea [e.g. Wang et al, 2017]; in the Central Mediterranean Area [e.g. Giovanetti, et al, 2016]; in the Barents Sea [Franek et al, 2014]; in the Sea of Marmara (SoM) [e.g. Tary et al, 2012, Embriaco et al, 2013, Bayrakci et al, 2014], etc. The "signature" of SDEs varies in terms of amplitude, duration, frequency range or waveform. Hence, SDEs may result from a variety of possible causes, such as: (i) fish bumps, generated by fish hitting the instruments, [e.g. Buskirk et al, 1981], (ii) mass rearrangement within the volcano [e.g. Giovanetti, et al, 2016], (iii) hydrothermal activity [D'Alessandro, et al, 2009], [Sohn et al, 1995], (iv) movement of water in cracks through the hydrothermal circulation system [e.g. Tolstoy, et al, 2002], (v) resonance of bubble clouds in water, produced by fluids and/or methane venting [e.g. Pontoise and Hello, 2002], etc.

Based on a 3-weeks long OBS deployment in the Sea of Marmara, [Tary et al, 2012] reported that SDEs were: i) recorded by the geophones, but generally not by the hydrophones (except when the hydrophone is located less than a few tens of cm above the seafloor); ii) not recorded by separate OBSs distant by more than a few meters, which suggests that they are produced locally by a source located within the immediate vicinity of the OBS; iii) characterized in general by durations of less than one second (generally between 200 and 500 milliseconds), by frequencies ranging between 4 and 30 Hz (e.g. these values could vary depending on the geological environment), by highly variable amplitudes and by one single-wave train, e. g. with no identified P- nor S-wave arrivals. Based on the presence of gas in the near-by superficial sediments and on analogies with laboratory experiments, [Tary et al, 2012] suggested that gas expulsion followed by the collapse of fluid-filled fractures could be the source of a swarm of SDEs. However, testing the hypothesis that SDEs are related to gas emission is a difficult task to achieve that requires multi-parameter datasets. None of the experiments conducted so far was completely successful (e.g. using OBSs combined to an acoustic bubble detector [Bayrakci et al, 2014] or to methane sensors [Embriaco et al, 2013], etc). Here, we propose a more thorough study, based on the analysis of 10 OBS recordings, that provides new insights on the possible origin of SDEs.

II. Study area

The SoM represents the submerged section of the North-Anatolian Fault Zone, in north-western Turkey (Figure 1a). Since the Mw 7.4, Izmit earthquake of 1999, the SoM has been the subject of numerous marine surveys. Hence the geological background of the submarine area is now relatively well known and abundantly described in the scientific literature (e.g. [Sengör et al, 2005], [Sengör et al, 2014]). Over the last decade, the SoM has become a unique natural laboratory for studying the relationship between gas and seismicity, as gas emissions were reported, not only at shallow depths in the area of the Izmit earthquake (e.g. [Alpar 1999], [Kuşçu et al, 2015], [Gasperini et al, 2012]), but also in the deeper parts. In the deep Marmara domain, which consists in a series of E-W trending deep basins (Tekirdağ, Central, Çınarcık basins), separated by NNE-SSW trending ridges (Western High, Central High), gas emissions in the water column were successively reported by [Halbach et al. 2004], [Armijo et al. 2005], [Géli et al. 2008]. In a comprehensive, reference study, based on the acoustic imaging of the water-column [Dupré et al, 2015] showed that gas emissions in the SoM are spatially controlled by a combination of different factors such as : (i) fault and fracture networks in connection to the Main Marmara Fault system and inherited faults, (ii) the nature of thickness of sediments (e.g. occurrence of impermeable or gas-bearing sediments and landslides) and (iii) the connectivity between the seafloor and gas sources.

III. Experimental setting

III.1 OBS description

A total number of 10 OBSs were deployed by Ifremer in the western part of the SoM, from April 15th to July 31st, 2011 (Figure 1b and Table 1) for studying and better characterizing the micro-seismicity of the area. The data is available on SEANOE data repository (Géli et al, 2017, <http://doi.org/10.17882/49764>). The central station of the network, OBS02, did not function properly and stopped recording on June 30th, 2011. The OBSs were all identical, equipped with three, short period (4.5 Hz) velocity sensors (one vertical and two non-oriented horizontal components) recording at 125 samples per second (sps) and one hydrophone recording at 125 sps. The OBSs have a height of ~ 70 cm and a weight of 65 kg. Electronics and batteries are housed in a glass sphere, while the geophones (Geospace 4.5 Hz GS 11-D) lie directly on the seafloor. The hydrophone (HTI 90U) is fixed on the instrument's frame, ~ 40 cm above seafloor. The geophones and the hydrophone have all known de-scaling factors, based on the ADC coefficient (counts to volts), on the pre-amplifier and amplifier gains, and on the geophone or hydrophone sensibility. Hereafter, measurements will be presented in "counts" because we are not absolutely sure of the conversion factor (supposedly 10000 counts equals to 127 microns per second for the geophones; and 0.315 Pascal for the hydrophones). Finally, the total drift of the internal clock was directly estimated for each instrument, based on GPS synchronization before deployment and after recovery, 3.5 months later. Then, based on laboratory results obtained in comparable pressure and temperature conditions, linear corrections were applied to the instrument's internal clock.

III.2 Seismicity during the recording period

From April 15th to July 31st, 2011, more than 750 earthquakes were recorded by the submarine network ([Lomax, 2014], [Cros et al, 2013]). A large number of these events were not relocated, either because they were recorded only locally (with 3 OBSs or less); either because they occurred outside the area delineated by the OBS network. KOERI' catalog (<http://www.koeri.boun.edu.tr/sismo/2/earthquake-catalog/>) indicates that a large number of earthquakes of magnitude $M \geq 3$ occurred during this period in the search area shown in Figure 1a ($38.50^\circ \leq \text{latitude} \leq 42.00^\circ$ and $24.50^\circ \leq \text{longitude} \leq 30.50^\circ$), namely the Marmara $M_{5.1}$ earthquake and aftershock sequence starting on 2011, July, 25th and the Kütahya-Simav $M_w 5.9$ earthquake and aftershock sequence, starting on May 19th, 2011, that will be discussed later in the text.

IV. Methods: SDE detection and Principal Component Analysis (PCA)

In addition to earthquakes, SDEs were recorded with the OBSs (Figure 2). SDEs were automatically detected using an algorithm based on the Short Term Average (STA) / Long Term Average (LTA) method, commonly used to detect sudden changes in the signal amplitude over a sliding time window. The SDE is picked when the STA/LTA ratio exceeds a given threshold (Figure 3). The times when the ratio exceeds 1 or falls to 1 are, respectively, the beginning and the end of the SDE (Figure 3). Based on [Tary et al, 2012], SDEs generally last less than 1.0 second. The length of the short window must be smaller than the length of any SDE. The SDE is triggered 0.075 s before the maximum peak, for a duration of 1.0 s (Figure 3). Several tests were carried out by considering different values during the detection process and finally a common threshold value of 5 was used for all the OBS stations, on both the geophone and the hydrophone.

The Principal Component Analysis (PCA) method of Jurkevics [1988] was also used, to characterize and classify SDEs. First, signal windows of 1 s duration were extracted from the three component continuous signal, from 0.1 s before to 0.9 s after the beginning of each given SDE. Secondly, the three-component temporal series in the OBS reference frame were rotated in the wave reference frame and converted into radial, transverse and vertical components. Then the covariance matrix between all signals $??_i, ??_j$ was computed for one given component (radial, transverse or vertical) following the formula:

$$??_i, ??_j = \sum_{m=1}^M (??_i(??_m) \cdot ??_j(??_m)), \text{ with } 1 \leq ?? \leq ?? \text{ and } ??_1 \leq ??_2, ??_2 \leq ??_3$$

where $??_i$ and $??_j$ are the time series of the given component, M the number of SDEs, and N the number of samples within the (one-second long) selected windows. Finally, the covariance matrix was diagonalized, with the eigenvectors representing the characteristic signals and the eigenvalues representing the representativeness of each characteristic signal, the "representativeness" being expressed as the percentage of the total energy of all analysed data.

V. Classification of SDE activity

V.1 The global picture

Only the vertical component and the hydrophone are presented here for analysis, but similar results (not shown) were found for the two horizontal components. The number of SDEs detected at each station is highly variable, both in space and in time, as shown by the plot of daily occurrence of SDEs versus time after deployment (Figure 4). Indeed, the maximum daily occurrence of SDEs varies spatially, from 2000 at OBS05 up to 20000 at OBS01; at every single station, “peaks of SDEs” (with more than 30 SDEs per hour); in between the “peaks”, the “SDE activity” is reduced, but never reaches zero levels. Hereafter, we will thus consider and analyse separately the “background SDE activity” (“Family 1”), defined by the activity that occurs in between the peaks, and the “swarmed SDE activity” (Family 2), which correspond to the SDEs that produce the “peaks”. The two categories of SDEs are differentiated based on their mode of occurrence only. We have not tried to classify these two families based on waveform, amplitude or frequency.

V.2 Characteristics of “background SDEs”

The “background SDE activity” occurs permanently, but not regularly, at a rate of a few tens to a few hundreds of SDEs per day. “Background SDEs” (hereafter grouped in “Family 1”) are illustrated for example in Figures 5a and 5b, with seismograms and spectrograms recorded on April, 15th, 2011, from 15:00 to 16:00. As previously noted by [Tary *et al*, 2012], background SDEs do not appear on the hydrophone recordings. Background SDEs are visible only on the geophone components, where they can be easily distinguished from ship noise. Only one single wave train can be identified (e. g. there is no separated P- and S-arrival). Frequencies of background SDEs typically range from ~ 10 to ~ 30 Hz. The PCA method was applied to the « background SDEs ». As an example, here we show in Figure 6 the results for the SDEs recorded by OBS 3 during the « off-peaked » period of May 10th – 14th, 2011. There is no eigenvector having a representativeness greater than ~ 18% (Figure 6). This applies to all OBSs, which means that there is a large variety of sources causing the « background » SDEs.

V.3 Characteristics of “swarmed SDEs”

A quick look at the seismograms show that the “Swarmed SDEs” (“Family 2”) occur by sequences of a few hours, which consists in a succession of “packets” of SDEs alternating by phases of rest of about the same duration. “Packets” of SDEs are here arbitrarily characterized by a SDE occurrence of more than 30 SDEs per hour. In addition, two sub-categories of “swarmed SDEs” appear: those that are recorded on the geophones only (Sub-Family 2a) and those that are recorded on **both** the geophone and hydrophone (Sub-Family 2b).

- **“Swarmed SDEs” of Sub-Family 2a** are illustrated in Figures 7a, 7b and 7c, with seismograms and spectrograms recorded on June 8th 2011, from 02:00 to 06:00. By definition of Family 2a, no SDE appear on the hydrophone recordings ; in contrast, on the geophone components, SDEs can be easily be distinguished from ship noise (Figure 7a). The packets of SDEs last some minutes (~ 5 to 10 minutes), are followed by a short period of quiescence of roughly 5 minutes and in general they do not occur simultaneously at distant OBSs (Figure 7d). The frequencies for each individual SDE typically range from ~ 5 to ~ 55 Hz and there is no clear separation of P-arrival and S-arrival. The PCA method was applied to some swarms of SDEs, that we arbitrarily selected as having more than 30 SDEs per hour. For the “swarmed SDEs” shown in Figure 7, for example, one eigenvector is found, having a representativeness of more than 50%, which means that there is a predominant physical mechanism that is representative for the source of the « swarmed » SDEs (Figure 8). The corresponding characteristic signal is predominant along the radial component in the wave reference frame, whereas the vertical and transverse components present lower amplitudes, five times less and 25 times less, respectively, than the radial component. So the particle motion is primarily in the radial direction, (which in principle is consistent with P-waves) with a secondary component in the vertical direction. As suggested by [Tary *et al*, 2012], this kind of motion could be considered as surface waves (Stoneley-Scholte waves).
- **“Swarmed SDEs” of Sub-Family 2b** are illustrated in Figures 9a, 9b and 9c, with seismograms and spectrograms recorded at OBS09 on the hydrophone and on the geophone components, on May 21st, 2011, from 11:00 to 12:00. A detailed look at the signal reveals the existence of pulses of very low amplitude (10^3 counts on the geophones), of frequency ranging between 40 and 50 Hz, that occur almost periodically, every ~ 1.6 2.0 seconds. Therefore, these puzzling events are hereafter called “periodic SDEs”. This striking periodicity cannot be due to instrumental (electronic) effects as they seem to occur almost at the same time at different, distant OBSs (Figure 9d). They appear as “packets” of ~ 20 to 30 minutes duration, followed by a pause of the same duration and then they start over.

The swarms of SDEs displayed in Figure 4 appear to be visually correlated from one station to the other. The eye-correlation is enhanced if one considers those SDEs that are recorded on the geophones (e.g. Family 2a; Figure 10) and those that are recorded on both the hydrophone and the geophone (e.g. Family 2b; Figure 11). The correlation is further confirmed in Figure 12, which displays the matrix of cross-correlation between the different stations (the cross-correlation factor for stations 7 to 10 is greater than 5). This clearly suggests that the causes that originate the “swarmed SDEs” are not independent from one station to the other. In contrast to “background SDEs”, “swarmed SDEs” have remote (non-local) causes capable to produce effects that are detectable over the whole study area. Also, the characteristics of the “periodic SDEs” of sub-Family 2b are different from those of the individual SDEs of sub-Family 2a, in terms of amplitude, frequency and waveforms. In addition, “periodic SDEs” always occur along with events of sub-family 2a, but the reverse is not true, e. g. events of sub-family 2a may occur without any detectable “periodic SDEs”. It is thus expected that the physical processes generating the SDEs from the 2 sub-families are different, but not totally independent. A genetic link between the two sub-families cannot be precluded.

VI. Discussion

VI.1 Potential causes for the “background SDE activity”

Numerous (unpublished) experiments conducted by Ifremer in the lab and at sea show that background SDEs may be created by any kind of small perturbation affecting seafloor sediments: sediment motion resulting from bottom currents, fluid (seawater or fluidized sediment) transfer at the sea-bottom, punctual gas emissions from the seafloor, fish bumps, biological activity, bioturbation, etc. None of these causes can be precluded to explain the observed SDEs.

Among all possible causes, let us here examine the hypothesis of bioturbation. The numerous deep seafloor surveys conducted within the SoM since 2002 with submersibles have revealed the existence of an intense biological activity perturbing the seafloor sediments. For instance, langoustines (e.g. *Nephrops Norvegicus*) such as those shown in Figure 13, are known to live in 20 to 30 centimetres deep burrows, dug into muddy seabed sediments (see also [Volkenborn et al, 2007] for bioturbation in coastal environments). When in the burrows, the langoustines pump oxygenated seawater and expel CO₂-rich seawater, from the sediments into the water column. The fluid transfer associated to this respiration process is expected to perturb the surface sediments and originate SDEs. More generally, numerous species live in buried cavities within the uppermost centimetres of sediments, displacing fluids or fluidized sediments. When the fluids are expelled into the water column, the cavities may collapse and eventually produce SDEs.

In the SoM, tide amplitudes are less than 10 cm [Alpar and Yüce, 1997]. Thus tides are expected to have no effect on SDEs. However, the number of SDEs per hour seems to increase from the early morning until about mid-day and to decrease at the end of the afternoon [Casellato, 2014]. The dependence of SDE activity relatively to the time of occurrence (hour of the day) was thus tested by stacking, at each station, the number of SDEs that occurred at a given hour, for the whole duration of the recording period. For instance, for station n, we stacked all SDEs detected between 00:00 am and 01:00 am during the full recording period; then all those between 01:00 am and 02:00 am; etc. Eventually, the number of SDEs appears to be maximum around noon. More generally, the number of SDEs appear to be systematically higher during day-time, e.g. between ~ 06:00 and ~ 20:00, than during night time (from ~ 20:00 to ~ 06:00). This tendency is documented at each different site and also when the number of SDEs are globally stacked, as shown in Figure 14. Hence, the dependence of backgrounds SDEs on the hour the day cannot be precluded. We have not enough information to go any further in our analysis at this stage.

VI.2 Potential causes of “swarmed SDE activity”

As mentioned in the introduction, previous studies suggest that swarms of SDEs may result from many different causes : resonance of fluid-filled cracks (e.g. [Diaz et al, 2007]); harmonic tremors at submarine calderas (e.g. [Bowman and Wilcock, 2013]) or at mud-volcanoes (e.g. [Franek et al, 2014]); gas hydrate dissociation (e.g. [Pontoise and Hello, 2002]); collapse of gas filled fissures in surface sediments (e.g. [Tary et al, 2012]); high frequency (> 20 Hz), non-volcanic seismic tremors [Guilhem et al, 2010]; hydrothermal micro-seismicity recorded at one single station [Sohn et al, 1995]; marine mammals (e.g. [Pereira et al, 2016]), etc. Our study area being characterized by an important seismicity, let us first examine the potential relationship between "swarmed SDEs" and micro-seismicity.

- **The 2011 Kütahya-Simav M_w 5.9 earthquake and its aftershock sequence**

On the 19th of May 2011 at 20:15 UTC, a M_w 5.9 earthquake occurred as normal faulting at 7 km depth in the Simav district of Kütahya province in Western Turkey, within a distance of 210 km from the study area. The region was subject to an intense aftershock activity, where remarkably six weeks after the mainshock the total number of aftershocks had reached 3500 [e.g. Yilmaz and Avsar, 2013]. The daily occurrence of SDEs plotted vs time for the full recording period (Figures 10 and 11) suggest that the M_w 5.9, Simav earthquake and its aftershock sequence may have triggered a series of "swarmed SDEs". This is particularly visible on Figure 11, where only those SDEs that are recorded by both the hydrophone and the geophone (e.g. Family 2a) are plotted. However, the correlation is impossible to be fully established, as there is no direct correlation between one given earthquake and one swarm of SDEs. There is almost a continuous sequence of aftershocks in the Simav area after the mainshock and a global increase in the swarm activity, as but no one-to-one correlation, as shown in Figures 15, which displays the seismicity versus time, along with the hourly distribution of SDEs at each different OBS (e.g. from west to east, OBS01 to OBS04) for the first 12 days following the mainshock, from the 19th until the 30th of May, 2011 (it is worth noting that OBS01 during this period did not detect any periodic events on the hydrophone, most probably due to the elevated level of noise). At this stage, however, it is impossible to go any further for confirming the existence of a possible causative correlation.

- **The 2011 Marmara M_w 5.1 earthquake and its aftershock sequence**

On the 25th of July 2011 at 17:57 UTC a deep strike-slip earthquake of magnitude M_w 5.1 occurred in the western part of the SoM, near the area where hydrocarbon gas and gas hydrates were found. This earthquake was followed by a sequence of more than 550 aftershocks ([Lomax, 2014], [Cros et al, 2013]). Again, like in the case of the M_w 5.9 Kütahya-Simav earthquake, the daily occurrence of SDEs plotted vs time for the full recording period (Figures 10 and 11) suggests that this local, M_w 5.1 earthquake and its aftershock sequence may have triggered a series of "swarmed SDEs" Note: unfortunately the central station, OBS02, stopped working just one month before the M_w 5.1 earthquake. However, the hourly histograms (e.g. from west to east, OBS01 to OBS04) plotted versus the seismicity distribution, (Figures 16a and 16b) for the period between the 25th and the 31st of July (end of the deployment) indicate that there is no one-to-one correlation between one given earthquake and a swarm of SDEs.

- **Other observations :**

Figure 11 also indicates that other crises of "swarmed SDEs" were simultaneously recorded at many different OBS, like for example: (i) the crisis on the 7th of May 2011, which seems to be related with the occurrence of the local micro-

seismicity that occurred within the Central Basin, (ii) the crisis on the 24th of April 2011, which, in contrast, occurred without any significant local or remote earthquake being recorded and hence does not seem to have a clear correlation with local or remote earthquakes, etc.

Statistical methods and numerical modelling are needed to demonstrate the causative correlation -if any- between seismicity and swarmed SDEs. However, the hypothesis that "swarmed SDEs" may occur in response to earthquakes cannot be precluded. For example, in areas where gas-prone sediment layers are present (e. g. like in the Sea of Marmara or in the northern South-China Sea), the following, hypothetical scenario proposed in [Tary *et al*, 2012] needs to be tested: i) An earthquake may induce gas ex-solution and trigger gas migration from depth (~ a few hundreds to a few thousands of meters) up to the surface through pre-existing conduits, like faults; ii) gas fills up a cavity located near the seabed (with thickness of ~ a few meters to a few tens of meters); iii) gas is released when the pressure exceeds the resistance of the cavity, causing the cavity to collapse; iv) repeated collapses around the main outlet generate swarms of SDEs. This scenario however greatly depends on the local conditions, e.g.: sediment permeability, near-surface faulting, connectivity from the surface to the gas sources, etc.

Some words on the "periodic SDE activity" (Family 2b)

The "periodic SDEs" (family 2b) are produced periodically every 1.6 to 2 seconds and characterized by higher frequencies (~40 to 50 Hz) compared to the individual SDEs of families 1 and 2a. They appear in sequences lasting ~ 30 minutes duration, followed by a phase of relative quietness (of ~ 10 to 12 minutes) and start again. Apparently, based on Figure 9d, the source of these signals is locatable, but we leave this for future studies. Periodic signals have been already observed by 4-components OBSs, specifically on hydrophones during numerous surveys around the world. Several possible causes have been proposed as possible mechanisms for producing them such as: (i) anthropogenic causes, like for example submarines [Matsumoto *et al*, 2010], (ii) marine mammals [McDonald and Fox, 1999, Nieukirk, *et al*, 2004], (iii) seismological or geological causes (e.g. periodic shallow earthquakes, [Iverson *et al*, 2006]), (iv) electronic noise, (v) seismic airguns, etc. Here we can forthwith eliminate the possibility of electronic noise (e.g. family 2b is recorded by different stations) or airguns (e.g. the frequency range is lower, is not in kHz, the signal's amplitude is not attenuated, etc.). In contrast, none of the other hypotheses can be precluded. Most particularly, we cannot exclude that the "periodic SDEs" could result from tremors along the Main Marmara Fault, triggered by local or remote earthquakes of sufficiently large magnitude.

Conclusions

We have shown here that there are at least two families of SDEs in the western part of the SoM:

- i) "Background SDEs", occur on a permanent, but irregular basis at a rate of few tens to a few hundreds times per day. "Background SDEs" are likely related to local, deep seafloor processes at work in the immediate vicinity of the OBSs, such as micro-degassing phenomena at the seafloor, biological activity near the seabed (including fish bumps), bioturbation, etc. We have no bullet proof to favour one hypothesis relative to the other.
- ii) "Swarmed SDEs" generally occur synchronously at distant OBSs, which suggests that they occur in response to an external cause capable to produce effects that are recordable over the whole Sea of Marmara. Two sub-families of "Swarmed SDEs" have been identified: those that are recorded by the geophone only; and those that are recorded by the hydrophones and by the geophones. The SDEs of the latter sub-family are pulses occurring periodically, ~ every 1.6 to 2 seconds. These periodic signals may result from different causes: anthropogenic causes (e.g. submarines); marine mammals; gas emissions, etc. The correlation between these puzzling "periodic SDEs" and seismicity is possible, but not demonstrated at this stage.

In conclusion, SDEs are still not understood, but very promising. The study of SDEs certainly paves the road for fascinating new research to improve our understanding of both deep sea processes (at the seabed and in the water column) and tremor triggering processes at active faults.

REFERENCES

- Alpar B, Yuce H (1997) Short and tidal period sea-level variations along the Turkish Strait system. *Turk J Mar Sci* 3:11–22
- Armijo, R. et al, (2005). Submarine fault scarps in the Sea of Marmara pull-apart (North Anatolian Fault): implications for seismic hazard in Istanbul, *Geochem. Geophys. Geosyst.*, **6**, Q06009, doi:10.1029/2004GC000896.
- Bayrakci, G., et al, (2014). Acoustic monitoring of gas emissions from the seafloor. Part II: a case study from the Sea of Marmara, *Mar. Geophys. Res.*, **35**, 211-229, doi: 10.1007/s11001-014-9227-7.
- Bowman D.C. and Wilcock S.D., (2013), Unusual signals recorded by ocean bottom seismometers in the flooded caldera of Deception Island volcano : volcanin gases or biological activity? *Antarctic Science* **23**(3), 267-275, doi:10.1017/S0954102013000758
- Buskirk R.E., et al (1981), Evidence that biological activity affects Ocean Bottom Seismograph Recordings, *Marine Geophysical Researches* **5**, 189-205
- Caselatto, A., (2014). Relations between gas emissions and seismicity within the Sea of Marmara, *Rapport de fin d'études d'ingénieur, ENSTA-Bretagne / Mémoire de Stage de Master-2, Université de Bretagne Occidentale*.
- Cros, E., & Géli, L. (2013), Characterisation of microseismicity in the Western Sea of Marmara: implications in terms of seismic monitoring, *Project Report, Institut Carnot Ifremer-Edrome, Abondement 2011, N°06/11/2013, 29 pages*, available on-line: <http://dx.doi.org/10.13155/38916>
- D'Alessandro A., D'Anna G., Luzio D. and Mangano G., (2009), The INGV's new OBS/H: Analysis of the signals recorded at the Marsili submarine volcano. *J. Volcanol. Geotherm. Res.* doi:10.1016/j.jvolgeores.2009.02.008
- Díaz J., Gallart J., and Gaprà O., (2007), Atypical seismic signals at the Galicia Margin, North Atlantic Ocean, related to the resonance of subsurface fluid-filled cracks, *Tectonophysics* **433** (2007) 1-13
- Dupré S., et al, (2015), Tectonic and sedimentary controls for widespread gas emissions in the Sea of Marmara, Results from systematic, ship-borne multibeam echosounder water column imageries, *J. Geophys. Res., Solid Earth*, **120**, doi: 10.1002/2014JB011617 (<http://onlinelibrary.wiley.com/doi/10.1002/2014JB011617/full>)
- Embricco, D., Marinaro, G. Frugoni, F., Giovanetti, G., Monna, S., Etiopie, G., Gasperini, L., Çagatay, N., Favali, P., Monitoring of gas and seismic energy release by multiparametric benthic observatory along the North Anatolian Fault in the Sea of Marmara (NW Turkey), (2013), *Geophys. J. Int.*, doi: 10.1093/gji/ggt436
- Gasperini, L., et al (2012), Gas seepage and seismogenic structures along the North Anatolian Fault in the eastern Sea of Marmara, *Geochem. Geophys. Geosyst.*, **13**, Q10018, doi:10.1029/2012GC004190.
- Géli, L., et al, (2008). Gas emissions and active tectonics within the submerged section of the North Anatolian Fault zone in the Sea of Marmara. *Earth Planet. Sci. Lett.*, **274**(1-2): 34-39.
- Geli Louis, Pelleau Pascal, Batsi Evangelia, Namik Çagatay (2017). Ocean Bottom (OBS) data of the two the temporary seismic networks of Ifremer in 2011 (4 months). SEANO. <http://doi.org/10.17882/49764>
- Géli et al, (2017), Gas related seismicity within the Sea of Marmara, *Nature Scientific Report*, submitted February 2017
- Giovanetti G., et al (2016), Observing Volcanoes from the Seafloor in the Central Mediterranean Area, *Remote Sens.* **2016**, **8**, 298; doi:10.3390/rs8040298
- Guihem A., et al, (2010), High-frequency identification of non-volcanic tremor triggered by regional earthquakes, *Geoph. Research Letters*, Vol. **37**, L16309, doi:10.1029/2010GL044660
- Halbach, P., E. et al, (2004), Migration of the sulphate-methane reaction zone in marine sediments of the Sea of Marmara—can this mechanism be tectonically induced?, *Chem. Geol.*, **205**(1-2), 73-82
- Jurkevics, A. (1988), Polarization analysis of three-component array data, *Bull. Seism. Soc. Am.* **78**, 1725-1743.
- Iverson, R.M. (2006), Dynamics of seismogenic volcanic extrusion at Mount St Helens in 2004-05, Vol **444**, *Nature*, doi:10.1038/nature05322
- Kuscu, I., et al, (2005) Seafloor gas seeps and sediment failures triggered by the August 17, 1999 earthquake in the Eastern part of the Gulf of Izmit, Sea of Marmara, NW Turkey. *Mar. Geol.* **215**, 193–214.
- Lomax, A., (2014), Mise en oeuvre et support pour logiciels de traitement automatisé de données sismologiques acquises dans le cadre du projet Européen FP7 Marsite, *Contract report, Reference CNRS MA201301A*, available on line: http://alomax.net/projects/marsite/MA201301A_report_v0.2.pdf
- Matsumoto, H., et al, (2010), Hydroacoustics of a submarine eruption in the northeast Lau Basin using an acoustic glider, *Oceans* 1–6, 20–23
- McDonald M.A. and Fox C.G. (1998), Passive acoustic methods applied to fin whale population density estimation, *J. Acoust. Soc. Am.* **105** (5)
- Nieukirk S.L., et al, (2004) *Low-frequency whale and seismic airgun sounds recorded in the mid-Atlantic Ocean*, *J. Acoust. Soc. Am.* **115** (4)
- Pereira, A., Harris D., Tyack, P., Matias L.-M., (2016), Lloyd's mirror effect in fin whale calls and its use to infer the depth of

- vocalizing animals, *Acoustical Society of America, Proceedings of Meetings on Acoustics*, DOI: 10.1121/2.0000249, **27**, 070002
- Pontoise B. and Hello Y., (2002), Monochromatic infra-sound waves recorded offshore Ecuador: possible evidence of methane release, *Terra Nova*, **14**, No. 6, 425-435
- Şengör, A. M. C., *et al* (2005), The North Anatolian Fault: A new look, *Annu. Rev. Earth Planet. Sci.*, **33**, 37-112, doi:10.1146/annurev.earth.32.101802.120415.
- Şengör, A. M. C., *et al*, (2014), The geometry of the North Anatolian transform fault in the Sea of Marmara and its temporal evolution: Implications for the development of intracontinental transform faults, *Can. J. Earth Sci.*, **51**(3), 222-242, doi:10.1139/cjes-2013-0160
- Sohn, R.A., *et al* (1995), Hydrothermal micro-seismicity at the megaplume site on the southern Juan de Fuca Ridge, *Bulletin of the Seismological Society of America*, Vol. **85**, No. 3, pp. 775-786
- Shi, C., Li, S., Zhu, J., He, B. S., (2017), Insights on natural degassing processes from the northern South-China Sea seafloor, based on the analysis of Ocean Bottom Seismometer data: analogies with observations from the Sea of Marmara, *Deep Sea Research II*, submitted (mars 2017)
- Ruffine, L., *et al*. (2015), Pore water geochemistry at two seismogenic areas in the Sea of Marmara, *Geochem. Geophys. Geosyst.*, **16**, 2038-2057, doi:10.1002/2015GC005798.
- Tary, J.-B., *et al.*, (2012), Micro-events produced by gas migration and expulsion at the seabed: a study based on sea bottom recordings from the Sea of Marmara, *Geophys. J. Int.*, doi: 10.1111/j.1365-246X.2012.05533.x
- Tolstoy M., *et al* (2002) Breathing of the seafloor: tidal correlations of seismicity at axial volcano, *Geology* **30** (6), 503-506
- Volkenborn, N., Hedtkamp, S. I. C., van Beusekom, J. E. E., Reise, K., (2007), Effects of bioturbation and bioirrigation by lugworms (*Arenicola marina*) on physical and chemical sediment properties and implications for intertidal habitat succession, *Estuarine, Coastal and Shelf Science* **74** 331- 343
- Yılmaz N. and Avsar O., (2013) Structural damages of the May 19,2011, Kütahya-Simav earthquake in Turkey, *Nat Hazards*, **69**:981-1001, doi 10.1007/s11069-013-0747-2

Acknowledgments: The data used in this paper were collected within the MARMARA-DM Demonstration mission of the ESONET (European Seas Observatory NETWORK) NoE supported by the 7th Framework Programme (FP7) of the EU. Special acknowledgments to Jean-François Rolin (Ifremer) and Roland Person (Ifremer), coordinators of ESONET and to Namik Cagatay (ITU), Pierre Henry (Cerege), co-PIs of Marmara-DM. The Istanbul Technical University (ITU) provided R/V Yunuz and long-term, valuable support for the operations at sea. Ronan Apprioual and Pascal Pelleau, from IFREMER, are also acknowledged for their technical support. Gaye Bayrakci was supported by Total under CONTRACT n° 11/2 212 159YF / FR00005168. Marc Lescanne, from Total, is acknowledged. Evangelia Batsi benefited from a PhD grant co-funded by Ifremer and by Région Bretagne (ARED).

OS data available at: <http://doi.org/10.17882/49764>

TABLES (1 to 4)

OBS	Latitude	Longitude	Depth (m)	Drift (ms)
OBS01	N40° 53,0880'	E27° 41,9761'	1024	695
OBS02	N40° 49,0233'	E27° 46,8266'	652	-2875
OBS03	N40° 45,0243'	E27° 42,0111'	516	1535
OBS04	N40° 51,6689'	E28° 34,8177'	328	1264
OBS05	N40° 44,0049'	E27° 55,2393'	775	-22
OBS06	N40° 50,493'	E27° 54,935'	906	1344
OBS07	N40° 47,1735'	E28° 02,4321'	1100	-683
OBS08	N40° 53,1648'	E28° 04,6726'	1181	369
OBS09	N40° 44,0647'	E28° 08,6169'	634	136
OBS10	N40° 50,0611'	E28° 12,7331'	720	692

Table 1: OBS coordinates of the 2011 submarine network, deployment depth and OBS drift in milliseconds. Drift is the time difference measured at the end of the deployment between the OBS internal clock and the GPS time.

STA/LTA ratio	5
Length of the short window	0.02
Length of the long window	8
Minimum length of triggered sections	0.075
Maximum length of triggered sections	0.8

Table 2: Parameters used in the STA/LTA detection algorithm

No	Date	Time	Latitude (°)	Longitude (°)	Depth (km)	Magnitude
1	01/05/2011	08:36:30	40.8447	28.1410	10.4	3.2
2	07/05/2011	17:28:02	40.8067	27.9738	9.2	3.1
3	08/05/2011	03:05:50	40.8068	27.7095	5.1	3.0
4	19/05/2011	04:38:50	40.8455	28.1653	9.5	3.4
5	22/05/2011	22:39:39	40.843	28.1490	16.8	3.0
6	25/07/2011	17:57:20	40.8112	27.7382	17.0	5.2
7	25/07/2011	20:43:52	40.8165	27.7335	7.2	3.5
8	27/07/2011	11:39:57	40.8015	27.7355	18.1	3.0
9	28/07/2011	09:33:45	40.8035	27.7417	12.0	3.3
10	30/07/2011	16:42:57	40.83	27.7433	8.4	3.0

Table 3: List of local earthquakes within the rectangular of $40.70^{\circ} \leq \text{latitude} \leq 40.93^{\circ}$ and $27.68^{\circ} \leq \text{longitude} \leq 28.25^{\circ}$ with $M > 2.5$, taken from the KOERI's catalogue.

No	Date	Time	Latitude (°)	Longitude (°)	Depth (km)	Magnitude
1	22/04/2011	07:50:40	40.0817	24.9418	7.3	4.4
2	19/05/2011	20:15:22	39.1553	29.0893	6.9	5.9
3	19/05/2011	20:25:31	39.1253	29.0883	5.0	4.6
4	19/05/2011	20:41:44	39.1038	29.1273	5.0	4.0
5	19/05/2011	20:43:30	39.1238	29.0902	5.0	5.0
6	19/05/2011	21:12:50	39.1117	29.0380	5.6	4.6
7	19/05/2011	21:21:29	39.1127	29.0180	5.0	4.5
8	19/05/2011	21:33:10	39.1457	29.1062	4.5	4.4
9	20/05/2011	00:13:07	39.1165	29.1387	5.0	4.1
10	24/05/2011	02:55:29	39.0962	29.0195	8.3	4.2
11	27/05/2011	07:43:37	39.1187	29.0410	8.6	4.5
12	28/05/2011	05:47:16	39.1162	29.0213	7.5	5.0
13	28/05/2011	07:35:26	39.1062	29.1240	7.6	4.0
14	29/05/2011	01:31:39	39.1243	29.0810	9.9	4.6
15	29/05/2011	18:06:46	39.1058	29.0378	5.0	4.1
16	29/05/2011	01:31:39	39.1243	29.0810	9.9	4.6
17	04/06/2011	13:51:06	39.1230	29.0958	5.4	4.2
18	05/06/2011	21:29:12	39.1593	29.0988	8.1	4.0
19	10/06/2011	22:47:04	39.0870	28.3598	13.9	4.6
20	27/06/2011	21:13:58	39.1160	29.0152	8.8	4.9
21	27/06/2011	21:28:51	39.1012	29.0342	5.4	4.4
22	27/06/2011	22:24:50	39.1043	28.9888	4.9	4
23	27/06/2011	23:41:40	39.0743	28.9955	8.3	4.0
24	29/06/2011	11:40:47	39.1247	29.0197	4.5	4.0
25	03/07/2011	14:16:28	39.1167	29.0215	5.4	4.0
26	11/07/2011	16:09:12	40.1730	29.9600	6.5	4.6
27	13/07/2011	01:31:49	39.1220	29.0335	5.0	4.2
28	17/07/2011	19:51:50	39.1197	29.0955	9.5	4.1

Table 4: List of remote earthquakes within the rectangular of $40.70^{\circ} \leq \text{latitude} \leq 40.93^{\circ}$ and $27.68^{\circ} \leq \text{longitude} \leq 28.25^{\circ}$ with $M > 4$, taken from the KOERI's catalogue.

LIST OF FIGURES (1 to 16)

Figure 1a: Regional map indicating the study area (within the black rectangular frame) and the locations of the earthquakes that occurred during the recording period, from April 15th to July 31st, 2011. Thin black lines underline fault traces, after [Sengör et al, 2015]. Orange dots are for the events located within the Sea of Marmara of $M > 3$ (see details in Figure 1b and in Table 3). Red dots are for all the remote earthquakes of magnitude $M_w \geq 4$ (Table 4). Local and remote earthquakes are reported from the catalog of Kandilli Observatory and Earthquake Research Institute - KOERI- (<http://www.koeri.boun.edu.tr/sismo/2/earthquake-catalog/>).

Figure 1b: Bathymetric map of the study area within the Sea of Marmara. Thin black lines underline fault traces, after [Sengör et al, 2015]. Red dots indicate acoustically detected, gas emission sites, after [Dupré et al, 2015]. Stars are for OBS locations. Orange dots indicate the position of local earthquakes detected by KOERI between the 15th of April to the 31st of July 2011. Only earthquakes of $M \geq 3$ with epicentres located within the OBS network were selected (see Table 3).

Figure 2: Top: Example of seismogram for a SDE detected by OBS01 (vertical-component, Z). Bottom left: SDE frequency content. Bottom right: temporal evolution of the SDE.

Figure 3: Example of SDE detection using a STA/LTA-based algorithm. Detection is triggered when STA/LTA exceeds a given threshold (equal to 5 in the present study).

Figure 4: The upper panels display the total number of SDEs recorded per day at each given OBS (e.g. obs01 to obs04, from west to east) during the deployment of 2011, from April 15th to July 31st, detected on the vertical component. The bottom panels show the seismicity distribution versus depth, for the local (orange dots) earthquakes of $M > 3$ and for the remote earthquakes (red dots) of magnitude $M > 3$, $M > 4$, $M > 5$ respectively. Seismicity is extracted from the catalog of KOERI.

Figure 5a : Example of a one hour-long data sample recorded at OBS10 on the 15th of April 2011, from 15:00 to 16:00 on the vertical (upper panel) and hydrophone (bottom panel) components. Background SDEs and ship-related noise are indicated.

Figure 5b: Spectrogram (up) and seismogram (bottom) showing the characteristics of a background SDE recorded on the vertical component of OBS10, between 15:14:32 and 15:14:44, on the 10th of April, 2011.

Figure 6: Results from the principal component analysis applied on a 3-days long time series recorded at OBS03, displaying only background SDEs (from May, 10th 01:00 to May 14th 01:00, 2011). Upper panel: first eigenvector displayed in the time domain (with amplitude expressed on 10^4 counts) for the radial, transverse and vertical

components. Lower panel: plot of representativeness for the 10 first eigenvectors, showing that there is no predominant physical mechanism to account for background SDEs.

Figure 7a : Example of a four hours-long data sample recorded by OBS10 on the 8th of June 2011, from 02:00 to 06:00 on the vertical (upper figure) and hydrophone (bottom figure) components. Swarmed SDEs and ship-related noise are indicated.

Figure 7b: Spectrogram (up) and seismogram (bottom) for a 30-minutes long data sample, recorded on the vertical component of OBS10, from 02:30 to 03:00, showing that swarmed SDEs occur by packets lasting ~ 10 minutes followed by phases of relative quiescence of about the same duration.

Figure 7c: Spectrogram (up) and seismogram (bottom) of a 10 s-long data sample, recorded on the vertical component of OBS10 from 02:37:38 to 02:37:48, on the 8th of June, 2011, showing the characteristics of an individual "swarmed SDE".

Figure 7d: Example of a four hours-long sample from 02:00 to 06:00, on the 8th of June, 2011, recorded on the vertical components of each given OBS (e.g. OBS01 to OBS10). Swarmed SDEs of Family 2a are indicated within the red ellipses. Note that within the selected time-window displayed in the figure, the OBSs recorded many different crises of swarmed SDEs. However, the individual crises do not appear to be correlated from one OBS to the other.

Figure 8: Results from the principal component analysis applied on a 3-hours long time series recorded by OBS10, displaying only "swarmed SDEs" (on June, 8th, 2011, from 00:00 to 05:00). Upper panel: first eigenvector displayed in the time domain (with amplitude expressed on 10^4 counts) for the radial, transverse and vertical components. Lower panel: plot of representativeness for the 10 first eigenvectors, showing that there is likely one predominant physical mechanism that accounts for more than 50% of the recorded "swarmed SDEs".

Figure 9a: One hour seismogram recorded on the 21st of May 2011, from 11:00 to 12:00 on the vertical (upper figure) and hydrophone (bottom figure) components of OBS09. SDEs and earthquakes are indicated with lines, while periodic SDEs are shown within the box, on the two components of OBS09.

Figure 9b: Fifteen minutes seismogram of the 21st of May 2011, from 11:15 to 11:30 on the hydrophone (upper figure) component of OBS09. Periodic SDEs spectrogram (up) and seismogram (bottom) of 22 seconds duration, from 11:22:50 to 11:23:22, on the 21st of May, 2011, on the hydrophone component of OBS09 (bottom figure).

Figure 9c: Periodic SDEs spectrogram (up) and seismogram (bottom) of 6 seconds duration, from 11:23:01 to 11:23:07, on the 21st of May, 2011, on the hydrophone component of OBS09, showing the characteristics of individual "periodic SDEs".

Figure 9d: Periodic SDEs seismograms of 2:40 minutes duration, from 11:42:40 to 11:45:00, on the 27th of July, 2011, on the hydrophone components of different OBSs. Note that the correlation from one OBS to the other, suggesting that the source of these SDEs is locatable.

Figure 10: The upper panels display the number of SDEs per day that were recorded on the geophone components only (families 1 and 2a) at each given OBS (e.g. obs01 to obs04, from west to east) during the deployment of 2011, from April 15th to July 31st, detected on the vertical component. Compared to Figure 4, all SDEs recorded on the hydrophone were from the above plot. The bottom panels show the seismicity distribution versus depth, for the local (orange dots) earthquakes of $M > 3$ and for the remote earthquakes (red dots) of magnitude $M > 3$, $M > 4$, $M > 5$ respectively. Seismicity extracted from the catalog of KOERI.

Figure 11: The upper panels display the number of SDEs per day that were recorded on both the hydrophone and geophone components (family 2b) at each given OBS (e.g. obs01 to obs04, from west to east) during the deployment of 2011, from April 15th to July 31st, detected on the vertical component. The bottom panels show the seismicity distribution versus depth, for the local (orange dots) earthquakes of $M > 3$ and for the remote earthquakes (red dots) of magnitude $M > 3$, $M > 4$, $M > 5$ respectively. Seismicity extracted from the catalog of KOERI.

Figure 12: Correlation matrix between the hourly SDE distributions recorded at each OBS and expressed as a function of time. X- and Y-axes are OBS numbers. OBSs 7, 8, 9, 10 appear to be correlated (with correlation Coefficient > 0.5).

Figure 13: Photograph of the seafloor taken with ROV/Victor during the Marsite cruise of R/V *Pourquoi pas?* on the November 11th, 2014 at 13:17:28 UTC, with coordinates LAT : N 40 42.800417 Long : E 29 10.751178 showing the intense biological activity on the Marmara seafloor and an example of langoustine (*Nephrops Norvegicus*).

Figure 14: Hourly occurrence of SDEs, stacked over the 10 OBSs and plotted versus the hour of the day (from 0 to 24 hours). The stack is obtained by summing (over the whole recording period and over the 10 OBSs) the number of SDEs that were detected between 00h00 and 01h00, between 01h00 and 02h00, between 02h00 and 03h00, etc.

Figure 15a: The upper panels display the number of SDEs per day that were recorded on the geophone components only (families 1 and 2a) at each given OBS (e.g. obs01 to obs04, from west to east) from May 19th to May 30th, detected on the vertical component. The bottom panels show the seismicity distribution versus depth, for the local (orange dots) earthquakes of $M > 3$ and for the remote earthquakes (red dots) of magnitude $M > 3$, $M > 4$, $M > 5$ respectively. Seismicity extracted from the catalog of KOERI.

Figure 15b: The upper panels display the number of SDEs per day that were recorded on both the geophone and hydrophone components only (sub-family 2b) at each given OBS (e.g. obs01 to obs04, from west to east) from May 19th to May 30th, detected on the hydrophone component. The bottom panels show the seismicity distribution versus

depth, for the local (orange dots) earthquakes of $M > 3$ and for the remote earthquakes (red dots) of magnitude $M > 3$, $M > 4$, $M > 5$ respectively. Seismicity extracted from the catalog of KOERI.

Figure 16a: The upper panels display the number of SDEs per day that were recorded on the geophone components only (families 1 and 2a) at each given OBS (e.g. obs01 to obs04, from west to east) from July 25th to July 31st, detected on the vertical component. The bottom panels show the seismicity distribution versus depth, for the local (orange dots) earthquakes of $M > 3$ and for the remote earthquakes (red dots) of magnitude $M > 3$, $M > 4$, $M > 5$ respectively. Seismicity extracted from the catalog of KOERI.

Figure 16b: The upper panels display the number of SDEs per day that were recorded on both the geophone and hydrophone components only (sub-family 2b) at each given OBS (e.g. obs01 to obs04, from west to east) from July 25th to July 31st, detected on the hydrophone component. The bottom panels show the seismicity distribution versus depth, for the local (orange dots) earthquakes of $M > 3$ and for the remote earthquakes (red dots) of magnitude $M > 3$, $M > 4$, $M > 5$ respectively. Seismicity extracted from the catalog of KOERI.

Appendix 1- OBS characteristics

This OBS has a height of ~70 cm and a weight of 65 Kg. Electronics and batteries are housed in a glass sphere, while the geophones (Geospace 4.5 Hz GS11-D) lie directly on the seafloor. The hydrophone (HTI 90U) is fixed on the instrument's frame, ~0.4 m above the seafloor.

General characteristics of the geophone Geospace 4.5 Hz GS11-D and its acquisition chain:

Natural frequency: 4.5 Hz

Sampling frequency: 250 Hz

Frequency Bandwidth: 4.5 to 1000Hz

Sensitivity: 0.81 V/inch/s (32 V/m/s)

ADC conversion factor (card Cirrus Logic 24 bits): 3.974E-7 V/count

Gain: 46 dB

Decaling factor: 6.2234 m/s/count

General characteristics of the hydrophone HTI 90U and its acquisition chain:

Sampling frequency: 125 Hz

Frequency Bandwidth: 2 to 2000Hz

Sensitivity: -158 dB ref 1V/ μ Pa (~1.26E-2 V/Pa)

ADC conversion factor (card Cirrus Logic 24 bits): 3.974E-7 V/count

Gain: 20.24 dB

Decaling factor: 3.07E-6 Pa/count

LIST OF FIGURES (1 to 16)

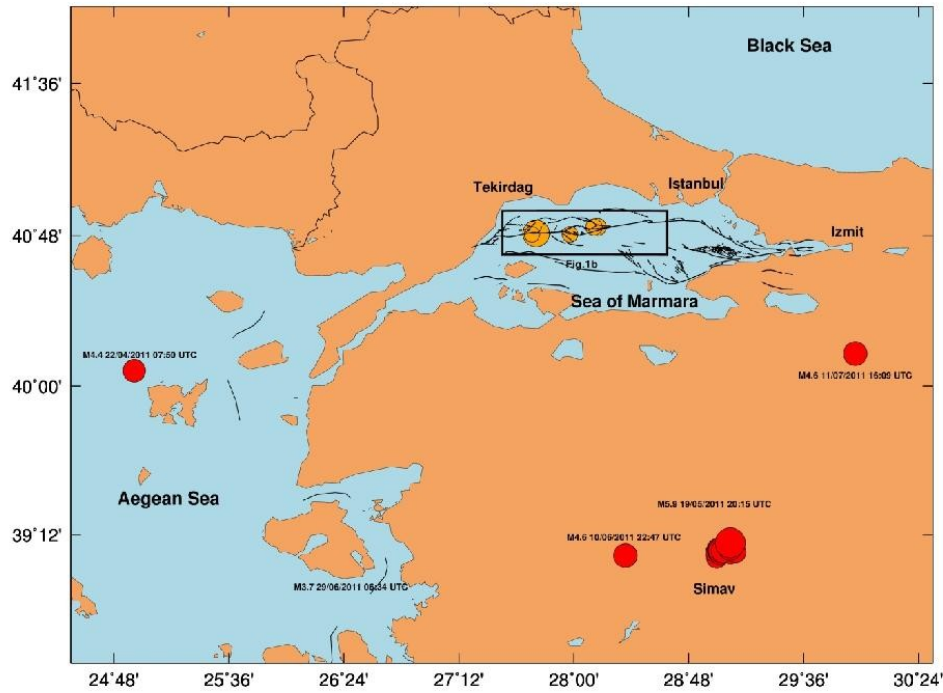


Figure 1a: Regional map indicating the study area (within the black rectangular frame) and the locations of the earthquakes that occurred during the recording period, from April 15th to July 31st, 2011. Thin black lines underline fault traces, after [Sengör et al, 2015]. Orange dots are for the events located within the Sea of Marmara of $M > 3$ (see details in Figure 1b and in Table 3). Red dots are for all the remote earthquakes of magnitude $M_w \geq 4$ (Table 4). Local and remote earthquakes are reported from the catalog of Kandilli Observatory and Earthquake Research Institute - KOERI- (<http://www.koeri.boun.edu.tr/sismo/2/earthquake-catalog/>).

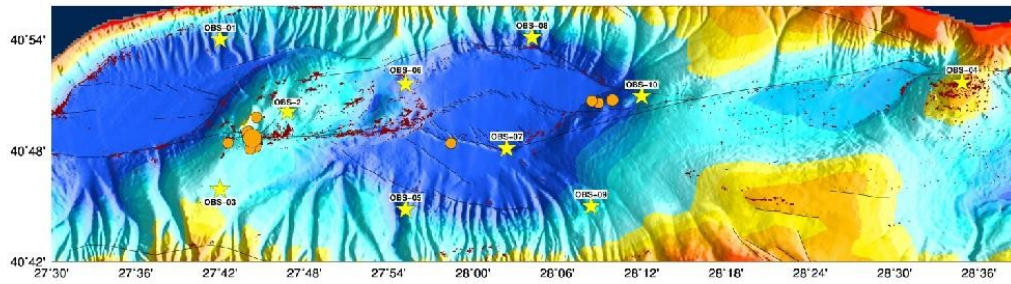


Figure 1b: Bathymetric map of the study area within the Sea of Marmara. Thin black lines underline fault traces, after [Sengör et al, 2015]. Red dots indicate acoustically detected, gas emission sites, after [Dupré et al, 2015]. Stars are for OBS locations. Orange dots indicate the location local earthquakes detected by KOERI that occurred between the 15th of April to the 31st of July 2011. Only earthquakes of $M \geq 3$ with epicentres located within the OBS network were selected (see Table 3).

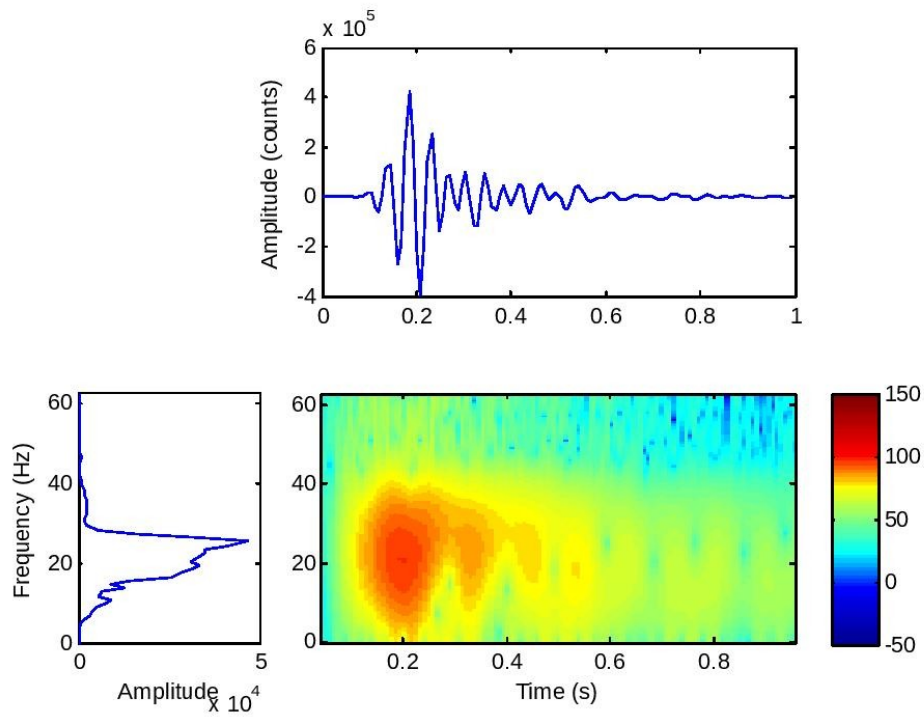


Figure 2: Top: Example of seismogram for a SDE detected by OBS01 (vertical-component, Z). Bottom left: SDE frequency content. Bottom right: temporal evolution of the SDE.

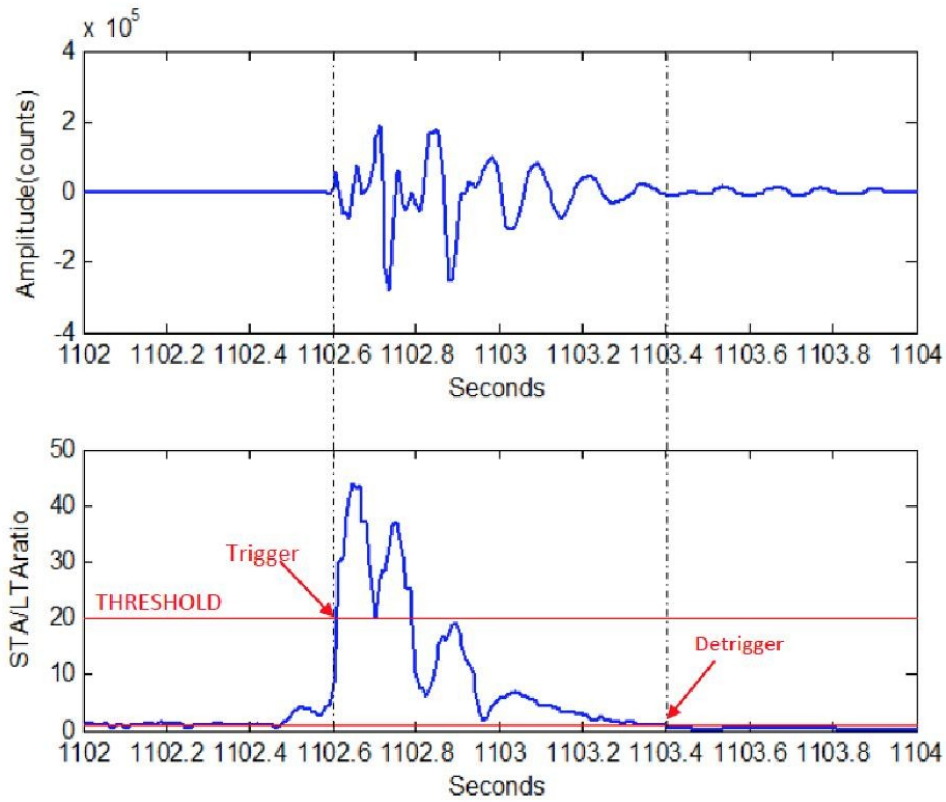


Figure 3: Example of SDE detection using a STA/LTA-based algorithm. Detection is triggered when STA/LTA exceeds a given threshold (equal to 5 in the present study).

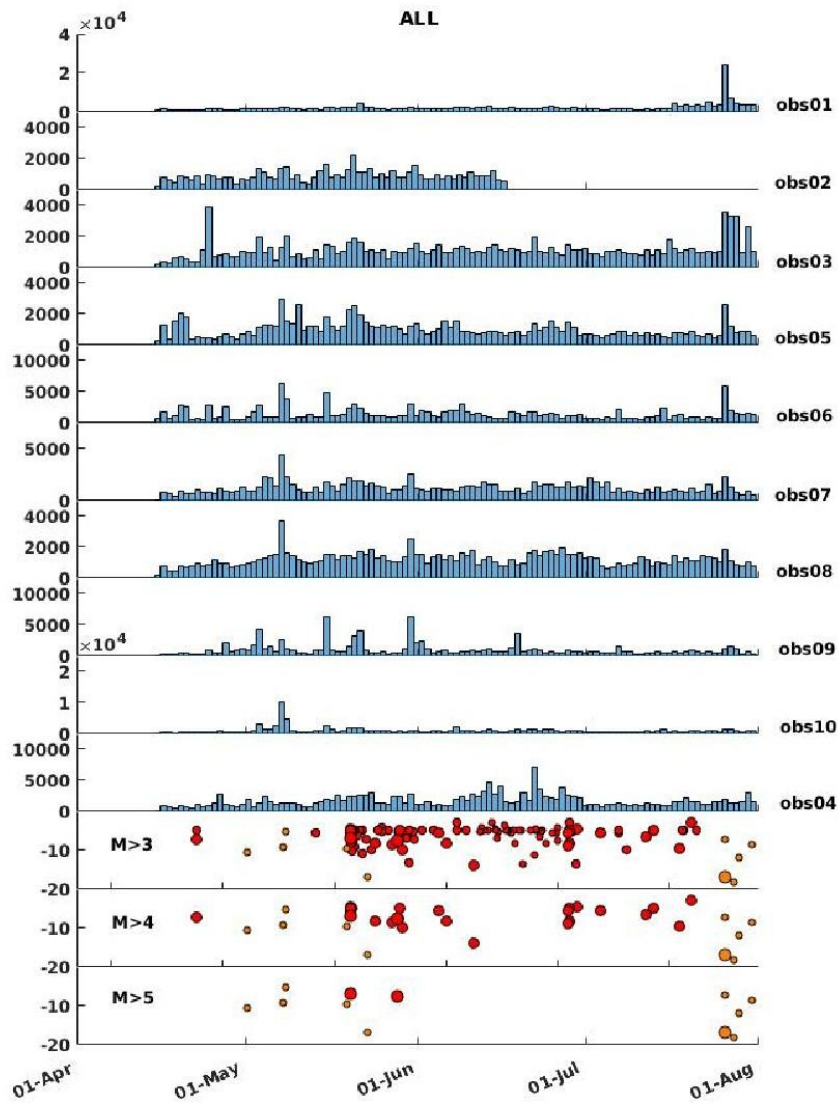


Figure 4: The upper panels display the total number of SDEs recorded per day at each given OBS (e.g. obs01 to obs04, from west to east) during the deployment of 2011, from April 15th to July 31st, detected on the vertical component. The bottom panels show the seismicity distribution versus depth, for the local (orange dots) earthquakes of $M > 3$ and for the remote earthquakes (red dots) of magnitude $M > 3$, $M > 4$, $M > 5$ respectively. Seismicity extracted from the catalog of KOERI.

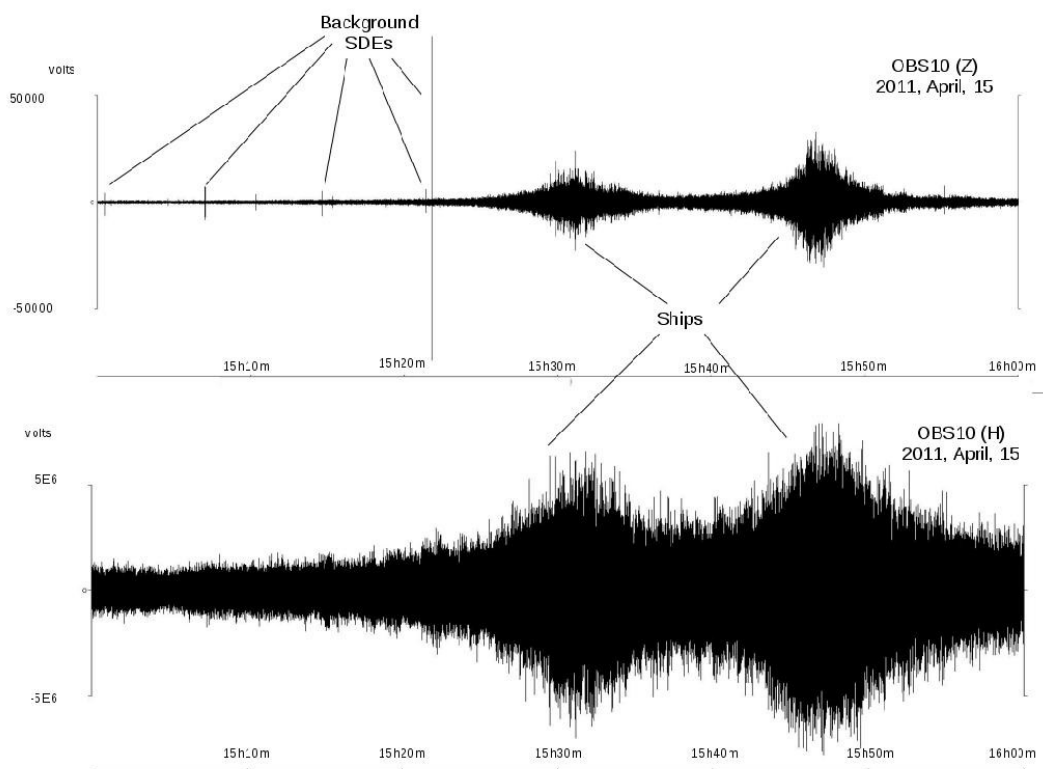


Figure 5a : Example of a one hour-long data sample recorded at OBS10 on the 15th of April 2011, from 15:00 to 16:00 on the vertical (upper panel) and hydrophone (bottom panel) components. Background SDEs and ship-related noise are indicated.

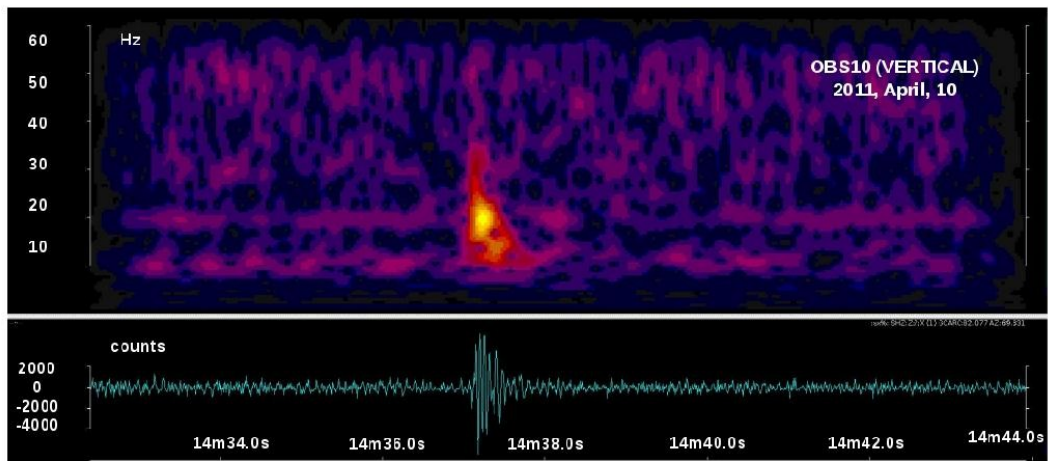


Figure 5b: Spectrogram (up) and seismogram (bottom) showing the characteristics of a background SDE recorded on the vertical component of OBS10 between 15:14:32 and 15:14:44, on the 10th of April, 2011.

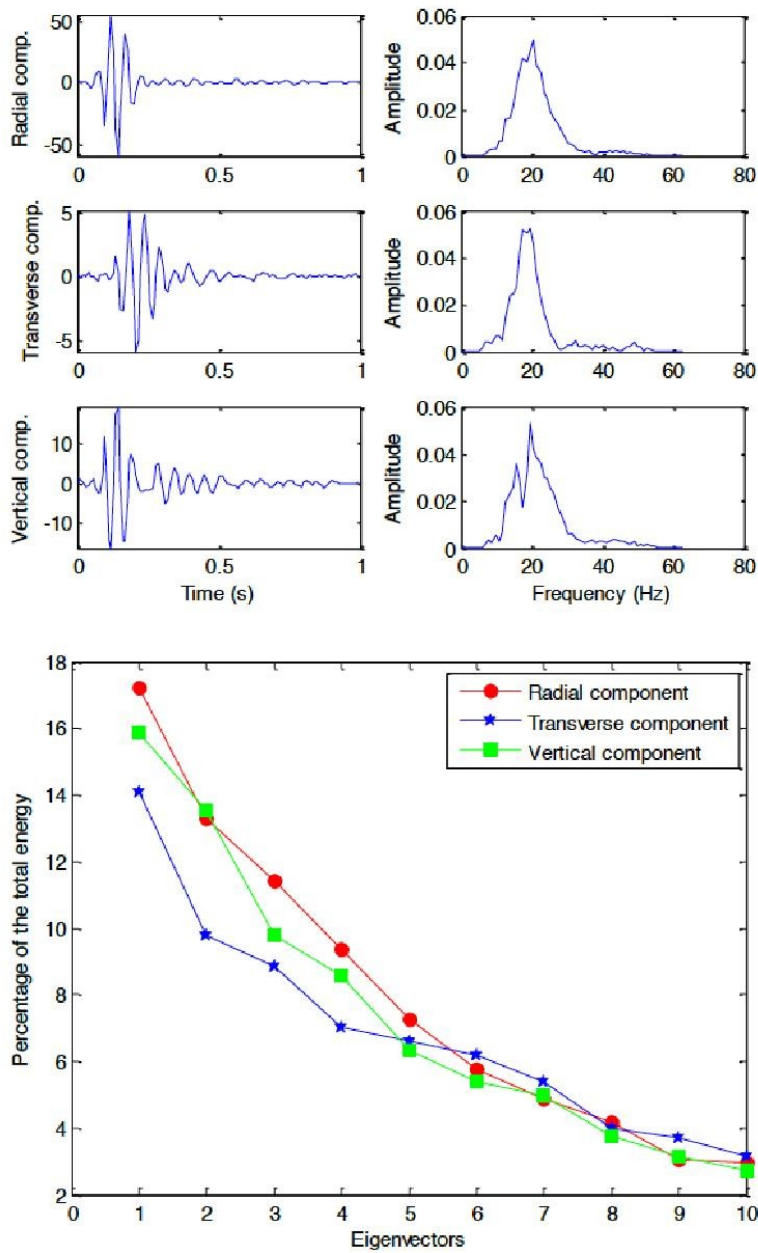


Figure 6: Results from the principal component analysis applied on a 3-days long time series recorded at OBS03, displaying only background SDEs (from May, 10th 01:00 to May 14th 01:00, 2011). Upper panel: first eigenvector displayed in the time domain (with amplitude expressed on 10⁴ counts) for the radial, transverse and vertical components. Lower panel: plot of representiveness for the 10 first eigenvectors, showing that there is no predominant physical mechanism to account for background SDEs.

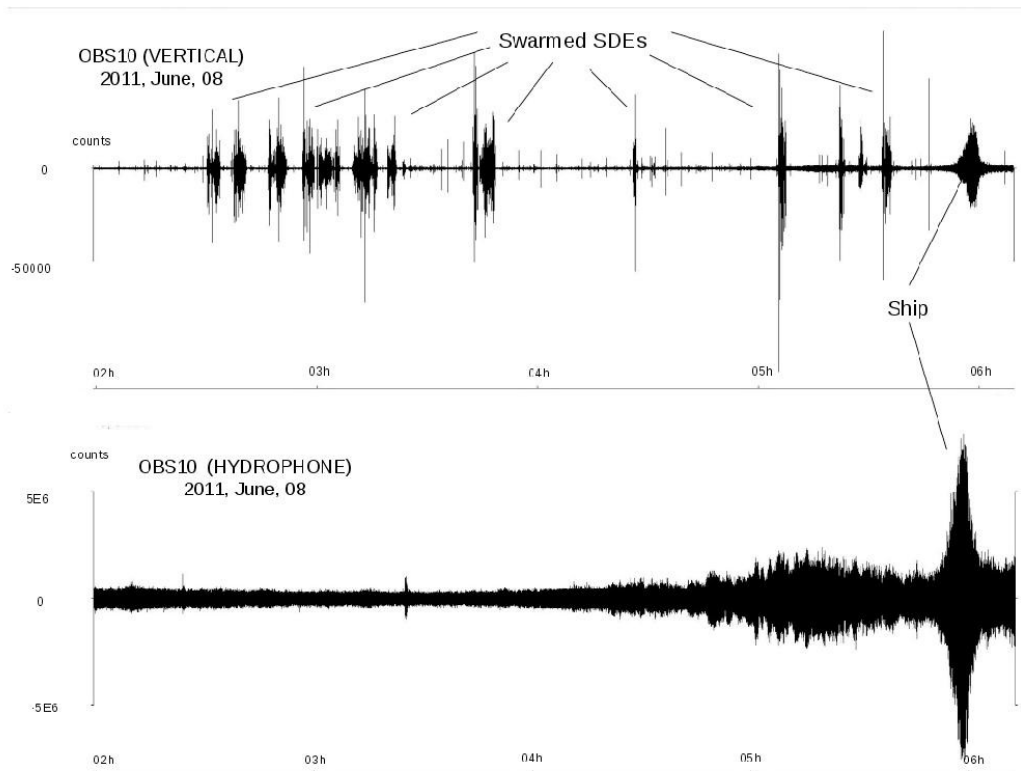


Figure 7a : Example of a four hours-long data sample recorded by OBS10 on the 8th of June 2011, from 02:00 to 06:00 on the vertical (upper figure) and hydrophone (bottom figure) components. Swarmed SDEs and ship-related noise are indicated.

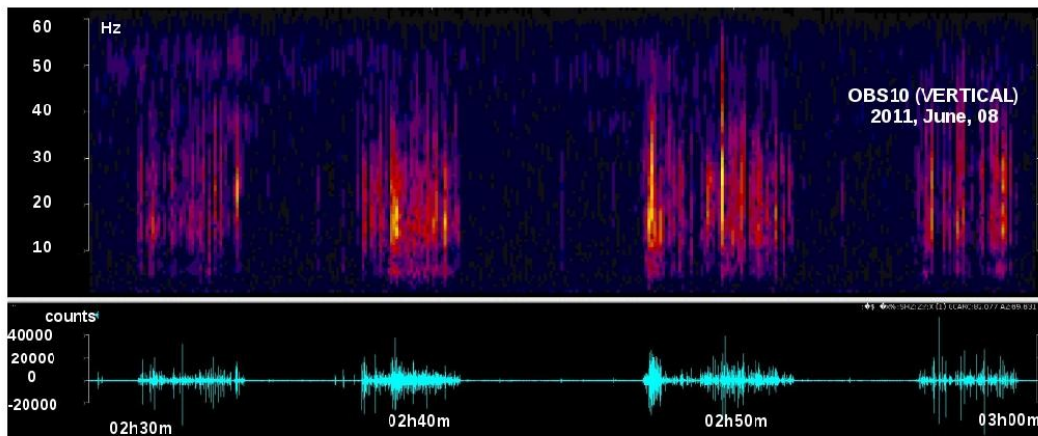


Figure 7b: Spectrogram (up) and seismogram (bottom) for a 30-minutes long data sample, recorded on the vertical component of OBS10, from 02:30 to 03:00, showing that swarmed SDEs occur by packets lasting ~ 10 minutes followed by phases of relative quiescence of about the same duration.

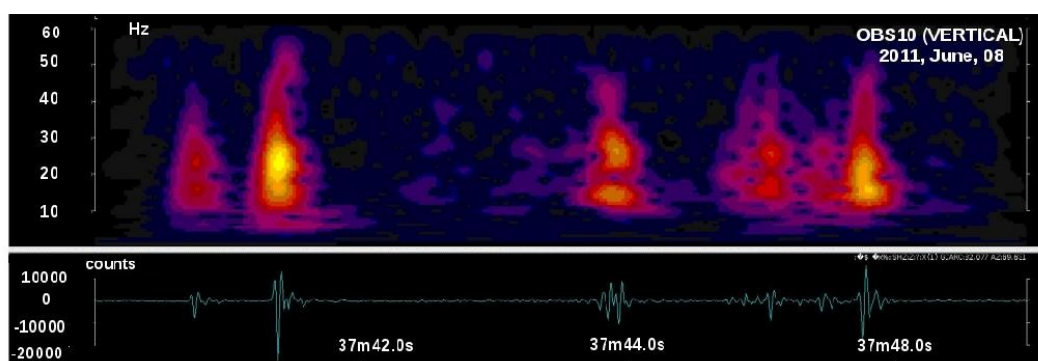


Figure 7c: Spectrogram (up) and seismogram (bottom) of a 10 s-long data sample, recorded on the vertical component of OBS10 from 02:37:38 to 02:37:48, on the 8th of June, 2011, showing the characteristics of an individual "swarmed SDE".

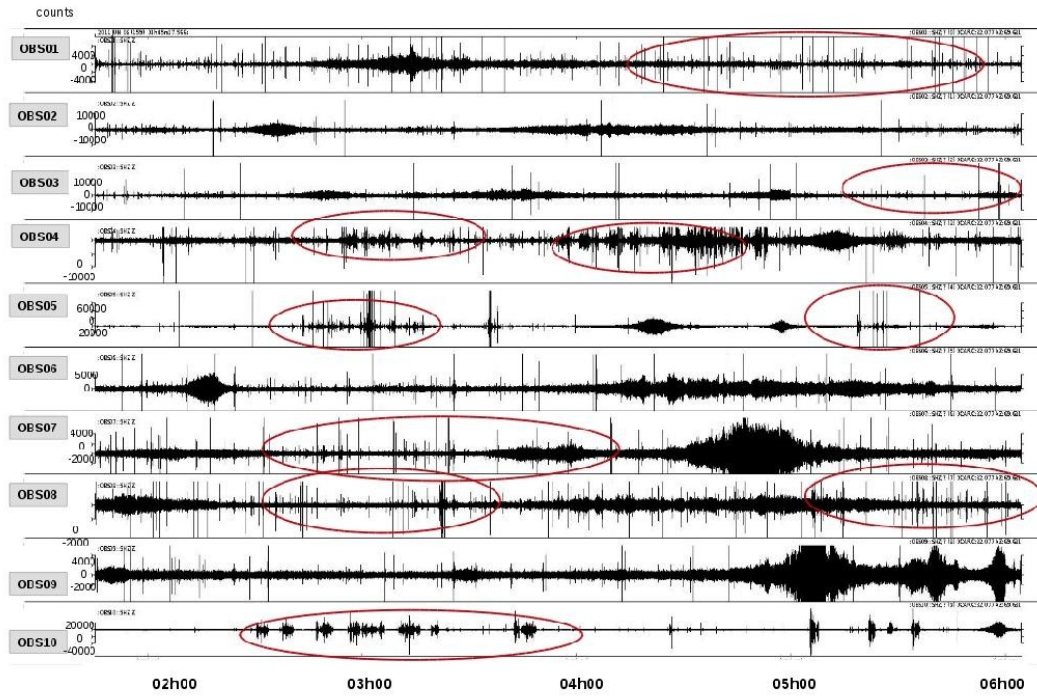


Figure 7d: Example of a four hours-long sample from 02:00 to 06:00, on the 8th of June, 2011, recorded on the vertical components of each given OBS (e.g. OBS01 to OBS10). Swarmed SDEs of Family 2a are indicated within the red ellipses. Note that within the selected time-window displayed in the figure, the OBSs recorded many different crises of swarmed SDEs. However, the individual crises do not appear to be correlated from one OBS to the other.

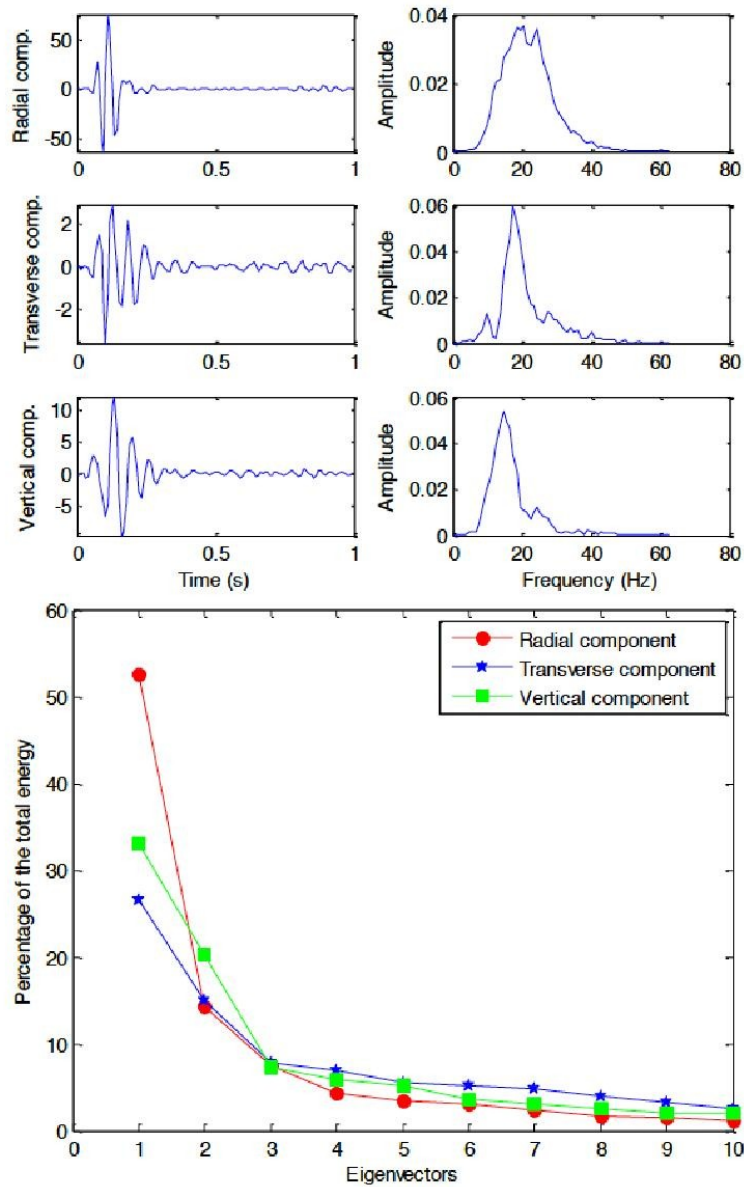


Figure 8: Results from the principal component analysis applied on a 3-hours long time series recorded by OBS10, displaying only “swarmed SDEs” (on June, 8th, 2011, from 00:00 to 05:00). Upper panel: first eigenvector displayed in the time domain (with amplitude expressed on 10^4 counts) for the radial, transverse and vertical components. Lower

panel: plot of representativeness for the 10 first eigenvectors, showing that there is likely one predominant physical mechanism that accounts for more than 50% of the recorded "swarmed SDEs".

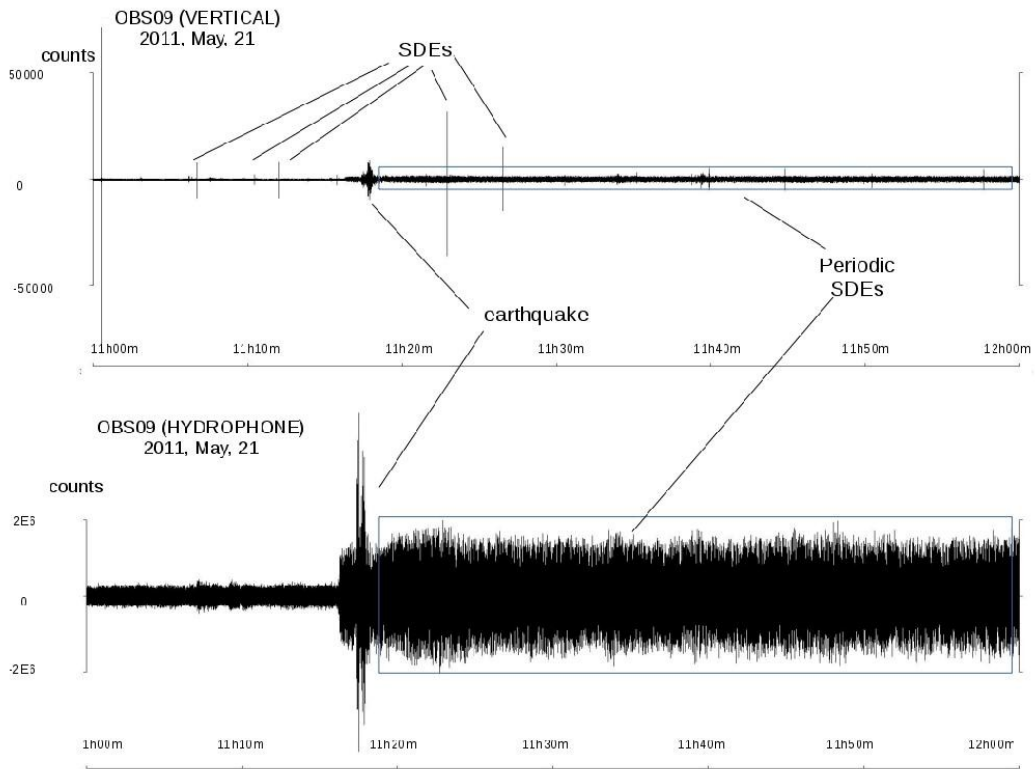


Figure 9a: One hour seismogram of the 21st of May 2011, from 11:00 to 12:00 on the vertical (upper figure) and hydrophone (bottom figure) components of OBS09. SDEs and earthquakes are indicated with lines, while periodic SDEs are shown within the box, on the the two components of OBS09.

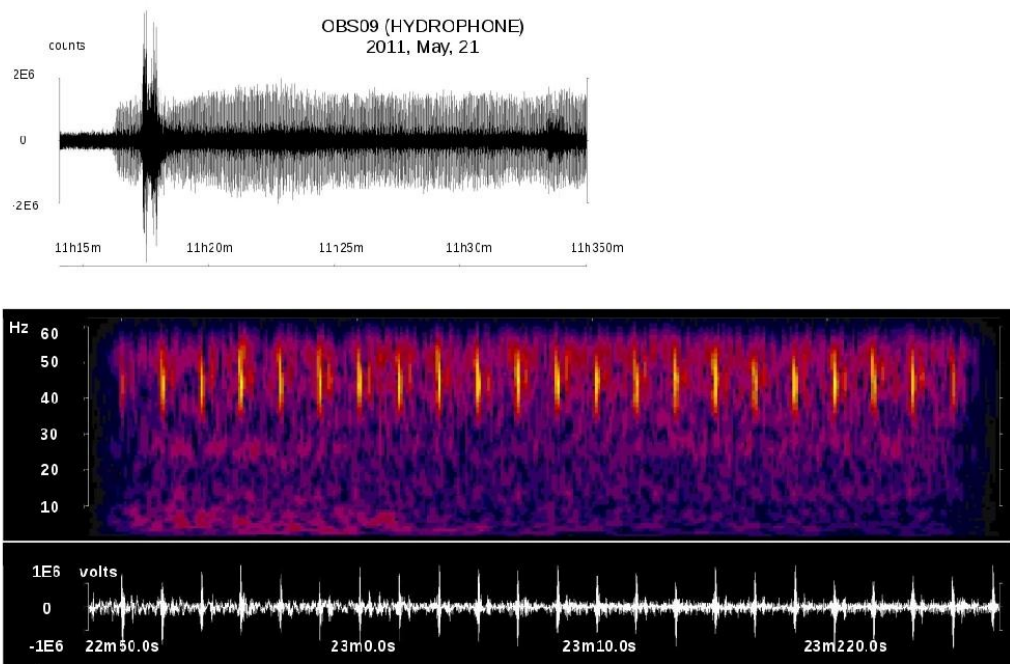


Figure 9b: Fifteen minutes seismogram of the 21st of May 2011, from 11:15 to 11:30 on the hydrophone (upper figure) component of OBS09. Periodic SDEs spectrogram (up) and seismogram (bottom) of 22 seconds duration, from 11:22:50 to 11:23:22, on the 21st of May, 2011, on the hydrophone component of OBS09 (bottom figure).

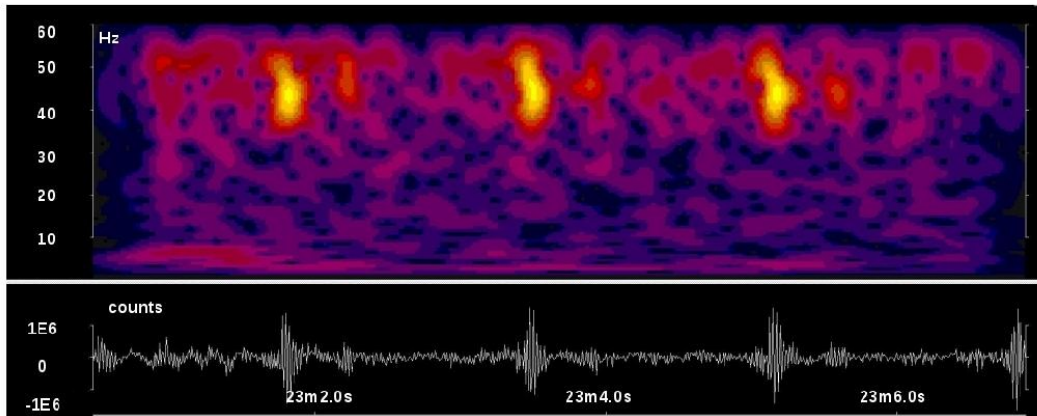


Figure 9c: Periodic SDEs spectrogram (up) and seismogram (bottom) of 6 seconds duration, from 11:23:01 to 11:23:07, on the 21st of May, 2011, on the hydrophone component of OBS09, showing the characteristics of individual “periodic SDEs”.

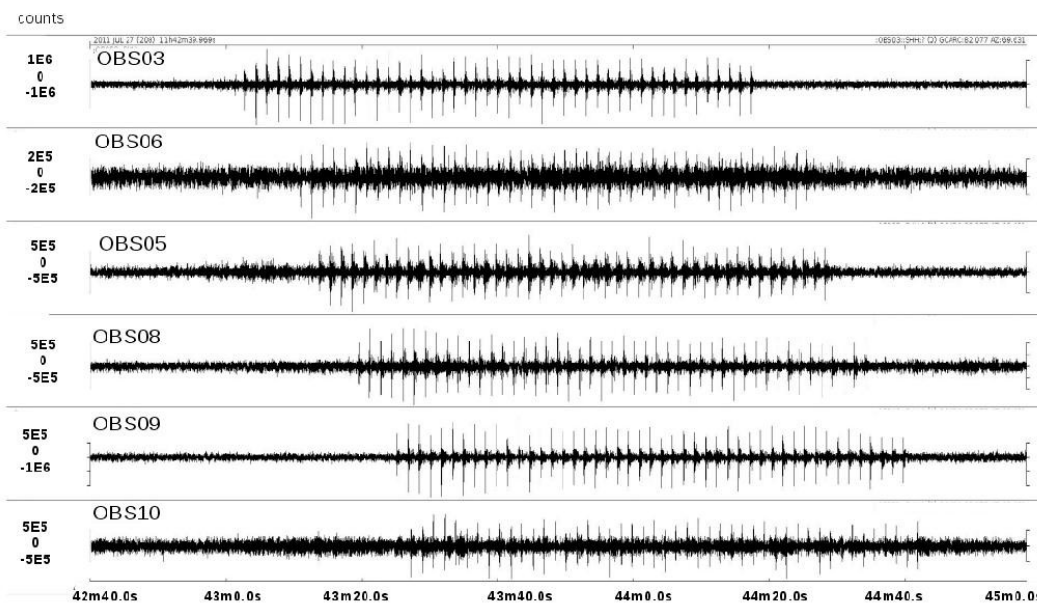


Figure 9d: Periodic SDEs seismograms of 2:40 minutes duration, from 11:42:40 to 11:45:00, on the 27th of July, 2011, on the hydrophone components of different OBSs. Note that the correlation from one OBS to the other, suggesting that the source of these SDEs is locatable.

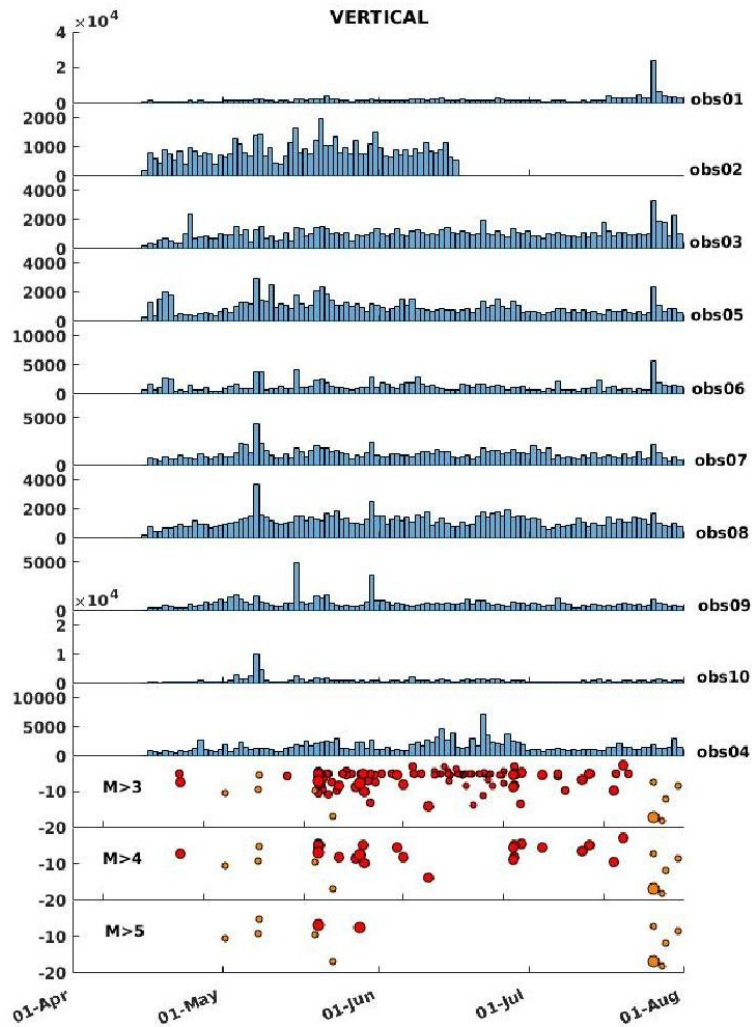
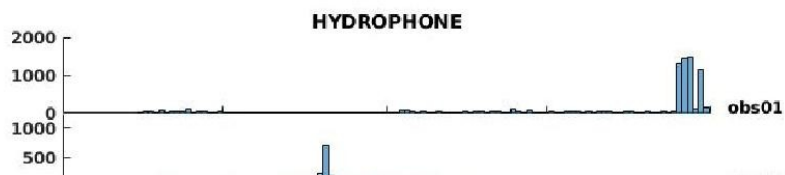


Figure 10: The upper panels display the number of SDEs per day that were recorded on the geophone components only (families 1 and 2a) at each given OBS (e.g. obs01 to obs04, from west to east) during the deployment of 2011, from April 15th to July 31st, detected on the vertical component. Compared to Figure 4, all SDEs recorded on the hydrophone were from the above plot. The bottom panels show the seismicity distribution versus depth, for the local (orange dots) earthquakes of $M > 3$ and for the remote earthquakes (red dots) of magnitude $M > 3$, $M > 4$, $M > 5$ respectively. Seismicity extracted from the catalog of KOERI.

37



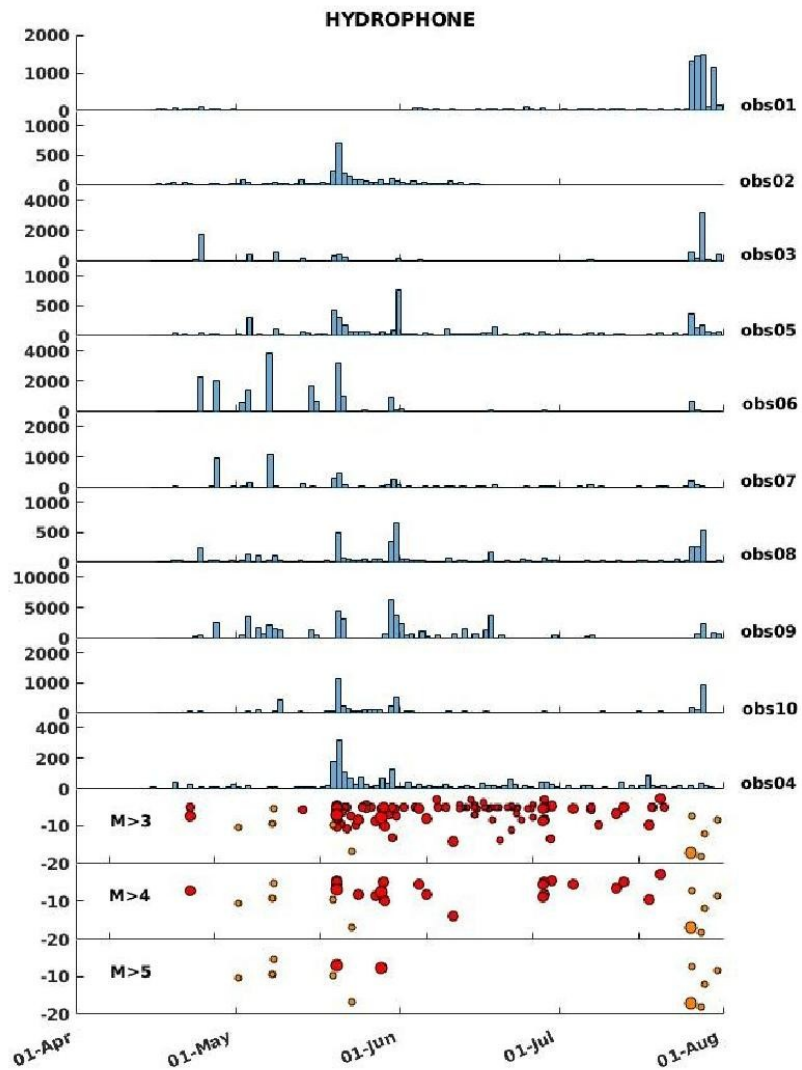


Figure 11: The upper panels display the number of SDEs per day that were recorded on both the hydrophone and geophone components (family 2b) at each given OBS (e.g. obs01 to obs04, from west to east) during the deployment of 2011, from April 15th to July 31st, detected on the vertical component. The bottom panels show the seismicity distribution versus depth, for the local (orange dots) earthquakes of $M > 3$ and for the remote earthquakes (red dots) of magnitude $M > 3$, $M > 4$, $M > 5$ respectively. Seismicity extracted from the catalog of KOERI.

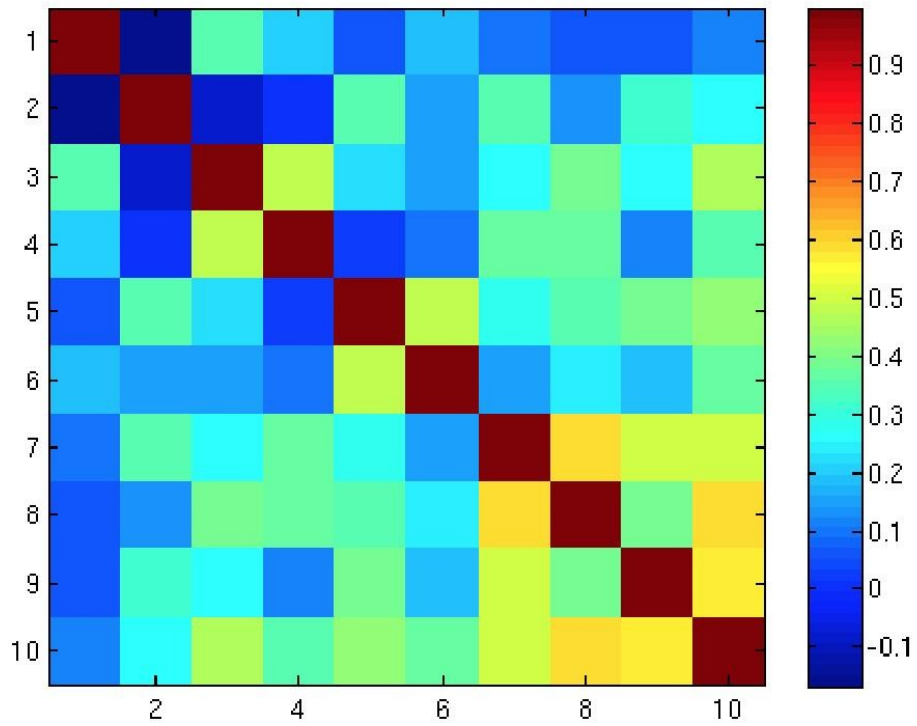


Figure 12: Correlation matrix between the hourly SDE distributions recorded at each OBS and expressed as a function of time. X- and Y-axes are OBS numbers. OBSs 7, 8, 9, 10 appear to be correlated (with correlation Coefficient > 0.5).



Figure 13: Photograph of the seafloor taken with ROV/Victor during the Marsite cruise of R/V *Pourquoi pas?* on the November 11th, 2014 at 13:17:28 UTC, with coordinates LAT : N 40 42.800417 Long : E 29 10.751178 showing the intense biological activity on the Marmara seafloor and an example of langoustine (*Nephrops Norvegicus*).

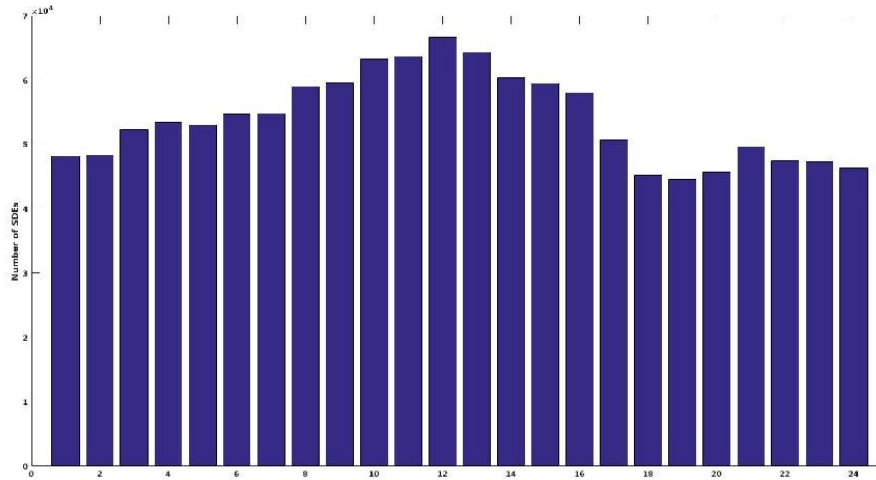


Figure 14: Hourly occurrence of SDEs, stacked over the 10 OBSs and plotted versus the hour of the day (from 0 to 24 hours). The stack is obtained by summing (over the whole recording period and over the 10 OBSs) the number of SDEs that were detected between 00h00 and 01h00, between 01h00 and 02h00, between 02h00 and 03h00, etc.

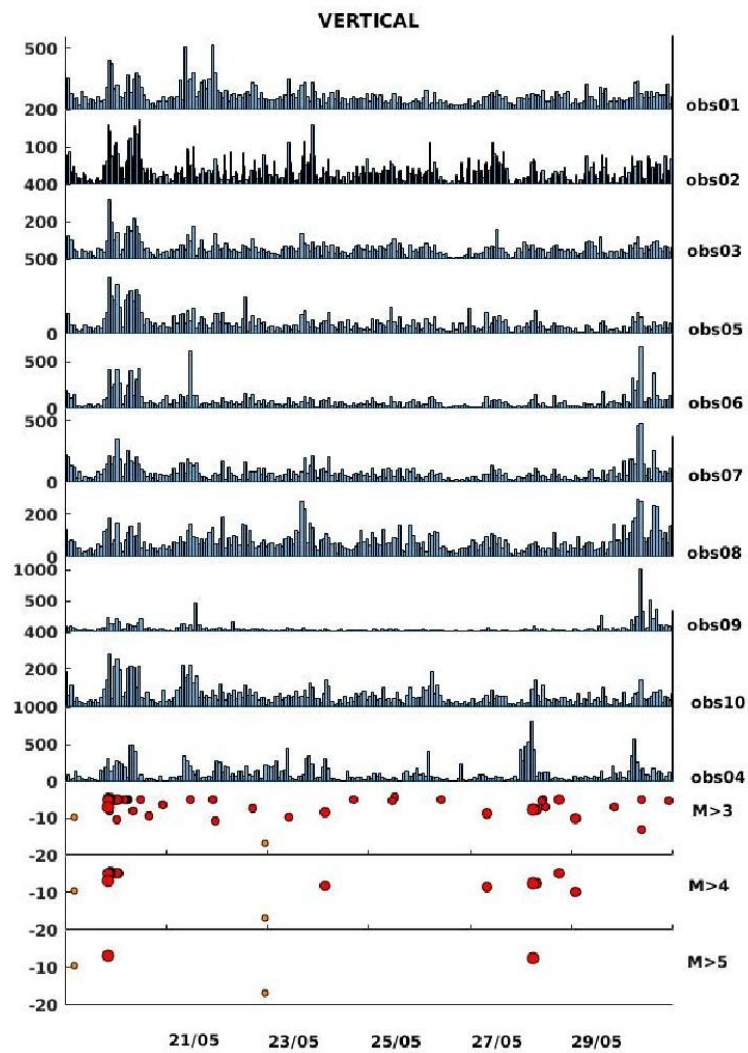


Figure 15a: The upper panels display the number of SDEs per day that were recorded on the geophone components only (families 1 and 2a) at each given OBS (e.g. obs01 to obs04, from west to east) from May 19th to May 30th, detected on the vertical component. The bottom panels show the seismicity distribution versus depth, for the local (orange dots) earthquakes of $M > 3$ and for the remote earthquakes (red dots) of magnitude $M > 3$, $M > 4$, $M > 5$ respectively. Seismicity extracted from the catalog of KOERI.

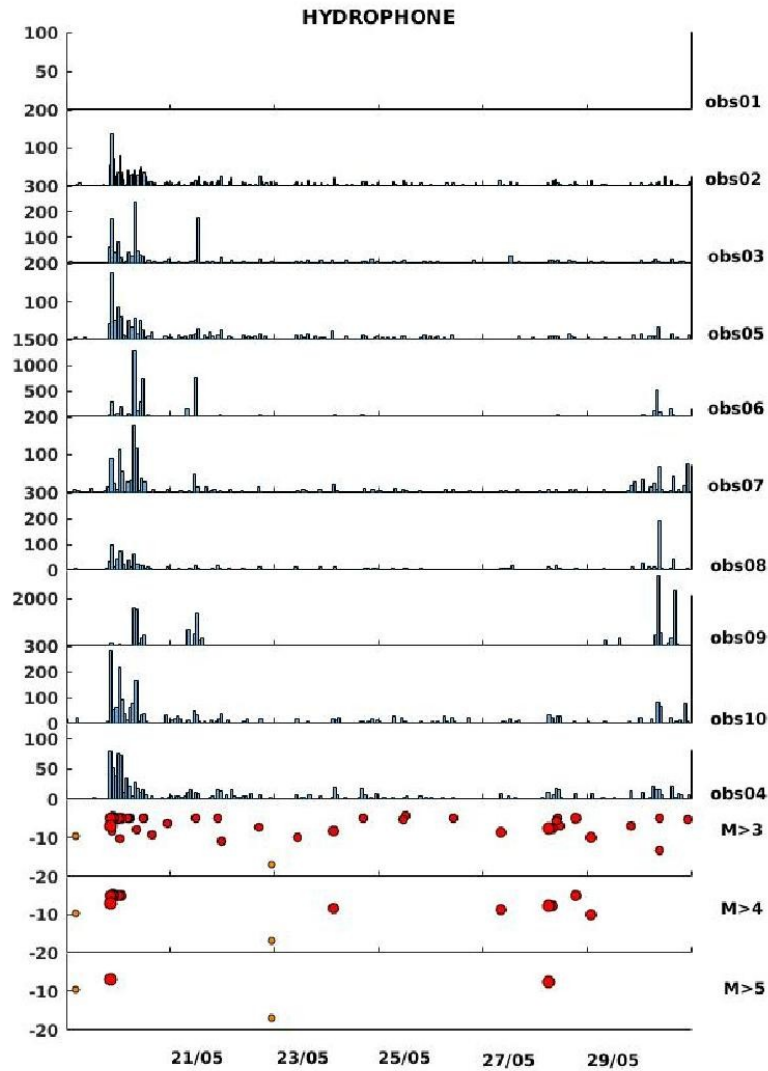


Figure 15b: The upper panels display the number of SDEs per day that were recorded on both the geophone and hydrophone components only (sub-family 2b) at each given OBS (e.g. obs01 to obs04, from west to east) from May 19th to May 30th, detected on the hydrophone component. The bottom panels show the seismicity distribution versus

depth, for the local (orange dots) earthquakes of $M > 3$ and for the remote earthquakes (red dots) of magnitude $M > 3$, $M > 4$, $M > 5$ respectively. Seismicity extracted from the catalog of KOERI.

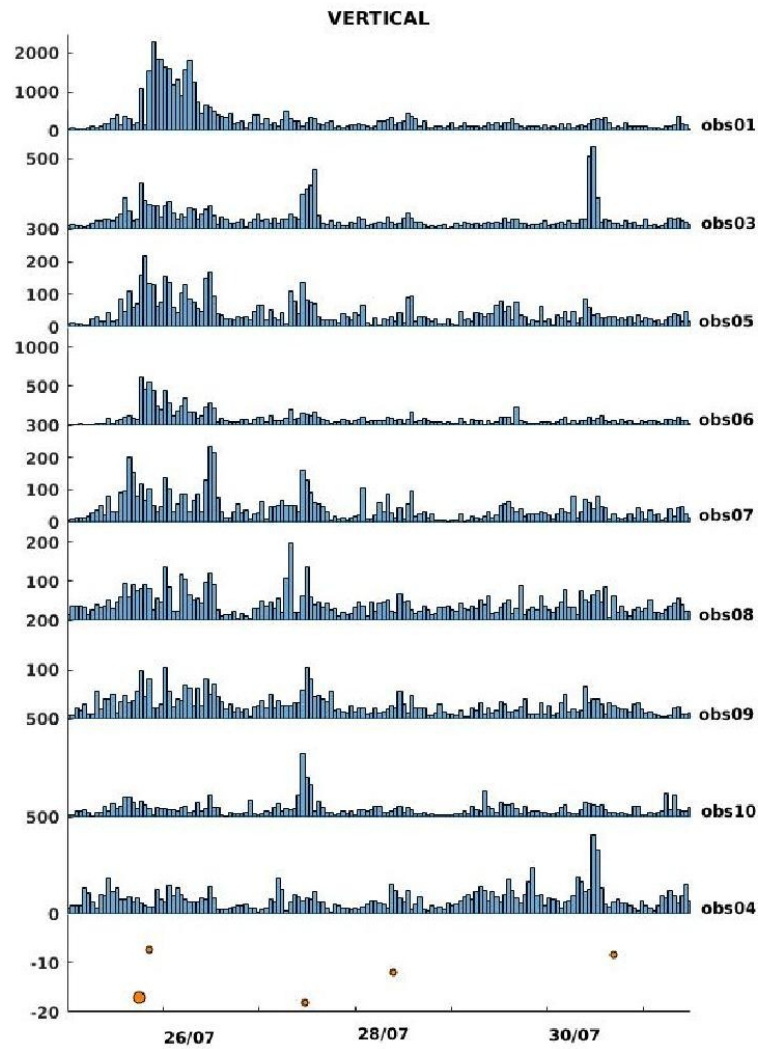


Figure 16a: The upper panels display the number of SDEs per day that were recorded on the geophone components only (families 1 and 2a) at each given OBS (e.g. obs01 to obs04, from west to east) from July 25th to July 31st, detected on the vertical component. The bottom panels show the seismicity distribution versus depth, for the local (orange

dots) earthquakes of $M > 3$ and for the remote earthquakes (red dots) of magnitude $M > 3$, $M > 4$, $M > 5$ respectively. Seismicity extracted from the catalog of KOERI.

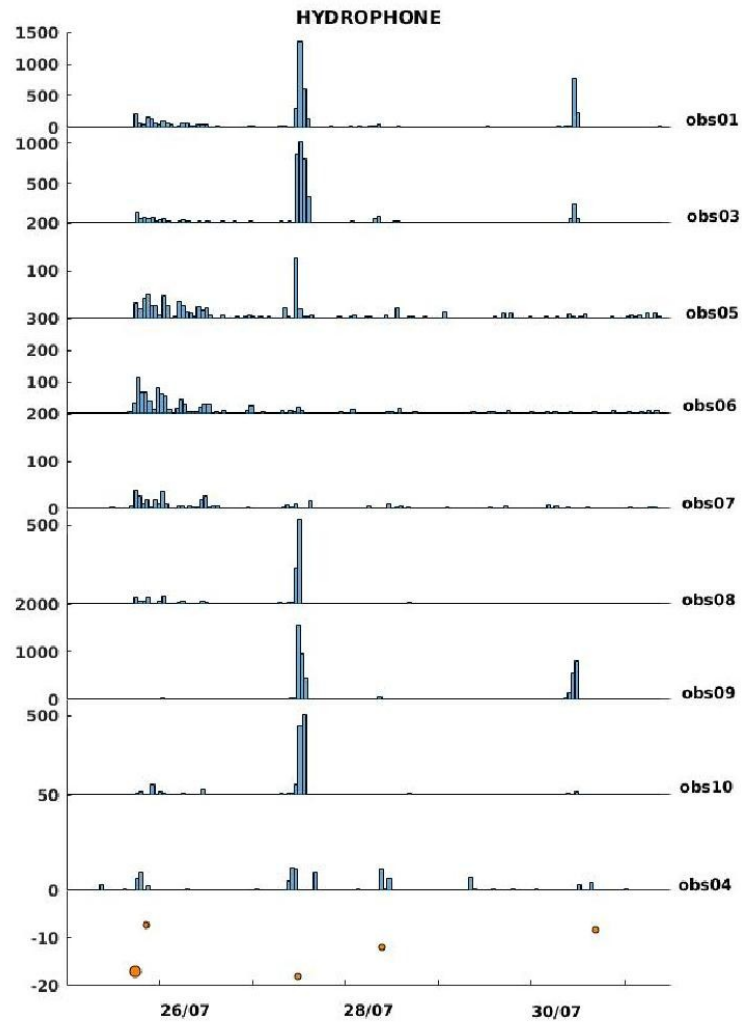


Figure 16b: The upper panels display the number of SDEs per day that were recorded on both the geophone and hydrophone components only (sub-family 2b) at each given OBS (e.g. obs01 to obs04, from west to east) from July 25th to July 31st, detected on the hydrophone component. The bottom panels show the seismicity distribution versus

depth, for the local (orange dots) earthquakes of $M > 3$ and for the remote earthquakes (red dots) of magnitude $M > 3$, $M > 4$, $M > 5$ respectively. Seismicity extracted from the catalog of KOERI.

V. Conclusion and perspectives

V.1 Conclusions

V.1.1 On the importance to improve earthquake location (particularly for shallow seismicity)

The most important outcome of our study is certainly to reveal the importance of shallow seismicity along the western Sea of Marmara, as well as the importance of off-axis seismicity, along secondary faults oblique to the MMF. This has been possible only by using a focused network of OBSs centered on the Western High and a high-resolution velocity model.

To improve earthquake location (particularly shallow seismicity), it is recommended to prefer a network of networks with simple but numerous sensors rather than sophisticated sensors but in limited number, in order to ensure maximum coverage near the MMF.

V.1.2 On the existence of ultra-shallow seismicity within gas prone sediment layers

Our study has revealed the existence of ultra-shallow seismicity occurring in gas-prone sediment layers, in response to a mainshock (of magnitude 5.1 in the present case). Continuous deep seafloor exploration over the last decades has shown that gas is commonly found in shallow sediment layers. Hence, it is reasonable to expect that such ultra-shallow, low-magnitude earthquakes may also occur in other tectonically active settings (e.g. at subduction zones, for instance), wherever gas is present in shallow layers.

V.1.3 On the mechanical behaviour of the western segments of the SoM

A number of critical questions remains regarding the mechanical behavior of the different segments

of the 140 km long, submerged section of the fault. Namely: which segment is currently locked? which one is creeping? In contrast to offshore domains in other geological settings (e.g. the San Andreas Fault), the presence of water cover above the fault trace within the SoM limits the use of standard geodetic measurements within a 10 to 20 km wide stripe along the fault (e.g. [Klein et al, 2017]) and hence complicates the characterization of the fault's behavior since the strain accumulation and slip deficit cannot be directly estimated.

For addressing this question, numerous studies have been carried out the last years by using different approaches. Based on local seismicity recordings and on the use of land-based geodetic measurements, [Bohnhoff et al, 2013] and [Ergitav et al, 2014], respectively, interpreted the eastern portion of the MMF, that corresponds to the Princess island segment offshore Istanbul, as a locked patch over a creeping base. In addition, an innovative effort was the study by [Sakic et al, 2016], which was based on a seafloor acoustic ranging experiment, by using ten transponders, installed at a depth of 800 m, in the central part of the SoM (e.g. along the submarine Istanbul-Silivri fault segment) for monitoring distance variations along 15 baselines, from november 2014 to December 2017 (e.g. 3 years in total). Their preliminary results (e.g. 6 months of data) derived from forward modeling, showed that the data better fit a locked state or a very moderate surface creep, indicating that the Istanbul-Siliviri fault segment is currently accumulating stress.

The question (locked versus creeping) fault has also been addressed by studying repeating micro- and local earthquakes, since highly correlated repeating events constantly activate the same patch of an active fault portion and could therefore be considered as an indicator for identifying and evaluating the amount of fault creep (e.g. [Bohnhoff, M., et al, 2017]). In regard to this, [Schmittbuhl et al, 2016] and [Bohnhoff et al, 2017] have proposed that the western Marmara section is creeping based on the observation of small-magnitude repeating earthquakes at the central Basin. This view is consistent with the one proposed by [Schmittbuhl et al, 2015], who also proposed that the western segments were creeping, while the eastern segments could be locked.

Our results do not contradict (but do not demonstrate) this view.

V.1.4 On the strange, short duration events recorded by the OBSs

Our study has demonstrated the existence of “background SDEs”, occurring on a regular basis (e.g. a few tens to hundreds times a day). OBSs are very sensible to any perturbation affecting the seafloor sediments, hence background SDEs resulting from different causes, e.g.: bioturbation; relative motion of seafloor sediment grains in response to bottom currents or to biological activity; cavity collapse with the near surface sediments; etc. “Background SDE activity” may be enhanced in response to external causes, such as earthquakes, which may also produce natural degassing from the seafloor.

Our study has also revealed that, in contrast to what was reported by [Tary *et al*, 2012], SDEs may also be recorded by the hydrophones. Most particularly, we have documented a class of SDEs characterized by signals that occur repeatedly at a period of one event every ~ 2 seconds. To date, however, we are unable to explain the origin of such SDEs, as many different scenarios may be proposed (e.g. anthropogenic sources, biological sources –among which marine mammals-, tremors, etc.) . The correlation between “periodic SDEs” and earthquakes is not precluded, but still to be proven.

V.2 Perspectives for future research

The present study has revealed new insights on the micro-seismicity and on the deep seafloor processes at work in the western part of the SoM. It has also revealed a number of puzzling observations that pave the road for future research. The most important points to address are listed below:

V.2.1 Investigating the role of triggering effects on micro-seismicity

Puzzling observations reported in § III.1.3.2 suggest that earthquakes of moderate magnitude ($\sim M_1$ 4) along the Ganos Fault could trigger swarms of low magnitude ($\sim 1 < M_1 < 2$) events in the western part of the SoM ; similarly, the M_w 5.8 Kütahya earthquake, which struck the Simav area at an estimated depth of 9 km on 2011, May, 19th, was followed by a crisis of shallow seismicity and SDEs within the Central Basin. Such coincidences remain unexplained. Further research, based on statistics, and also on modelling, is needed to determine if the coincidence is purely fortuitous, or if it results from a causative correlation.

V.2.2 Investigating ultra-shallow seismicity by joint modelling of OBS/piezometer data

A unique data set, including piezometer data and OBS data, was acquired within the Marsite Programme, from October 2013 to November 2014. During this PhD study, we did not have time for modelling the unique, combined dataset (including piezometer data and OBS data) that was acquired by Ifremer and INGV from October 2013 to November 2014. Such modelling could certainly contribute to investigate the response of shallow sediments to remote earthquakes.

V.2.3 Further analysis and modelling of SDEs

Our visual analysis of the OBS data has revealed many puzzling observations regarding the occurrence of SDEs that still remain unexplained. Our analysis was carried out at the end of the *PhD* work and based on visual correlations. Due to the lack of time, we could not develop the appropriate methodology to definitely prove that a systematic correlation exists between “swarmed SDEs”, “periodic SDEs” and earthquake (remote or local). We did not either have the time for numerical modelling.

Therefore, the perspectives for future work are many, to develop the appropriate methods:

- For the automatic detection and characterization of SDEs, including the discrimination between the different types of SDEs: “background”, “swarmed” and “periodic”.
- For locating the source of “swarmed SDEs” and “periodic SDEs”, using noise correlation analysis method.
- For the modelling (numerical and analogical) of SDEs, in order to test the different hypotheses on their origin and physical mechanism:
 - “swarmed SDEs” have been hypothesized to occur in response to earthquakes
 - “periodic SDEs” are supposed to be related to many possible causes: anthropogenic sources; marine animals (e.g. mammals, fishes); but also tremors from the MMFs; fluid emissions; etc. All the hypotheses need to be tested.

References

- Agurto-Detzel, H., M. Bianchi, G. A. Prieto, and M. Assumpção (2017), Earthquake source properties of a shallow induced seismic sequence in SE Brazil, *J. Geophys. Res. Solid Earth*, **122**, doi:10.1002/2016JB013623.
- Akyüz, H.S., et al, (2000). Field observations and slip distribution of the November 12, 1999 Duzce earthquake (M=7.1) Bolu Turkey. The 1999 Izmit and Duzce Earthquake : preliminary results (Ed. Barka, A., Kocaci, O., Akyuz, S.).
- Aksu, A.E., et al, (2000). Anatomy of the North Anatolian fault zone in the Marmara Sea, Western Turkey: Extensional basins above a continental transform, *GSA Today*, **10**, 6, 1-2.
- Alpar, B., (1999). Underwater signatures of the Kocaeli Earthquake (August 17th 1999), *Turkish, J. Mar. Sci.*, **5**, 111-130.
- Aochi, H., and Ulrich, T. (2015). A Probable Earthquake Scenario near Istanbul Determined from Dynamic Simulations, *Bull. Seism. Soc. Am.* **105**,1468-1475, doi:10.1785/0120140283.
- Aretusini, S., S. Mitterpergher, O. Pimper, E. Spagnuolo, A. F. Gualtieri, and G. Di Toro (2017), Production of nanoparticles during experimental deformation of smectite and implications for seismic slip, *Earth and Planetary Science Letters*, **463**, 221–231, doi:10.1016/j.epsl.2017.01.048.
- Barka, A., (1996). Slip distribution along the North Anatolian Fault associated with the large earthquakes of the period 1939 to 1967, *Bull. Seism. Soc. Am.*, **86**, 1238-1254.
- Barka et al, (2000a). The August 17, 1999 Izmit earthquake, M = 7.4, Eastern Marmara region, Turkey: study of surface rupture and slip distribution. See Barka et al. 2000b, pp. 15–30.
- Bayrakci, G., et al, (2014). Acoustic monitoring of gas emissions from the seafloor. Part II: a case

study from the Sea of Marmara, *Mar. Geophys. Res.*, **35**, 211-229,
doi: 10.1007/s11001-014-9227-7.

Bécel, A., (2006). Structure Sismique de la Faille Nord Anatolienne en Mer de Marmara,
Phd Thesis, Institut de Physique du Globe de Paris.

Bécel, A., et al, (2010). North Marmara Trough architecture of basin infill, basement and faults,
from PDSM reflection and OBS refractions seismics, *Tectonophysics*, **490**: 1-14.

Blouin, A. (2015). Compte-rendu: contexte géologique et déplacements de fluides autour des
piézomètres Ifremer (Western High, Mer de Marmara). Stage en entreprise de dixième
année, ENSG.

Bohnhoff, M., et al, (2013). An earthquake gap south of Istanbul. *Nature Communications*, **4**, doi:
10.1038/ncomms2999.

Bonhoff, M., et al, (2017), Repeating Marmara Sea Earthquakes: Indications for fault creep,
Geophysical Journal International, **210**, 332-339, doi.org/10.1093/gji/ggx169.

Bourry, C., et al, (2009). Free gas and gas hydrates from the Sea of Marmara, Turkey: Chemical and
structural characterization. *Chem. Geol.*, doi:10.1016/j.chemgeo.2009.03.007.

Bowman D.C. and Wilcock S.D., (2013), Unusual signals recorded by ocean bottom seismometers in
the flooded caldera of Deception Island volcano : volcanin gases or biological activity?
Antartic Science **23(3)**, 267-275, doi:10.1017/S0954102013000758

Buskirk R.E., et al (1981), Evidence that biological activity affects Ocean Bottom Seismograph
Recordings, *Marine Geophysical Researches* **5**, 189-205.

Çagatay, M.N., (2000). Glacial–Holocene palaeoceanography of the Sea of Marmara: timing of
connections with the Mediterranean and the Black Sea. *Mar. Geol.* **167**,191–206

Çagatay, M.N., et al, (2009). Late Pleisto-cene–Holocene evolution of the northern shelf of the Sea
of Marmara: *Marine Geology*, v. **265**, p. 87–100, doi:10.1016/j.margeo.2009.06.011.

- Carton, H. et al, (2007). Seismic imaging of the three-dimensional architecture of the Çınarcık Basin along the North Anatolian Fault: *Journal of Geophysical Research, Solid Earth*, v. **112**, B06101, doi:10.1029/2006JB004548.
- Caselatto, A., (2014). Relations between gas emissions and seismicity within the Sea of Marmara, Rapport de fin d'études d'ingénieur, ENSTA-Bretagne / Mémoire de Stage de Master-2, Université de Bretagne Occidentale.
- Cros, E., and Géli, L. (2013). Characterization of microseismicity in the Western Sea of Marmara: implications in terms of seismic monitoring, Project Report, Institut Carnot Ifremer-Edrome, Abondement 2011, N°06/11/2013, 29 pages.
- De Landro, G., et al, (2015). High precision Differential Earthquake Location in 3D models: Evidence for a rheological barrier controlling the microseismicity at the Irpinia fault zone in southern Apennines, *Geophys. J. Int.*, **203 (3)**: 1821-1831, doi: 10.1093/gji/ggv397.
- D'Alessandro A., et al, (2009), The INGV's new OBS/H: Analysis of the signals recorded at the Marsili submarine volcano, *J. Volcanol. Geotherm. Res*, doi:10.1016/j.jvolgeores.2009.02.008
- Dupré S., et al, (2015). Tectonic and sedimentary controls for widespread gas emissions in the Sea of Marmara, Results from systematic, ship-borne multibeam echosounder water column imageries, *J. Geophys. Res., Solid Earth*, **120**, doi:10.1002/2014JB011617.
- Egeran N., and Lahn E., (1944). Note sur la carte sismique de la Turquie, *Bull. Min. Res. Explor. Inst. Turkey* **9**,65-63.
- Embriaco, D., et al, (2013) Monitoring of gas and seismic energy release by multiparametric benthic observatory along the North Anatolian Fault in the Sea of Marmara (NW Turkey), *Geophys. J. Int.*, doi: 10.1093/gji/ggt436.
- Ergitav, S., et al, (2014). Istanbul's earthquake hot spots: Geodetic constraints on strain

accumulation along faults in the Marmara seismic gap, *Geophys. Res. Lett.*, 41, 5783–5788, doi:10.1002/2014GL060985.

Eyidogan, H., et al, (1991). Türkiye büyük depremleri makro-sismik rehberi (1900–1988) (in Turkish), Istanbul Technical University, Faculty of Mining, Department of Geological Engineering. Kurtis Matbaasi, Istanbul, 198 pp.

Faulkner, D. R., T. M. Mitchell, J. Behnsen, T. Hirose, and T. Shimamoto (2011), Stuck in the mud? Earthquake nucleation and propagation through accretionary forearcs, *Geophys. Res. Lett.*, 38(18), doi:10.1029/2011GL048552.

Fischer, T., C. Matyska, and J. Heinicke (2017), Earthquake-enhanced permeability – evidence from carbon dioxide release following the ML 3.5 earthquake in West Bohemia, *Earth and Planetary Science Letters*, 460, 60–67, doi:10.1016/j.epsl.2016.12.001.

Franek P., et al, (2014). Character of seismic motion at a location of a gas hydrate-bearing mud volcano on the SW Barents Sea margin. *Jour. of Geoph. Res.: Solid Earth*, doi:10.1002/2014JB010990

Gambino, S., Cammarata L. and Rapisarda, S., (2009), High precision locations of long-period events at La Fossa Crater (Vulcano Island, Italy), *Annals of Geophysics*, 2, 137-147.

Garagash, D. I., and L. N. Germanovich (2012), Nucleation and arrest of dynamic slip on a pressurized fault, *J Geophys Res*, 117(B10), 4221–27, doi:10.1029/2012JB009209.

Geist, E. L., and S. L. Bilek (2001), Effect of depth-dependent shear modulus on tsunami generation along subduction zones, *Geophys. Res. Lett.*, 28(7), 1315–1318, doi:10.1029/2000GL012385.

Géli, L., et al, (2008). Gas emissions and active tectonics within the submerged section of the North Anatolian Fault zone in the Sea of Marmara. *Earth Planet. Sci. Lett.*, 274 (1-2): 34-39.

Géli, L., et al, (2018). Gas related seismicity within the Istanbul seismic gap, submitted to *Nature*

Scientific Reports (in press).

Grall, C., et al, (2012). Heat flow in the Sea of Marmara Central Basin, possible implications for the tectonic evolution of the North Anatolian Fault, *Geology*, 40:3-6,

doi:10.1130/G32192.32191.

Halbach, P.E., et al, (2004). Migration of the sulphate–methane reaction zone in marine sediments of the Sea of Marmara-can this mechanism be tectonically induced?, *Chem. Geol.*, **205** (1-2), 73-82.

Havskov, J., and Ottemoller, L., (1999). Seisan earthquake analysis software, *Seismol. Res. Lett.*, **70** (5), 532-534.

Helmstetter, A., et al, (2002). Is Earthquake Triggering Driven by Small Earthquakes? *Phys. Rev. Lett.*, DOI: [10.1103/PhysRevLett.91.058501](https://doi.org/10.1103/PhysRevLett.91.058501).

Imren, C.X., et al, (2001). The North Anatolian Fault within the Sea of Marmara: A new interpretation based on multi-channel seismic and multi-beam bathymetry data, *Earth Planet. Sci. Lett.*, **186**, (2), 143-158.

Jaeger, J. C., N. Cook, and R. Zimmerman (2007), *Fundamentals of rock mechanics*.

Karabulut, H., et al, (2011). Evolution of the seismicity in the eastern Marmara Sea a decade before and after the 17 August 1999 Izmit earthquake, *Tectonophysics*, **510**, 17–27.

Karabulut, H., and Aktar, M., (2013). Strategies and tools for Real Time Earthquake Risk Reduction (REAKT), Eu-Funded Project, FP7/2007-2013, Theme: ENV.2011.1.3.1-1, Deliverable D2.2, 22/03/2013.

King, G.C.P., et al, (1994). Static stress changes and the triggering of earthquakes, *Bull. Seism. Soc. Am.* **84**, 3, 935-953.

Klein, E., et al, (2017). Aseismic slip and seismogenic coupling in the Marmara Sea: What can we learn from onland geodesy? *Geoph. Res. Lett.*, doi:10.1002/2017GL072777.

- Kusçu, I., et al, (2005). Seafloor gas seeps and sediment failures triggered by the August 17, 1999 earthquake in the Eastern part of the Gulf of Izmit, Sea of Marmara, NW Turkey. *Mar. Geol.* 215, 193–214.
- Le Pichon, X., et al, (2001). The active Main Marmara Fault, *Earth Planet. Sci. Lett.*, **192**, 595–616.
- Le Pichon, X., et al, (2003). The North Anatolian fault in the Sea of Marmara, *Journal of Geophysical Research-Solid Earth*, **108** (B4), p.2179.
- Lienert, B.R., and Havskov, J., (1995). , A computer program for locating earthquakes both locally and globally, *Seismol. Res. Lett.*, 66(5), 26–36.
- Lomax, A., et al, (2009). Earthquake Location, Direct, Global-Search Methods, in *Complexity In Encyclopedia of Complexity and System Science, Part 5*, Springer, New York, pp. 2449-2473, doi:10.1007/978-0-387-30440-3.
- Lomax, A., (2014). Mise en oeuvre et support pour logiciels de traitement automatisé de données sismologiques acquises dans le cadre du projet Européen FP7 Marsite, Contract report, Reference CNRS, MA201301A.
- Meade, B.J., et al, (2002). Estimates of seismic potential in the Marmara Sea region from block models of secular deformation constrained by Global Positioning System measurements, *Bull. Seismol. Soc. Am.*, **92** (1), 208–215.
- Okada, Y. (1992), Internal deformation due to shear and tensile faults in a half-space, *Bulletin of the Seismological Society of America*, **82**(2), 1018–1040.
- Okay, A.I., et al, (1996). Paleo- and Neo-Tethyan events in northwest Turkey: Geological and geochronological constraints. In A. Yin & M. Harrison (Eds.) *Tectonics of Asia*, 420-441, Cambridge: Cambridge University Press.
- Okay, A.I., and Tuysuz, O., (1999). Tethyan sutures of northern Turkey. In “The Mediterranean Basins: Tertiary extension within the Alpine orogen” (eds. B. Durand, L. Jolivet, F. Horvath

and M. Séranne), *Geological Society, London*, Special Publication **156**, 475-515

Parsons, I. D., J. F. Hall, and G. A. Lyzenga (1988), Relationships between the average offset and the stress drop for two- and three-dimensional faults, *Bulletin of the Seismological Society of America*, *78*(2), 931–945.

Rangin et al, (2004). Strain localization in the Sea of Marmara: Propagation of the North Anatolian Fault in a now inactive pull-apart: *Tectonics*, v. **23**, TC2014, doi:10.1029/2002TC001437.

Remitti, F., S. A. F. Smith, S. Mittempergher, A. F. Gualtieri, and G. Di Toro (2015), Frictional properties of fault zone gouges from the J-FAST drilling project (M w9.0 2011 Tohoku-Oki earthquake), *Geophys. Res. Lett*, *42*(8), 2691–2699, doi:10.1002/2015GL063507.

Rice, J.R., Cleary, M.P., 1976. Some basic stress diffusion solutions for fluid-saturated elastic porous media with compressible constituents, *Reviews of Geophysics and Space Physics*, *14*(2), 227-241. doi:10.1029/RG014i002p00227.

Romano, F., E. Trasatti, S. Lorito, C. Piromallo, A. Piatanesi, Y. Ito, D. Zhao, K. Hirata, P. Lanucara, and M. Cocco (2014), Structural control on the Tohoku earthquake rupture process investigated by 3D FEM, tsunami and geodetic data, *Sci. Rep.*, *4*, doi:10.1038/srep05631.

Saffer, D. M., D. A. Lockner, and A. McKiernan (2012), Effects of smectite to illite transformation on the frictional strength and sliding stability of intact marine mudstones, *Geophys. Res. Lett*, *39*(11), L11304, doi:10.1029/2012GL051761.

Sakic, P., et al, (2016). No significant steady state surface creep along the North Anatolian Fault offshore Istanbul: Results of 6 months of seafloor acoustic ranging, *Geophys. Res. Lett.*, *43*, 6817–6825, doi:10.1002/2016GL069600.

Şaroğlu et al, (1987). Türkiye'nin diri faylari ve depremsellikleri, Min. Res. Expl. Inst. Turkey

Rept. No. 8174.

Şaroğlu et al, (1992). The East Anatolian fault zone of Turkey, *Ann. Tectonicae*, **VI**, 99–125.

Sato, T., et al, (2004), A study of microearthquake seismicity and focal mechanisms within the Sea of Marmara (NW Turkey) using ocean bottom seismometers (OBSs), *Tectonophysics*, **391:303**, 314. doi:10.1016/j.tecto.2004.07.018.

Sengör, A.M.C. and Yilmaz, Y., (1981). Tethyan evolution of Turkey : A plate tectonic approach. *Tectonophysics*, **75**, 181-241

Şengör, A. M. C., et al, (2005), The North Anatolian Fault: A new look, *Annu. Rev. Earth Planet. Sci.*, **33**, 37–112, doi:10.1146/annurev.earth.32.101802.120415.

Şengör, A.M.C., et al, (2011). Broad shear zones and narrow strike-slip faults in orogens and their role in forming the orogenic architecture: The North Anatolian Fault as an active example, Joint Meeting GeoMunich, Fragile Earth. Geological Processes from Global to Local Scales, associated Hazards and Resources, 14-2, A18, Munich, Germany, September 4–7.

Şengör, A. M. C., et al, (2014). The geometry of the North Anatolian transform fault in the Sea of Marmara and its temporal evolution: Implications for the development of intracontinental transform faults, *Can. J. Earth Sci.*, **51**(3), 222–242, doi:10.1139/cjes-2013-0160

Schmittbuhl, J., et al, (2015). Seismicity distribution and locking depth along the Main Marmara Fault, Turkey, , *Geochemistry, Geophysics, Geosystems*, DOI:10.1002/2015GC006120

Schmittbuhl, J., et al, (2016). Long-lasting seismic repeaters in the Central Basin of the Main Marmara Fault, *Geophys. Res. Lett.*, **43**, 9527–9534, doi:10.1002/2016GL070505.

Schorlemmer, D., and Wiemer, S., (2005). Microseismicity data forecast rupture area, *Nature*, **434**, doi:10.1038/nature03581.

Sibson, R., and G. Xie (1998), Dip range for intracontinental reverse fault ruptures: truth not stranger than friction, *Bulletin of the Seismological Society of America*, **88**(4), 1014–1022.

- Sultan, N., et al, (2011). Dynamics of fault-fluid-hydrate system around a shale-cored anticline in deepwater Nigeria, *J. Geoph. Reas.*, **116**, B1210, doi:10.1029/2011JB008218.
- Tary, J.-B., et al, (2011). Sea-Bottom Observations from the Western Escarpment of the Sea of Marmara, *Bull. Seism. Soc. Am.*, **101** (2), 101, 775-791, doi:10.1785/0120100014.
- Tary, J.-B., et al, (2012). Micro-events produced by gas migration and expulsion at the seabed: a study based on sea bottom recordings from the Sea of Marmara, *Geophys. J. Int.*, doi: 10.1111/j.1365-246X.2012.05533.x
- Thomas, Y., et al, (2012). Contribution of high-resolution 3D seismic near-seafloor imaging to reservoir scale studies: application to the active north Anatolian Fault, Sea of Marmara, *Near Surface Geophysics*, **10**, 291-301, doi:10.3997/1873-0604.2012019.
- Ujiiie, K., and G. Kimura (2014), Earthquake faulting in subduction zones: insights from fault rocks in accretionary prisms, *Prog Earth Planet Sci*, *1*(1), 7–30, doi:10.1186/2197-4284-1-7.
- Zitter, T.A.C., et al, (2008). Cold seeps along the main Marmara Fault in the Sea of Marmara (Turkey). *Deep Sea Research Part I: Oceanographic Research Papers* **55**, 552–570.
- Viesca, R. C., and J. R. Rice (2012), Nucleation of slip-weakening rupture instability in landslides by localized increase of pore pressure, *J Geophys Res*, *117*(B3), 255–21, doi:10.1029/2011JB008866.
- Vreme, A., B. Pouligny, F. Nadal, and G. Liger-Belair (2015), Does shaking increase the pressure inside a bottle of champagne? *Journal of Colloid and Interface Science*, *439*, 42–53, doi:10.1016/j.jcis.2014.10.008.
- Waldhauser, F., and Ellsworth, W.L., (2000). A double-difference earthquake location algorithm: Method and application to the northern Hayward fault, California, *Bull. Seismol. Soc. Am.*, **90** (6), 1353-1368.

Yamamoto, Y., et al, (2017). Geometry and segmentation of the North Anatolian Fault beneath the Marmara Sea, Turkey, deduced from long-term ocean bottom seismographic observations, *JGR*, doi:10.1002/2016JB013608.

Yilmaz, I., and M. Üstünkaya (2004), Unconsolidated clays from the inner shore of the Gemlik Gulf in the Marmara Sea (Bursa-Turkey), *Bull Eng Geol Environ*, 63(2), doi:10.1007/s10064-004-0229-6.

Titre de la thèse: Micro-seismicité et processus de fond de mer dans la partie ouest de la Mer de Marmara: nouveaux résultats fondés sur l'analyse des données de sismographes et hydrophones sous-marins

RÉSUMÉ

Depuis les séismes dévastateurs de 1999 d'Izmit et de Duzce, la partie immergée de la Faille Nord Anatolienne (FNA) en Mer de Marmara fait l'objet d'une intense surveillance. Malgré cela, la micro-sismicité demeure mal connue. Par ailleurs, alors que la connexion avec le système pétrolier du Bassin de Thrace est établie, le rôle du gaz sur la sismicité n'a pas été identifié.

Dans ce travail, nous avons analysé des données d'OBS (Ocean Bottom Seismometers) acquises dans la partie ouest de la Mer de Marmara (en avril-juillet 2011 et septembre-novembre 2014), à partir de méthodes non-linéaires -NonLinLoc- et d'un modèle 3D de vitesses. Une grande partie de la sismicité se produit à des profondeurs inférieures à 6 km environ : le long de failles secondaires, héritées de l'histoire complexe de la FNA ; ou dans des couches de sédiments superficiels (< 1 km) riches en gaz. Cette sismicité superficielle semble être associée à des processus liés au gaz, déclenchés par les séismes profonds de magnitude $M_1 > 4.5$ qui se produisent régulièrement le long de la MMF.

Par ailleurs, 2 familles de signaux de courte durée (<1s), dits « SDE » (pour Short Duration Event) apparaissent sur les enregistrements : 1) les SDE se produisant à raison de quelques dizaines de SDE/jour, en réponse à des causes locales (i.e. bioturbation, activité biologique, micro-bullage de fond de mer, mouvements à l'interface eau/sédiment), etc ; 2) les SDE se produisant par «paquets», dont certains sont enregistrés sur les 4 composantes (y compris l'hydrophone) et apparaissent de manière périodique, toutes les 1.8 s environ, en réponse à diverses causes qui restent à déterminer (parmi lesquelles : les mammifères marins ; l'activité humaine ; la sismicité ; le dégazage ; les «trémors» sismiques ; etc).

Mots-clés: *micro-seismicité, localisation, sismomètres de fond de mer, sismicité induite par le gaz.*

Dissertation's Title: Micro-seismicity and deep seafloor processes in the Western Sea of Marmara: insights from the analysis of Ocean Bottom Seismometer and Hydrophone data

ABSTRACT

Since the devastating earthquakes of 1999, east of Istanbul, the submerged section of the North Anatolian Fault (NAF), in the Sea of Marmara (SoM) has been intensively monitored, mainly using land stations. Still, the micro-seismicity remains poorly understood. In addition, although the connection of the SoM with the hydrocarbon gas system from the Thrace Basin is now well established, along with the presence of widespread gas within the sedimentary layers, the role of gas on seismicity is still not recognized.

Here, we have analyzed Ocean Bottom Seismometer (OBS) data from two deployments (April-July 2011 and September-November 2014) in the western SoM. Based on a high-resolution, 3D-velocity model, and on non-linear methods (NonLinLoc), our location results show that a large part of the micro-seismicity occurs at shallow depths (< 6 to 8 km): along secondary faults, inherited from the complex history of the North-Anatolian shear zone; or within the uppermost (< 1 km), gas-rich, sediment layers. Part of this ultra-shallow seismicity is likely triggered by the deep earthquakes of intermediate magnitude ($M_1 > 4.5$) that frequently occur along the western segments of the MMF.

In addition, OBSs also record at least two families of short duration (<1 sec) events (SDEs): 1) "background SDEs" occurring on a permanent, at a rate of a few tens of SDEs/day, resulting from many possible, local causes, e. g.: degassing from the seafloor, biological activity near the seabed, bioturbation, etc; 2) "swarmed SDEs", among which some are recorded also on the hydrophone, and characterized by a periodicity of ~ 1.8 seconds. The causes of these SDEs still remain to be determined (among which: anthropogenic causes, marine mammals, gas emissions, regional seismicity, tremors from the MMF, etc).

Keywords: *micro-seismicity, earthquake location, ocean bottom seismometers, gas-related seismicity*